Modelling of Adsorption of Atomic and Molecular Species on Defective Surfaces

Julian Gaberle

A dissertation submitted in partial fulfillment

of the requirements for the degree of

Doctor of Philosophy

of

University College London.

Department of Physics and Astronomy

University College London

January 24, 2019

I, Julian Gaberle, confirm that the work presented in this thesis is my own. Where information has been derived from other sources, I confirm that this has been indicated in the work.

Abstract

This thesis focuses on the study of adsorption phenomena on pristine and defective surfaces with respect to surface reactions, functionalisation and thermodynamic stability. For that purpose the thesis is split into three parts:

Part I discusses entropic effects to molecular adsorption. Free energy profiles were calculated using classical potentials and molecular dynamics simulations for two large organic molecules and the entropic contribution to adsorption was derived, which was used to explain dewetting behaviour at higher temperatures. Furthermore, the entropic contributions to step adhesion and dimer formation were calculated for one of the molecules. It is shown that entropic effects counteract step adhesion enthalpies and lead to desorption above room temperature, whereas dimers retain some rotational and translational entropy and are thus stable even at higher temperatures. These results are important for self-assembled films, where entropic contributions dictate film stability at room temperature.

Part II investigates the rutile TiO_2 (110) surface and how surface reduction impacts Ti interstitial defect formation and diffusion from the surface to the bulk. Point defects were calculated in the bulk as well as at a surface of TiO_2. The barrier for Ti interstitial formation is significantly lowered for reduced (110) surfaces and their diffusion barrier rapidly recovers bulk diffusion due to effective screening of the Ti vacancy and the interstitial.

In Part III point defects in black phosphorus, a novel 2D material, are studied as well as how their presence influences adsorption of O_2, H_2O, H_2 and H atoms in the context of surface degradation. Comparing first principles calculations to experimental data, observed defects could be attributed to SnP defects. Furthermore, the degradation mechanism under ambient conditions was found to be exothermic, leading to rapid oxidation of the surface and subsequent decomposition into phos-

phoric acid. These results are relevant for future applications of black phosphorus, since its instability hinders its integration into novel technologies.

Impact Statement

This thesis entails work from three collaborative projects researching molecular adsorption on pristine and defective crystal surfaces. Part I is investigating how entropy affects molecular adsorption and inter-molecular interactions for large organic molecules via classical molecular dynamics and thermodynamic integration calculations. The presented results are important for the research community of self-assembled molecules on insulating substrates, as they highlight the need to consider entropic contributions. Counterintuitive relationships were found for step adhesion, which signifies that entropic contributions are difficult to predict a priori.

In Part II the influence of surface phenomena on the bulk crystal is examined. Surface reduction of TiO_2 facilitates the formation of Ti interstitials (Ti_i), which can diffuse into the bulk and alter the electronic properties of the material. The presented work confirms an experimentally proposed mechanism through first principle's calculations. Therefore, it is of particular relevance to the academic community, but also is important for the future development of many real world applications such as gas sensors, catalysis, solar cells and coatings.

2D materials and particularly black phosphorus have seen rapid increase in research interest due to their potential application in ultra-thin electronics, energy storage materials or biomedical applications. To that purpose the fundamental properties of black phosphorus need to be understood. The data presented in Part III predicts Sn impurities to be the main source of defects in the material, matching scanning tunnelling experiments and confirming experimentally observed p-doping. Tin is implanted in the crystal during growth, thus emphasising the need to improve the crystal growth process in order to obtain pristine black phosphorus. Inversely, the presented work lays the groundwork for doping studies to produce magnetic monolayers or p-n junctions.

Acknowledgements

Over the past four years I have been very fortunate to have been working with a number of people, whose guidance and help was and is invaluable. First and foremost my supervisor Alex Shluger, whose supervision and expertise set the foundation to my success. Looking back over the past four years I spend as a researcher in his group, I feel deeply indebted to his unabating support, be it professional or personal. Secondly, I would like to extend my sincere gratitude to Prof. Masahiko Tomitori and Prof. Ryo Maezono, who supervised me during my time at JAIST, Japan and who forgave the occasional yet inevitable cultural faux-pas.

A special thanks to David Gao for countless discussions and day-to-day help in the office, without whom this work would not have been possible. Thanks also to Christian Loppacher, Alexander Schwarz, Mark Wentink, Steven Schofield, Tony Kenyon, Johannes Lischner, Matthew Watkins and the rest of the Shluger group for productive discussions and collaborations.

I would like to further acknowledge the London Centre of Nanotechnology and the Thomas Young Centre for offering an environment of learning through seminars, workshops and paper discussions. Thanks to the Materials Chemistry Consortium and JAIST supercomputing facilities for providing the computational resources for this work.

Lastly, a heartfelt thank you to my friends and family, who have been a beacon through these four years, accompanying me along the way with great understanding and inspiration. Vielen Dank!

Contents

List of Figures

List of Tables

List of Publications

The following publications were derived from the work presented in this thesis:

1. Gaberle, J., Gao, D. Z., Watkins, M. B., Shluger, A. L. (2016). Calculating the Entropy Loss on Adsorption of Organic Molecules at Insulating Surfaces. Journal of Physical Chemistry C, 120(7), 3913-3921. http://doi.org/10.1021/acs.jpcc.5b12028

2. Gaberle, J., Gao, D. Z., Shluger, A. L., Amrous, A., Bocquet, F., Nony, L., Cherioux, F. (2017). Morphology and Growth Mechanisms of Self-Assembled Films on Insulating Substrates: Role of Molecular Flexibility and Entropy. Journal of Physical Chemistry C, 121(8), 4393-4403. http://doi.org/10.1021/acs.jpcc.6b12738

3. Gaberle, J., Gao, D. Z., Shluger, A. L. (2017). Calculating Free Energies of Organic Molecules on Insulating Substrates. Beilstein Journal of Nanotechnology, 8(1), 667-674. http://doi.org/10.3762/bjnano.8.71

4. Gaberle, J., Shluger, A. L. (2018). Structure and Properties of Intrinsic and Extrinsic Defects in Black Phosphorus. Nanoscale, 10(41), 19536-19546. http://doi.org/10.1039/C8NR06640J

Chapter 1

Introduction and Personal Motivation

Whether it is a catalytic converter in a diesel car, the solar cells erected on rooftops, the oil in an engine or the teflon coating on frying-pans, surface science impacts everyday life in a plethora of ways. Nature has long harnessed the power of surface phenomena to its advantage, such as for example the lotus effect. Being able to understand and control the processes which take place at material surfaces is essential for the development of novel technologies and applications.

The adsorption of molecules on surfaces plays a crucial role in surface catalysis. For instance the production of essential chemical compounds such as ammonia, hydrogen gas or ethene is driven by special catalysts. Consequently, understanding the adsorption process and the steps which are involved in surface reactions is imperative to enhance catalytic performance. But adsorption processes are not limited to catalysts. Gas sensors also exploit the interactions of molecules adsorbed on surfaces. For example TiO_2 is used as an oxygen sensor in car exhausts, detecting the oxygen concentration in the exhaust gas in order to optimise the fuel to air ratio in the engine.

With the advent of affordable supercomputers, the ability to model bulk materials and interfaces has resulted in a growing field of computational material scientists. Advanced modelling techniques allow the study of molecules, which may not even have been synthesised before, on surfaces in great detail in a fraction of the time required to study the same system experimentally. It also allows the study of systems under extreme conditions such as at very high temperature or metastable materials,

which is difficult or impossible to do in the lab.

The work presented in this thesis investigates a range of surface phenomena via computational modelling. Specifically, this thesis culminates three research projects, which I have been involved with over the course of my four years as a PhD student. Thus, the thesis is divided into three parts, each addressing one project.

In my first year I worked on molecular self-assembly on insulating surfaces in collaboration with researchers at Aix-Marseille University in France. Two large organic molecules were studied with respect to the influence their conformational flexibility has on surface adsorption and film nucleation. Experimentally the molecules were studied with non-contact atomic force microscopy. Obtained images represent snapshots of the system under controlled conditions with molecular resolution. 2D monolayer structures and molecules at surface defects such as step edges were resolved. However, the data acquisition time is orders of magnitude slower than the rate of surface dynamics, which means the snapshots cannot give insight into the self-assembly process. Furthermore, the surface energetics are very difficult to probe: changes in entropy can affect the self-assembly process leading to disordered structures or molecular crystals, yet it is difficult to investigate entropic effects experimentally. Computational modelling offers a useful tool to obtain insight into such processes and study the fundamental forces, which drive self-assembly. To those means classical molecular dynamics and force fields were employed, which allow the computation of long trajectories. In a post processing step the trajectories can be analysed using thermodynamic integration to calculate entropic contributions to e.g. adsorption.

During the second year of my PhD I was working at JAIST, Japan, under the supervision of Prof. M. Tomitori investigating the surface reduction of TiO_2. Further, the research plan involved the study of interactions between water and SiO_x with the (110) surface. TiO_2 crystals are annealed at temperatures over 1000 K in a quartz tube under conventional vacuum or ambient air conditions for up to 48h. After the annealing process Si can be detected on the surface of TiO_2 and small island growth is observed in non-contact atomic force microscopy images. The al-

tered surface exhibits some interesting properties, such as super-hydrophilicity. If a water-droplet on a surface spreads to the extend that the internal angle between the water-gas and water-solid interface approaches 0°, then the surface is called super-hydrophilic. Preliminary studies were performed before I arrived in Japan, however, due to changes in the timeline of the experimental collaborators, the focus of the study was shifted to understand the reduction and Ti_i creation mechanism at the (110) rutile TiO_2 surface.

Classical simulations are not able to capture the various interactions taking place at the surface as it becomes reduced. Therefore, an ab initio method, precisely density functional theory, was chosen for this study. Intrinsic point defects, primarily oxygen vacancies and Ti interstitials, were calculated and analysed with respect to their electronic structure. Such static investigation was supplemented with the calculation of diffusion barriers in the bulk crystal in order to gain insight into the transport properties of TiO_2. The study was then extended to the (110) surface, where Ti interstitials and their indiffusion mechanism was analysed as a function of surface reduction.

After I arrived back at UCL, I began to collaborate with M. Wentink and Prof. A. Kenyon to research the "novel" 2D material black phosphorus. 2D materials have seen tremendous growth in interest since the discovery of graphene. As a semiconductor with a direct bandgap, anisotropic transport properties and high carrier mobilities, black phosphorus has the potential to surpass graphene due to its more suitable properties for modern electronic applications. However, in order it to reach its full potential, if it ever will, the fundamental properties of black phosphorus and its defect chemistry needs to be better understood. For example experimentally it is found to be p-doped, yet the origin of the doping is unclear.

In the third part of this thesis intrinsic and extrinsic defects are investigated and compared to experimental data from secondary ion mass spectrometry and scanning tunnelling microscopy. Furthermore, the degradation of black phosphorus under ambient conditions is researched, since rapid degradation is one of the biggest challenges to bridge the gap from research laboratories to future technologies. Lastly,

the thesis is concluded in the last chapter and a brief outlook for future work is given.

Chapter 2

Theoretical Background

For the scope of this work a combination of classical and quantum methods have been used, which are described in this chapter. Firstly, an introduction to quantum methods is given including the most relevant approximations and limitations of these methods. Particular emphasis is placed on density functional theory, which has been used extensively in parts II and III of this thesis for calculations of defects in black phosphorus and rutile TiO_2. Standard DFT albeit being a powerful tool to study the electron density of quantum systems has its limitations due to the lack of non-local electron correlation and electron self-interaction errors. Corrections to standard DFT are discussed such as hybrid-DFT and van der Waals corrections. Furthermore, for the study of self-assembled monolayers classical force fields in combination with molecular dynamics was used. An introduction to classical simulations is given in Section 2.1.6.

The results from quantum and classical calculations can be analysed by employing various methods. The second half of this chapter is focussing on describing such methods. Firstly, an introduction to the computation of defect formation energies (DFE) is given, along with important corrections to obtain accurate DFEs. For the study of defects in black phosphorus theoretical calculations were compared to scanning tunnelling microscopy (STM) images obtained by our collaborators. In order to directly compare the calculated defects to STM images, the Tersoff-Hamann model was used, which transposes the electron density into a tip-surface current map.

Defects can induce localised states, which can be analysed by calculating the inverse participation ratio (IPR) as described in Section 2.2.2. Also related to the study of defects (but not exclusive to it) are nudged elastic band (NEB) calculations.

NEB allows the investigation of transition states between two energetic minima of the potential energy landscape, which was employed for the study of defect diffusion barriers.

Lastly, the calculation of entropy contributions to adsorption, step adhesion and dimer formation in part I was only possible by using classical force fields and long timescale MD simulations, which were analysed using themodynamic integration as described in Section 2.2.5.

2.1 Simulation Methods for Material Science

2.1.1 Quantum Mechanics

In quantum mechanics, the non-relativistic Hamiltonian for a system containing N_n nuclei and N_e electrons is given in atomic units by:

$$\begin{aligned}\hat{H} = &-\frac{1}{2}\sum_{i}^{N_e}\nabla_i^2 - \frac{1}{2}\sum_{A}^{N_n}\frac{\nabla_A^2}{M_A} - \sum_{i,A}^{N_e,N_n}\frac{Z_A}{|\mathbf{r}_i - \mathbf{R}_A|} \\ &+ \sum_{i<j}^{N_e}\frac{1}{|\mathbf{r}_i - \mathbf{r}_j|} + \sum_{A<B}^{N_n}\frac{Z_A Z_B}{|\mathbf{R}_A - \mathbf{R}_B|} \quad ,\end{aligned} \tag{2.1}$$

where the indices A,B (A≠B) run over all nuclei with mass M and charge Z and i,j run over all electrons (i≠j). The position of the nuclei is given by $\mathbf{R}$ and of the electrons by $\mathbf{r}$. The terms in the sum from left to right represent the kinetic energy of the electrons, the kinetic energy of the nuclei, the electrostatic attraction between nuclei and electrons, the Coulomb interaction between electrons and finally, the Coulomb interaction between nuclei.

Wavefunction based methods aim to solve the Schrödinger equation:

$$\hat{H}|\Psi(\mathbf{r},\mathbf{R},t)\rangle = i\hbar\frac{\partial}{\partial t}|\Psi(\mathbf{r},\mathbf{R},t)\rangle \quad , \tag{2.2}$$

where $\Psi(\mathbf{r},\mathbf{R},t)$ represents the time-dependent wavefunction of the nuclei and electrons. Thus, Equation 2.2 describes the time evolution of a quantum mechanical system. While the time evolution is important for e.g. excited states spectroscopy,

oftentimes the time domain is not necessary and instead the time independent Schrödinger equation is solved. This can be achieved by separating the wavefunction into a product of a spatial and temporal term, $\Psi(\mathbf{r}, \mathbf{R}, t) = \psi(\mathbf{R}, \mathbf{r})\psi(t)$. The Schrödinger equation then reads:

$$\hat{H}|\psi(\mathbf{R}, \mathbf{r})\rangle\psi(t) = i\hbar\frac{\partial}{\partial t}|\psi(\mathbf{R}, \mathbf{r})\rangle\psi(t) \quad , \tag{2.3}$$

which can be solved by separation of variables and shown to give:

$$\hat{H}|\psi(\mathbf{R}, \mathbf{r})\rangle = E|\psi(\mathbf{R}, \mathbf{r})\rangle \quad \text{, and} \tag{2.4}$$

$$i\hbar\frac{d}{dt}\psi(t) = E\psi(t) \quad . \tag{2.5}$$

Equation 2.4 is often called the time-independent Schrödinger equation.

Since Equation 2.1 contains a two-body sum over all electron positions, Equation 2.4 can only be solved analytically for very simple systems. Two main approaches to solving the time-independent Schrödinger equation can be identified: theories based on wavefunctions such as Hartree-Fock theory (HF) and theories based on the electron density such as density functional theory (DFT). In fact, many theoretical physicists today use a combination of the two theories to solve for the energy eigenvalues of a system. Therefore, a brief description of the two theories is given in the following sections, but readers are referred to standard quantum chemical textbooks for an in depth derivation of these well established methods.

2.1.2 Born-Oppenheimer Approximation

Both DFT as well as HF theory take advantage of the fact that nuclei are orders of magnitude heavier than electrons and therefore, electron density can be regarded as adapting instantaneously to moving nuclei. Hence, the electron density is a function of nuclear positions only and not of their momenta. This allows the separation of the nuclear and electronic parts of the wavefunction, such that $\psi(\mathbf{R}, \mathbf{r}) = \psi_n(\mathbf{R})\psi_e(\mathbf{r}, \mathbf{R})$, which is called the Born- Oppenheimer (BO) approximation. The time-independent Schrödinger equation can then be expressed as:

$$\left(-\frac{1}{2}\sum_{i}^{N_e}\nabla_i^2 + \sum_{i<j}^{N_e}\frac{1}{|\mathbf{r}_i-\mathbf{r}_j|} + \sum_{i,A}^{N_e,N_n}\frac{Z_A}{\mathbf{r}_i-\mathbf{R}_A} + \sum_{A<B}^{N_n}\frac{Z_A Z_B}{|\mathbf{R}_A-\mathbf{R}_B|}\right)\psi_e(\mathbf{r},\mathbf{R}) = E^{el}(\mathbf{R})\psi_e(\mathbf{r},\mathbf{R}) \tag{2.6}$$

$$\left(-\frac{1}{2}\sum_{A}^{N_n}\frac{\nabla_A^2}{M_A} + E^{el}(\mathbf{R})\right)\psi_n(\mathbf{R}) = E\psi_n(\mathbf{R}) \quad . \tag{2.7}$$

It can be seen that E^{el} depends parametrically on R. Therefore, the time-independent Schrödinger equation can be solved for stationary nuclear positions, in whose electrostatic potential the electrons move. Parametrically varying R allows the computation of the potential energy landscape, on which the nuclei move. Note, the electronic wavefunction will be written as $\psi_e(\mathbf{r})$ in the following sections.

While the BO approximation is a powerful tool to reduce the degrees of freedom of a system, thus reducing the computational cost, there are instances, where it fails. The coupling of the electronic and nuclear motion is assumed to be zero in the Born-Oppenheimer approximation, which is not generally true, for example at conical intersections, which are related to non-radiative decay of excited states.[1] Non-adiabatic processes are related to many effects such as chemiluminescence, heterolytic dissociation and many photochemistry reactions.[2]

2.1.3 Hartree Fock Theory

The wavefunction of a system is not typically known a priori. Fortunately, one can make use of the variational theorem, which states that the energy calculated from a guess wavefunction will always be greater than the true ground state energy. Therefore, one can systematically improve the wavefunction which minimises the energy. The electronic wavefunction $\psi_e(\chi)$ is a many-body wavefunction of N electrons with 4N variables. HF theory simplifies $\psi_e(\chi)$ by assuming it can be factorised

into single-particle, orthonormal spin orbitals:

$$\psi_e(\chi) \approx \phi_1(\chi_1)\phi_2(\chi_2)\dots\phi_N(\chi_N) \quad , \tag{2.8}$$

where $\phi_1(\chi_1)$ indicates a single-particle spin orbital of electron 1. However, this equation does not obey Pauli's exclusion principle for indistinguishable electrons. Instead, one can use Slater determinants:

$$\psi_e(\chi_1, \chi_2, \dots, \chi_N) \approx \frac{1}{\sqrt{N!}} \begin{vmatrix} \phi_1(\chi_1) & \phi_2(\chi_1) & \dots & \phi_N(\chi_1) \\ \phi_1(\chi_2) & \phi_2(\chi_2) & \dots & \phi_N(\chi_2) \\ \vdots & \vdots & \vdots & \vdots \\ \phi_1(\chi_N) & \phi_2(\chi_N) & \dots & \phi_N(\chi_N) \end{vmatrix} \tag{2.9}$$

Note, for closed shell systems typically only one Slater determinant is required, which is not generally true for open shell systems, where a linear combination of Slater determinants is needed. The expectation value of the Hamiltonian $\langle \hat{H} \rangle$ with respect to a wavefunction that consists of a single Slater determinant can be expressed as:

$$\langle \hat{H} \rangle = E^{HF} = \sum_{j=1}^{N} I_j + \frac{1}{2} \sum_{i=1}^{N} \sum_{j=1}^{N} \left(J_{ij} - K_{ij} \right), \text{with} \tag{2.10}$$

$$I_j = \langle \phi_j(\mathbf{r}_1) | -\frac{1}{2}\nabla_j^2 - \sum_{A=1}^{N_n} \frac{Z_A}{\mathbf{r}_1 - \mathbf{R}_A} | \phi_j(\mathbf{r}_1) \rangle \tag{2.11}$$

$$J_{ij} = \langle \phi_i(\mathbf{r}_1)\phi_j(\mathbf{r}_2) | \frac{1}{|\mathbf{r}_1 - \mathbf{r}_2|} | \phi_j(\mathbf{r}_2)\phi_i(\mathbf{r}_1) \rangle \tag{2.12}$$

$$K_{ij} = \langle \phi_i(\mathbf{r}_1)\phi_j(\mathbf{r}_2) | \frac{1}{|\mathbf{r}_1 - \mathbf{r}_2|} | \phi_j(\mathbf{r}_1)\phi_i(\mathbf{r}_2) \rangle \quad , \tag{2.13}$$

where I_j represents the energy of an electron in orbital ϕ_j in the field of the nucleus. J_{ij} is termed the Coulomb integral, which represents the interaction of an electron with the average local potential and K_{ij} is termed the exchange integral, which arises due to the anti-symmetry condition of the wavefunction. It is worth noting, that the Coulomb integral is a repulsive interaction, whereas the exchange integral is an attractive interaction for electrons of the same spin. Thus, HF theory includes

some form of electron correlation for electrons of the same spin.

The two-body terms K_{ij} and J_{ij} are equal for $i = j$, which can be understood as electrons not interacting with themselves. This is one of the most important differences to density based methods such as DFT. Further, it becomes apparent, that an electron feels the effect of the average charge distribution and thus, HF theory is called a mean-field theory. One of the biggest shortcomings of HF theory is its neglect of electron correlation. Correlation energy can be divided into dynamic and static correlation. Dynamic correlation is the correlated motion of electrons, which is not included in the mean-field approach of HF. Static correlation arises from representing the many-electron wavefunction by a single Slater determinant, which can be a poor description of systems with nearly degenerate ground states or excited states, where a linear combination of Slater determinants is required.

2.1.4 Møller-Plesset Theory

In order to account for electron correlation in many-electron systems, HF theory can be extended to include a wavefunction of more than one Slater determinant, i.e. including Slater determinants of a system's excited electronic configurations. Hence, this approach is called configuration interaction (CI), which is an exact theory in the limit of a complete basis. However, CI is computationally extremely demanding, even when restricting the excited states to singly and doubly excited configurations. Thus, it is only feasible for very small systems, such as diatomics.[3]

Møller-Plesset theory (MP) is a less robust method to account for electron correlation, which is computationally less expensive than CI and thus can be applied to comparatively large systems. The idea is to treat the difference between the HF operator and an exact Hamiltonian as a perturbation, such that corrections to E_{HF} can be made. The most popular correction is MP2, which includes an additional energy term in the Hamiltonian:

$$E_{corr}^{MP2} = \frac{1}{4} \sum_{ij}^{occ} \sum_{kl}^{virt} \frac{|\langle \phi_i \phi_j | \phi_k \phi_l \rangle - \langle \phi_i \phi_j | \phi_l \phi_k \rangle|^2}{\epsilon_i + \epsilon_j - \epsilon_k - \epsilon_l} \quad , \tag{2.14}$$

where ϕ_i and ϕ_j represent occupied spin orbitals and ϕ_k and ϕ_l represent unoccupied

virtual spin orbitals. Thus, MP2 includes doubly excited states in the representation of the total energy. While MP2 is relatively fast (MP2 scales as N^5) and size consistent, it is not variational. Thus, the estimate of the correlation energy can be too large. Higher order excitations (MP3 or MP4 level) are computationally excessively expensive, particularly since a good basis set is imperative in MP theory, hence coupled cluster techniques are often preferred. Furthermore, MP2 is not suitable for metallic systems, where the correlation energy diverges with decreasing k-point spacing.[4] Nevertheless, progress is being made to reduce the computational cost of MP2 by localising the orbitals and only evaluate spatially close pairs, known as local MP2 (L-MP2).[5] This reduces the dependence of the computational effort on the number of atoms, however, scaling for the number of basis functions per atom is still poor.

2.1.5 Density Functional Theory

It has been 20 years since Kohn was honoured with the Nobel Prize in chemistry and his formulation is still widely used today for the study of material properties. The main advantage of the Hohenberg-Kohn formulation lies in its ability to calculate material properties based on the electronic density, rather than the many-electron wavefunction.

The first Hohenberg-Kohn theorem states that for a system of N_e electrons the external potential V_{ext} is a unique functional of the electron density $\rho(\mathbf{r})$. The density $\rho_0(\mathbf{r})$ that minimises the energy is the ground state (second HK theorem):

$$E[\rho_0(\mathbf{r})] \leq E[\rho'(\mathbf{r})] \tag{2.15}$$

Therefore, the variational principle can be used to find the ground state density by minimising the total electronic energy.

Similar to HF theory, single particle orbitals are used to construct a Slater determinant to express the wavefunction, since electrons are treated as non-interacting

particles. The electron density can then be derived as:

$$\rho(\mathbf{r}) = \sum_{i}^{N} |\psi_i(\mathbf{r})|^2 \quad , \tag{2.16}$$

where the summation runs over all N single particle orbitals $\psi_i(\mathbf{r})$.

The exact kinetic energy of interacting electrons is unknown. Hence, the kinetic energy is calculated for a reference system of non-interacting electrons instead, which is given by:

$$E^T[\rho(\mathbf{r})] = -\frac{1}{2}\sum_{i}^{N} \langle \psi_i(\mathbf{r}) | \nabla_i^2 | \psi_i(\mathbf{r}) \rangle \quad . \tag{2.17}$$

Thus, an effective Hamiltonian can be written:

$$\hat{H} = -\frac{1}{2}\nabla^2 + V_{eff} \quad , \tag{2.18}$$

where

$$V_{eff} = V^{ext} + \int d\mathbf{r}' \frac{\rho(\mathbf{r}')}{|\mathbf{r} - \mathbf{r}'|} + \frac{\delta E^{XC}[\rho(\mathbf{r}')]}{\delta \rho(\mathbf{r})} \quad , \tag{2.19}$$

Investigating the terms in the electronic Schrödinger equation (Equation 2.6) and the effective Hamiltonian, it follows, that the total energy of a system can be written as a functional of the electron density:

$$E[\rho(\mathbf{r})] = E^T[\rho(\mathbf{r})] + E^V[\rho(\mathbf{r})] + E^{Ha}[\rho(\mathbf{r})] + E^{XC}[\rho(\mathbf{r})] \quad , \tag{2.20}$$

where $E^T[\rho(\mathbf{r})]$ is the kinetic energy of non-interacting electrons, $E^V[\rho(\mathbf{r})]$ is the electrostatic interaction energy between electrons and nuclei, $E^{Ha}[\rho(\mathbf{r})]$ is the classic Coulomb repulsion between electrons and $E^{XC}[\rho(\mathbf{r})]$ is an umbrella term for corrections to the total energy, which arises due to approximations made to the kinetic energy of electrons and their Coulomb interaction:

$$E^{XC}[\rho] = (T[\rho] - T_s[\rho]) + (V_{ee}[\rho] - V_H[\rho]) \quad , \tag{2.21}$$

where the first term describes the difference between the kinetic energy of interacting

particles and non-interacting particles and the second term is the error made in calculating the electron-electron interaction classically. For the exact E^{XC}, the exact ground state density can be obtained, making DFT an exact theory. However, E^{XC} is not known exactly and thus approximations to its form need to be made, making DFT a non-exact theory in practise.

2.1.5.1 Exchange-Correlation Functionals

There is no way to systematically improve the energies obtained from the exchange-correlation (xc) operator and many different xc-functionals have been developed with varying accuracy.[6–8] The first approximations to the xc-functional were based on the homogeneous electron gas (HEG), which assumes that the positive charge of the nuclei and ergo the electron density are uniformely distributed such that the electron denisty is constant for an infinite number of electrons in an infinite volume.[9] For such a system the exchange energy is known and the correlation energy can be calculated from methods such as random phase approximation or quantum Monte Carlo.

In the local density approximation (LDA) the inhomogeneous electron density is divided into infinitesimally small volumes of constant density. Using the HEG approximation the exchange and correlation energies can be calculated for these densities and integrated over the whole electron density:

$$E_{LDA}^{XC} = \int \rho(\mathbf{r})\epsilon_{xc}(\rho(\mathbf{r}))d\mathbf{r} \quad , \tag{2.22}$$

where $\epsilon(\rho(\mathbf{r}))$ is the xc-energy per particle in a HEG of density $\rho(\mathbf{r})$. Although Kohn and Sham did not expect the HEG to be a good approximation, it describes most systems reasonably well. This is mostly attributed to cancellation of errors in the calculation of the exchange and correlation energies. LDA performs better for metallic systems, where the electron density varies slowly, than for ionic or insulating systems.

In order to better approximate the non-homogeneous electron density in the HEG model, the gradient of the density is included, which is commonly known as

generalised gradient approximation (GGA):

$$E_{GGA}^{XC} = \int f(\rho(\mathbf{r}), \nabla\rho(\mathbf{r}))d\mathbf{r} \quad , \tag{2.23}$$

where f is a function of the density and its gradient. Many different formalisms exist for GGA functionals (PBE,[8] PW91,[10] BLYP[11,12]), which generally perform better than LDA for atomisation energies or lattice constants for example.[13] However, for some properties, such as surface energies, binding energies of weakly bound species or vibrational frequencies, GGAs can perform worse than LDA.[13–15]

LDA and GGAs can give realistic atomic structures, elastic, and vibrational properties for a wide range of materials. However, both approximations have common limitations or failures. Firstly, correlation effects are still poorly described with these approximations. While local correlation due to electron density is included, non-local correlation due to the spontaneous creation of dipoles, which induce dipoles in their vicinity, are not accounted for. These long-range interactions are also called dispersion interactions. Methods have been developed in order to improve the description of dispersion interactions such as Grimme-D2/Grimme-D3[16] corrections to DFT, random phase approximation (RPA),[17] or dispersion corrected atom centred potentials (DCACP)[18] to name a few. Grimme-D2 corrections add an extra term to the total energy formalism:

$$E^{dispersion} = -\frac{1}{2}\sum_{A,B} f_d(\mathbf{r}_{AB})\frac{C_{6,AB}}{\mathbf{r}_{AB}^6} \quad , \tag{2.24}$$

where $f_d(\mathbf{r}_{AB})$ is a damping function, which reduces the interaction at small interatomic distances, $C_{6,AB}$ is the dispersion coefficient for atom pair A and B, which have been tabulated, and $\mathbf{r}_{AB}$ is the interatomic separation. It is worth pointing out, that due to the parametric form of the correction, the accuracy of such corrections is system dependent.[19,20]

Secondly, since the electrostatic repulsion is calculated from a mean-field approach, an electron will feel the effect of all electrons, including itself, which is

commonly known as self-interaction. While in HF theory the self-interaction energy (Hartree energy) cancels with the exchange energy, it does not in DFT, since the exact xc-functional is unknown. Therefore, electrons feel more repulsion, which leads to more delocalised electron densities. This is particularly problematic for materials, which have polaronic states, such as TiO_2. The self-interaction error in GGA-DFT leads to a delocalisation of a polaron and thus is not a suitable method for the study of such trapped charges. A common practise to reduce the self-interaction error is to include a certain percentage of HF exchange, which improves the description of bandgaps, polarons and strongly correlated systems. Various different functionals have been developed, which include some fraction of exact exchange and two will be outlined in Section 2.1.5.2.

2.1.5.2 Hybrid Functionals: HSE06 and PBE0

Using standard DFT such as in the local density approximation (LDA) or generalised gradient approximations (GGA) can yield accurate results for geometries, frequencies and bond energies. However, the self-interaction error does not cancel as it does in HF theory and thus leads to spurious energy contributions. Thus, the introduction of exact HF exchange is often used to correct for self-interaction. There are various different approaches to how exact exchange can be included in DFT. For the scope of this work screened exchange was used, as the computational cost of calculating exact exchange at long distances is eliminated. Various xc-functionals have been developed, which include screened HF exchange and two will be outlined below.

Calculations in chapter 6.1 were performed using the Heyd, Scuseria and Ernzerhof hybrid functional (HSE06),[21] which uses an error function to screen the long range Coulomb potential. The screened Coulomb operator is split into a short-range (SR) and a long-range (LR) part by means of an error function. The mathematical form of the error function allows for analytical integration, giving computational advantages over other splitting functions. Generally the choice of splitting function is arbitrary as long as the SR and LR part add up to the original Coulomb operator.

In HSE the operator is given by:

$$\frac{1}{\mathbf{r}} = \left(\frac{erfc(\omega\mathbf{r})}{\mathbf{r}}\right)_{SR} + \left(\frac{erf(\omega\mathbf{r})}{\mathbf{r}}\right)_{LR} \quad , \tag{2.25}$$

where erfc($\omega\mathbf{r}$) = 1 - erf($\omega\mathbf{r}$) and ω is an adjustable parameter. In the limit of $\omega \to 0$ the LR term is zero and the SR term is equivalent to the full Coulomb operator and vice versa for $\omega \to \infty$. This screening is only applied to the exchange interaction and all other Coulomb interactions, such as the Coulomb repulsion of electrons, do not use any screening. The exchange-correlation is then calculated as:

$$E_{\mathrm{XC}}^{\mathrm{HSE}} = \alpha E_X^{\mathrm{HF,SR}}(\omega) + (1-\alpha)E_X^{\mathrm{PBE,SR}}(\omega) + E_X^{\mathrm{PBE,LR}}(\omega) + E_C^{\mathrm{PBE}} \quad , \tag{2.26}$$

where subscript X denotes the exchange part and subscript C denotes correlation. The parameters α and ω were set to their standard values of 0.25 and 0.11, respectively.[21]

The second functional used is a modified form of the PBE0 functional.[22] In this case the exact exchange is truncated at a radius R_c such that:

$$g_{TC}(\mathbf{r}_{12}) = \begin{cases} \frac{1}{\mathbf{r}_{12}}, & \mathbf{r}_{12} \leq R_c \quad (SR) \\ 0, & \mathbf{r}_{12} > R_c \quad (LR) \end{cases} \tag{2.27}$$

Similar to the HSE functional, a correction for the missing exact long-range exchange is added to E_{XC} calculated from PBE such that the final expression reads:

$$E_{\mathrm{XC}} = \alpha E_X^{\mathrm{HF,SR}} + \alpha E_X^{\mathrm{PBE,LR}} + (1-\alpha)E_X^{\mathrm{PBE}} + E_C^{\mathrm{PBE}} \tag{2.28}$$

The use of the LR exchange correction allows for very small R_c ($\approx$ 2-6 Å) without loss of accuracy, however, the choice of cutoff radius should be carefully tested. Particular care should be taken that it is smaller than the shortest edge of the unit cell to avoid self-interaction accross the periodic boundary. Since the computational cost increases with larger cutoff radius, it is desirable from a practical poit of view to

have a smallest R_c as possible, while still reproducing the electron density correctly.

2.1.5.3 Auxiliary Density Matrix Method

Calculating the HF energy in hybrid DFT calculations is computationally very expensive and scales to the fourth power with the number of basis functions, ϕ, included in the calculation due to the evaluation of electron repulsion integrals (ERIs):

$$(\mu\nu|\lambda\zeta) = \int \phi^*_\mu(\mathbf{r})\phi_\nu(\mathbf{r})\frac{1}{|\mathbf{r}-\mathbf{r}'|}\phi^*_\lambda(\mathbf{r}')\phi_\zeta(\mathbf{r}')d\mathbf{r}d\mathbf{r}' \tag{2.29}$$

However, many ERIs are negligibly small and can be ignored. Particularly, the product of two Gaussian functions centred on different atoms decays with the atomic distance. The Cauchy-Schwarz inequality[23] is applied in order to reduce the number of computed ERIs:

$$(\mu\nu|\lambda\zeta) \leq \sqrt{(\mu\nu|\mu\nu)}\sqrt{(\lambda\zeta|\lambda\zeta)} \leq \textit{upper bound} \tag{2.30}$$

Despite this screening, evaluation of ERIs is still computationally expensive, particularly for very diffuse basis functions with slow long range decay (such as the MOLOPT basis sets commonly used in CP2K).

In order to circumvent this cost, the auxiliary density matrix method (ADMM)[24] was developed, which uses a reduced basis matrix $\hat{P} \approx P$ of rapidly decaying basis functions for the calculation of the HF exchange energy following:

$$\begin{aligned} E_X^{HFX}[P] &= E_X^{HFX}[\hat{P}] + (E_X^{HFX}[P] - E_X^{HFX}[\hat{P}]) \\ &\approx E_X^{HFX}[\hat{P}] + (E_X^{DFT}[P] - E_X^{DFT}[\hat{P}]) \quad , \end{aligned} \tag{2.31}$$

where the superscripts indicate the method used to calculate the exchange energy E_X. The underlying assumption is that the difference in energy introduced by calculating the HF exchange in the smaller auxiliary basis set can be estimated by GGA DFT calculations. Since typically only a fraction of HF exchange is included in the calculation, any error in the exchange energy due to the change in basis is further reduced. Since the correction requires the evaluation of additional terms, it

is inefficient for small systems such as molecules, but can give orders of magnitude speed-up for larger systems.

The HF exchange energy can thus be calculated using:

$$E_X^{HFX}[\hat{P}] = -\frac{1}{2}\sum_{\lambda\zeta\mu\nu} \hat{P}^{\mu\zeta}\hat{P}^{\lambda\nu}(\mu\nu|\lambda\zeta) \quad , \tag{2.32}$$

where $(\mu\nu|\lambda\sigma)$ are the ERIs of the auxiliary basis functions and $\hat{P}^{\mu\zeta}, \hat{P}^{\lambda\nu}$ are the elements of the auxiliary density matrix as calculated from the molecular orbital coefficients: $\hat{P}^{\mu\zeta} = \sum_i \hat{C}_{\mu i}\hat{C}_{\zeta i}$.

2.1.5.4 Introduction to CP2K

In order to calculate the KS-orbitals a suitable basis set needs to be chosen, which fall in two main categories: Plane wave basis sets and Gaussian basis sets. Plane wave basis sets are advantageous for periodic systems due to their naturally periodic mathematical form and fast Fourier transform algorithms. They are independent of chemical species and atomic position and are relatively easy to converge. However, it often requires a larger number of basis functions to describe the density accurately. Particularly for systems with areas of zero electron density such as isolated molecules or surfaces, the computational cost can be significant since empty space is described with the same accuracy as areas with electron density.

This is not the case for atomically centred Gaussian basis sets, which allow for compact description of the electron density. Single particle orbitals can be constructed systematically out of Gaussians to improve the representation of the electron density, but thus are not guaranteed to be transferable between different systems. Since the core electrons do not participate in chemical bonding, they can be described by a pseudo-potential as well as the effective electron density in the near core region. Doing so eliminates the cusp behaviour of the wavefunction near the nucleus and thus fewer basis functions (in both representations) are required, reducing the overall computational expense.

The herein used code (CP2K) combines Gaussian and plane wave basis sets (GPW) to utilise their respective advantages. The electron density, $\rho(\mathbf{r})$ is repre-

sented in a Gaussian basis set as:

$$\rho(\mathbf{r}) = \sum_{i}^{N} |\psi_i(\mathbf{r})|^2 \quad , \tag{2.33}$$

where N is the number of electrons and $\psi_i(\mathbf{r})$ is the i'th molecular orbital. The molecular orbitals themselves are represented as a linear combination of atomic orbitals:

$$\psi_i = \sum_{j} C_{ij}\phi_j \quad , \tag{2.34}$$

where C_{ij} are the mixing coefficients of the atomic orbital ϕ_j, which are represented using a contracted Gaussian g_k:

$$\phi_j = \sum_{k} C'_{jk} g_k \quad , \tag{2.35}$$

where C'_{jk} denotes the mixing coefficient. In a typical wavefunction optimisation calculation the coefficients C_{ij} are varied in order to obtain the ground-state density, while the Gaussian mixing coefficients C'_{jk} are fixed.

The electron density can then easily be mapped onto a plane wave basis using Fourier transform and is given by:

$$\tilde{\rho}(\mathbf{r}) = \frac{1}{\Omega} \sum_{\mathbf{G}} P(\mathbf{G}) \exp(i\mathbf{G} \cdot \mathbf{r}) \quad , \tag{2.36}$$

where Ω is the cell volume, $\mathbf{G}$ are reciprocal lattice vectors and P($\mathbf{G}$) are the expansion coefficients such that $\rho(\mathbf{r}) = \tilde{\rho}(\mathbf{r})$ in real space. The electronic energy is then

calculated using both representations of the density following:

$$\begin{aligned} E^{el}[\rho] &= E^{T}[\rho] + E^{V}[\rho] + E^{Ha}[\rho] + E^{XC}[\rho] \\ &= \sum_{\mu\nu} P^{\mu\nu} \langle \psi_\mu(\mathbf{r})| -\frac{1}{2}\nabla^2 |\psi_\nu(\mathbf{r})\rangle \\ &+ \langle \psi_\mu(\mathbf{r})|V_{loc}^{PP}|\psi_\nu(\mathbf{r})\rangle + \langle \psi_\mu(\mathbf{r})|V_{nl}^{PP}|\psi_\nu(\mathbf{r})\rangle \\ &+ 2\pi\Omega \sum_{\mathbf{G}} \frac{\tilde{\rho}^*(\mathbf{G})\tilde{\rho}(\mathbf{G})}{G} + \int E_{XC}[\rho(\mathbf{r})] \quad , \end{aligned} \tag{2.37}$$

where the first term is the kinetic energy of the non-interacting electron gas, the second and third term are the contributions from the local and non-local parts of the pseudo-potential, the fourth term describes the Hartree energy and the fifth term the exchange-correlation energy. Combining Gaussian basis sets for the kinetic and potential energy computation and plane-wave basis sets for the Hartree energy reduces the computational cost and thus allows larger systems to be studied.

2.1.6 Classical Force Fields

DFT is a powerful tool to study fundamental material properties, but is severely limited by the computational cost. Systems of several thousands of atoms or long time-scale molecular dynamics (MD) are not feasible and alternative methods need to be utilised. Classical force fields (FF) have been well established and offer a cheap alternative to study dynamics of large systems or surface phenomena. They map complex atomic interactions onto simple mathematical formulas, which allow for fast and cheap calculations. However, any information of the electronic structure is lost. Therefore, chemical reactions including charge transfer can not be modelled. Furthermore, prior knowledge of the system either from experiment or higher accuracy theory is required in order to validate chosen parameters of the FF. A set of parameters may yield an accurate description of a crystal structure at 0 K but may fail to reproduce the thermal expansion at higher temperatures. Thus, a set of parameters is usually developed for the study of a specific purpose and are not necessarily transferrable to the study of any quantity of interest. Thus the employed

FF should be carefully validated.

For the study of free energy profiles in this thesis classical molecular mechanics (MM) in conjunction with a FF was used. The FF splits the quantum-mechanical interactions between atoms into different classical contributions:

$$E_{\text{Total}} = E_{\text{Bond}} + E_{\text{Angle}} + E_{\text{Dihedral}} + \dots \quad , \tag{2.38}$$

where the contributions from molecular bonds, bond angles, dihedral angles etc. are expressed by simple mathematical equations, such as a classical spring for bonds for example.

In order to evaluate these interactions all bonds, angles etc. need to be predefined. No new bonds can be formed and consequently bonds also cannot be broken. Thus, chemical reactions or dissociation mechanisms cannot be studied with this FF. For such studies a force field such as ReaxFF could be used, which calculates connectivity based on atomic separation.

Non-bonded interaction energies are also included: the main types are Coulomb and van der Waals interactions. Setting charges for atom types allows to simulate charged species, such as ionic crystals or solvated ions by computing the Coulomb interactions. Charges are typically treated as point charges at the position of the nuclei, however, more complex representations have been developed.[25,26]

Van der Waals interactions can be represented by Lennard-Jones, Buckingham or Morse-type potentials. It is important to note that the mathematical form of the FF typically has no physical meaning and is often chosen for simplicity or computational efficiency. Furthermore, the chosen parameters may work well for fitted systems, but are not guaranteed to be transferable to other systems. More details on the FF used for this work is given in Chapter 4.

2.2 Methods of Data Analysis

2.2.1 Calculation of Accurate Defect Formation Energies

The defect formation energy (DFE) of point defects is given by:[27,28]

$$E_{DFE} = E^{q}_{defect} - E_{pristine} + \sum_{i} \mu_i N_i + q(E_f + \Delta V) + E_{\mathrm{IIC}} \ , \tag{2.39}$$

where q is the charge state of the defect, μ_i is the chemical potential of species i, N_i is the number of removed atoms of species i and E_f is the Fermi level of the pristine system. ΔV is a potential alignment term, which arises from the neglect of average potential in DFT calculations and E_{IIC} is an image charge correction (IIC) (see Fig. 2.1). Both ΔV and E_{IIC} are finite size dependent terms, which arise from periodic boundary conditions and tend to zero with increasing simulation box size. The method proposed by Lany and Zunger was used to account for image charge corrections.[29] This method builds on the Makov-Payne (MP) model,[30] which assumes the periodic interacting charge can be modelled by an interacting point charge:

$$E^{MP}_{\mathrm{IIC}} = \frac{q^2 \alpha_M}{2\epsilon L} \ , \tag{2.40}$$

where ϵ is the dielectric of the material, L is the separation between the defects and α_M is the Madelung constant. The LZ method assumes the defect draws an additional screening charge from the supercell, which reduces E_{IIC}. Thus, in the LZ approximation the image charge correction can be represented by a screened MP correction:

$$E^{LZ}_{\mathrm{IIC}} = \left[1 - c_s(1 - \epsilon^{-1})\right] E^{MP}_{\mathrm{IIC}} \ , \tag{2.41}$$

were the shape factor c_s only depends on the supercell size and has been tabulated for common supercells.[31] Due to the screening of the image charge interactions by the dielectric constant, the IIC term is typically small for high dielectric materials such as TiO_2. Potential alignment is a volume dependent term, which arises from the convention of setting the average electrostatic potential($\langle V \rangle$) to zero in periodic DFT calculations. Thus, $\langle V_{defect} \rangle \neq \langle V_{pristine} \rangle$ and the electrostatic potential of

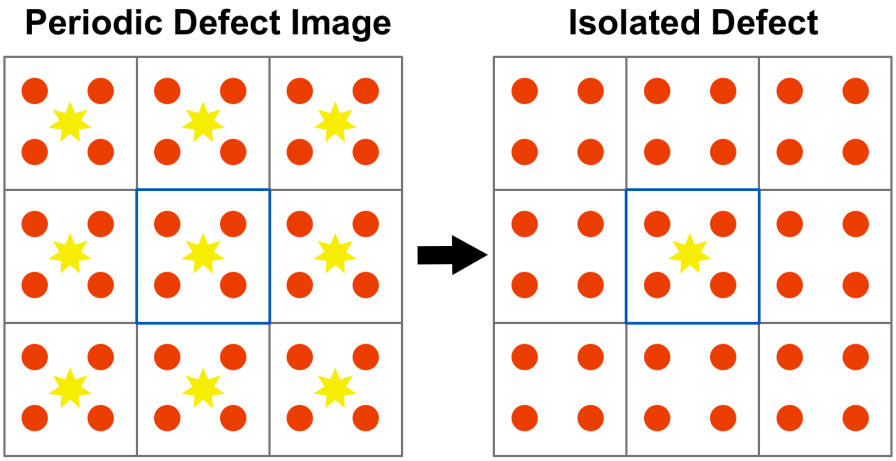

Figure 2.1: Illustration of the periodic interaction between a charged defect (star) and it's image charges via the periodic boundary conditions. The blue square represents the simulation box, which is infinitely repeated in space (grey boxes). Image charge corrections aim to recover the isolated defect from a periodically interacting defect.

pristine bulk material is not recovered far away from the defect. Thus, this shift in energy needs to be accounted for by aligning the electrostatic potential of defect and pristine supercells, which can be the dominant correction to DFEs.[28]

2.2.2 Inverse Participation Ratio

The inverse participation ratio (IPR) is a useful descriptor for the degree of localisation of vibrational or electronic states in a material.[32,33] The method takes advantage of the atom centred basis set used in the DFT calculations by calculating the degree of localisation of each eigenvector in the basis set and is given by:

$$IPR(\psi_n) = \frac{\sum_{i=1}^{N} a_{ni}^4}{\left(\sum_{i=1}^{N} a_{ni}^2\right)^2} \tag{2.42}$$

where

$$\psi_n = \sum_{i=1}^{N} a_{ni}\phi_i \tag{2.43}$$

is the n-th Kohn-Sham eigenvector, N is the number of atomic orbitals and ϕ_i is the i-th atomic orbital. Thus the more atomic orbitals contribute to an Kohn-Sham state, the lower its IPR value will be and ultimately reaching the $1/N$ limit,

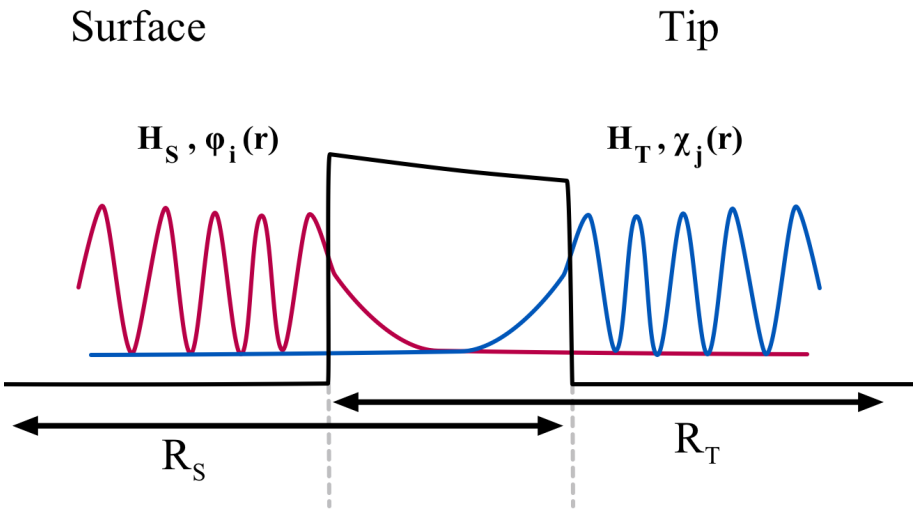

Figure 2.2: Schematic of the separability of the system as used in the TH model.

where the state has contributions from all N orbitals in the system. Equally if only one atomic orbital contributes to the eigenstate then the IPR value will be 1 (upper limit). Thus IPR analysis can be used to identify localised states such as polaronic states, defect states or defect induced states, which can sit in the valence or conduction band of a material or localised states in amorphous materials, which may alter the mobility edge for charge carriers.[32]

2.2.3 Tersoff-Hamann Model

In scanning tunnelling microscopy (STM) the measured current is a convolution of the STM tip wave-functions and the surface wave-functions. However, the tip structure and thus its wave-functions are typically not known. The Tersoff-Hamann (TH) model[34] is a simplification, which represents the tip potential and wavefunction arbitrarily localised in space and thus obtained images are a reflection of the surface wave-functions only and not of the convoluted tip-surface system. Since the STM current originates from the overlap of tip and surface wave-functions, which decays exponentially with distance, only the wave-functions localised on the tip apex are modelled. This approximation has been found to reproduce many observed features of STM images such as surface superstructures, scattered waves of surface states and surface adsorbates.[35–37]

Fig. 2.2 illustrates a simplified tip-surface system. The surface and tip are sep-

arated by an finite potential barrier, through which an electron can tunnel. The Hamiltonian of such a system is given by:

$$H = H_S + H_T + H_{Tr} \tag{2.44}$$

$$H_S = \frac{-\hbar^2}{2m}\nabla^2 + V_S(\mathbf{r}) \quad \mathbf{r} \in R_S \tag{2.45}$$

$$H_T = \frac{-\hbar^2}{2m}\nabla^2 + V_T(\mathbf{r}) \quad \mathbf{r} \in R_T \quad , \tag{2.46}$$

where H_T is the Hamiltonian of the tip, H_S is the Hamiltonian of the surface and H_{Tr} is the transfer Hamiltonian, which is typically unknown. Employing Fermi's Golden Rule, the probability of transmission from surface states ψ_i to tip states χ_j can be calculated:

$$P = \frac{2\pi}{\hbar}\sum_{j,i}|M|^2\delta(E_{T,j} - E_{S,i}) \tag{2.47}$$

$$\text{where} \qquad M = \langle\chi_j|H_T + H_{Tr}|\psi_i\rangle \tag{2.48}$$

$$\equiv \langle\chi_j|H - H_S|\psi_i\rangle \quad . \tag{2.49}$$

$E_{T,j}$ represents the energy eigenvalues of the tip wavefunction χ_j and $E_{S,i}$ represents the energy eigenvalue of the surface wavefunctions ψ_i.[34, 38]

Since the exact Hamiltonian H is not known, approximations to it must be made. In the surface region the wavefunction of the tip is approximately zero. Thus, the Hamiltonian H is well approximated by H_S and similarly for the tip region. The matrix element M can then be rewritten:

$$M = \frac{\hbar^2}{2m}\int_A \left(\psi_0\nabla\chi_j^* - \chi_j^*\nabla\psi_0\right)dA \tag{2.50}$$

where A is a plane separating the tip and the surface. If the tip wavefunction is approximated by a spherical s-orbital centred at $\mathbf{r}_0$, then M simplifies to:

$$M = -\frac{2\pi C\hbar^2}{\kappa_i m}\psi_i(r_0) \quad , \tag{2.51}$$

where κ is a decay constant ($\kappa_i = \sqrt{2m|E_{S,i}|}/\hbar$, where $E_{S,i}$ is the eigenvalue of ψ_i) and C is a normalisation constant. Thus the current I is proportional to the square of the surface wave-functions ψ_i:

$$I \propto \sum_i |\psi_i(\mathbf{r}_0)|^2 \delta(E_i - E_F) \quad , \tag{2.52}$$

where E_F is the Fermi energy.

The sum in Equation 2.52 can then be integrated over an energy range from the Fermi energy to the Fermi energy shifted by a set bias voltage. Thus, the tunnelling current is proportional to the integrated local density of states of the surface at the tip position $\mathbf{r}_0$ in that defined energy range only. This is important to keep in mind when setting a bias lower than E_F, where the TH model only calculates the current from that bias to E_F. In order to obtain the current from filled states below this setpoint, several TH simulations need to be run and the calculated current summed up.

It is worth noting that the normalisation constant C is unknown and thus absolute values of current can not be calculated. Furthermore, this simplified model is only approximate: most STM tips are made from transition metals, which have strong d-orbital character, however, the TH model assumes a spherical orbital (s-orbital) at the tip apex. Also, effects due to spin and magnetisation of the tip or the sample are not included. Extensions to the TH model have been developed, which try to incorporate more complex interactions.[37,39,40] However, for the scope of this work, the simplified TH model was found to be sufficient.

2.2.4 Nudged Elastic Band

Within the Born-Oppenheimer approximation the electronic and geometric ground state can be found. However, transition points of e.g. chemical reactions or diffusion paths require knowledge of the energy landscape outside the ground state in order to estimate reaction barriers and thus deduct rates of processes. For such purposes methods that determine minimum energy pathways (MEP) are required. A MEP is the trajectory between two points on a potential energy surface with the lowest

energy barrier between them. Such barriers can be obtained by finding the energy of first order saddle points.

For these purposes the climbing-image nudged elastic band (CI-NEB) method has been developed.[41] CI-NEB is an efficient method for finding transition states on a potential energy surface, however, the start and end states have to be known *a priori*. Thus CI-NEB cannot be used to explore unknown energy landscapes such as complex multi-step reaction pathways. Furthermore, CI-NEB will yield the local MEP along the predefined pathway; there may be a lower MEP, which is inaccessible due to the choice of initial pathway.

The starting point for a CI-NEB calculation is the plain elastic band (PEB) method, where N_i "images" between an initial and a final state are connected by springs forming a band whose energy can be optimised to provide the MEP. At this point it is vital to check if the interpolated path is reasonable, since linear interpolation may yield structures where atoms are unphysically close together or overlapping.[42]

The force F exerted on each image i is:

$$F_{total,i}^{PEB} = F_i + F_{spring,i} \qquad \text{, where} \tag{2.53}$$

$$F_{spring,i} = k_{i+1}(\mathbf{r}_{i+1} - \mathbf{r}_i) + k_i(\mathbf{r}_i - \mathbf{r}_{i-1}) \quad , \tag{2.54}$$

where F_i is the force due to the potential energies of each image and $F_{i,spring}$ is the force on each image due to the springs attached.

Furthermore, an objective function can be defined:

$$S(\mathbf{r}_1, \mathbf{r}_2, \ldots) = \sum_{i=0}^{N_i} V(\mathbf{r}_i) + \sum_{i=1}^{N_i} \frac{1}{2} k(\mathbf{r}_i - \mathbf{r}_{i-1})^2 \quad , \tag{2.55}$$

where the first term constitutes the sum over the potential energies of each image i and the second term is the additional potential energy due to the springs with spring constant k. Suitable algorithms can then be used to find the energetic minimum with respect to the atomic coordinates of the images and thus minimise the energy

of the band. However, the PEB has several shortcomings; images can slide down the band leading to non-uniform spacing between them and the resulting band can cut corners giving an inaccurate estimate for the MEP.[42]

In order to prevent images from sliding down the band or cutting corners some restrictions need to be set. Only the spring force parallel to the band and only the potential force perpendicular to the band are used, nudging the band onto the true MEP, which is termed the nudged elastic band method (NEB).[42]

Since the forces of the springs pull the saddle point image slightly down in energy, the true MEP saddle point is underestimated. Removing the springs connecting the highest energy image and inverting the force felt by this image to push it onto the true saddle point gives a better estimate of the MEP transition state. This method is called climbing image (CI) NEB. CI-NEB has been used throughout this thesis for the estimation of reaction barriers such as e.g. diffusion of Ti interstitials through bulk rutile TiO_2.

2.2.5 Calculation of Entropy: Thermodynamic Integration

The Hamiltonian of a classical system of N indistinguishable atoms can be written as:

$$\mathscr{H}(\mathbf{p},\mathbf{r}) = E_{kin}(\mathbf{p}) + E_{pot}(\mathbf{r}) \quad , \tag{2.56}$$

where E_{kin} and E_{pot} are the kinetic and potential energy, respectively and $\mathbf{r},\mathbf{p}$ are the Cartesian coordinates and momenta, respectively. For a canonical ensemble, the partition function is then given by:

$$Q(N,V,T) = \frac{\iint \exp(-\mathscr{H}(\mathbf{p},\mathbf{r})/k_B T) d\mathbf{p} d\mathbf{r}}{h^{3N} N!} \quad , \tag{2.57}$$

where V is the volume, T is the temperature k_B is the Boltzmann constant and h is Planck's constant.[43] Further, one can define the probability density in phase space of finding the system in any given state of the ensemble as:

$$\pi(\mathbf{p},\mathbf{r})_{NVT} = \frac{\exp(-\mathscr{H}(\mathbf{p},\mathbf{r})/k_B T)}{h^{3N} N! Q(N,V,T)} \quad , \tag{2.58}$$

such that the average of a property $X(\mathbf{p},\mathbf{r})$ is given by:

$$\langle X \rangle = \iint X(\mathbf{p},\mathbf{r})\pi(\mathbf{p},\mathbf{r})d\mathbf{p}d\mathbf{r} \quad . \tag{2.59}$$

The entropy S can then be found from the Helmholtz free energy A as given by:

$$S = -\left(\frac{\partial A}{\partial T}\right)_{N,V} \quad , \text{ where} \tag{2.60}$$

$$A = -k_B T \ln(Q(N,V,T)) \tag{2.61}$$

$$= +k_B T \ln\langle \exp(\mathscr{H}(\mathbf{p},\mathbf{r})/k_B T)\rangle \quad . \tag{2.62}$$

In order to determine the change in entropy between two states 1 and 2, thermodynamic integration can be used, in which the Hamiltonian is made a function of a parameter λ. The parameter λ can be a spatial coordinate, such as the distance between two molecules, or an energy for example. The Helmholtz energy $A(N,V,T,\lambda)$ and the partition function $Q(N,V,T,\lambda)$ are therefore also functions of λ. The entropy S is then given by:

$$\begin{aligned} S(N,V,T,\lambda) &= k_B \ln(Q(N,V,T,\lambda)) \\ &\quad + \frac{\iint \mathscr{H}(\mathbf{p},\mathbf{r},\lambda)\exp(-\mathscr{H}(\mathbf{p},\mathbf{r},\lambda)/k_B T)d\mathbf{p}d\mathbf{r}}{T\iint \exp(-\mathscr{H}(\mathbf{p},\mathbf{r},\lambda)/k_B T)d\mathbf{p}d\mathbf{r}} \quad . \end{aligned} \tag{2.63}$$

The entropy difference between the two states a and b can then be expressed as:

$$\Delta S_{ab} = \frac{1}{k_B T^2}\int_a^b \left[\left\langle \frac{\partial \mathscr{H}}{\partial \lambda}\right\rangle_\lambda \langle \mathscr{H}\rangle_\lambda - \left\langle \frac{\partial \mathscr{H}}{\partial \lambda}\mathscr{H}\right\rangle_\lambda\right] d\lambda \quad . \tag{2.64}$$

Equation 2.64 can be used to calculate the entropy change of adsorption for a molecule on a surface or for interactions of molecules on surfaces. The parameter λ is used to ensure efficient sampling of the ensemble for the process, i.e. for adsorption the molecule will feel a strong attraction to the surface at close distances and hence sampling of configurations with molecule surface separation slightly larger than the equilibrium separation is poor. Thermodynamic integration with steered molecular

dynamics is a useful tool in these instances to compute the entropy change.

Molecular dynamics simulations were performed in the (NVT) ensemble with a Nosé-Hoover thermostat[44] to control the temperature of the system and using the velocity Verlet integrator to ensure positions and velocities are updated during the same time step. MD runs were set up by placing molecules on a KCl substrate, which was represented using a four layer slab composed of 1024 atoms. To prevent the substrate from drifting the bottom layer of the four substrate layers was frozen and a 80 Å vacuum gap was used to eliminate interactions across the periodic boundary.

Part I

Influence of Molecular Flexibility on Early Stages of Self-Assembled Film Growth on Insulating Substrates

3.1 Introduction

Adsorption of organic molecules on insulating surfaces offers a powerful tool to design surface properties. It has applications in sensor technologies,[45,46] coatings,[47] catalysis,[48] functional films[49] and molecular electronics.[50–52] When using organic molecules to functionalise the surface properties, self-assembly benefits from a vast variety of organic compounds and well established chemical synthesis methods.

In order to design molecules and surfaces which target these applications deep knowledge of the molecular interactions is imperative. The balance between intermolecular and molecule-surface interactions determines how molecules arrange on the surface. In a narrow range the forces balance to allow the self-assembly of 2D molecular films.[46,53–56] Reversible bond formation and breaking allows for large domains of structurally well defined films to grow.

The interactions which drive self-assembly can be split into molecule-molecule and molecule-surface interactions. Strong molecule-molecule interactions can lead to molecular crystals forming on the surface. Consequently, strong molecule-surface interactions prevents molecules from diffusing and rearranging in order to adapt the optimum film structure and thus can lead to disordered structures.

Some control over the molecule-surface interaction can be achieved by functionalising organic molecules. For example benzene physisorbs on TiO_2 in a planar configuration.[54] However, attaching a carboxylic group to form benzoic acid leads to chemisorption whereby the molecule deprotonates and forms two O-Ti bonds to a surface 5-fold coordinated Ti atom.[57] Such a functionalisation drastically increases the molecule surface interactions and changes the binding behaviour.

For self-assembly, choosing a functional group which leads to desired film structures is non-trivial and often based on a trial and error basis. Fig. 3.3 illustrates how the molecule-surface interactions can be tuned. Firstly, various functional groups can be chosen such as a carboxylic group, OH group or cyano (CN) group for example. These functional groups will interact differently with the substrate and thus alter the molecule-surface interactions. For weakly adsorbed molecules the number of functional groups can be increased to strengthen molecule-surface interactions.

Lastly, the geometry of the molecule can be altered: for example the positioning of the functional groups can be changed or additional components can be added to the molecule in order to match the surface structure. The choice of molecular alteration is driven by the specific substrate, e.g. an ionic crystal surface such as KCl interacts strongly with very polar CN groups, while some oxide surfaces can bind strongly to carboxylic/carboxylate or OH groups.[55,58–60]

However, changing the structure of the molecule also changes the molecule-molecule interactions. And while attaching a certain functional group can increase molecule-surface interactions, it can disadvantageously impact the molecule-molecule interactions and thus prevent self-assembly to occur.[53] It is this interplay of the two interactions which makes predicting self-assembled structures difficult.

As well as altering the molecular structure, a different substrate can also be used to steer the self-assembly process, e.g. change from NaCl to KCl.[56,58] This is based on the idea of epitaxy, where the surface structure determines the molecular adsorption geometry. Thus, matching the unit cell spacing of an ionic crystal to optimise the interactions between functional groups and surface atoms can strengthen the interactions: for example optimising the interaction between a polar CN group and the cation sites of an ionic crystal.[56,58,61]

So far the discussion of self-assembly has been focussed on static descriptions of a molecule on a surface. However, in reality molecules can vibrate, rotate and translate at non-zero temperatures. Indeed, it is the ability of the molecules to diffuse across the surface and change their coordination and orientation that enables self-assembly in the first place. At too low temperatures molecules do not have sufficient energy to overcome diffusion barriers and are frozen on the surface.[62] Similarly, if the influx of molecules is too high, they get trapped in local structures (kinetically limited growth) and self-assembly is limited.

But temperature affects self-assembly also through entropy. Large oligopyridine molecules are stabilised in a disordered (also termed liquid) phase on Ag (111) at room temperature due to rotational entropy.[63] In a self-assembled film molecules gain enthalpy through molecule-molecule interactions, but they also lose entropy

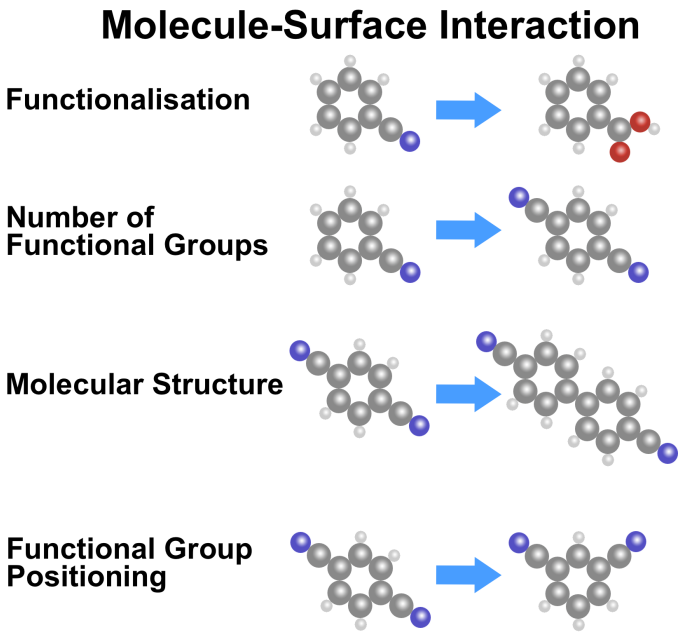

Figure 3.3: Different techniques used to tune the molecule-surface interactions.

as they become more constrained in the film structure. Therefore, the molecule-molecule and molecule-surface interactions are dependent on temperature also. Nevertheless, the temperature dependence of adsorption and intermolecular interactions is still poorly understood.

This part of the thesis discusses the effect of temperature on the self-assembly process, starting with the molecule-surface interaction of two isolated large organic molecules in Chapter 4. The loss of entropy upon adsorption is discussed with respect to conformational flexibility of these two molecules. Furthermore, diffusion of the two molecules at room temperature and above is studied and insight into their dynamic behaviour is derived from molecular dynamics (MD) simulations.

The change in entropy upon step adhesion is also calculated and used to explain experimental observations in Chapter 5. Insight from MD simulations is used to investigate small molecular structures such as dimers. These small structures were then used as building blocks for large domains of self-assembled film structures, which were compared to experimental data on self-assembled monolayers. The calculated thermodynamic stability of these structures matches experimental observations of dewetting and surface phase transitions.

3.2 Methods

Calculations of entropy changes were performed using classical MD and previously parameterised force fields (FF).[64,65] The FF were constructed to include inter-molecular, intra-molecular, inter-surface and molecule-surface interactions. Each of these interactions is computed individually and summed up to yield the total interaction of the system.

For inter-molecular interactions the CHARMM FF[66] was used, which models bonds and angles by classical harmonic springs, and torsional angles by cosine functions. Non-bonded van der Waals (vdW) interactions are also calculated via a 12-6 potential. The total potential energy can then be expressed as:

$$\begin{aligned} E = &\sum_{bonds} k_b(r - r_0)^2 + \sum_{angles} k_\theta(\theta - \theta_0)^2 + \sum_{dihedral} k_\phi(1 + \cos(n\phi - \delta)) \\ &+ \sum_{improper} k_\omega(\omega - \omega_0)^2 + \sum_{non-bonded} \epsilon_0 \left[\left(\frac{\sigma}{r_{ij}} \right)^{12} - \left(\frac{\sigma}{r_{ij}} \right)^{6} \right] + \sum_{i \neq j} \frac{q_i q_j}{\epsilon r_{ij}} \quad , \end{aligned} \tag{3.65}$$

where $r - r_0$ is the atomic displacement from equilibrium bond distance, $\theta - \theta_0$ is the change in angle between three bonded atoms, ϕ is the dihedral angle with phase shift δ and multiplicity n, $\omega - \omega_0$ is the out of plane improper angle, σ is the finite distance at which the vdW potential is zero, ϵ_0 is the depth of the vdW potential well, q are partial charges assigned to each atom, ϵ is the dielectric of the environment and k_x are force constants.

Intramolecular and molecule-surface interactions are non-bonded interactions (for this system, not generally), which are modelled by 12-6 potentials and electrostatic interactions as given in the last two terms in Equation 3.65. The force field for the surface was adopted from Catlow et al.,[67] which employs a Buckingham type potential to model the interactions between the alkali-halide surface atoms:

$$E_{ij}(r) = A_{ij} \exp(-r/\rho_{ij}) - C_{ij}/r^6 \quad , \tag{3.66}$$

where A, C and ρ are fitting parameters.

Partial charges were assigned to the atoms of the molecule based on Bader analysis of an isolated molecule as calculated by DFT using the B3LYP functional. For the KCl surface atoms classical charges of ± 1 were used for K and Cl, respectively.

All calculations were performed using the LAMMPS[68] code, which is well optimised for classical energy minimisation and MD simulations. A particle-particle particle-mesh (P3M) solver was used to compute the long range electrostatic interactions and all forces were minimised to be less than 0.01 eV/Å. The KCl surface was represented by a four layer slab with the bottom layer frozen in its bulk geometry in order to prevent drift in the simulation cell.

MD simulations were run in the NVT ensemble with a Nosé-Hoover thermostat[44] controlling the temperature of the system, whereby the molecules and the surface were controlled by separate thermostats. The system was equilibrated for 1 ps before data acquisition.

The accuracy of the force fields was checked against ab initio calculations using dispersion crrected DFT as well as MP2 calculations of organic molecules on KCl.[64] It was found that adsorption geometries were reproduced well, giving good agreement between the three methods to within 0.05Ådeviations. Adsorption energies calculated with the force field overestimated the binding by $\sim 7\%$ compared to DFT results, which was acceptable for the scope of this investigation.

Chapter 4

Modelling of Entropic Contributions to Adsorption

4.1 Introduction

Adsorption energies and geometries of functionalized molecules have been successfully characterised in the past using various experimental techniques.[69–77] Non-contact atomic force microscopy (NC-AFM) can give insight into the molecular arrangement.[62,78,79] However, obtaining atomic resolution is still challenging[80] and often requires supplementary theoretical calculations.[81–83]

Theoretical calculations can provide a better understanding of adsorption geometries, film structures and nucleation sites. Previous work on molecular adsorption on insulators using DFT has been often restricted to ground state calculations that represent a frozen 0K system.[84,85] However, most experiments are performed at elevated temperatures (i.e. room temperature), where entropic effects contribute to the adsorption free energy. The importance of entropy has been recognised before[86] and detailed studies started to appear more recently in the context of molecular association in solutions,[87] molecular adsorption from solutions,[88] formation of ordered monolayers at surfaces,[89] and in understanding temperature programmed desorption (TPD) experiments.[90]

For small organic molecules such as alkanes experimentally measured enthalpies and entropies of adsorption have been reported.[91] For larger organic molecules detailed studies of adsorption are still challenging and often focus on static calculations.[84,85,92] Attempts to compute free energies have been made for i.e. pro-

teins,[93–95] ion solvation,[96,97] small molecular clusters[98,99] and small molecules on surfaces.[100–102] While well converged results can be obtained for small systems, the larger the configurational space the more challenging the calculations become and convergence is not guaranteed.[93,103] In particular, when the free energy landscape varies by several kT along the reaction coordinate, MD is often insufficient for sampling the high energy states.

In order to calculate the change in entropy upon adsorption long timescale MD simulations need to be performed. Due to the excessive computational cost associated with DFT MD, FFs need to be used which allow lang timescale MD simulations to be run at reasonable computational expense. Thermodynamic integration can then be used to analyse MD trajectories and calculate entropy changes as outlined in Chapter 2.

In this chapter the interaction of isolated molecules with a KCl (001) surface is investigated. Firstly, the effect of temperature and molecular flexibility on adsorption is studied for two molecules, namely 1,4-bis(cyanophenyl)-2,5-bis(decyloxy)benzene (CDB) and 1,3,5-tri-(4-cyano-4,4 biphenyl)-benzene (TCB), whose chemical structures are shown in Fig. 4.1. Due to their molecular structure, TCB and CDB differ in their flexibility: TCB is a rigid planar tripod molecule, whereas CDB has a rigid central body with two flexible hydrocarbon chains attached either side. The molecule-surface interaction also influences diffusion of a molecule across the surface, which, as described before, is crucial to achieve self-assembly. Hence, mean squared displacement analysis was performed on long MD trajectories of TCB and CDB on the KCl (001) surface in order to deduce diffusion barriers.

4.2 Verification of the Force Fields

The TCB FF was tested against previous DFT data (obtained by D. Gao and M. Watkins[64]) by comparison of its minimum energy geometry in vacuum as well as adsorption geometries and energies on the KCl (001) surface. A grid search was performed to find the lowest energy adsorption geometry, where at each grid point energy minimisation was performed for rotations around the surface normal of 0° to

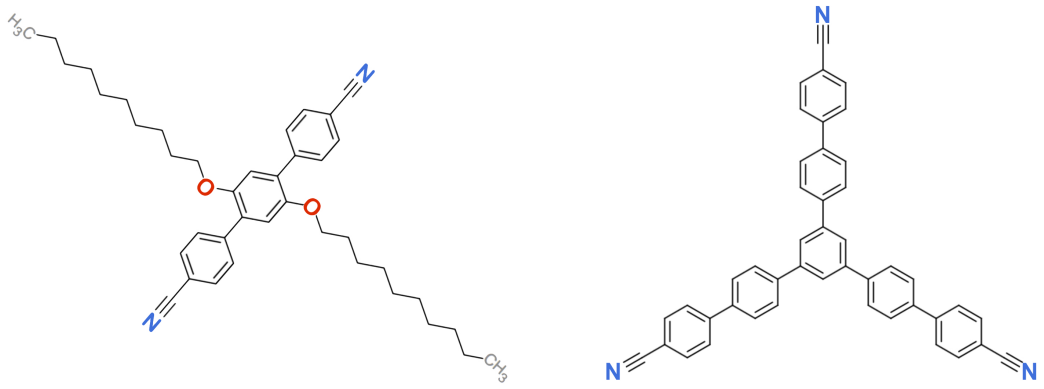

Figure 4.1: Chemical structure of CDB (1,4-bis(cyanophenyl)-2,5-bis(decyloxy)benzene) on the left and TCB (1,3,5-tri-(4-cyano-4,4 biphenyl)-benzene) molecule on the right.

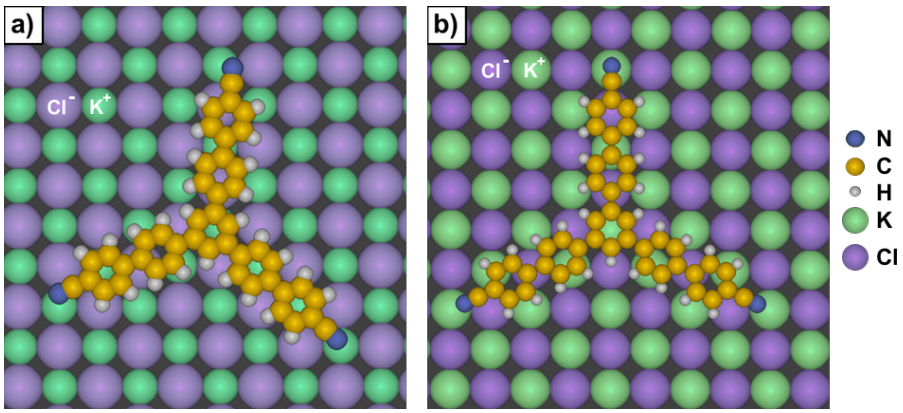

Figure 4.2: Two stable adsorption geometries of a single TCB molecule on a KCl(100) surface. The geometry (a) is the most stable with an adsorption energy of 4.55 eV compared to the meta- stable state (b) with an adsorption energy of 4.3 eV.

30° in 2° increments.

Two stable configurations found in the classical simulations are shown in Fig. 4.2. In both configurations the cyano-groups (CN groups) are located nearest to a cation site (potassium, K site), indicating electrostatic anchoring of the molecule by the functional CN-groups.

The configuration (a) (Fig.4.2) exhibits mirror symmetry along the ⟨110⟩ direction, where one leg of the molecule aligns with a cation row. This is energetically favourable with an adsorption enthalpy of 4.55 eV at an average molecule-surface distance of 2.89 Å. The strong interaction between the molecule and the surface leads to a flatter molecular geometry compared to the vacuum geometry. The tor-

sional angle between the benzene rings of the molecule's legs is reduced from 31° to 0.6° (leg along ⟨110⟩) and 4° (other two legs). This adsorption geometry matched well the minimum structure found in DFT calculations with a 7% overestimation of the adsorption energy.

In configuration (b) (Fig. 4.2) the molecule exhibits mirror symmetry along the ⟨100⟩ direction of the KCl surface. The adsorption energy of this configuration was found to be a slightly lower 4.3 eV with an average distance of 2.89 Å between the molecule and the surface. The angles between the legs of the molecule are compressed/stretched in order to maximise the interactions of the CN-groups with surface cation sites. Due to the rigid geometry of the molecule and the three anchoring sites which pin the molecule to the surface, no other minima were found.

The CDB FF was adopted from previous studies of the molecule on KCl (001) and has been discussed in detail in refs.[58,65] In its lowest adsorption geometry the molecule attaches with the two CN groups (see Fig. 4.3) to cations on the surface with an adsorption energy of 3.1 eV. The benzene rings are slightly tilted with respect to the surface plane to minimise interactions between neighbouring H atoms. The hydrocarbon chains are stretched orthogonal to the molecule's body along the ⟨110⟩ surface direction, however, since these chains are very flexible, many local minima exist where the chains are not fully stretched out. One such local minimum structure is shown in Fig. 4.3 on the right. The main body of the CDB molecule aligns with the ⟨100⟩ surface direction and one arm aligns with the main body while the other is still aligned with the surface ⟨110⟩ direction. The adsorption energy of this configuration is 2.8 eV. Overall, ab initio adsorption geometries are well reproduced with the FF and adsorption energies match the DFT results to within 5%.[65]

4.3 Results

With increasing temperature entropic contributions to adsorption become important in order to correctly describe the dynamic behaviour of molecules on surfaces.[63] Particularly for flexible molecules, where many degrees of freedom become con-

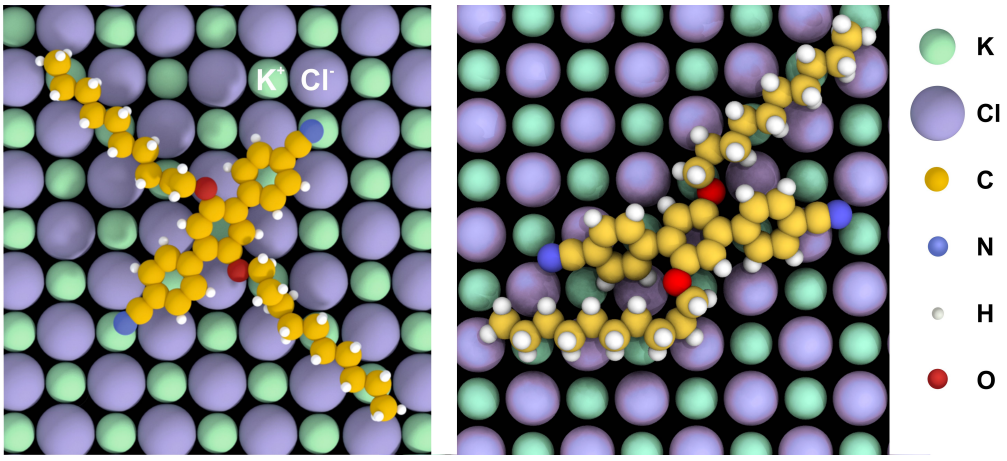

Figure 4.3: Left: Lowest energy adsorption geometry of a single CDB molecule on KCl (001). Right: One of many local minimum structures.

strained during adsorption, entropy changes can be significant.[91]

4.3.1 Conformational Entropy

The flexibility of molecules can be described in terms of conformational entropy, which can be estimated using rotamers (see Fig. 4.4), which has previously been used to describe the conformational entropy of proteins.[104,105]

Assuming that there are N different conformations of a molecule each with probability p_i, then the conformational entropy per molecule is given by:

$$\Delta S_{conf} = -k_B \sum_{i=1}^{N} p_i \ln(p_i) \quad . \tag{4.1}$$

For example a molecule with three possible configurations (e.g. ethane), each equally probable, the conformational entropy is $S = -R\sum_1^3 1/3 \ln(1/3) = -R\ln(1/3)$.

In order to evaluate conformational entropy of a molecule, it is useful to begin by defining the number of conformations in terms of populated rotamers. A rotamer is a conformational isomerism, where different conformations can be interconverted by rotating single bonds. CDB has four kinds of rotamers; the C-C bond in the carbonyl chains, the C'-C' bond between the benzene rings and the C-O bond of the carbonyl chain, while TCB has only C'-C' rotamers between the phenyl groups, where C' indicates a carbon atom that belongs to a benzene ring.

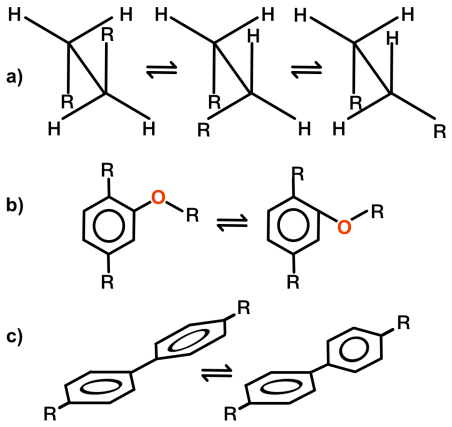

Figure 4.4: Different rotamers present in the system and their commensurate configurations, for a) a single bond in a linear carbonyl chain, b) the benzene-oxygen bond in CDB and c) the benzene-benzene bond.

The C-C bond of the carbonyl chains has three different conformations (see Fig.4.4), the C'-C' bond of the phenyl groups has two conformations, since the torsional angle between the two benzene rings can be $\pm 31°$ and the C-O bond has two conformations as well, one where the C'-O-C angle is pointing up out of the benzene plane and one where it is pointing down. Hence the conformational entropy per C'-O bond is the same as for a C'-C' bond. Note the C-C≡N bonds are linear and do not have rotational isomers. Therefore, they do not contribute to the conformational entropy.

The CDB molecule contains 18 C-C bonds, two C-O bonds and two C'-C' bonds, compared to the TCB molecule which only has 6 C'-C' bonds. Summing up the corresponding energies at 300 K, the conformational entropy amounts to $\Delta S_{conf.}^{CDB} = 0.64$ eV and $\Delta S_{conf.}^{TCB} = 0.11$ eV. While this model is a simplification of the actual configurational space, it gives valuable insight into the difference between TCB and CDB. This difference in conformational entropy can be used as a metric to distinguish between more flexible and rigid molecules.

4.3.2 Entropy Contribution to Adsorption

The entropic contribution to adsorption energies can be estimated by thermodynamic integration. As outlined in Section 2 steered MD is used to sample the

ensemble space of the adsorption process. The starting configuration is a desorbed molecule 20 Å above the KCl surface and the final configuration is an adsorbed molecule. The reaction coordinate is the z-component of the distance between the molecule's centre of mass (COM) and the surface, which is divided into 30 increments. Thus, with it's COM fixed at each incremental separation R the molecule is allowed to rotate and translate freely.

Equation 2.64 can then be rewritten as a function of the molecule-surface separation R:

$$-TS(r) = -TS(r_0) + \frac{1}{kT}\int_{r_0}^{r} dR\left[\left\langle E\frac{\partial E}{\partial R}\right\rangle_R - \langle E\rangle_R\left\langle\frac{\partial E}{\partial R}\right\rangle_R\right] \quad , \tag{4.2}$$

which allows the calculation of the change in entropy upon adsorption. The first term is chosen such that the entropy of a molecule at 20 Å is zero, where it is fully desorbed from the surface.

Fig. 4.5 illustrates the change in entropy (TΔS) of adsorption for a single TCB molecule at temperatures 300 K, 400 K and 500 K. It can be seen that upon adsorption a TCB molecule loses about 0.5 eV at 300 K. The entropy change displays three stepwise decreases as the TCB molecule adsorbs onto the KCl (001) surface. Initially, as the molecule approaches the surface one of the legs will attach to it and the molecule will lose some translational and rotational entropy. This initial change in entropy is illustrated in Fig. 4.5 at position (c). Since the COM is fixed in these calculations, initially the molecule's motion becomes trapped in this position and it is unable to translate across the surface, leading to a large drop in entropy. The minima for the molecule in this configuration is very steep and thus sampling of the entire configurational space is difficult. The entropy of the system increases again when the COM is brought nearer to the surface as the molecule can reorient itself, which allows for more molecular motion.

A second drop in entropy is observed when another leg attaches to the surface (Fig. 4.5b) and the entropy continues to decrease until the optimum adsorption geometry is reached in the configuration shown in Fig. 4.5a. Forcing the molecule

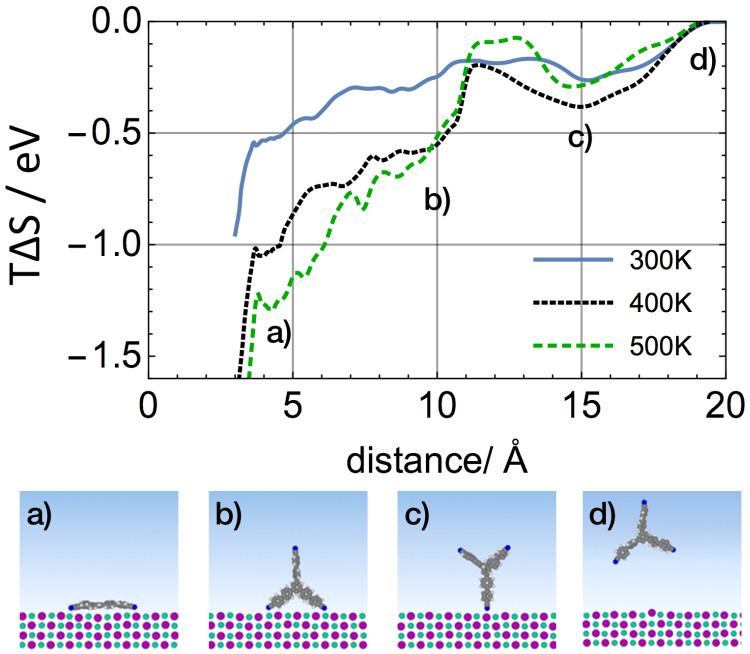

Figure 4.5: Change in entropy plotted against distance from surface for a TCB molecule. The curves represent a system at 300 K, 400 K and 500 K, respectively. Below the graph are snapshots of TCB at various stages in the adsorption, as indicated in the plot.

even closer to the surface will lead to a drastic decrease in entropy, as all molecular motion is frozen and its degrees of freedom become fixed.

A similar trend can be observed at higher temperatures: at 400 K the change in entropy amounts to -1.0 eV and at 500 K to -1.25 eV. Thus, the entropic contribution to the adsorption free energy is smaller than the enthalpic contribution and the molecule is not expected to desorb even at 500 K.

In comparison Fig. 4.6 illustrates the change in entropy upon adsorption for a CDB molecule. A similar behaviour can be observed for the CDB molecule with some key differences. First, the entropy decreases more smoothly at all three temperatures. This can be attributed to the fact that CDB is more flexible and has many more degrees of freedom. As the molecule adsorbs on the surface, these degrees of freedom are gradually restricted, leading to a smoother decrease in entropy. Secondly the magnitude of the change in entropy upon adsorption is much larger.

At 300 K the loss in entropy amounts to 1.0 eV, which increases to 2.1 eV at

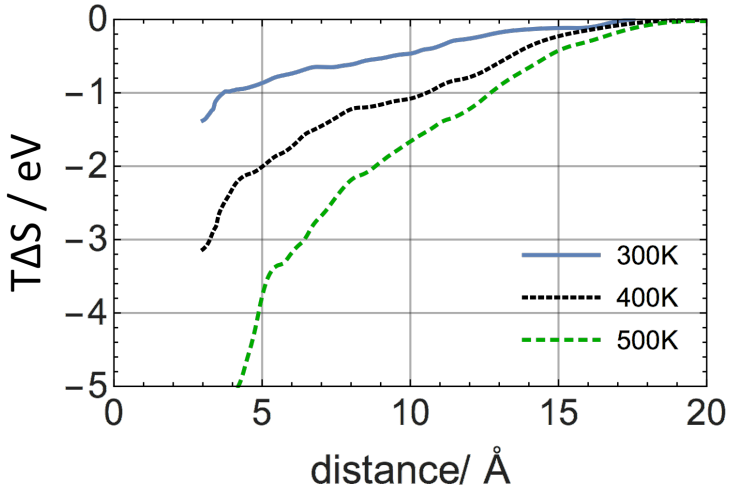

Figure 4.6: Change in entropy plotted against distance for the CDB molecule at temperatures of 300 K, 400 K and 500 K, respectively.

400 K and over 3.5 eV at 500 K. Furthermore, the equilibrium distance at which the molecule adsorbs, changes. At 300 K the COM of the molecule sits closer to the surface than at 500 K. This is due to the hydrocarbon chains, which tend to lift off the surface at higher temperatures, as observed in MD trajectories and thus lead to larger surface COM distances. Pushing the molecule closer to the surface than the equilibrium distance again leads to a sharp reduction in entropy.

The change in entropy can be attributed to a loss of degrees of freedom of the molecule upon adsorption. Rotational, vibrational, translational and conformational degrees of freedom become restrained, leading to a reduction in entropy. For TCB the initial estimate of conformational entropy loss is about 20% of the total change in entropy, whereas for CDB it accounts for about 60%. However, the conformational entropy estimate is based on the assumption that all conformational degrees of freedom become restrained, which is a crude assumption for the flexible CDB molecule. It displays many conformations, particularly related to the hydrocarbon chains, in MD simulations and thus the conformational entropy loss is overestimated.

4.3.3 Molecular Diffusion and Rotation

As the molecules adsorb on the surface, their translational degree of freedom is reduced from three dimensional to two dimensional dynamics. Using the optimised

FF, the diffusion of a single TCB/ CDB molecule on the KCl (001) surface was investigated.

To study diffusion of CDB and TCB molecules, classical MD calculations were performed for 30 ns by placing a single molecule on the KCl (001) surface with the plane of the molecule parallel to the surface plane. The simulations were performed using a 1 fs timestep and a 4 layer thick slab of KCl(001) to represent the surface. The bottom layer was fixed while the top 3 layers and all TCB/CDB atoms were allowed to relax. From the molecular trajectories, the diffusion coefficients and diffusion barrier can be calculated using a standard mean-squared-displacement approach (as outlined in refs.[106, 107]).

The MD simulations give insight into the translational and rotational motion of the molecules. At 300 K the CDB molecule displayed fast dynamics. The hydrocarbon chains are very flexible and have enough energy to access many configurations, occasionally lifting off the surface. This became more pronounced as the temperature was increased to 400 K and 500 K.

At the same time, the central ring of the CDB molecule showed slower dynamics, indicating a stronger attraction to the surface. The molecule can rotate to access several local minima, at which the CN groups always point towards surface cation sites. Additionally, it can translate across the surface, with an average mean distance travelled of 1 nm per 10 ns MD. At 400 K, CDB molecules became predictably more mobile and were observed to occasionally roll or flip across the surface. Finally, at 500 K these effects were further pronounced, and in one rare instance the molecule became fully desorbed from the surface.

In comparison, molecular diffusion occurs at a much slower rate for TCB molecules. During 10 ns MD runs at 300 K the central benzene ring of the molecule stayed above the same cation site for the entire simulation or moved only to a neighbouring cation 4 Å away. This is indicating high diffusion barriers for the molecule to traverse the surface.

However, the molecule is still able to rotate readily on the surface. For this system a rotational motion was defined as a change in which leg was aligned with a cation

Temperature	Diffusion Coefficients /(cm^2/s)	
	TCB	CDB
450 K	$(1.13 \pm 0.02) \times 10^{-7}$	$(6.49 \pm 0.01) \times 10^{-7}$
500 K	$(4.38 \pm 0.02) \times 10^{-7}$	$(2.56 \pm 0.01) \times 10^{-6}$
550 K	$(1.33 \pm 0.02) \times 10^{-6}$	$(2.26 \pm 0.01) \times 10^{-5}$

Table 4.1: Diffusion coefficients of TCB and CDB molecules on a KCl (001) surface as calculated from MD trajectories using a mean-squared displacement approach.

row. An average of 8 such rotations were observed within the 10 ns simulations. Note that these rotations are not directly comparable to those of the CDB molecule since they represent unique motions. At 400 K the molecule became more mobile and rotated rapidly. Occasionally one leg would lift up from the surface for less than 10 ps before going back to the planar adsorption geometry. At 500 K the dynamics became even faster, with very rapid rotation and the molecule diffusing over the surface with a mean squared displacement of 6 nm per 10 ns MD run.

Diffusion coefficients calculated from the trajectories at elevated temperatures are given in Table 4.1. The magnitude of the diffusion coefficients compares well with the coefficients found for similar systems.[108] Diffusion barrier calculated from the gradient of a linear fit to an Arrhenius plot of the diffusion coefficients *vs.* inverse temperature amount to 0.52 eV for TCB and 0.36 eV for CDB.

These results are in good agreement with experimental NC-AFM images taken at room temperature, where single molecules cannot be resolved on clean KCl (001) terraces. Due to the large difference between the time scales relevant for molecular diffusion and those relevant to NC-AFM imaging, both the CDB and TCB molecule would undergo many rotations and translations during the time needed to collect a single experimental image at room temperature. These mobile individual molecules are therefore not expected to be imaged, unless they are stabilised by a feature such as a step edge, kink, or other trapping site.

4.4 Discussion

The adsorption and diffusion of TCB and CDB reveals differences, which can be traced back to their chemical structure. TCB is a rigid molecule with three anchoring CN-groups. Adsorbing one leg at a time leads to a stepwise decrease in entropy of the molecule, as its few degrees of freedom are reduced. The more flexible CDB molecule, however, does not show this stepwise reduction and instead the change in entropy is gradual. This is due to the many more degrees of freedom of the CDB molecule compared to the TCB. Interestingly, assuming the molecule is frozen in one conformation after adsorption, the change in translational and rotational entropy is very similar between the two molecules.

The dynamics of the TCB and CDB molecule at elevated temperatures depends not on the adsorption strength, but on the barrier for diffusion. Typically these barriers are estimated from NEB calculations at a fixed temperature. However, the molecule changes it's adsorption height as the temperature is increased. Thus, the barrier for diffusion is reduced as the molecule feels less of the surface potential. Combined with the increases in kinetic energy, the molecules display fast dynamics at temperatures above 300 K.

Self-assembly requires a fine balance between molecule-molecule and molecule-surface interactions. At low temperatures the molecules do not have enough energy to diffuse and reorient themselves to form self-assembled films, called kinetically limited self-assembly. This can also occur if the deposition rate of molecules is too high such that they get trapped in an amorphous phase.

Experimentally, the system can be heated up in order to allow for faster dynamics of the adsorbed molecules. This can facilitate the formation of self-assembled films or the transition between different self-assembled phases. However, entropic effects lead to dewetting of the CDB molecule above 400 K and it has previously been reported that a low density amorphous phase (also called liquid phase) is favoured at higher temperatures, since it allows for more molecular motion (e.g. rotation).[63] Thus, temperature control is critical in order to steer the formation of such self-assembled structures.

4.5 Conclusions

The comparative study of adsorption of two organic molecules on the KCl (001) surface revealed that entropy losses upon adsorption are significant for flexible molecules; at high enough temperatures they can match the enthalpic contribution to adsorption energy thus leading to dewetting or desorption.

A thorough understanding of dynamics of organic molecules at insulating surfaces is imperative for the development of molecular devices. The adsorption energy and geometry are dependent on both the character of interactions and temperature. As a molecule adsorbs on a surface, some of its degrees of freedom become constrained, leading to the entropy loss. For example, we found that for the relatively rigid TCB molecule the entropy loss does not exceed the adsorption enthalpy up to 500 K. However, the flexible CDB molecule exhibits an entropy loss comparable to the adsorption energy already below 400 K and can desorb from the surface.

These results complement static calculations of molecular adsorption and shed further light on the dynamic behaviour of molecules at surfaces. They can be useful for our understanding of expected stability of molecular structures and the mechanisms of self-assembly.

Chapter 5

Role of Molecular Flexibility and Entropy in the Self-Assembly Process

5.1 Introduction

In the previous chapter the entropic contributions of adsorption for two organic molecules, TCB and CDB, were investigated. The molecule-surface interaction plays a crucial role in driving surface adsorption of such molecules at elevated temperatures.[53,64] However, in order to form well defined 2D self-assembled film structures, the molecule-surface interaction needs to be carefully counterbalanced with molecule-molecule interactions. A deviation from this balance leads to disordered structures or molecular crystals on the surface.[59,78]

It has previously been shown that for specific molecules on insulating surfaces several film structures can be achieved.[58,109,110] The phases are often observed to coexist on the surface indicating shallow potential energy landscapes. By gently heating the surface the phase of the self-assembled film can be changed,[61] however, heating too much can lead to dewetting of molecules into molecular crystals.[58,111] Therefore, the precise thermodynamic stability of self-assembled phases is difficult to probe experimentally, as very accurate temperature control is difficult to achieve or the reorganisation time for film structures is too long.

Theoretical energy minimisation calculations can give insight into the lowest energy arrangement of molecules and study possible film structures.[112–114] Predictions

about their relative stability can be made from their packing densities, coordination, molecular strain and their epitaxy. However, energy minimisation calculations do not give insight into the thermodynamic stability of these structures at elevated temperatures.

Entropic contributions have been shown to determine the relative stability between a 2D "liquid" phase (disordered) and a self-assembled monolayer structure.[63] Furthermore, large molecules have been observed to alter the surface structure of kink sites.[115] Therefore, a static investigation of adsorption and self-assembly is insufficient and effects due to temperature have to be considered.

Thus, understanding the behaviour of TCB and CDB molecules once they have adsorbed on the KCl (001) surface is crucial to gain insight into the mechanisms which drive self-assembly. In this chapter interactions with step edges, surface kink sites and between molecules in molecular structures is investigated in energy minimisation calculations. Further, the entropic loss upon step adhesion and dimer formation is calculated, which can explain experimental observations. Lastly, combining these results with knowledge gained from molecular dynamics simulations, the stability of two possible TCB film structures is studied.

5.2 Methods

5.2.1 Entropy Change Calculations

Chapter 4 discusses how the entropy loss upon adsorption of CDB and TCB molecules on a clean terrace greatly contributes to the adsorption free energy and is comparable to the enthalpy of adsorption at high temperatures for CDB.[64] The loss in entropy originates in the reduction of degrees of freedom of the system. These degrees of freedom can further be reduced, when a molecule adheres to a step edge or forms molecular structures.

It has previously been reported that for large, organic molecules physisorbed on an insulating surface changes in rotational entropy play a dominant role.[63] A rough estimate of the rotational entropy of a single molecule can be obtained using the rigid rotor model.[116] The rotational entropy of a molecule is estimated relative to

a state where the molecule does not rotate and the barrier for rotation is assumed to be zero, meaning the molecule is free to rotate 360° around its centre of mass as given by:

$$T \cdot \bar{S}_{rot}^{ads} = k_B T[\frac{1}{2} + \ln(z_{rot}^{ads})] \quad , \tag{5.1}$$

$$z_{rot}^{ads} = \frac{1}{\sqrt{\pi}\sigma} \left(\frac{8\pi^2 k_B T}{h^2} \right)^{\frac{1}{2}} (I_z)^{\frac{1}{2}} \ . \tag{5.2}$$

The symmetry factor σ denotes how many configurations are identical if the molecule is rotated by 360° around the surface normal and the moment of inertia is given by: $I_z = \sum_i m_i(x_i^2 + y_i^2)$, where x_i and y_i are the molecules coordinates with the origin at its centre of mass and the z axis pointing along the surface normal. Importantly, the molecule is assumed to be rigid during the rotation, such that its moment of inertia is constant.

A more accurate estimate of entropy changes can be attained using Equation 4.2. The reaction coordinate was defined as the distance between a molecule and a step edge or the centre of mass (COM) of another molecule. The average is taken over 50 ns MD simulations, after a 1 ps equilibration time. Using shorter simulation times is not sufficient to sample the configuration space (see Appendix A). The convergence of our results was checked by increasing the MD simulation time to 80 ns. With longer simulation times more of the high energy, low probability phase-space will be sampled, which is critical for obtaining accurate entropy changes. The entropy change was calculated relative to an isolated molecule on a flat terrace, where the entropy was defined as zero. The reaction coordinate R was varied in 0.1 Å intervals and the centre of mass was fixed at each R.

5.3 Experimental Background: NC-AFM Imaging of CDB and TCB Molecules on KCl(001)

For the study of self-assembly theoretical calculations are supplemented with experimental data, which was obtained by collaborators under the supervision of Prof.

C. Loppacher. A short overview of the experimental results is given in this section and more details can be found in ref.[58,61]

TCB and CDB molecules were synthesised, deposited onto KCl(001), and imaged at room temperature using NC-AFM. The adsorption behaviour of these two molecules is compared in order to gain insight into the effects of molecular flexibility on nucleation, growth and morphology of film structures.

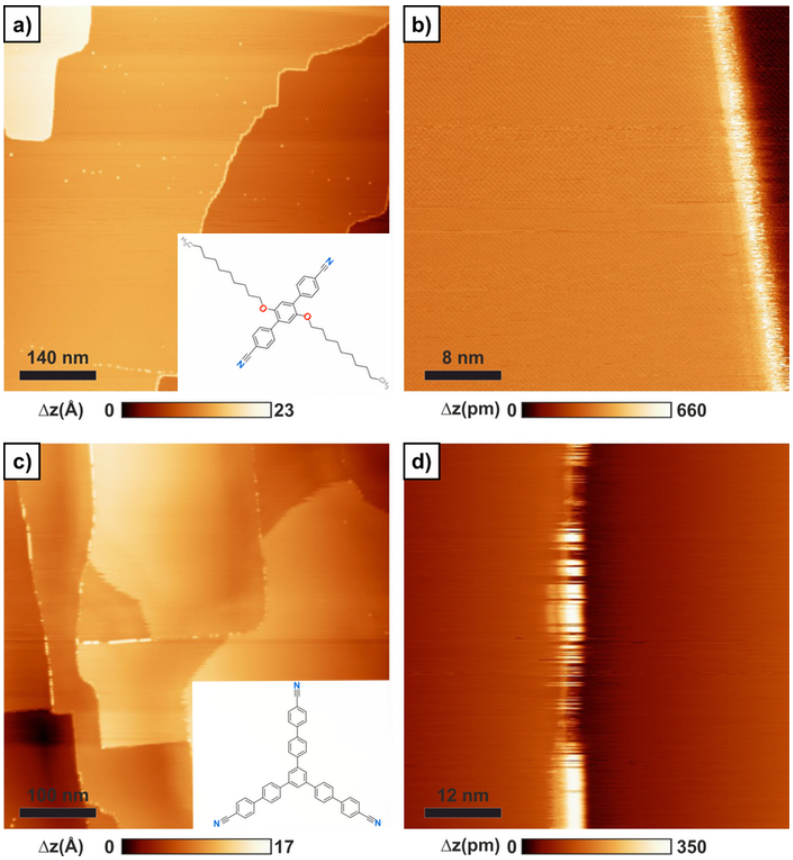

Figure 5.1: a) A topography image where 0.05 monolayer (ML) of CDB molecules were deposited onto KCl(001). In the upper left corner there is a terrace, which is completely covered by CDB molecules and all step edges are fully decorated. b) A topography image of 0.06 ML of CDB molecules deposited onto KCl(001) showing a decorated step edge. c) A topography image of TCB molecules deposited onto KCl(001), which shows mostly undecorated step edges and fuzzy stripes. These reproducible fuzzy stripes represent areas where molecules diffuse along crystallographically oriented steps. d) A representative zoomed in image over a fuzzy step edge area. A few of the bright objects are stably imaged, however, larger fuzzy stripes can be observed over several scans. Images reprinted with permission from ACS J. Phys. Chem. C[64]

Upon depositing CDB molecules on the KCl (001) surface, step edges become decorated with molecules first. Fig. 5.1a shows homogeneous bright rims, which run along all KCl steps at low molecule coverage. The top left corner shows a monolayer film of CDB molecules and bright features on the terrace are attributed to surface defects, which are formed during the *ex situ* cleaving and *in situ* annealing process. A zoomed in image of a step edge is shown in Fig. 5.1b.

In contrast, TCB molecules do not completely cover the substrate step edges (see Fig. 5.1c and d), even at coverages as large as 0.06 ML. Step edges appear partly covered with molecules along steps aligned with the crystallographic high symmetry directions of KCl. However, these molecules can not be resolved atomically and instead appear as fuzzy stripes in zoomed in AFM scans (Fig. 5.1d). This may be due to molecules diffusing along the step edge or due to interactions with the tip, which attracts molecules and drags them along the step edge.

These results indicate that CDB molecules interact more strongly with step edges on KCl (001) surface than TCB molecules, which may have important implications for nucleation and film growth for molecular self-assembly. CDB molecular films are proposed to grow from step edges on the KCl(001) surface while self-assembled films composed of TCB molecules is expected to exhibit island growth on clean terraces. Indeed some island growth was observed at room temperature, as shown in Fig. 5.2b.

At higher coverages, CDB forms very large molecular islands, which often appear to be single domains at step edges.[58] Even at low coverages no small molecular clusters could be observed, but instead molecules form large islands. The large island size is an indication of fast diffusion with a large diffusion length, however, the edges of an island appear fuzzy and are unstable under repeated scanning of the same area. This indicates that molecules are weakly bound in the monolayer structure and can be perturbed by the presence of the AFM tip or thermal motion.

For TCB at low coverage ($\sim$0.1 ML) small islands with drop like shapes can be observed to grow on terraces (Fig. 5.2b). These small islands are mobile and diffuse over the surface under repeated scanning, however, once they reach a step edge they get immobilised. This is an indication of a different growth mode compared to CDB,

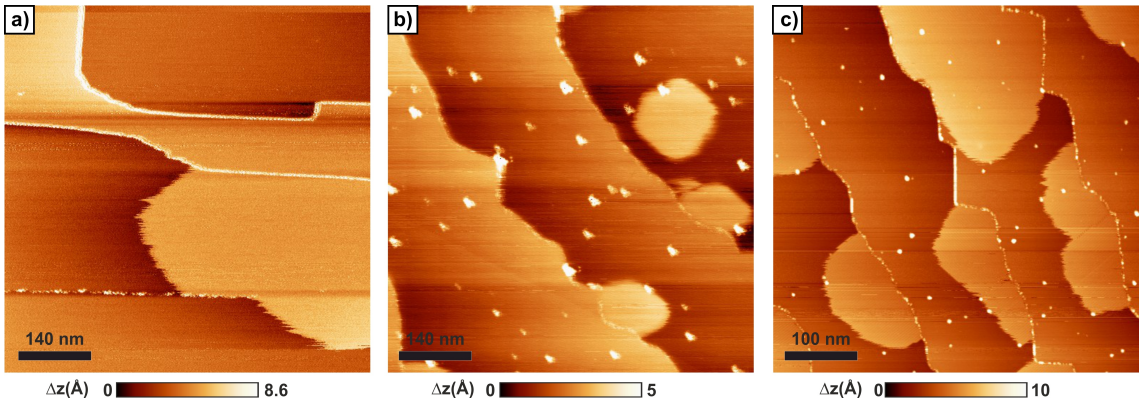

Figure 5.2: a) 0.15 ML of CDB deposited on KCl: Island borders are unstable and molecular layers diffuse on the surface, all step edges are decorated. b) 0.1 ML and c) 0.3 ML coverage of TCB on KCl: typical drop like islands growing on terraces and steps, few smaller islands observed to diffuse on the surface. Images reprinted with permission from ACS J. Phys. Chem. C[64]

where small isolated islands were not observed on terraces. At higher coverages and smaller terraces (∼0.3 ML, Fig. 5.2c), TCB islands are more often observed at step edges, however, still with drop-like shapes and rarely decorating complete terraces, whereas CDB islands often span $> 1\mu m^2$.

Fig. 5.3a illustrates two monolayer film structures, which are termed line structure and porous network structure. The line structure is the more densely packed film at 2.5×10^{-3} TCB/Å^2 and repeats with a lattice of about (17 Å×31 Å)±2Å. In comparison, the square structure has a density of $2.3{\times}10^{-3}$ TCB/Å^2 and a lattice of 41 Å×41 Å. At room temperature these two structures can be observed to coexist and no transition from one to the other could be identified. However, upon heating to 370°C the porous network is converted to the line structure, indicating a thermodynamic phase transition.

Several features could also be observed within the line structure, such as line splitting (Fig. 5.3a), varying orientations of the lines (Fig. 5.3b) as well as different contrasts (Fig. 5.3b top right corner). These indicate the presence of several stable polymorphs of the line structure at room temperature. Fig. 5.3c and d show molecular resolution images of the two film structures with overlaid proposed atomic geometries.

In order to understand these experimental findings, TCB and CDB molecules

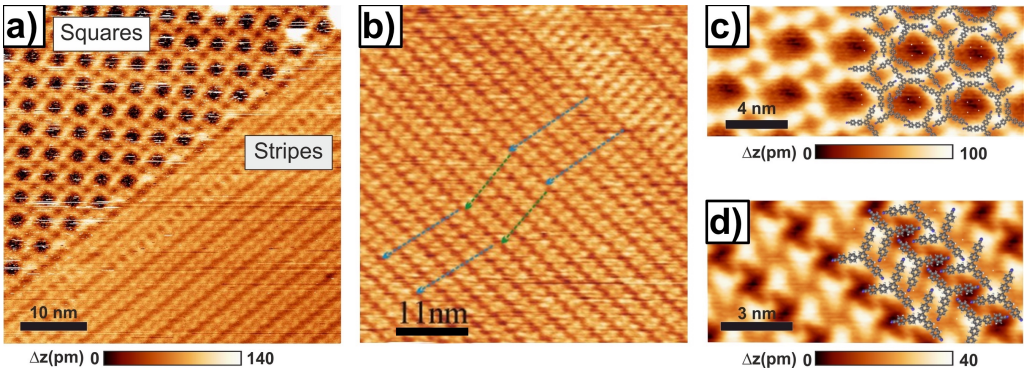

Figure 5.3: a) An overview of both the porous structure and the line structure formed by TCB molecules on the KCl(001) surface at room temperature. b) Large linear domain showing alternating orientations of the line structure. c) A zoomed in mesh average image of the square porous structure along with a proposed atomistic model. d) A zoomed in mesh average image of the denser line structure along with a proposed atomistic model. Images reprinted with permission from ACS J. Phys. Chem. C[64]

were investigated adsorbed on step edges on the KCl (001) surface as well as on kink sites. Steered MD was performed to estimate the entropic loss of step adhesion and thus derive insight into dynamics of film nucleation.

5.4 Results

5.4.1 TCB and CDB Interaction with Step Edges and Kinks

Modelling the interaction of TCB and CDB with step edges and kinks provides a very sensitive test for the balance of molecule-surface interactions because they characterise the difference provided by the specific interaction with a relatively small number of step and kink atoms with respect to the strong interaction with the terrace mainly governed by the vdW forces. Experimental evidence suggests that at room temperature CDB molecules are more strongly bound to steps than TCB, which has implications for self-assembled film nucleation.

5.4.1.1 TCB Molecules at Step Edges and at Kinks

In order to gain insight into the step adhesion process and possible adhesion geometries, a 50 ns trajectory of temperature accelerated MD (T=500 K) of 100 TCB molecules, corresponding to about 0.5 ML coverage, on a slab containing a step edge

was analysed.

At 500 K molecules were observed to be mobile on the surface, rotating and translating, indicating they had enough thermal energy to overcome diffusion barriers and access several minima. After 50 ns the step edge showed a 75% coverage with TCB molecules. These molecules adopted one of two configurations, attaching with either one or two legs to the step edge, where the two leg attached geometry accounted for about 2/3 of the molecules.

Using this information energy minimisation calculations were performed to study the adsorption geometry of individual TCB molecules at a step edge. Three minima were identified: in the first configuration, only one leg of the molecule is attached to the step at a cation site (see Fig. 5.4a). This geometry is very similar to the lowest adsorption geometry for TCB on a clean KCl (001) terrace (see Fig. 4.2). The interaction energy of the molecule with the step amounts to about 0.15 eV giving a total adsorption energy of 4.7 eV and the molecule displays very little deformation.

In the second configuration, two legs interact with K^+ sites on the step edge. However, the angle between the legs needs to distort (stretch) in order to maximise interactions between the CN groups and K atoms (see Fig. 5.4b). Despite the distortion of the molecule, the adsorption energy in this geometry was calculated to be 4.8 eV highlighting strong electrostatic interactions between the polar CN group and the cation atoms.

Finally, in the third configuration the angle between the molecule's legs decreases instead of stretching in order to attach two legs to two K^+ sites at the step edge, which has an adsorption energy of 4.5 eV. This value is slightly smaller than the 4.55 eV adsorption energy calculated for an isolated TCB molecule on the KCl (001) terrace and thus this configuration will be unstable over longer periods of time. Indeed this configuration is very short lived in the MD simulations and the molecule quickly adopts one of the other two more stable configurations on the step edge. Overall these calculations are consistent with observed adsorption behaviour in MD simulations.

The calculations of TCB adsorption at kink sites show that in the most energet-

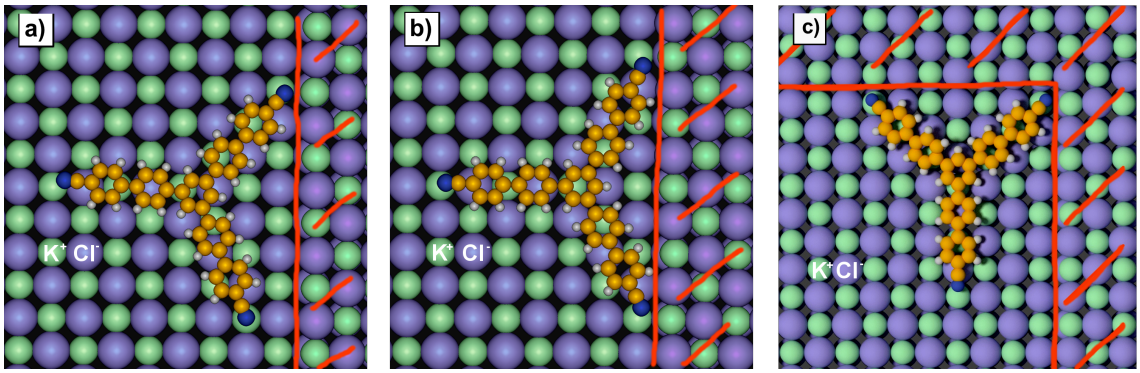

Figure 5.4: Two possible adsorption geometries for a TCB molecule at a monatomic step edge are shown along with the adsorption geometry at a kink site. Both configurations are energetically favourable in comparison to adsorption on a clean terrace. a) The TCB molecule adsorbs with one CN group positioned near the step edge cation site. b) The TCB molecule distorts to adsorb with two CN groups positioned near step edge cations. c) The TCB molecule adsorbs with one CN group in the kink site and a second CN group positioned near the step edge at a cation site.

ically favourable configuration one leg of the molecule is pointing into the kink and attaching to the two cations of the step edge, which corresponds to the molecule interacting with a total of three cations, as illustrated in Fig. 5.4c. Interestingly, the most stable configuration at a kink site is one where the angle between the two legs, that are attached to the step, gets compressed. This is unexpected, since this configuration corresponds to the lowest energy structure found for a monatomic step edge. However, the configuration with a stretched angle between the legs would lead to the CN group in the kink to sit slightly further to the left, reducing the interaction between it and the kink cations. The adsorption energy of the optimised configuration was calculated to be 5.1 eV. A TCB molecule adsorbing next to a molecule adsorbed at a kink site has an adsorption energy of about 4.8 eV with only one leg attached to the step edge and one pointing towards the COM of the molecule in the kink site.

5.4.1.2 CDB Molecules at Step Edges and Kinks

Similarly, long time-scale simulations of CDB molecules on the KCl (001) surface with the [100] step edge at 500 K were performed in order to investigate possible step adhesion geometries.

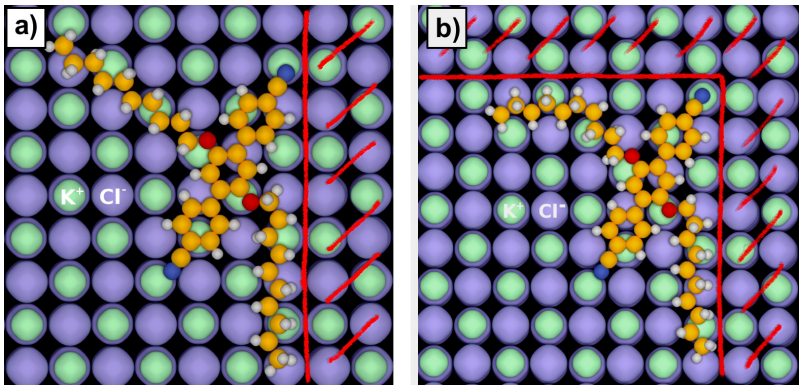

Figure 5.5: a) The optimised adsorption geometry for a single CDB molecule at a step edge on the KCl (001) surface. The CN anchoring group simultaneously interacts with two surface cations while the hydrocarbon chain adsorbs along the step edge itself. b) The optimised adsorption geometry for a single CDB molecule at a kink feature on the KCl(001) surface. The CN anchoring group simultaneously interacts with three surface cations, while the two hydrocarbon chains lie along the step edges.

In its lowest adsorption geometry as shown in Fig. 5.5a the molecule has an adsorption energy of 4.0 eV, which is a 0.9 eV increase compared to adsorption on a flat terrace. The increase can be attributed to two key factors: firstly, the CN group can interact with surface as well as step edge cations and secondly vdW interactions of the step edge with the main body of the molecule and the arm, which is aligned with the step edge, contribute to the increase in adsorption energy.This result is consistent with the experimental images that show decorated step edges at low coverages of CDB molecules at room temperature (see Fig. 5.2a).

At kink and corner sites, the CDB adsorption energy increases further as at these sites, the CN group can interact with a total of three cation sites and the second hydrocarbon chain can now lie along a step edge as well, as shown in Fig. 5.5b. The adsorption energy of CDB at a kink site was determined to be 4.4 eV, indicating that molecules at kink sites are more stable than at step edges or on flat terraces.

Comparing the two molecules, the conformational freedom of the more flexible CDB molecule allows it to adapt its geometry to maximise its interactions with the step edge or a kink site. In contrast, the more rigid TCB molecule has very little conformational freedom and can only minimally adapt to step edges.

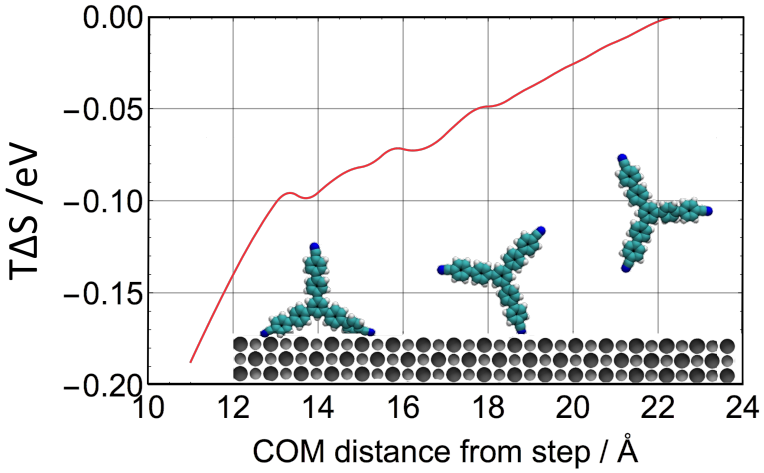

Figure 5.6: Change in entropy for a single TCB molecule as a function of the centre of mass distance to the step edge at 300 K. At 23Å the interaction between the molecule and the step edge is negligible and at this separation the entropy was defined to be zero. Initially only one leg of the molecule attaches to the step edge and a rapid decrease in entropy can be observed as two legs adhere to the step edge.

5.4.1.3 Entropy Changes Due to Adsorption at Steps and Kinks

In the initial MD simulations investigating the dynamic behaviour of CDB and TCB on KCl (001) it was observed that both molecules rotate rapidly on the surface. However, molecules attached to a step edge do not rotate any more and thus will have lost their rotational entropy. The balance of lost entropy and increased step adhesion enthalpies dictates the thermodynamic stability of these molecules at step edges.

Using a rigid rotor model we estimate that single TCB molecule would lose $T\Delta S_{rot} = 0.14$ eV and a single CDB molecule in the configuration with stretched out carbonyl chains $T\Delta S_{rot} = 0.15$ eV of rotational entropy and 0.14 eV with the arms aligned along the aromatic body. However, these estimates need to be regarded with caution, since the rigid rotor model does not include molecular flexibiliy or surface rotation barriers.

The simple rigid rotor model can be compared to entropy calculations using thermodynamic integration, which can provide a more accurate estimate.[117] Thermodynamic integration relies on averaging over all configurations of the molecule

in MD simulations at a constant distance from the step edge. The COM of the molecules was fixed along the reaction coordinate but was free to explore the configurational space parallel to the step edge, in order to allow for efficient sampling.

The average change in entropy for TCB calculated in this way as a function of the distance of the COM of the molecule from the step at 300 K is shown in Fig. 5.6. As the molecule approaches the step edge, its entropy is reduced almost linearly. Upon step adhesion TCB has lost 0.2 eV of entropy, in a configuration with two legs attached to the step edge. In that geometry the molecule does not rotate or translate and is essentially frozen. In order to translate, one leg needs to detach from the step edge, which leads to a larger distance of the COM to the step edge, which can be observed in the initial MD simulations. However, at no point was a TCB molecule observed to climb to the upper terrace of the step edge, indicating the presence of a Schwöbel Barrier.

The TCB molecule gains 0.15 eV of enthalpy by adsorbing on a step edge, but loses about 0.2 eV in entropy. Thus the adsorption energy is significantly lowered, which may explain that only partially covered step edges are observed by NC-AFM (see Fig. 5.1d).

The change in entropy for CDB at 300 K shown in Fig. 5.7 is almost three times larger than for the rigid TCB molecule. Upon adhesion to a step edge the CDB molecule loses 0.55 eV of entropy. The process can be divided into two regimes. Initially the tip of one hydrocarbon chain attaches to the step edge leading to a small decrease in entropy. As the COM of the molecule gets closer to the step edge the hydrocarbon chain aligns with the step edge (around 20 Å mark), leading to a large drop in entropy. Thereafter, the entropy is reduced further as one CN group attaches to the step edge. In its final adsorption geometry one hydrocarbon chain will retain its degrees of freedom, while the other chain and the main body of the CDB molecule are constrained by the step edge.

The loss in entropy (ΔS=0.55 eV) is smaller than the gain in enthalpy (ΔH=0.9 eV) as a CDB molecule adsorbs at a step edge. Therefore, it is stable at a step edge at room temperature, which is consistent with NC-AFM findings of

	$\Delta H_{ads}^{terrace}$	-T$\Delta S_{ads}^{terrace}$	$\Delta F_{ads}^{terrace}$	ΔH_{ads}^{step}	-TΔS_{ads}^{step}	ΔF_{ads}^{step}
TCB	-4.55 eV	0.5 eV	-4.05 eV	-0.15 eV	0.2 eV	-4.0 eV
CDB	-3.1 eV	1.0 eV	-2.1 eV	-0.9 eV	0.5 eV	-2.5 eV

Table 5.1: Overview of thermodynamic properties for TCB and CDB molecules on KCl(001). ΔH_{ads}^{X} gives the adsorption enthalpy on a terrace or step edge and ΔS_{ads}^{X} gives the change in entropy for adsorption at 300 K. The free energy ΔF_{ads}^{X} can be calculated from $\Delta F_{ads}^{X} = \Delta H_{ads}^{X} - T\Delta S_{ads}^{X}$.

step edges covered with CDB molecules.

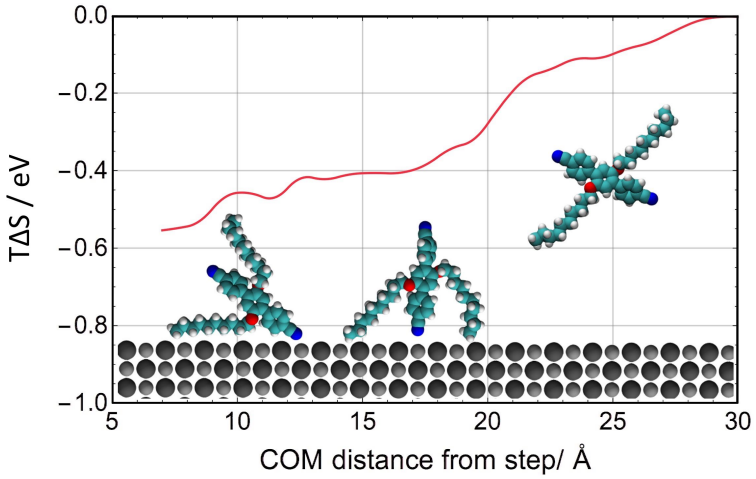

Figure 5.7: Change in entropy for a single CDB molecule as a function of the centre of mass distance to a monatomic step edge at 300 K. The initial decrease in entropy can be attributed to one arm of the CDB molecule adhering to the step edge. As the molecule gets even closer to the step, a cyano group will attach at a cation site of the step edge, leading to a further drop in entropy

A summary of the values of enthalpy, entropy change and free energy for adsorption of CDB and TCB is given in Table 5.1. The free energy is calculated as the difference of the enthalpy of adsorption and the entropy of adsorption (ΔF=ΔH-TΔS). At 300 K the TCB molecule adsorbs on flat terraces and step edges equally favourable, whereas the CDB molecule adsorbs more strongly on step edges.

The change in entropy calculated from thermodynamic integration can be compared to the initial estimate using the rigid rotor model. For TCB the two models give comparable values. However, the rigid rotor model fails for the more flexible CDB molecule which displays a more complex step adhesion mechanism, where the

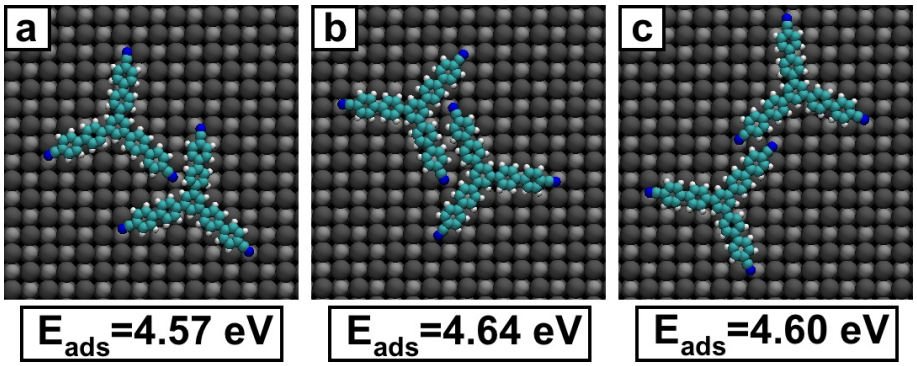

Figure 5.8: Three stable dimer configurations as observed in MD simulations. Energy minimisation calculations were performed to find the energetically lowest geometries. The adsorption energy of a single TCB molecule in the respective configuration is given below each image.

molecule adapts its geometry to maximise its interaction with the step edge while retaining conformational freedom of one hydrocarbon chain.

Furthermore, translational motion of the molecule cannot be ignored, since CDB has a higher diffusion coefficient and a lower diffusion barrier. Thus only considering rotational entropy and treating the molecule as a rigid body results in an underestimation of the free energy change upon step adhesion.

5.4.2 TCB Dimers

MD simulations of 100 TCB molecules were performed in order to gain an initial idea about possible molecular structures. While most molecules changed their orientation and coordination throughout the MD simulation, small clusters were observed to be stable for longer periods of time as shown in Fig. 5.8.

The first structure consisted of a chain of TCB molecules, where one leg of a molecule points towards the central benzene ring of a neighbouring molecule (Fig. 5.8a). In this configuration the molecules are sterically hindered to adopt the lowest energy configuration with respect to the surface, leading to an energy penalty of 0.1 eV in the molecule-surface interaction. Nevertheless, this arrangement has an adsorption energy of 4.57 eV per molecule, which is marginally lower than an isolated TCB molecule on a flat terrace.

A second stable configuration is shown in Fig. 5.8b, where two TCB molecules align side by side. This configuration has been observed most often during the

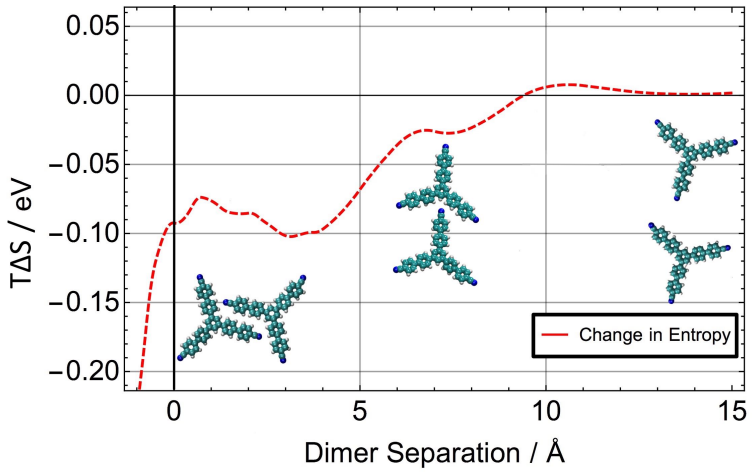

Figure 5.9: The change in entropy upon dimer formation is plotted as a function of molecular separation. Zero on the x axis corresponds to the equilibrium dimer separation as obtained in energy minimisation calculations and shown by the inset.

MD simulations and indeed was found to have the lowest adsorption energy of the structures considered at 4.64 eV per molecule. Both molecules adapt the lowest energy adsorption geometry as found for an isolated molecule, thus there is no energy penalty associated with forming these dimers and their interaction energy amounts to 0.2 eV as calculated using energy minimisation calculations.

In configuration shown in Fig. 5.8c the TCB molecules also adopt the lowest adsorption geometry of an isolated molecule. The two TCB molecules align just their CN-groups, forming a dipole-dipole bonded dimer with an adsorption energy of 4.60 eV.

The lowest energy dimer structure is proposed to be the basic building block for both observed film structures and has also been observed in experimental studies of TCB on Si:B(111).[109] However, as the dimer is formed the TCB molecules become more constrained leading to a loss in entropy. The loss in entropy determines the stability of the dimers at non-zero temperatures and hence influences the film formation.

5.4.3 Entropy Loss upon Dimer Formation

Applying the same methodology as for step adhesion, the entropy loss of dimer formation was calculated. The distance between the COMs of the two molecules

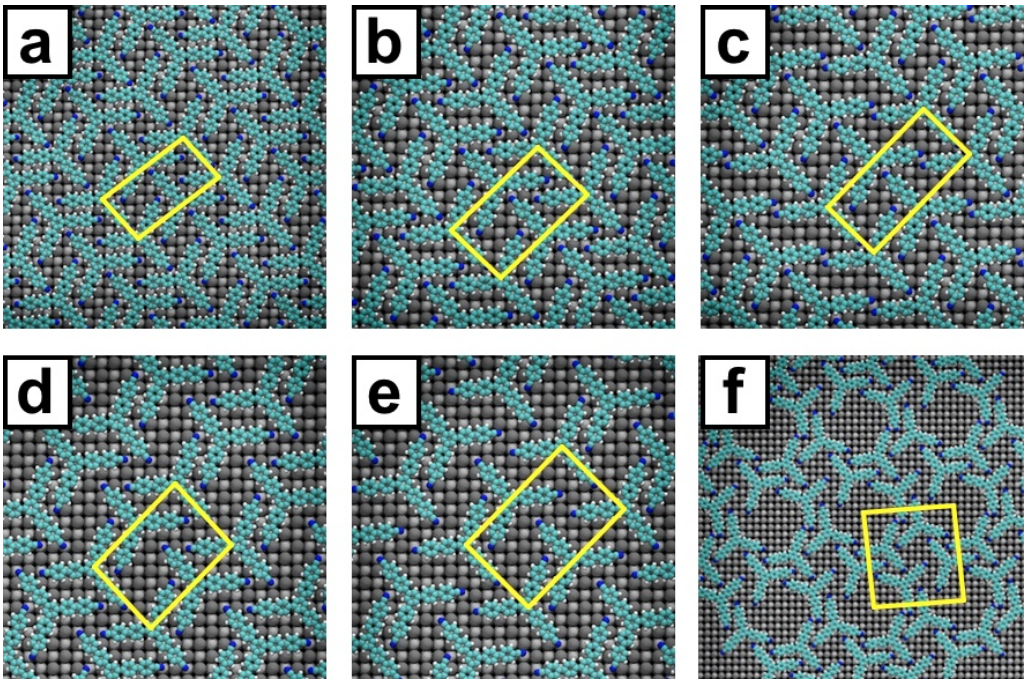

Figure 5.10: Proposed self-assembled structures for TCB molecules. The respective unit cell vectors are a) 31.4Å × 17.8Å with $\alpha = 82°$ b) 31Å × 17.8Å with $\alpha = 90°$ c) 35.5Å × 17.8Å with $\alpha = 90°$ d) 31Å × 22.2Å with $\alpha = 90°$ e) 35.5Å × 22.2Å with $\alpha = 90°$ f) 40.9Å × 40.9Å with $\alpha = 90°$.

was fixed at each step, but the molecular motion was not frozen to allow for efficient sampling of the entire configuration space. Each individual MD simulation was performed at 300 K with a 1 fs time step over 50 ns.

Fig. 5.9 illustrates the change in entropy upon dimer formation as a function of molecular separation. The equilibrium distance between the COM of the molecules as obtained from energy minimisation calculations is indicated by the vertical black line. As the TCB molecules form the dimer, a loss of entropy of 0.1 eV can be observed. Since the dimer formation enthalpy is 0.2 eV, these dimers are expected to be stable for considerable length of time at room temperature.

5.4.4 Film Structures

The dynamics of the molecules is too low to simulate film growth directly. However, MD simulations are useful to determine small building blocks, which suggest clear motifs for constructing prototype periodic infinite structures. Fig. 5.10 illustrates possible film structures for TCB of varying density and coordination.

The lowest adsorption energy was found for configuration (b) at 4.75 eV per molecule, followed by configuration (c) at 4.73 eV per molecule. This is consistent with the experimentally observed structures (Fig. 5.3a), where the configuration (b) reproduces well the experimentally measured film unit cell and the observed line splitting (Fig. 5.1a,b) is due to the energetically close structure (c).

The configuration (f) represents the lowest energy porous structure found with an adsorption energy of 4.65 eV per molecule. At room temperature both the line and porous structure can be observed. Since entropic factors have not been considered, these can have an impact on the relative stability of the two films at various temperatures. However, the calculation of entropy changes upon film formation is non-trivial and was not attempted in this work.

To probe the film stability, MD simulations starting from large island of the lowest enthalpy structures at 300 K and 400 K were performed. The line structure is stable at 300 K and no diffusion of molecules at the domain boundary could be observed, whereas at 400 K isolated TCB molecules broke the film symmetry and broke away from the molecular island.

The porous structure displayed unstable edges at 300 K, indicating weaker molecule-molecule interactions and at 400 K it was found to be unstable as a disordered film was formed. Experimental observations agree with these results, where a transition from the porous to the line structure was observed as the temperature was increased from 300 K to 400 K. In both structures TCB dimers formed the basic building block, which agrees with reports of structures of other tripod molecules.[110,112,118–121]

5.5 Discussion and Conclusions

Despite progress in recent years, nucleation and growth mechanisms of monolayers and ordered films of organic molecules at insulating surfaces are still poorly understood. It is often assumed that step edges serve as nucleation sites, where molecules get trapped and film-growth may start. This study sheds a new light on the possible dynamics of this process and the resulting structure.

In order for a well-defined film structure to grow, molecules need to have enough degrees of freedom to find stable nucleation sites, from where film growth may start. Calculations in the previous chapter and experimental data indicate rapid diffusion of single TCB and CDB molecules across the KCl (001) surface. The nucleation at step edges is temperature dependent.

Single CDB molecules favourably interact with step edges and the entropy loss upon step adhesion is not large enough to compensate the gain in enthalpy. However, TCB molecules display opposite dynamics. It is unable to adapt its geometry to step edges and kinks to maximise molecule-step interactions and can only interact with the step edge through CN functional groups. However, even then some energy is lost due to the molecular distortions required to position both CN groups near cation sites on the step edge. The entropy loss upon adsorption in this case is significant and destabilises the molecule at a step edge. Thus the free energy of step adhesion and isolated adsorbed molecules on a flat terrace is comparable (see Table 5.1).

This behaviour is consistent with NC-AFM measurements, which show covered step edges for CDB at low coverage, but for low coverage of TCB, step edges show partially coverage and molecules are noticeably absent.

While organic molecules adsorbed on insulators do not typically display epitaxial growth, the addition of anchoring groups which bind to specific surface sites, such as the CN-group for TCB and CDB, can lead to epitaxial growth and attempts to apply the concept of epitaxy to organic thin films have been made.[59, 122, 123] However, large organic molecules can display complex film structures with low plane group symmetry, thus introducing more complexity. Balancing the interactions between molecules with the molecule-surface interactions is vital in order to achieve large domains of self assembled monolayers, which are commensurate with the surface symmetry.

Strong interactions between the cyano anchoring groups of TCB with the surface cations prevents TCB molecules from diverting significantly from their minimum adsorption geometry. Thus, “point-on-point” commensurism can be observed in the self-assembled film structures.

In summary, molecular flexibility plays a crucial role in nucleation at elevated temperatures due to its effect on entropic contributions to step adhesion. Tuning the conformational flexibility and functionality of molecules are powerful parameters that can be used to design molecules for self-assembly. However, predicting nucleation behaviour and the final self-assembled structures is still unfeasible, motivating further research into the underlying factors that steer film growth.

Part II

Mechanism of Ti Interstitial Formation in Rutile TiO_2

Chapter 6

Point Defects in Bulk Rutile TiO_2

6.1 Introduction

Titanium Dioxide (TiO_2) finds applications in many different areas such as e.g. paints and coatings,[124,125] catalysis,[126,127] optical instruments,[128] solar cells[129,130] and gas sensors.[131,132] Its high refractive index is exploited in sunscreen and to make white pigments. The discovery of the ability of TiO_2 to split water for hydrogen production has fuelled intense research.[133–136] TiO_2 has become a model metal oxide for surface science studies, as the number of publications shown in Fig. 6.1 illustrates. The (110) surface is the most stable rutile surface structure and has been studied extensively with almost 200 articles per year for the last decade.

During the preparation of TiO_2 samples defects can easily be introduced, which

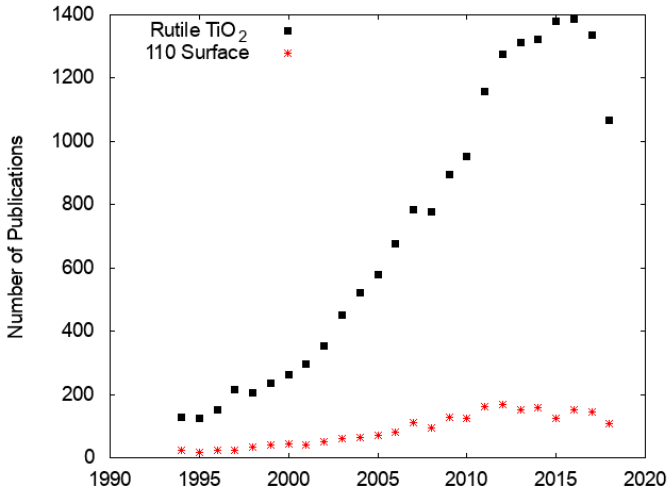

Figure 6.1: Timeline of the number of publications on rutile TiO_2 and on the rutile (110) surface. The data was obtained from ISI database Web of Science (www.webofknowledge.com) accessed 17 Sept. 2018.

results in high conductivity and enhanced catalytic activity.[137] Indeed, rutile TiO_2 has a very rich phase diagram with many substoichiometric phases of the type Ti_nO_{2n-1}, termed Magneli phases, which are related to the formation of crystallographic shear planes. In the range of $TiO_{1.9996}$ to $TiO_{1.9999}$ (3.7×10^{18} to 1.3×10^{19} missing O atoms per cm^3) interstitial Ti atoms are the dominant defects.[138] Oxygen can be removed through high temperature annealing or ion sputtering, which are commonly used procedures in sample preparation for surface probe experiments.[139,140] Consequently, many different surface structures of varying defect density and reconstructions have been reported.[137,141,142] It is commonly accepted that excess Ti in the form of interstitial atoms results from oxygen removal, which is a surface mediated effect. However, the Ti defects can penetrate the entire crystal.[143,144]

The experimental evidence for Ti^{3+} species, which are linked to Ti interstitials (Ti_i) as well as oxygen vacancies (v_O), is considerable: the introduction of Ti_i leads to the crystal changing colour from transparent to blue with increasing Ti_i concentration, which is related to d-d transitions.[145] Further, a gap state about 1 eV below the CBM is induced as measured by photoelectron spectroscopy and energy loss experiments.[146–148] A Ti $3d^1$ state is also responsible for the measured g-tensor in EPR measurements[149,150] and Ti-3d states are observed in Auger electron spectroscopy.[151]

Point defect diffusion has been reported to drive surface reconstruction,[152] surface reoxidation,[144] surface catalytic activity[153] and self-limiting growth of TiO_x encapsulated Pt nanoparticles.[154] In isotopically labeled secondary ion mass spectrometry experiments, Ti interstitials were identified to be the main diffusing species at temperatures above 400 K.[143] However, at temperatures below 800 K the concentration of surface Ti_i accounts for more than 95% compared to bulk. The balance starts to shift with increasing temperature with a more even split at 1073K annealing temperature indicating indiffusion of Ti_i species.[155]

However, the behaviour of intrinsic defects is still not fully understood despite intensive research over the past decades. Particularly the question which defect is

dominant in reduced TiO_2 can not be answered definitely, partly due to polaronic effects in TiO_2, which mean many defects display similar experimental signatures. TiO_2 samples also exhibit a dependence on the history of the sample, its exact heat treatment and presence of oxygen or reducing agents during sample preparation, which are not always well documented in the literature. Furthermore, polaronic effects are challenging to capture theoretically as well, limiting the predictive power of ab initio calculations (see Section 6.5).

Theoretical reports on point defects in bulk rutile TiO_2 show defect geometries and formation energies.[156–158] However, a large number of studies was performed with GGA functionals, which are not suitable for the study of rutile TiO_2, especially its surfaces, defect induced states and localised charge carriers (see 6.5).[157,159] Hybrid functionals, particularly HSE06 can reproduce bulk structures, electronic charge trapping energies, defect geometries, molecular adsorption and polaronic states in good agreement with experimental data.[160–163]

In this part of the thesis point defects in rutile TiO_2 are investigated using a hybrid functional DFT approach. Firstly, intrinsic defects in bulk rutile TiO_2 are calculated and compared to experimental data from the literature in Chapter 6. Respective defect formation energies and their dependence on oxygen pressure and temperature are calculated for bulk TiO_2 and insight into the diffusion of interstitial Ti atoms is obtained from calculations of diffusion barriers.

6.2 Methods

Rutile TiO_2 was studied using DFT as implemented in the CP2K code,[164] which employs a mixed Gaussian and plane wave basis-set (GPW). A triple zeta basis set was used for Ti and O together with Goedecker-Teter-Hutter (GTH) pseudopotentials.[165] In order to get an improved description of the electronic and geometric structure, the Ti $3s^2$, $3p^6$, $3d^2$ and $4s^2$ electrons were treated as valence. The plane wave cutoff was converged at 600 Ry, SCF convergence was set to 10^{-6} a.u. and residual forces on relaxed atoms were converged to smaller than 0.01 eV/Å. In the generalised gradient approximation (GGA, such as PBE) rutile is predicted to be

unstable, since imaginary phonon frequencies are found for the A_{2u} mode[159] and thus a more expensive hybrid calculation is needed to represent the electronic and geometric structure correctly. All results presented herein were obtained using the HSE06 hybrid functional with 25% Hartree-Fock exchange and an omega of 0.11, which reproduced experimental properties well (see Section 6.3). HSE06 obeys the generalised Koopman's Theorem, which means it can provide reliable vertical excitation energies, charge trapping energies and charge transition levels.[162] In order to reduce the computational cost of the hybrid functional calculations, the auxiliary density matrix method (ADMM)[24] was used, which uses a reduced basis set for the HF exchange calculation and thus allows the computation of larger cells, which would otherwise be prohibitively expensive in hybrid DFT. Defect formation energies were corrected for image charge interactions and potential alignment (see Chapter 2). For the surface calculations, a vacuum gap of 20 Å ensured that the interaction between the surface and its periodic image tends to zero. The reported bulk properties were obtained using a 3x3x3 supercell (162 atoms) and the surface model consisted of a 2x4x8 TiO_2 slab (384 atoms), unless stated otherwise.

6.2.1 Computation of Chemical Potentials

The choice of chemical potentials is critical to obtain physically accurate and relevant DFEs. While a plethora of studies use zero energy DFT values as chemical potentials, effects due to non-zero temperatures and gas pressure, particularly for O_2, have a significant effect on calculated DFEs. Thus, in this work a more thorough derivation of chemical potentials is performed as previously reported for $SrTiO_2$,[166] in order to match experimental conditions more closely.

The Gibbs free energy of formation, $\Delta G^0_{f,TiO_2}$, is given by:

$$\Delta G^0_{f,TiO_2} = g^0_{TiO_2} - g^0_{Ti} - g^0_{O_2} \equiv \mu^0_{TiO_2} - \mu^0_{Ti} - \mu^0_{O_2} \ , \tag{6.1}$$

where g^0_X is the Gibbs free energy of species X under standard conditions. The Gibbs free energy can be separated into its enthalpic and entropic contribution. One can simplify this expression by assuming the entropic contributions to $g^0_{TiO_2}$ and g^0_{Ti} are

negligible, which was shown to result in an error of about 0.02 eV in comparative studies.[166] The accuracy of the DFT calculations presented is about 0.01 eV due to limited basis-sets, finite size effects, energy convergence criteria etc., thus the approximation to ignore entropic contributions to these solids is justifiable. Then, Eq. 6.1 becomes:

$$\Delta G^0_{f,TiO_2} = h^0_{TiO_2} - h^0_{Ti} - (h^0_{O_2} - TS^0_{O_2}) \ . \tag{6.2}$$

While in chemistry the convention is to set the enthalpy of formation of elementary species to zero, the energy zero is different in DFT calculations. Thus, one can further deduce:

$$\Delta G^0_{f,TiO_2} = E^{DFT}_{TiO_2} - E^{DFT}_{Ti} - E^{DFT}_{O_2} + T^0 S^0_{O_2} \tag{6.3}$$

Using this expression and standard entropy values for oxygen[167] gives a heat of formation of -9.15 eV, which is an underestimation of the experimentally value of -9.72 eV. This can be explained by a poor representation of the complex electronic structure of the oxygen molecule in DFT, i.e. the atomisation energy of O_2 is not well reproduced with many DFT functionals.[168] We found an underestimation of the textbook value of 5.12 eV by 6% using the HSE06 hybrid functional. Furthermore, the electronic structure of Ti metal is difficult to calculate with a hybrid functional, since large cells (or in other codes large k-point sampling) is needed, which comes at a high computational cost and known problems to calculate metals in Hartree-Fock theory.

The Ti and O chemical potentials are unknown exactly in TiO_2, but bounds can be placed on their limits. Equilibrium of TiO_2 requires:

$$\mu_{TiO_2} = \mu_{Ti} + \mu_{O_2} \ , \quad \text{and} \tag{6.4}$$

$$\mu_{Ti_2O_3} > 2\mu_{Ti} + \frac{3}{2}\mu_{O_2} \ , \tag{6.5}$$

which shows, that the Ti and O chemical potentials are linearly dependent. Thus,

two regimes can be identified: the oxygen rich regime ($\mu_{O_2} \leq E_{O_2}^{DFT} - T^0 S_{O_2}^0 \equiv \mu_{O_2}^0$) and the Ti rich regime ($\mu_{Ti} \leq \mu_{Ti,Ti_2O_3}^{DFT}$). Furthermore, the dependence of chemical potentials on pressure and temperature need to be considered. While these are difficult to calculate, one can make use of thermochemical databases and thereby avoid errors inherent to ab initio methods.

Temperature and pressure affect μ_{Ti} minimally compared to the effect on μ_{O_2}, as can be seen by the order of magnitude smaller standard entropy for example.[167] Thus, μ_{O_2} will be adjusted to take T and p into account. The dependence on pressure can be derived from the thermodynamic relation of an ideal gas:

$$\left.\frac{\partial \mu_{O_2}}{\partial p}\right|_T = \frac{kT}{p} \quad , \tag{6.6}$$

where k is the Boltzmann constant. Integrating over p gives:

$$\mu_{O_2}(p,T) = \mu_{O_2}(p^0,T) + kT \ln\left(\frac{p}{p^0}\right) \quad . \tag{6.7}$$

The temperature dependence can be derived from thermochemical data, where change in enthalpies and entropies with T have been fitted to polynomials:

$$G(p^0,T) = A(T - T\ln(T)) - \frac{1}{2}BT^2 - \frac{1}{6}CT^3 - \frac{1}{12}DT^4 - \frac{E}{2T} + F - GT \tag{6.8}$$

where the coefficients A,B,C,D,E,F and G can be found in standard thermochemistry databases.[167] The final expression for μ_{O_2} is then given by:

$$\mu_{O_2}(p,T) = \mu_{O_2}^0 + G(p^0,T) - G(p^0,T^0) + kT \ln\left(\frac{p}{p^0}\right) \quad . \tag{6.9}$$

6.3 Testing of Computational Setup

The chosen method was verified by comparing the bulk electronic and geometric structure as well as the (110) surface structure to experimental results and theoretical calculations reported in literature. Fig. 6.2 illustrates the band structure of bulk rutile TiO_2. Since CP2K does not have k-point sampling implemented yet,

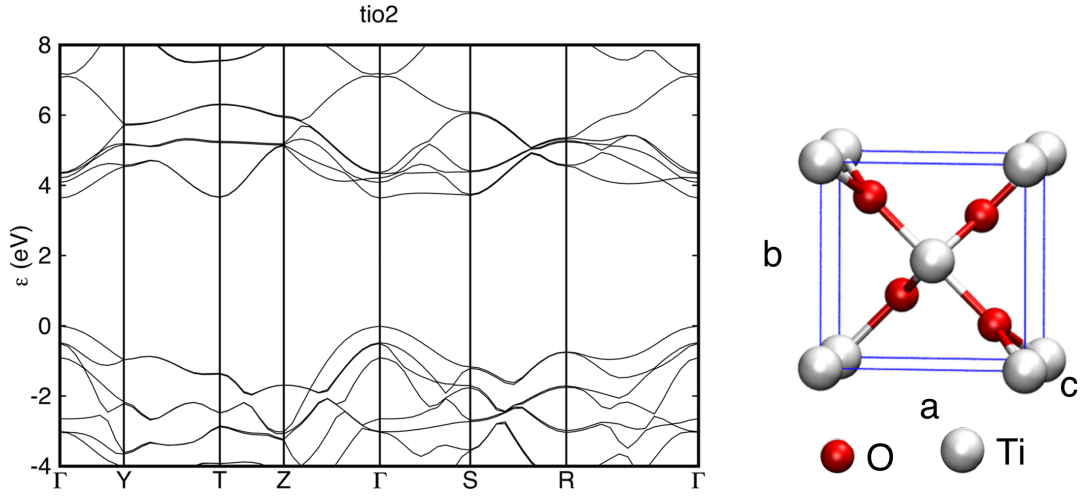

Figure 6.2: Bandstructure of TiO_2 illustrating the semi-conducting nature of rutile with a direct bandgap of 3.5 eV at the Gamma point. The unit cell of TiO_2 is illustrated on the right.

the CASTEP code was employed to calculate the bandstructure. A 7x7x7 k-point mesh along with the HSE06 functional and a 400 eV cutoff were used. Optimised cell vectors and atomic positions were found to be in good agreement with the ones obtained using CP2K. The optimised lattice vectors were found to be a = 4.60 Å and c = 2.93 Å, which is in good agreement with a = 4.59 Å and c = 2.96 Å found from neutron powder diffraction experiments.[169] An illustration of the tetragonal unit cell of rutile TiO_2 is given in Fig. 6.2. Each Ti atom is six fold coordinated, while every O atom is three fold coordinated. The Ti-O bonds can be separated in two types, axial and equatorial. Each Ti atom has two axial Ti-O bonds at an angle of 180° wrt. each other and four equatorial bonds, at 90° wrt. each other. The optimised bulk bond lengths are 1.99 Å for axial and 1.94 Å for equatorial Ti-O bonds, which is in good agreement with experimentally measured bond lengths (see Table 6.1). A direct bandgap of 3.5 eV at the Gamma-point is slightly larger than the experimentally measured value of 3.03 eV,[170,171] but compares well with reported values from DFT calculations using the same functional[160] and from full frequency G_0W_0 calculations.[172] The top of the valence band (VBM) is composed mostly of O 2p character, whereas the bottom of the conduction band (CBM) has predominantly Ti 3d character. Bader charges on Ti are +2.4e and on O -1.2e,

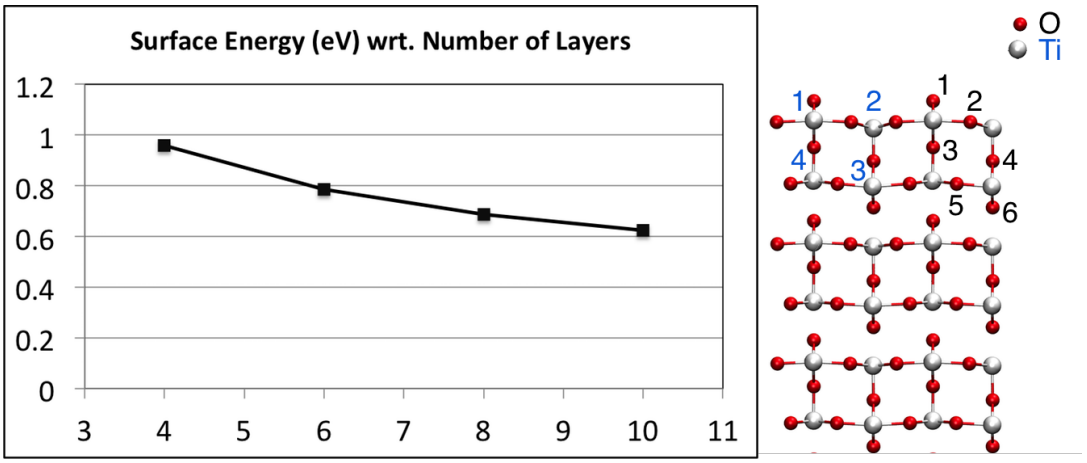

Figure 6.3: Left: Plot of surface energy versus number of layers in the 2x4 (110) surface slab of rutile TiO_2. Only even layer slabs were calculated to check convergence. Right: Six layer surface slab illustrating atomic surface relaxations.

respectively, indicative for ionic bonding. The heat of formation of a unit of TiO_2 was calculated at -9.15 eV, which is in agreement with the experimental value of -9.72 eV.[167]

The ability of our model to represent the (110) surface structure accurately was also verified. The (110) surface is the lowest energy rutile surface and has been studied extensively.[142,173–175] It consists of alternating corner sharing TiO_6 and TiO_5 octahedra, where the Ti atom is located in the centre of the octahedron. The Ti atoms lie in planes parallel to the surface plane with one oxygen per unit of TiO_2 sticking out of the plane, as illustrated in Fig. 6.3(right).

Previously theoretical studies show, that surface properties, such as surface energy or adsorption energies of small molecules, converge slowly with increasing number of TiO_2 layers in the simulated slab.[176,177] Methods to improve convergence include H termination of dangling bonds on the bottom surface or constraining the bottom two layers of the slab in their bulk geometry. However, H termination can lead to artificial dipoles in the system and thus can influence the electronic structure, which is particularly detrimental to shallow polaronic states. Bulk termination is useful for adsorption calculations, which primarily rely on accurate representation of the geometric and electronic structure of the surface and rely less on an accurate description of the bulk properties within the slab.

Atom Pair	Bulk Bond Length	Exp. Bond Length	This work	% difference
Ti(1)-O(1)	1.94	1.71	1.81	5.9
Ti(1)-O(2)	1.99	2.15	2.03	-5.6
Ti(1)-O(3)	1.94	1.99	2.09	5.0
Ti(2)-O(2)	1.94	1.84	1.94	5.4
Ti(2)-O(4)	1.99	1.84	1.80	-2.2
Ti(3)-O(4)	1.94	2.00	2.03	1.5
Ti(3)-O(5)	1.99	1.92	1.92	0.0
Ti(3)-O(6)	1.94	1.94	1.87	-3.6
Ti(4)-O(3)	1.99	1.97	1.83	-7.1
Ti(4)-O(5)	1.94	1.99	1.99	0.0
Ti(4)-O(7)	1.99	2.18	2.19	0.5

Table 6.1: Bond lengths in TiO_2, illustrating atomic relaxations on the (110) rutile surface. Experimental values have been adapted from,[141] which were obtained from surface X-ray diffraction measurements. The percentage change corresponds to the experimental value compared to the theoretical value. All bond lengths are given in Å and labeled according to Fig. 6.3.

However, in this work adsorption as well as substitution processes are investigated, which require a thick TiO_2 slab to be modelled, in order to get accurate bulk properties in the middle of the slab, as well as a correctly represented surface. Fig. 6.3 shows the convergence of surface energy with number of TiO_2 layers in the slab. The typical even-odd layer oscillations are not seen since only even layer slabs were calculated as they were found to converge even more slowly.[156] As expected convergence is slow and could not be reached up to a 10 layer system. However, the obtained value of about 0.6 eV per surface unit cell in a 10 layer slab compares well with published results.[156,176,177] As the computational cost increases drastically with the number of atoms modelled, a balance between accuracy and computational cost has to be achieved. Thus, an eight layer slab was chosen for this work, in which all atom positions are optimised. A 20 Å vacuum gap was found sufficient to minimise periodic interactions between slabs in the out of plane direction.

The slow convergence of surface energies, adsorption energies and other surface related properties can be traced back to atomic relaxations upon creating the surface, as illustrated on the right side in Fig. 6.3. When the TiO_2 crystal is cleaved to create a (110) surface, undercoordinated Ti and O atoms are produced. These

undercoordinated atoms show the largest surface relaxations from their bulk lattice sites (see Table 6.1). The O(1) is termed bridging oxygen (O_{Br}) and relaxes into the surface shortening the Ti-O bonds (1.81 Å). Similarly, the five fold coordinated surface Ti atom relaxes inwards, elongating the in-plane Ti-O bonds and compressing the Ti-O bond along the surface normal. The top layer of atoms displays the largest relaxations, which is consistent between theory and experiment, albeit the magnitude of relaxations varies by up to ∼6%. Interestingly, both experiment and theory indicate the formation of bi-layers. While the distance between the first and the second layer decreases, the distance between the second and third layer increases. This bi-layer formation leads to slow convergence of the out-of-plane bonds with increasing number of layers in the slab, while in-plane bonds converge more rapidly. In Fig. 6.3 the bi-layer formation is illustrated by omitting Ti-O bonds between the bi-layers. Overall, the agreement between our data and experimental data is largely within experimental error of about 0.1 Å.

6.4 Results

6.4.1 Calculation of Defect Formation Energies

To evaluate the defect chemistry of rutile TiO_2 several point defects were calculated: Oxygen vacancy (v_O) and oxygen interstitial (O_i) as well as Ti vacancy (v_{Ti}) and Ti interstitial (Ti_i) in various charge states. The DFE diagrams under Ti rich and O rich conditions are shown in Fig. 6.4 for 300K and 1 atm gas pressure and for 1000K and 10^{-6} atm gas pressure. These represent typical conditions of a sample exposed to the ambient atmosphere and a sample during a high temperature vacuum anneal. To maintain charge neutrality a charged point defect needs to be compensated by e.g. defects of the opposite charge: for example a Ti_i^{4+} can be compensated by a v_{Ti}^{4-}. Such a complex has a DFE of 6.64 eV and is the lowest energy Frenkel defect, in agreement with reported values in literature[178, 179] and independent of the choice of Ti chemical potential. The corresponding anti-Frenkel defect (v_O^{+2} and O_i^{-2}) has a DFE of 6.87 eV. The DFE of the Frenkel and anti-Frenkel defects are obtained by summing the DFEs of the corresponding isolated defects. Interactions between the

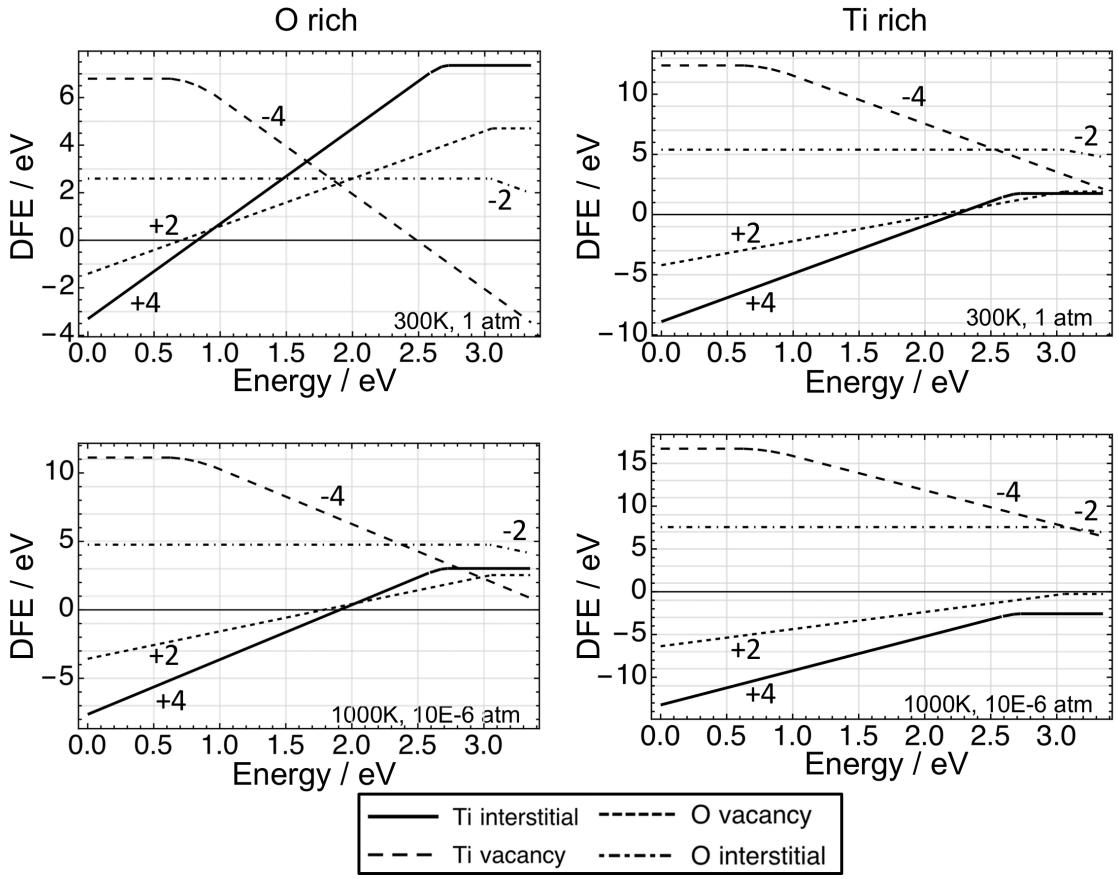

Figure 6.4: Defect formation energy diagrams for point defects in bulk rutile TiO_2 under O rich (left) and Ti rich (right) conditions. Only the lowest energy charge state is ploted for each Fermi level position.

defects are thus neglected, which previously have been shown to have a significant impact on calculated DFEs of Frenkel and anti-Frenkel defects.[180]

Besides a Frenkel pair defect, compensation can be achieved by creating Schottky defects. A Schottky defect consists of v_{Ti}^{4-} and two v_{O}^{+2}, which corresponds to one missing unit of TiO_2. Such a defect has a DFE of 6.32 eV, which compares well with reported values from self-interaction corrected ab initio calculations.[181] While literature reported DFE values for individual defects vary due to different choices for μ_{O_2} and μ_{Ti}, DFE for Frenkel and Schottky defects do not and are therefore useful for comparison.

The dependence of calculated DFEs on temperature and gas pressure can be seen from the difference between plots in Fig. 6.4. Under ambient conditions in the O rich limit the DFE of a Ti_i^0 is 7.35 eV, at 1000 K and 1 atm it becomes

4.21 eV and at 1000 K and 10^{-6} atm it is lowered to 3.02 eV. This illustrates that higher temperatures lower the formation of Ti_i and the same argument holds for oxygen vacancies, whereas O_i and v_{Ti} have higher DFEs. This change in DFE has implications of the formation of intrinsic defects during a sample anneal, where high temperatures of over 1000 K are used. In the following section, DFEs calculated under O rich conditions at 300 K and 1 atm gas pressure are discussed.

Fig.6.5a illustrates a neutral O interstitial defect. The interstitial atom displaces a lattice O atom by 0.74 Å and forms a dimer configuration. In fact, the dimer can be regarded as an O_2^{-2} defect (the lattice O atom has a formal charge of -2), which is termed a peroxide ion and is characterised by the 1.49 Å O-O bond and a singlet ground state. The thermodynamically most stable charge state is the neutral interstitial with a DFE of 2.59 eV, but at high Fermi energy (3.05 eV above VBM) a charge transition level (CTL) from neutral to -2e, $\epsilon(0/-2)$, is observed.

The corresponding oxygen vacancy is illustrated in Fig. 6.5b. The neutral vacancy adopts a triplet ground state with two electron polarons localised on two neighbouring Ti atoms. The polarons can also be identified in density of states plots (DOS), where two bandgap states appear at 0.8 eV and 1.31 eV below the CBM, consistent with recent electron paramagnetic resonance (EPR) measurements,[182] infrared adsorption measurements[183] and theoretical calculations.[184] The neutral vacancy has a DFE of 4.7 eV, however, the -2e charged vacancy is thermodynamically more stable at low Fermi level positions (see Fig. 6.4). An $\epsilon(-2/0)$ CTL was found at 3.07 eV above the VBM.

Fig. 6.5c illustrates a Ti interstitial, which adopts an octahedral configuration. The nearest neighbour O atoms bonding to the Ti interstitial relax slightly inwards, whereas the nearest neighbour Ti lattice atoms relax away from the interstitial. The four valence electrons of Ti_i induce four polarons localised on Ti sites, which create a bandgap state 1.12 eV below the CBM, which is in good agreement with infrared adsorption measurements showing a peak at 1.18 eV.[183] Thermodynamically the +4e charge state is most stable throughout the bandgap up to 2.57 eV above the VBM, where the $\epsilon(+4/+3)$ CTL lies (see Fig. 6.4). At 2.67 eV above the VBM

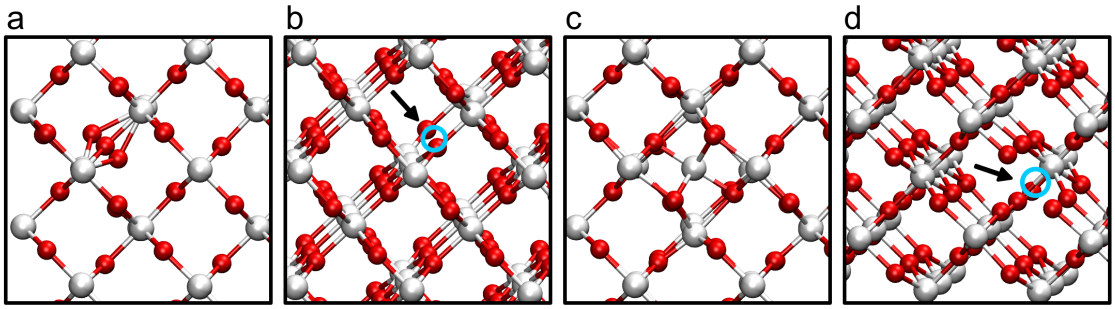

Figure 6.5: Geometries of point defects in rutile TiO_2: a) O interstitial; b) O vacancy (indicated by a blue circle and black arrow); c) Ti interstitial; d) Ti vacancy (indicated by a blue circle and black arrow). (Red = O, white = Ti)

the $\epsilon(+3/+1)$ CTL is positioned and at 2.73 eV the $\epsilon(+1/0)$ CTL. Thus, within a narrow range of Fermi level positions the most stable Ti_i state changes from +4 to neutral. The DFE for the neutral interstitial is 7.35 eV at 300 K and 1 atm air pressure. Experimental measurements of the activation energy for Ti interstitial creation at 1058°C and $1.69x10^{-16}$ atm yield a DFE of 11.97 eV,[185] which is in good agreement with the calculated DFE of 11.92 eV at the same temperature and oxygen pressure.

Lastly, a Ti vacancy is shown in Fig. 6.5d with a DFE of 6.79 eV and minimal lattice relaxation around the vacancy. The neutral vacancy is stable at low Fermi levels with the $\epsilon(0/-1)$, $\epsilon(-1/-2)$, $\epsilon(-2/-3)$ and $\epsilon(-3/-4)$ CTL positioned at 0.63 eV, 0.73 eV, 0.83 eV and 0.95 eV above the VBM, respectively. Since the neutral v_{Ti} adopts a S=2 configuration with four holes localised on the equatorial oxygen atoms next to the vacancy, the CTLs are related to the sequential removal of these holes.

While self-trapping of holes was found to be unfavourable in rutile TiO_2, electrons do self-trap and form polarons localised on a lattice Ti atom.[186] The Kohn-Sham level of the polaron lies 1.02 eV below the CBM, which is slightly shallower than the polaron level in the presence of a charged defect, such as a Ti_i^{3+}.

6.4.2 Polarons in TiO_2

As already indicated above, a Ti_i creates small polarons in rutile TiO_2.[140] A polaron is a quasiparticle, which is a result of electron-phonon coupling. An electron (or hole) in a crystal induces a strain field due to the Coulomb interaction with the lattice

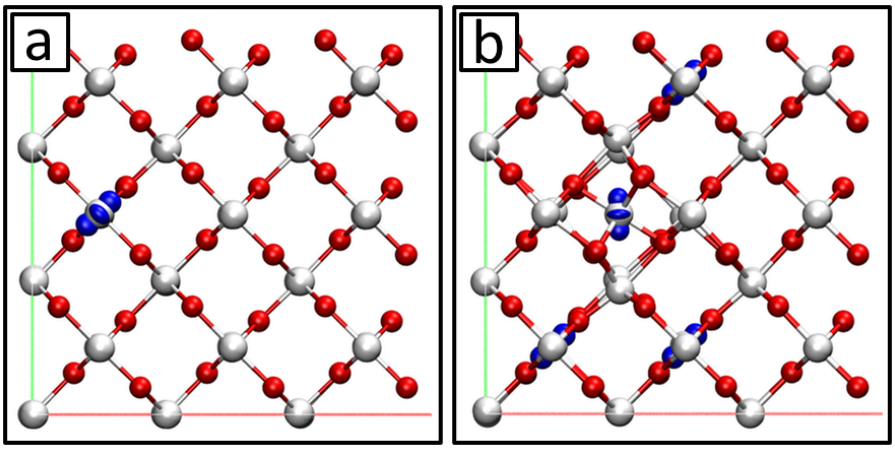

Figure 6.6: a) Self-trapped electron in bulk rutile TiO_2 localised on a Ti lattice site. b) Polarons induced by a Ti_i defect localised on the defect and lattice Ti sites. (Red = O, white = Ti)

ions. In a covalent crystal the interaction is typically weak, while in more ionic crystals the interaction is larger. Charge carriers can therefore locally deform the lattice, leading to charge trapping. Such a trapped polaron will tunnel through the crystal at low temperatures, whereas at higher temperatures it can hop through the crystal or get excited into the conduction band.

Rutile TiO_2 can self-trap an electron on a Ti lattice site creating a small polaron as shown in Fig. 6.6a. The lattice is distorted around the polaron creating an energy well for the electron which occupies a Ti 3d orbital. The polaronic Kohn-Sham state is located 1.02 eV below the CBM in the bandgap of TiO_2. Holes do not self-trap in rutile TiO_2 and instead will be delocalised in the valence band.

Similarly, a Ti_i induces polaronic states in bulk rutile TiO_2 (see Fig. 6.6b). The Ti interstitial has four valence electrons, which create four polaronic states. One polaron will remain on the interstitial Ti and three polarons are localised on lattice Ti atoms. Therefore, the Ti_i can be assigned a classical charge of +3, which is consistent with EPR measurements.[187] A positively charged interstitial refers to an interstitial with fewer polarons in the vicinity.

6.4.3 Ti Interstitial Diffusion

In order to better understand the mobility of the interstitial Ti atoms, NEB calculations determining diffusion paths were performed. There are two possible low energy diffusion paths for a Ti_i defect: along the (001) direction, which corresponds to diffusion through a hollow channel in the TiO_2 lattice, and via an interstitialcy mechanism along the (110) direction.

Fig. 6.7 illustrates the barriers for diffusion along the (001) and (110) crystallographic directions. For a neutral Ti interstitial (Ti_i^{+3}+3 polarons) the diffusion barrier along the (001) crystallographic direction is 0.34 eV, which is lower than previously reported values obtained with a GGA functional.[188, 189] Due to the lattice symmetry, the diffusion path has length $c/2$ for which the barrier is shown (see insets of atomic configurations).

The interstitialcy mechanism is the lowest in energy for diffusion along the (110) crystallographic direction. The calculated path displays a two step process with barriers 0.5 eV and 0.55 eV. Due to lattice symmetry, these two barriers should be equal and the discrepancy is attributed to not fully relaxed transition structures. A local minimum is found for a Ti_i-v_{Ti}-Ti_i complex, which is 0.23 eV higher in energy than the Ti_i configuration in a rutile lattice. Interestingly, previous reports show the intermediate structure to be lower in energy than the start and end configurations.[188]

The diffusion of a Ti_i^{+4} defect was also calculated, which has respective barriers of 0.25 eV along (001) and 0.31 eV along (110), which is close to reported values of 0.31 eV along (001) and 0.23 eV along (110).[188] During the diffusion process the electron which is localised on Ti_i leaves the interstitial to form a polaron on a nearby lattice Ti atom. The charged interstitial and the polaron states will attract each other, increasing the activation energy for diffusion. GGA barriers are lower, partly since the electrons of the interstitial are delocalised in the conduction band.

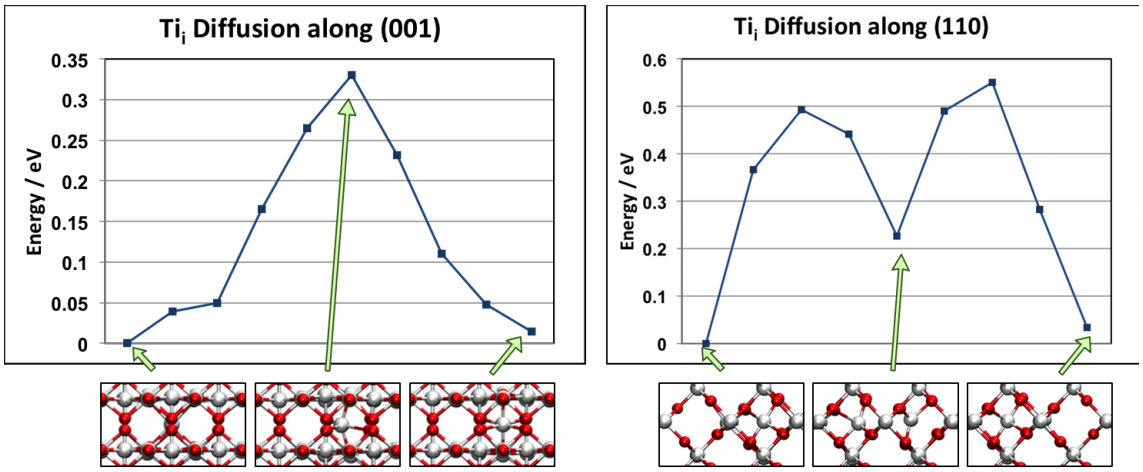

Figure 6.7: Barrier for Ti_i diffusion along the (001) and (110) crystallographic directions in bulk TiO_2. The insets illustrate atomic geometries of three points along the diffusion path as indicated by the arrows. (Red = O, white = Ti)

6.5 Discussion

Defect formation energies for intrinsic defects in bulk rutile TiO_2 were calculated in order gain knowledge of the rich defect chemistry of the material. TiO_2 finds many applications where the operating conditions vary, e.g. reduced TiO_2 crystals are used as oxygen sensors to analyse exhaust gases of cars. The defect chemistry is strongly dependent on these external conditions, specifically temperature and oxygen pressure. Therefore, the DFE of Ti/O interstitials and vacancies were calculated for four sample conditions: 300 K at 1 atm O_2 gas pressure as well as 1000 K at 10^{-6} atm O_2 gas pressure for Ti rich and O rich conditions.

Ti^{3+} interstitials are of particular interest as the main intrinsic bulk defect. They are more easily formed at high temperatures and low oxygen pressure, which corresponds to typical conditions during an annealing process. However, as an intrinsic charged defect, they need to be compensated by either O vacancies or Ti vacancies, i.e. forming a Frenkel or Schottky defect. The presented DFEs were computed from isolated individual defects in bulk TiO_2, however, defects can interact with each other. In fact, aggregation of defects has been reported before from theory[190] and experiment.[191]

It is important to point out that the choice of functional has a big impact on calculated DFEs. While a vast literature exists for point defects in rutile TiO_2, many were calculated using LDA, PBE and other GGA functionals.[156, 180, 192, 193] However, LDA and GGA functionals are not able to correctly describe the bandgap of TiO_2, the localisation of defect induced polarons due to self-interaction error and the related defect state below the CBM. While GGA+U calculations can give better agreement, particularly for localised defect states, calculated DFEs are overestimated due to an underestimation of the bandgap and associated error in μ_e.[157, 193] The herein presented defects match IR photo-absorption measurements[183] and EPR data,[187] giving confidence in the chosen computational method.

The calculated bulk diffusion barriers are low, resulting in fast diffusion of Ti_i at room temperature and above, enabling surface generated defects to diffuse into the bulk crystal. The barrier for diffusion along an open channel, (001) crystal direction, is slightly smaller compared to the diffusion barrier along (110). However, at room temperature and above diffusion will be rapid and the difference will only become significant at low temperatures.

The differences in absolute barrier height for neutral and positively charged Ti_i between the presented work and reports in literature is attributed to the different functionals used in this study (HSE06) and reported studies (PW91,PBE) and the respective pseudopotentials.[188, 189] GGA functionals do not reproduce the correct dynamic behaviour of the rutile phase, since the A_{2u} phonon mode is unstable.[159] Furthermore, the additional electrons of the Ti_i will be delocalised across the simulation cell in GGA calculations, not reproducing the polaronic states.

However, the precise process of how a surface Ti atom is moved from it's lattice site into an interstitial site as well as the path for indiffusion is still poorly understood, which therefore will be investigated in the next chapter.

6.6 Conclusions

The inability of standard GGA functionals to correctly describe the electronic structure of TiO_2 and its intrinsic defects has previously prevented theoretical calcula-

tions to match experimental measurements. Nevertheless, numerous publications using these functionals exist. The advent of more powerful computers allows for larger systems and hybrid functionals, which improved agreement between theory and experiment.

In this chapter intrinsic defects in rutile TiO_2 were discussed and differences to previous reports highlighted. DFEs, defect geometries, bandgap states and Ti_i diffusion barriers were calculated using a hybrid-DFT approach. A Ti_i adopts a 3+ charge state and induces three small polarons in its vicinity, which is consistent with EPR data and STM measurements of surface polarons. These interstitials have low diffusion barriers, leading to fast diffusion at elevated temperatures. These results are useful to better understand the rich defect chemistry of TiO_2 and motivate the investigation of surface mediated reduction of rutile crystals.

Chapter 7

Diffusion of Ti Interstitials From the Surface Into the Bulk

7.1 Introduction

As outlined in the previous chapter, TiO_2 displays rich defect chemistry. In fact most applications of TiO_2 exploit or rely on such defects. For example in solar cell technologies reduced or hydrogenated TiO_2 displays enhanced photo-absorption in the visible and IR spectral region.[194, 195]

A series of STM measurements during a sample anneal at 1000 K show shrinking step edges within a few minutes. Longer annealing leads to the formation of v_O on the surface and ultimately to the cross-linked 1×2 reconstruction.[196] It is postulated that oxygen is removed from the crystal in the form of gaseous oxygen and Ti moves as an interstitial into the bulk crystal.

The inverse of this process has also been studied experimentally: reoxidation studies show that surface adsorbed oxygen from the gas phase can react with Ti_i from the bulk to grow new strands,[196, 197] islands[144] and ultimately complete 1×1 layers of TiO_2,[137, 174, 196] indicating that the bulk crystal behaves as a defect reservoir. The uptake rate of O_2 was dependent on the reduction state of the sample with faster uptake for the more reduced samples.[198] Isotopically labeled ^{18}O and ^{46}Ti were used in secondary ion mass spectrometry measurements (SIMS) to show that Ti diffusion from the bulk to the surface is the dominant ion transport mechanism.[143]

Surface reoxidation of reduced crystals is a common procedure for STM experiments, since a conducting bulk reduced crystal is needed and reoxidising the

surface can yield a defect-free 1×1 (110) surface.[137,198] while the complex defect structure underneath the reoxidised surface is hidden, it impacts island growth[174] and is responsible in part for a dependence on sample treatment and sample history.[137,196,198]

Further evidence of Ti_i indiffusion was reported from EPR measurements.[199] The ratio of surface to bulk Ti^{3+} species was measured as a function of annealing temperature. It was shown that the surface signal dominates at annealing temperatures of 773 K, but as the temperature is raised the bulk signal becomes stronger. Nevertheless, the surface Ti^{3+} signal is stronger at all annealing temperatures. The Ti^{3+} species is closely related to Ti_i, but is not exclusive to this defect as discussed in the previous chapter.

Theoretical studies of near surface Ti_i and their indiffusion mechanism are still rare. The Ti_i injection barrier was recently reported from GGA+U calculations[200] and a micro-kinetic model.[201] However, no detailed first principles calculations of the indiffusion of Ti from a reduced surface have been reported. Experimental evidence for Ti_i diffusion shows linear diffusion coefficients with temperature for slightly reduced crystals, which breaks down for highly reduced samples.[185] However, the reported diffusion barrier of 2.47 eV is an order of magnitude larger than calculated diffusion barriers from ab initio calculations (see Section 6.4.3), motivating the investigation of Ti_i diffusion at the rutile TiO_2 (110) surface.

In this chapter, the behaviour of Ti_i at the (110) surface is analysed in order to derive knowledge of the indiffusion process of these interstitial atoms. Particularly the process of Frenkel pair formation and subsequent diffusion of the Ti_i away from the surface defect into the bulk is studied for stoichiometric as well as reduced (110) surfaces. The results show that Ti_i formation barriers are significantly reduced for substoichiometric (110) surfaces. Furthermore, the diffusion barrier quickly recovers the one for bulk diffusion as the Ti_i moves away from the v_{Ti}.

7.2 Ti Interstitials at the (110) Surface

In order to gain insight into the dependence of the DFE of an Ti_i as a function of distance from the surface, the defect was calculated at various positions in an eight layer slab. Table 7.1 lists these DFEs as well as the value calculated for an interstitial in bulk TiO_2. The chemical potential was chosen to refer to conditions during an annealing process (1000 K and 10^{-6} atm O_2 pressure) and no atoms were frozen in the slab for these calculations.

It can be seen that the DFE for a Ti_i in the first bilayer (i.e. between the surface plane and subsurface plane of Ti atoms) the DFE is almost 0.5 eV higher than for a bulk interstitial. This is related to the surface relaxation (see Section 6.3), where the top plane of atoms relaxes downwards upon creation of the (110) surface. Thus the two planes of atoms sit closer together leading to bigger distortion upon Ti_i incorporation and making it less energetically favourable. An interstitial in the next layer down, however, is more favourable with a DFE of 3.01 eV, which is within the error margin of the bulk value of 3.02 eV. As the interstitial is moved into the slab, ideally the bulk DFE should be recovered. However, the computational cost limits the number of layers which can be computed, which means that the middle layers do not fully recover bulk behaviour, as previously seen for the calculation of the surface energy (see Fig. 6.3). Nevertheless, the trend shows that subsurface interstitials in the second layer are more stable than ones in the top and third layer. This can have implications for interstitial indiffusion, where a higher concentration of interstitials sits close to the surface and can contribute to surface reactions.

A closer look at the geometry of the subsurface Ti_i reveals that two possible configurations are possible. The Ti_i can either bond to one surface O atom (ax-

Layer	DFE / eV
First	3.51
Second	3.01
Third	3.15
Fourth	3.12
Bulk	3.02

Table 7.1: DFE for a Ti_i at various depths below the surface of an 8 layer TiO_2 slab.

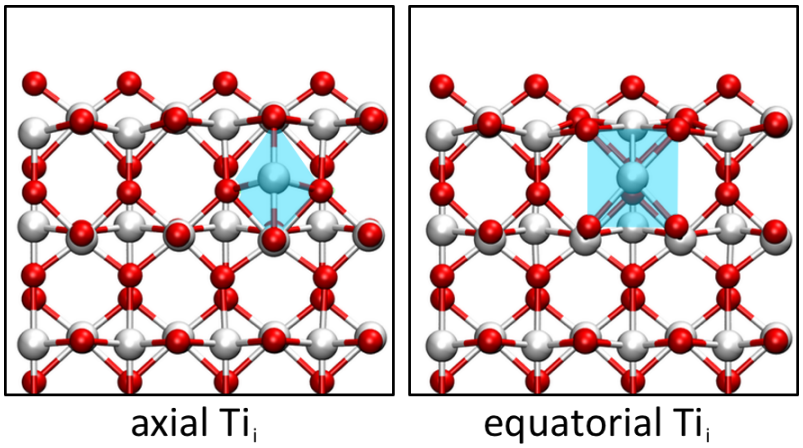

Figure 7.1: Axial and equatorial Ti_i at the (110) surface of rutile TiO_2. The blue surface represents the plane cut through the TiO_6 octahedron showing the elongated axial diamond base for axial Ti_i and the square base for equatorial Ti_i. (Red = O, white = Ti)

ial configuration) or to two surface O atoms (equatorial configuration). The two configurations differ in a 90° rotation of the distorted octahedron of the Ti_i and a translation by half a c lattice vector as shown in Fig. 7.1. Both configurations adopt a triplet Ti_i^{3+} state with three localised polarons in the vicinity, though the axial configuration is 0.24 eV higher in energy than the equatorial configuration. The difference can be traced down to the geometry of a Ti_i, which sits in an elongated octahedron. Since the distance between the top and second layer compresses upon creating the (110) surface, the octahedron preferentially orientates the longer axis parallel to the surface plane instead of along the surface normal. Two polarons localise on surface Ti^{5f} sites, which can contribute to the reactivity of the surface. Since the surface breaks the lattice symmetry, the polaron states sit at different positions in the bandgap. Three states can be identified at 0.67 eV, 1.18 eV and 1.57 eV below the CBM (see Fig. 7.2). As the interstitial is moved into the slab, these states become degenerate and recover the polaron state for a bulk Ti_i.

7.3 Surface to Bulk Diffusion

The DFE for a Ti_i show a favourable trend towards the bulk of rutile TiO_2. The proposed process for indiffusion is as follows: Surface oxygen is removed during annealing, leading to Ti_i formation at the surface. Due to the concentration gradi-

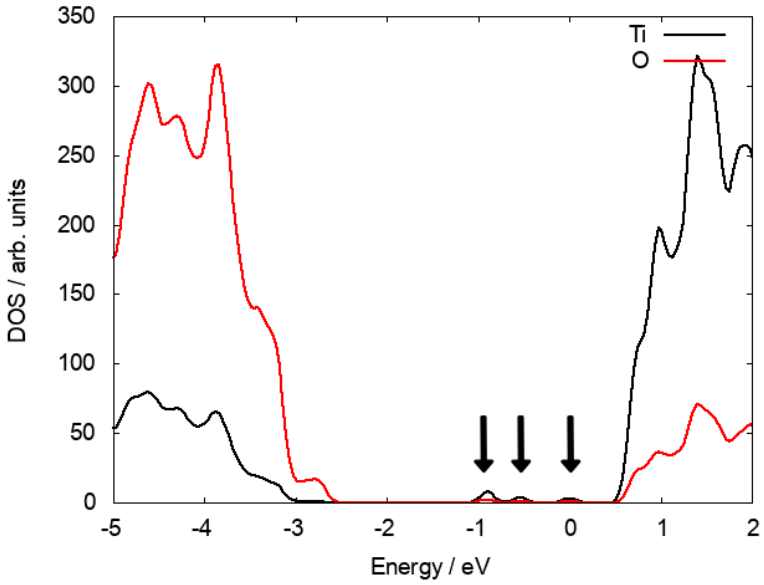

Figure 7.2: DOS plot of a subsurface Ti_i illustrating the polaronic states in the bandgap of TiO_2.

ent, Ti_i atoms diffuse into the bulk given the diffusion barrier can be overcome at sufficiently high temperatures, leading to an overall reduction of the crystal.

The barrier to create a Frenkel defect pair consisting of a Ti_i in the subsurface layer (referred to as top layer in Table 7.1) and a surface v_{Ti} is over 5 eV as shown in Fig. 7.3a, which is slightly lower than the predicted Frenkel DFE of 6.64 eV for isolated defects in bulk rutile TiO_2. However, the final state is not an energetic minimum, due to electrostatic attraction between the vacancy and the interstitial.

The same process can be calculated for a reduced surface, which is shown in Fig. 7.3b. Two neighbouring O_{Br} were removed exposing a four-fold coordinated Ti atom. The barrier to move this Ti atom into an interstitial position is much lower at 0.54 eV and the final interstitial site is an energetic minimum, which is 0.29 eV lower in energy than the fourfold coordinated Ti atom (Ti^{4f}) in its lattice site. Effectively a Schottky defect was formed, where the Ti atom maximises its coordination with lattice O atoms by adopting an interstitial geometry.

Fig. 7.3c and d illustrate the diffusion barriers along [110] and [001] for this newly created Ti_i at a reduced (110) surface. Both barriers are just over 2.5 eV, much higher than the bulk diffusion barrier along these crystallographic directions.

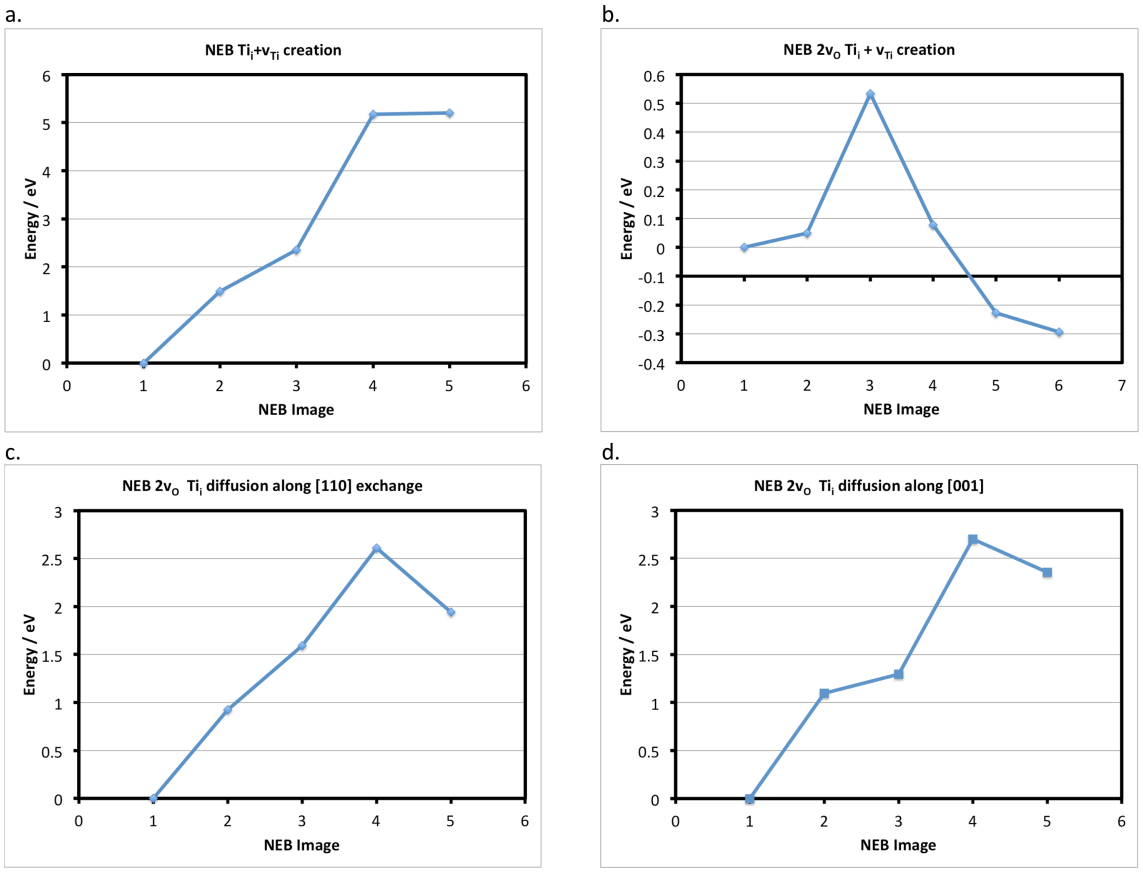

Figure 7.3: Barriers for a) moving fivefold coordinated surface Ti (Ti^{5f}) into an interstitial position, b) moving Ti^{5f} into an interstitial position with two neighbouring v_O, c) Ti_i diffusion away from v_{Ti} along [110] direction and d) Ti_i diffusion away from v_{Ti} along [001] direction.

This can be attributed to the bonding behaviour of the Ti interstitial with the defect complex. An interstitial in pristine TiO_2 bonds more weakly to the lattice O atoms, however, the Ti_i next to a Schottky defect binds strongly to the undercoordinated lattice O atoms, making diffusion more energetically costly.

Fig. 7.4 illustrates the complete potential energy path for the indiffusion of a surface Ti^{4f}. The separation of the interstitial from the defect complex constitutes the rate determining barrier, after which the diffusion barrier almost recovers bulk diffusion. From configuration (3) to (5) (see labels in Fig. 7.4) the barrier is 0.7 eV, which is 0.2 eV higher than the corresponding barrier in the bulk and the transition structure (4) is 0.3 eV higher than the split interstitial in bulk TiO_2.

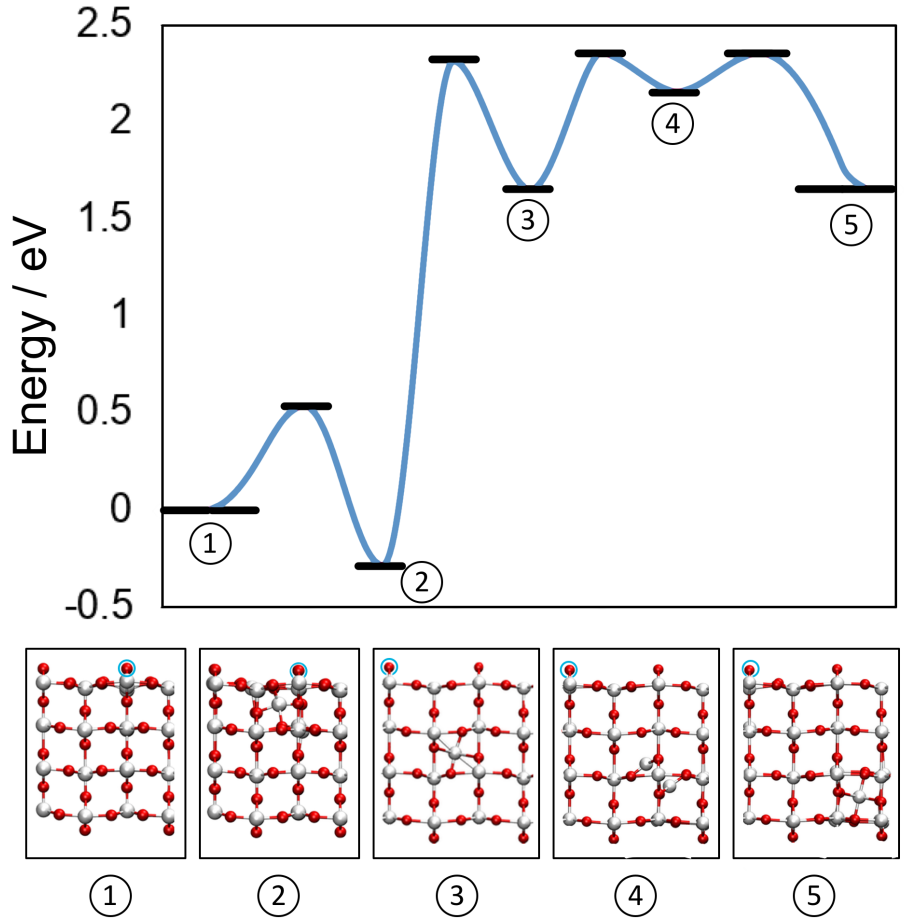

Figure 7.4: Schematic showing the barriers for the creation and diffusion of a Ti_i from a reduced (110) surface into the bulk. Zero energy refers to a surface with two neighbouring v_O. Atomic structures of the energetic minima are illustrated below. The cyan circles indicate the location of the two v_O on the surface of TiO_2. (Red = O, white = Ti)

7.4 Discussion

Near surface Ti_i have been linked to the chemical activity of the (110) surface of rutile TiO_2, but the behaviour of these defects is still poorly understood. In bulk rutile TiO_2 there exists only one possible interstitial site, which a Ti atom can occupy. Such an interstitial retains one of its four valence electrons and induces three small polarons, thus creating four Ti^{3+} species. An interstitial at the surface, however, can adopt one of two possible configurations, termed axial or equatorial geometry. The polarons associated with these subsurface Ti_i sit on surface and subsurface Ti lattice sites. Due to the difference in screening of these trapped charges on the surface, the

polaron states are not degenerate siting at 0.67 eV to 1.57 eV below the CBM and thus will impact the chemical reactivity of the surface. This is consistent with increased photo-absorption in the visible spectrum for reduced TiO_2 crystals.[145] As the interstitial is moved into the bulk, the polaron states move closer in energy and converge at 1.02 eV below the CBM for an interstitial in the fourth layer, which is slightly higher than the state at 1.12 eV below the CBM for a bulk Ti interstitial. Electron energy loss spectroscopy (EELS) has revealed a bandgap feature at either $\sim$1 eV[202,203] or 0.8 eV,[183,204,205] which are related to polaron states below the CBM of TiO_2. Oxygen vacancies agree well with the shallow polaron, whereas Ti_i defects induce a state in agreement with the deeper polaron state. The descripancy in the reported experimental values may be traced down to sample treatment and preparation methods, creating oxygen vacancies or near surface Ti interstitials.

The barrier to create a Ti_i at the surface was calculated at >5 eV for a fully oxidised (110) surface. However, this barrier is reduced to just $\sim$0.5 eV for a Ti atom next to two bridging oxygen vacancies. In that instance the interstitial site is actually lower in energy than the Ti atom at its lattice site. It has long been proposed that such a mechanism should exist, though these results constitute the first proof from detailed ab initio calculations.

In order to separate the Ti_i from the defect complex $\sim$2.5 eV is required (both for [110] and [001] diffusion). This barrier was calculated for a neutral interstitial, but the results from bulk diffusion indicate that the barrier is lower for Ti_i^{4+}. Since surface charge corrections are still challenging only the neutral case was calculated for the subsurface Ti interstitial, but it is proposed that Ti^{4+} ion diffusion will have a lower barrier.

The calculated barrier is comparable to a barrier of 3.3 eV, which was previously calculated for Ti_i dissociation from extended defects using a micro-kinetic model.[201] Furthermore, data from tracer self-diffusion suggests an activation energy of 2.47 eV for Ti_i migration in reduced TiO_2 crystals[185] and estimates from scanning probe measurements report a barrier of $\sim$3 eV for Ti to migrate from the surface into the bulk. However, the reverse barrier is much lower at 0.67 eV along [110] and 0.35 eV

along [001]. Therefore, reoxidation of TiO_2 should be much faster than reduction via heat treatment. This is in agreement with experimental procedures, where rutile TiO_2 crystals are annealed at 823 K for one hour, producing many subsurface Ti interstitials but the signal from bulk Ti^{3+} indicates very low concentrations. However, oxygen exposure at the same temperature will lead to the rapid reoxidation of the surface, pulling Ti_i out of the near-surface region to form new TiO_2 islands and ultimately a pristine (110) surface can be obtained in just minutes.[137,174,196]

After the interstitial has been separated from the defect complex on the surface, the diffusion barrier almost recovers bulk diffusion. This is due to the effective screening in TiO_2, which has a high dielectric constant of ∼100. Therefore, the indiffusion of Ti is limited by the barrier separating the interstitial from the $v_{Ti}+2v_O$ complex. Furthermore, it is postulated that the defect cluster will grow along the [001] direction, as the lattice atoms next to the defective area are less tightly bound. Such a process would explain the observed streaks in STM measurements[197] and could be related to the formation of the 1×2 reconstruction of the (110) surface. However, further theoretical work is required to confirm this proposed mechanism.

7.5 Conclusions

In this chapter the formation and mobility of a Ti_i at the (110) surface of rutile TiO_2 was investigated. Interstitials were found to be favoured in the second layer below the surface plane, where they induce polaron states at surface or subsurface lattice Ti atoms. Reduction of the surface lowers the barrier for Ti_i formation at the surface by an order of magnitude and the bulk diffusion barrier is recovered after the interstitial is moved away from the defect complex. These results have significant impact on the understanding of surface reduction and reoxidation, confirming an experimentally postulated mechanism from first principles.

Part III

2D Black Phosphorus as Post Graphene Material

8.1 Introduction

In 2004 researchers in Manchester were able to exfoliate single layers of graphene from graphite, a material which had been discovered in England in the 16th century and whose only large deposit in the world can be found there. Since 2004 the study of 2D layered materials has seen rapid growth and a quest to find other 2D materials besides graphene had begun. While several classes of layered 2D materials exist, such as layered ionic solids or metal oxides, most research has been concentrated on layered van der Waals (vdW) bonded materials, since atomically thin layers can often be produced relatively easily by mechanical exfoliation. The distinctive structure of layered 2D materials gives rise to unique properties, which often differ from their bulk crystal properties, such as mechanical flexibility, electric or thermal conductivity, transparency or robustness.

Amongst the post graphene vdW-bonded 2D materials is black phosphorus (BP). BP was first discovered by Percy Bridgman in 1914, when he studied the effect of high pressure on the higher energy white phosphorus allotrope. However, BP's poor stability under ambient conditions, its small bandgap and difficulties in controlling crystal quality meant interest in BP was diminutive.[206] With the discovery of graphene, exfoliation and processing techniques were developed, which helped revive interest in BP. In 2014 first reports of monolayer BP were published,[207–209] marking the beginning of rapidly expanding research on this material.

BP has a narrow, tunable band-gap and absorbs light in the visible through to IR spectral region. As a layered 2D material (see Fig. 8.5), it exhibits a change in physical properties going from bulk crystal to the nano-scale single layer limit. The bandgap opens from 0.3 eV for bulk BP to 1.5 eV for a single layer due to the suppression of interlayer interactions.[210] Similar to graphene, BP has very high charge carrier mobilities of up to 1000 $cm^2V^{-1}s^{-1}$[211] and displays anisotropic behaviour along the Γ-X and Γ-Y principal directions in properties such as charge mobility, thermal conductivity, bulk modulus and its optical adsorption to name a few. However, BP is highly reactive, which makes its properties sensitive to ambient conditions.[212–214] The rapid oxidation of BP can be prevented by capping layers,[215]

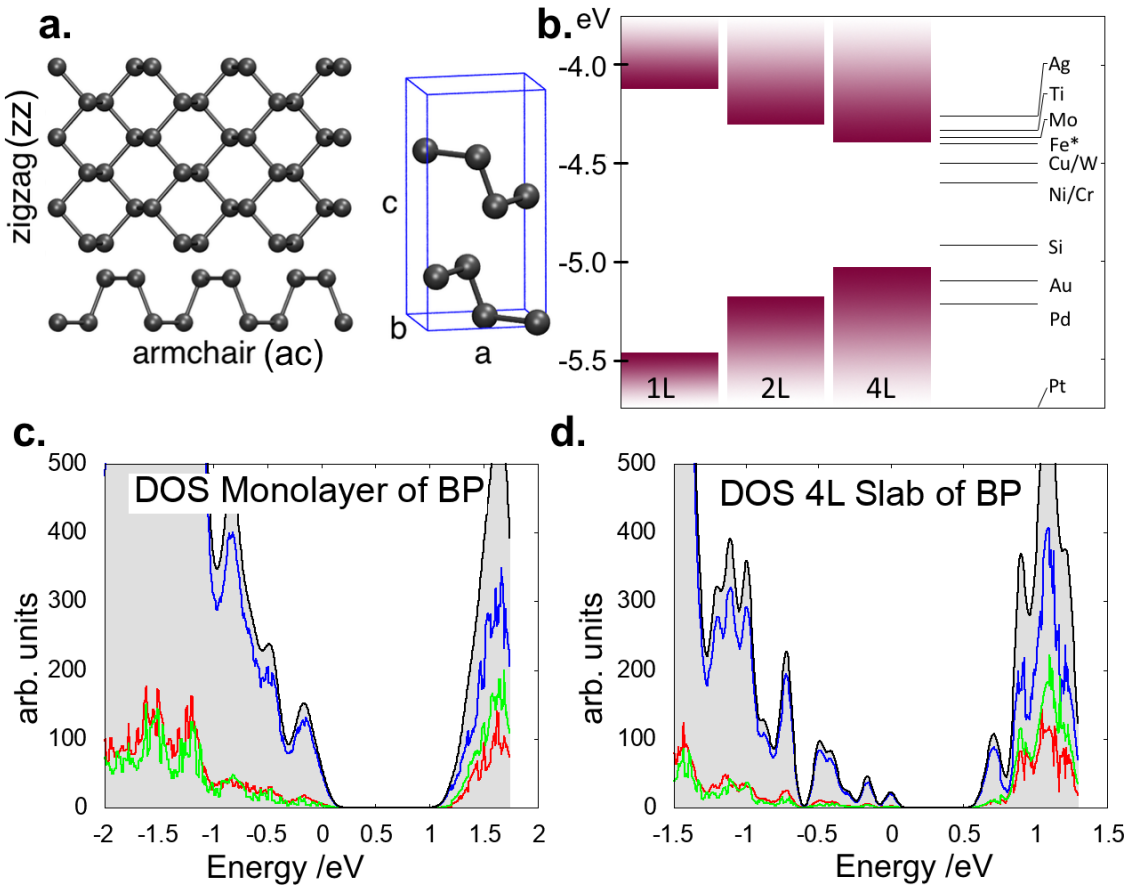

Figure 8.5: Top left: Black phosphorus monolayer and unit cell structure illustrating the lattice directions; top right: Position of the band edges with respect to the work-function of common metals (* stainless steel). Bottom left: Total DOS of monolayer BP (grey) and projections on 3s-orbital (red), 3p-orbitals (blue) and 3d-orbitals (green); bottom right: Total DOS of multilayer BP (grey) and projections on 3s-orbital (red), 3p-orbitals (blue) and 3d-orbitals (green).

and thus the stability and performance for future applications depends strongly on intrinsic descriptors such as point defects, line defects and crystal quality.

In this part of my thesis the defect chemistry of BP is studied with respect to experimentally observed defects. The nature of such defects is still disputed, with monovacancies and Sn impurities the two most favoured candidates. Thus, an analysis of various intrinsic and extrinsic defects is performed in order to elucidate the nature of observed defects.

In Chapter 9 the geometric and electronic structure of intrinsic point defects, such as vacancies, Stone-Wales defects, and self-interstitials, are investigated. Dif-

fusion barriers for vacancies are also discussed in order to gain insight into defect mobility. In Chapter 10 extrinsic defect impurities are discussed. Experimentally observed impurities, such as Sn, I, Fe, Ni, Cu, and Zn, were calculated in various configurations, since it is unknown how these species get incorporated into BP. These defects are further analysed with respect to their role in defect related doping. A short analysis of magnetic Fe impurities is also given. Lastly, the degradation of BP under ambient conditions is examined in Chapter 11. Interactions of oxygen, hydrogen and water with pristine and defective BP are calculated and degradation reaction enthalpies are estimated from first principle total energies.

8.2 Methods

8.2.1 Density Functional Theory

In order to study black phosphorus, a variety of theoretical methods have previously been employed, ranging from tight-binding methods and DFT to GW calculations.[216–220] The choice of method is mainly driven by the balance between its accuracy and computational cost. High accuracy calculations with ab-initio methods require extensive computer power, whereas semi-empirical methods such as tight-binding calculations can be run on a standard laptop machine. For this study DFT as implemented in the CP2K code was chosen, since it combines the accuracy of ab-initio calculations with the ability to simulate systems up to about 1500 atoms at reasonable expense. An overview of DFT can be found in Chapter 2.1.5. In order to obtain accurate results, the convergence of the band gap and lattice vectors against basis sets used and supercell size was checked. Using a double zeta MOLOPT basis set[165] for all species (P, I, Sn, Fe, Ni, Cu, Zn, O and H), a 400 Ry cutoff for the plane wave basis and a 9x9 supercell was found appropriate.

Bulk properties were calculated using a 1296 atom cell and the monolayer consisted of a 324 atoms cell. For the slab and monolayer calculations a vacuum gap of 20 Å was used in order to minimise interactions between periodically repeated slabs. Since dispersion forces are poorly reproduced in DFT, Grimme-D2 vdW corrections[16] were used to ensure the interlayer separation was reproduced accurately,

without which the interlayer interactions are significantly underestimated.

8.3 Calculation of Defect Formation Energies

Defect formation energies (DFE) can be calculated using:

$$E_{DFE} = E^{q}_{defect} - E_{pristine} + \sum_{i} \mu_i N_i + q(E_f + \Delta V) \ , \tag{8.1}$$

where q denotes the charge state of the defect, μ is the chemical potential of any species that has been added or removed from the system, N is the number of exchanged atoms, E_f is the Fermi level of the pristine system and ΔV denotes a potential alignment correction. Potential alignment is important for charged systems, since the average electrostatic potential is set to zero in DFT calculations. Thus, adding or removing atoms shifts the average electrostatic potential, which needs to be corrected for.[28]

For charged defects, charge interactions across the periodic boundary need to be corrected for, typically termed interaction image correction (IIC). Standard methods exist for bulk systems,[28] but not for 2D films. However, the interaction energy in the Markov-Payne correction (see Section 2.2.1) follows a 1/L dependence to first order, where L is the distance between the charged defects. Thus, IICs were performed by calculating the DFE with varying cell sizes from 5x5 up to 18x18 surface unit cells in 2D periodic boundary conditions and extrapolating to the infinite cell size limit.

From Equation 8.1 it can be seen that the choice of chemical potential is critical to obtain physically relevant DFEs. However, in most physical processes the exact chemical potential is unknown. Since dopant impurities are most commonly grown into the sample during the crystal growth process or during a high energy ion bombardment and subsequent anneal, any P atom, that is substituted by a different species, is assumed to then still reside on a P lattice site. Hence, the chemical potential of P was chosen to be the energy of a P atom in a monolayer of BP for the herein presented substitution defects. The same chemical potential was used in calculations reported in literature, thus allowing direct comparison of DFEs for intrinsic defects.

However, a more physically relevant P chemical potential is an isolated P atom in vacuum. Choosing such a chemical potential enables the comparison of bond breaking and forming reactions. Furthermore, the DFEs for vacancies calculated with this choice of P chemical potential correspond to the physical process of a P atom being moved out of the BP lattice into the gas phase. Therefore, the discussion of intrinsic defects will be performed on the basis of the gaseous P chemical potential.

Chemical potentials for iodine and oxygen were calculated as half the energy of an I_2 (singlet) and O_2 (triplet) molecule. For Sn and TMs the energy of an isolated atom in vacuum was used for the chemical potential. These potentials were chosen, since they most resemble the conditions under crystal growth, during which impurities are incorporated – oxygen and iodine exist in their molecular form, whereas the metals are considered as isolated gaseous atoms.

8.3.1 Charge Corrections

In order to obtain accurate DFEs charge corrections were performed. Standard techniques such as Makov-Payne (MP) or Lany-Zunger (LZ) are widely used techniques for charge corrections in bulk systems, but they are not applicable to 2D sheets in a large vacuum.[28] Thus an extrapolation to infinite supercell sizes was performed based on the MP correction. The MP correction to first order is given by:

$$E_{\mathrm{IIC}}^{MP} = \frac{q^2 \alpha_M}{2\epsilon L} \ , \tag{8.2}$$

where ϵ is the dielectric of the material, L is the separation between the defects and α_M is the Madelung constant. By inspection it becomes clear that the DFE scales with 1/L, where L is the supercell size. Thus, by calculating the DFE for various cell sizes, one can fit a linear regression to the data in order to deduce the infinite size limit, as shown in Fig. 8.6. By performing calculations with 2D periodic boundary conditions any dependence on the out-of-plane dimension is removed. The y-intercept of a linear fit (at $x = 0$) gives the best estimate for DFEs of charged defects. The convergence of the DFE for a MV is shown in Fig. 8.6 as an example.

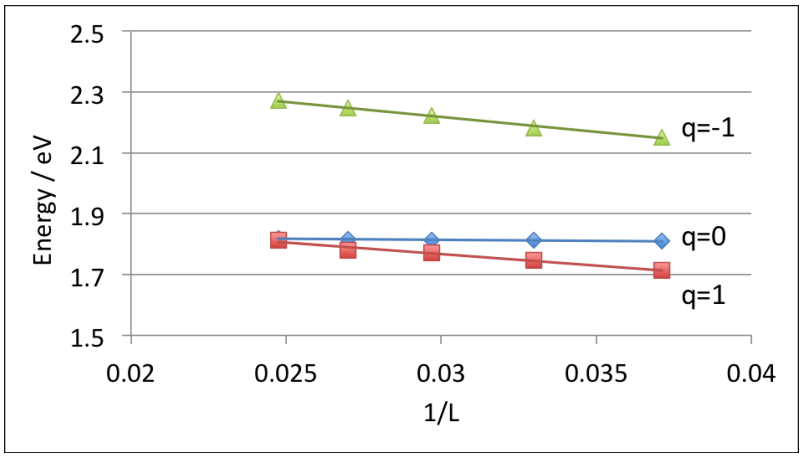

Figure 8.6: Linear fit to DFE as a function of inverse defect separation L for a neutral, positively charged and negatively charged MV. In the limit of infinitely separated defects the DFE approaches the value at x=0, which is the y-axis intercept of the linear fit.

8.3.2 2D Hydrogen

The correlated motion of an electron and hole on a 2D plane can be described by the motion of a particle with reduced mass $\mu{=}m_e m_h/(m_e + m_h)$ and energy E, which moves in a coulomb potential V($\mathbf{r}$). The static Schrödinger equation can then be written as:

$$\hat{H}\Psi(\mathbf{r}) = \left[-\frac{\hbar^2}{2\mu}\nabla^2 + V(\mathbf{r})\right]\Psi(\mathbf{r}) = E\Psi(\mathbf{r}) \quad , \tag{8.3}$$

where the potential $V(\mathbf{r}) = -e^2/\epsilon\mathbf{r}$ is a screened attractive electron hole interaction. Solving for the energy eigenstates one obtains:

$$E^{(n)} = -\frac{\mu e^4}{2\hbar^2\epsilon^2(n-1/2)^2} \quad , \tag{8.4}$$

where n is the principal quantum number.[221]

The 2D hydrogen model is used to discuss the interaction of an exciton, where the electron is trapped at a localised defect, such as a vacancy or impurity atom. However, the true excitonic states deviate from the ones predicted by the model significantly for small n, due to incorrect screening at short distances.[222,223] For 2D materials, the electric field between the electron and the hole permeates not only the material with dielectric ϵ, but also the surrounding vacuum with lower dielectric

ϵ_0, which leads to inhomogeneous screening.[222]

Chapter 9

Characterisation of Intrinsic Defects in Black Phosphorus

9.1 Introduction

Not long after the first reports on 2D BP, defects on the surface of BP have been observed in scanning tunnelling microscopy (STM) experiments.[217,224,225] These are characterised by bright, double-lobed areas of higher current, which extend up to ∼10 nm and show anisotropic contrast (see Section 9.2.1). Scanning tunnelling spectroscopy revealed that the defects induce a localised state in the bandgap at the valence band maximum (VBM). Depending on the apparent brightness of the feature, the defects were attributed to reside in the top surface layer or further down in the crystal. Studies have shown that defects can be identified as deep as four layers into the slab.[217] It was deduced that defects are evenly dispersed throughout the crystal since their concentration was found to be invariant with depth, suggesting that they may be ingrown or intrinsic to the crystal.

Theoretical calculations using a tight binding method have been used to attribute these defects to mono-vacancies (MV) on the surface of BP, where a single P atom is missing from the top row of the BP layer.[216,217] These reports illustrate that the charge density of the MV is very dispersed and is anisotropic depending on whether the defect sits on the left or the right side of the upper layer zigzag row. However, these calculations did not include surface relaxations around the missing P atom, nor did they investigate different charge states of the MV. Density functional theory (DFT) calculations show that atoms around a MV relax significantly to compensate

broken bonds.[218, 226] Thus unrelaxed geometries will lead to misinterpreting results, since dangling bonds can be passivated and electron density will redistribute around the relaxed defect. Furthermore, STM experiments show that the defect can be switched between two charge states. Calculations show that the electron density and defect geometry differ between different charge states of the MV, thus it is imperative to include relaxed geometries and consider different charge states for a successful identification of these defects.[226]

It was demonstrated that diffusion barriers of MVs are low at around 0.3 eV such that at room temperature mono-vacancies can rapidly diffuse.[218] While di-vacancies (DV) have been investigated theoretically, limited work has been reported from experiment. Similar to graphene, BP has a multitude of DV structures, which are less mobile than MVs as found in molecular dynamics simulations and ab initio calculations.[218] Their presence was inferred from pump-probe ultrafast spectroscopy measurements, where DVs are predicted to greatly prolong the lifetime of electron hole pairs and thus are responsible for the observed slow decay timescales.[227] Despite these findings, no scanning probe measurements have reported DVs on the surface of BP yet.

In this chapter possible defect candidates are investigated using DFT in conjunction with a hybrid functional. The geometric and electronic structure of neutral and charged intrinsic defects such as MVs, DVs, self-interstitials and Stone-Wales (SW) defects are analysed in monolayer and multilayer BP. These results are compared to previous studies, which mostly use GGAs to calculate defects in monolayer BP. GGA functionals do not correctly describe multilayer BP, since it predicts metallic BP. Thus no results on defect behaviour going from the monolayer to the multilayer limit have been reported. Furthermore, using a hybrid functional, electron correlation via exchange interactions is better described, reducing the self-interaction error. Results from our theoretical calculations are directly compared to experimental data in order to elucidate the nature of observed defects.

9.2 Experimental Background

Throughout this chapter theoretical results are compared to yet unpublished experimental data, which were obtained by our collaborators at University College London. A brief description of the experimental setup, data acquisition procedure and main findings is given in this section.

9.2.1 STM

Scanning Tunnelling microscopy and spectroscopy (STM/STS) measurement were performed by M. Wentink with help from S. Schofield and A. Kenyon at University College London on a commercial Omicron system operating at 77 K with a base pressure below 10^{-10} mbar. Tips were chemically etched from W wire and further refined in-situ through e-bombardment. The STM was operated in constant current mode with a dual bias in a typical range of 0 V - 1 V, while STS was performed at constant tip-sample separation. Images were analysed using home-built macros for the iGor Pro software, version 6.37. The BP crystals were heated to 150°C to evaporate residual water and subsequently cleaved in-situ at a base pressure of 10^{-10} mbar, then cooled down to 77 K for data acquisition.

STM images are shown in Fig. 9.1. At a bias of -0.4V, which corresponds to filled state imaging, defects can be identified as anisotropic bright spots with a central node. The shape of the defect resembles a p_x hydrogenic state and will henceforth be referred to as such. The bright rows of the perfect BP lattice can be identified, indicating that the defect is aligned along the armchair (ac) direction (see Fig. 8.5). The corresponding empty states image is shown in the top middle. A bright feature can be observed in the central region of the defect with an elongated bright feature along the ac direction. Interestingly, a dark circle can be identified around the defect, indicating charge density depletion in the near defect region. In both the filled and empty state image the defect extends about 5 nm along the ac- and about 2 nm along the zigzag (zz) direction (see Fig. 8.5).

As the bias is swept from inside the valence band of BP towards the band-edge, a change in contrast can be observed (left bottom image). The defect appears oblong

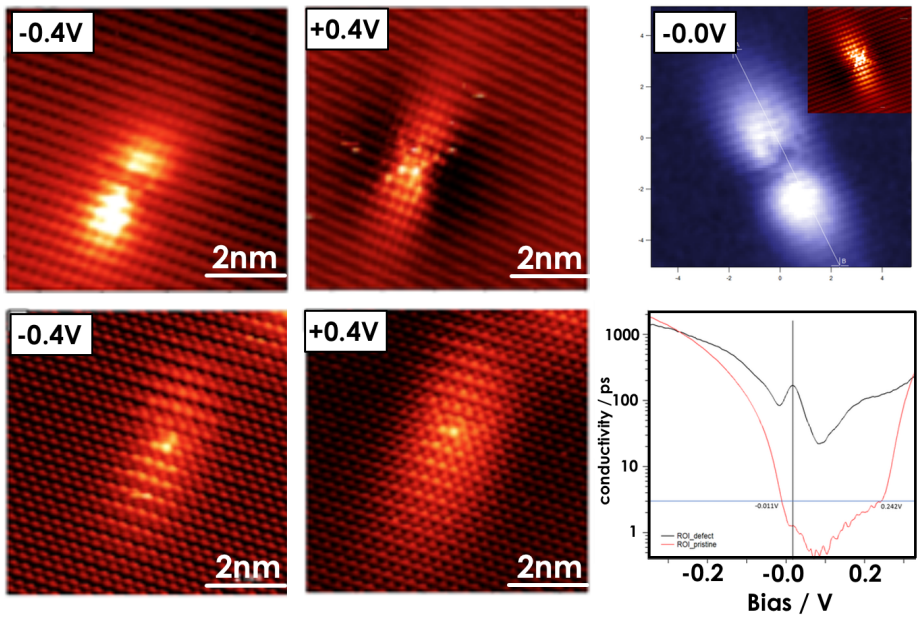

Figure 9.1: STM images of a surface defect at -0.4V bias (top left and bottom left) and at +0.4 bias (top middle and bottom middle). Top right: STS map of the defect at 0V bias, where the tip height was determined at +0.4V and subsequently held constant to avoid crashing the tip into the sample. Bottom right: average dI/dV curve along the line outlined in the STS image above (black line) and away from the defect (red line).

without a central node, resembling an anisotropic hydrogenic s-like state. As the bias is increased to scan the filled states, the shape of the defect still appears s-like with a depletion area surrounding it (see Fig. 9.1). Scanning tunnelling spectroscopy (STS) reveals a bandgap state $\approx$ 0.1 V above the VBM (bottom right). The base current is considerably higher compared to pristine BP (red line) and a shoulder appears at the CBM. In the top right image the bandgap state is visualised, where the tip height is set by finding a current set point at +0.4V (see inset in Fig. 9.1) and then held constant during the scan at 0V. This is necessary, since no current flows between the pristine BP monolayer and the STM tip at 0V bias. Thus, the tip would crash into the surface when trying to reach a set-point current.

9.2.2 Chemical Analysis

In order to identify possible impurities, chemical analysis was performed. X-ray photo-spectroscopy gives insight into binding energies. In Fig. 9.2 a wide spectrum XPS scan is shown for a VG and a HP sample. Both scans show expected peaks

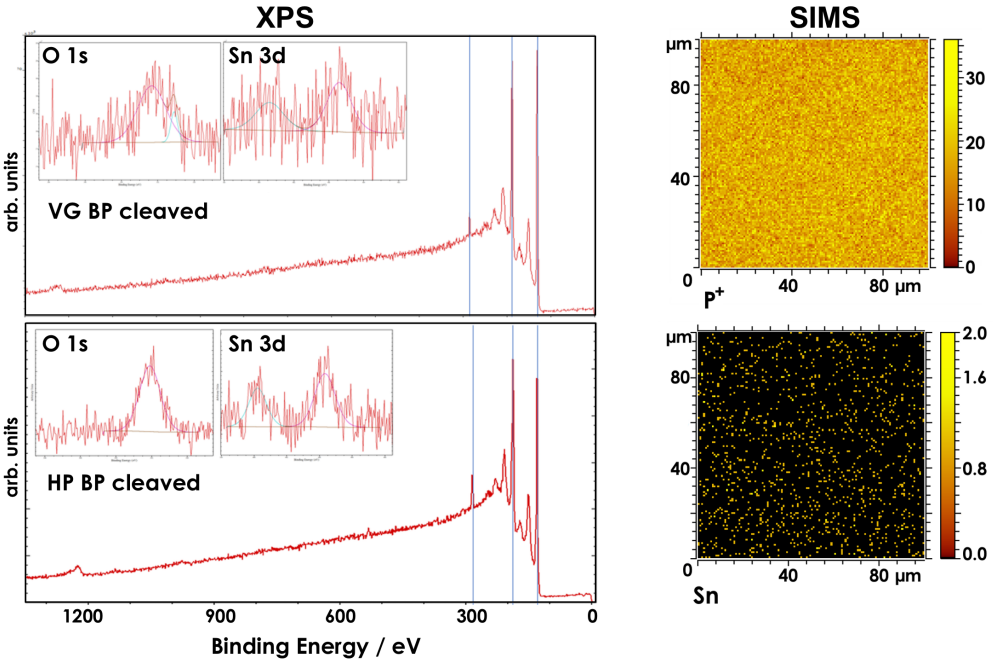

Figure 9.2: Left: XPS scans of two BP samples grown using the vapour growth (VG) method (top) and the high pressure (HP) growth method (bottom). The insets show the O 1s and Sn 3d peaks. Right: $100 \times 100 \mu m$ SIMS maps of a BP sample for P^+ (top) and Sn^+ (bottom). The colour legend refers to total counts per pixel.

related to P-P bonding in BP at 188 eV (2s) and 130 eV (2p), as well as two satellite peaks, which are related to plasmons. Further, a peak related to C impurities is observed which is expected to result from known contamination within the XPS chamber and is not related to the BP sample. Furthermore, a peak at 532 eV is observed, which is related to the 1s level of oxygen, bound as P=O or H_2O. Since the BP sample is cleaved ex situ and subsequently scanned in UHV, the surface may be partly oxidised and water may have adsorbed on it. Thus, the observed O peak is most likely related to the sample handling and not intrinsic to BP. The last peak observed is a doublet at 484 eV and 495 eV, which can be attributed to Sn $3d_{5/2}$ and $3d_{3/2}$ levels, respectively. Unlike other detected impurity species, the origin of tin is not known, which motivated further analysis using secondary ion mass spectrometry (SIMS) in order to verify the presence of tin in both samples and elucidate on their spacial distribution within the sample. SIMS maps of a cleaved HP-BP crystal are shown on the right in Fig. 9.2. The dominant species detected are P ions, as well as

P_2 and P_3 ions and small amounts of Sn are detected as well. The Sn impurities are evenly dispersed throughout the crystal and counted at a rate of ∼10 per second in a 100×100 μm scan. The dispersion of Sn impurities in BP is indicative of a sparse distribution of single Sn atoms instead of aggregated Sn in defective areas such as grain boundaries, thus motivating the study of Sn impurities in BP. More details about the experimental work can be found in our recent publication.[228]

9.2.3 Crystal Growth of BP

Black phosphorus crystals can commonly be grown in two ways, both using red phosphorus as a starting material. While early production of BP was done via high pressure conversion of white phosphorus or red phosphorus, a new low pressure route was discovered in 2007, which involved conversion of red phosphorus in the presence of gold, tin and tin-iodide (SnI_4).[229]

For the high pressure conversion process red phosphorus is wrapped in graphite foil and exposed to temperatures of 600°C at a pressure of 6 GPa.[230] After cooling at about 100 °C per minute BP can be obtained. BP produced following this method typically exhibits nano-crystalline structure.

Much bigger crystals (up to 0.5 cm) can be obtained using metallic catalysts to convert red phosphorus in a vapour transport process (VG).[231] Initially a mixture of Au, Sn, SnI_4 and red phosphorus was used, but the procedure was very sensitive to the ratios of reactants and the temperature profile during growth process. Furthermore, the reaction was often incomplete, resulting in high impurity concentrations and small crystal sizes.[231] In 2014 a revised growth method was reported by T. Nilges.[232] Mixing 500 mg red phosphorus with 20 mg Sn and 10 mg SnI_4 yields BP crystals of several millimetre size at high crystallinity and purity. SnI_4 is added as a mineralisation additive, while excess tin is used to suppress the formation of I_2 gas from decomposition of SnI_4.

As illustrated in Fig. 9.3, red phosphorus, tin and tin-iodine are placed at the hot end of a sealed quartz tube with a Hittorf's phosphorus crystal or BP crystal at the colder end, which will serve as a nucleation site. The hot side is heated to around 650°C, under which conditions P(g), PI_3(g), Sn_4P_3 and $Sn_{24}P_{19.3}I_8$ amongst

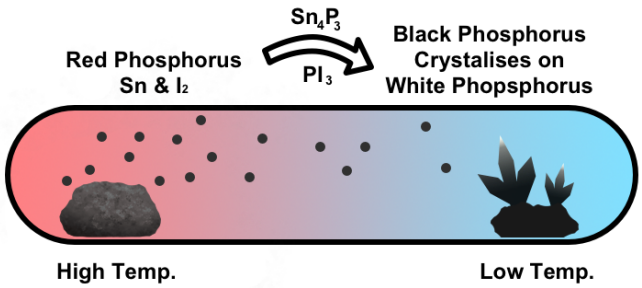

Figure 9.3: Schematic illustration of the CVT growth process by which red phosphorus is converted into BP.

others can be formed. These species facilitate the transport of phosphorus from the hot end to the colder end of the crucible, where consequently BP will grow.

Reports have shown large concentrations of tin and iodine in the final BP crystals,[230] yet the process by which these elements get incorporated is not clearly understood. Furthermore, the reaction is very sensitive to the purity of the starting materials as well as the growth conditions and residual Sn and SnI_4 can be observed on the surface of the so grown BP crystals. It was shown that Fe, Zn, Cu and Ni impurities can also be incorporated at considerable concentrations, even though they are not present at significant concentrations in the reactants, highlighting contamination from experimental apparatus as a possible impurity source.[230]

9.3 Results

9.3.1 Verification of Method

Black phosphorus consists of 2D layers stacked on top of each other in an AB configuration (see Fig.8.5), which are held together by vdW interactions between the layers. Each P atom is threefold coordinated with a lone pair orthonormal to the surface plane. BP exhibits a puckered geometry along the surface x direction, termed "armchair" (ac) direction (see Fig.8.5a) and a zigzag structure (zz) along the surface y direction. The optimised bulk unit cell vectors were found to be a = 3.37 Å, b = 4.55 Å and c = 10.87 Å, which is in good agreement with experimentally

measured cell vectors and other DFT studies.[209, 211, 218, 233–235] The bandgap for bulk BP was calculated to be 0.5 eV, which increased to 1.22 eV for a monolayer. Single point energy calculations were performed at various layer separations, which enables the extraction of the interlayer cohesion energy. As the layers are separated, their interaction subsides within a few Angstrom and the layer cohesion energy was found to be 25.4 meV/atom, which is in good agreement with previous studies[236, 237] and comparative to other vdW bonded materials such as graphite[238, 239] and h-BN.[238]

In its bulk crystal form, BP is a semiconductor with a narrow bandgap of 0.3 eV. The bandstructure of BP was calculated with the Castep code, since k-point functionality is not yet implemented in CP2K. The sX-exchange functional was employed, which adds a fraction of screened Hartree-Fock exchange[240] and a 3x3x3 k-point grid was used to sample the Brillouin zone. A plane wave cutoff of 600 eV gave results in good agreement with the data obtained with CP2K. As seen in Fig. 9.4a the bandgap is direct at the Γ point and displays an anisotropic effective mass in the in-plane Γ-X and Γ-Y directions in both the valence and conduction band. From the dispersion of the band along the Γ-Y direction the hole masses of about 6.35 m_e can be extracted. Yet still BP exhibits excellent hole conductivity, which was reported to be as high as 1000 $cm^2\ V^{-1}\ s^{-1}$ along the zz-direction and $640 - 700\ cm^2\ V^{-1}\ s^{-1}$ along the ac-direction in a monolayer.[211] Electron mobility in a monolayer is also anisotropic with values of $1100\ cm^2\ V^{-1}\ s^{-1}$ along ac and $80\ cm^2\ V^{-1}\ s^{-1}$ along zz.

Going from bulk BP to a monolayer the bandgap opens up, thus allowing tuning of the optical and electrical properties of BP by altering the number of layers. The DOS plots in Fig. 8.5 illustrate this opening of the bandgap as the number of layers is decreased. While for a four layer slab the bandgap is 0.5 eV, close to its bulk value, it increases to 1.22 eV for the monolayer.

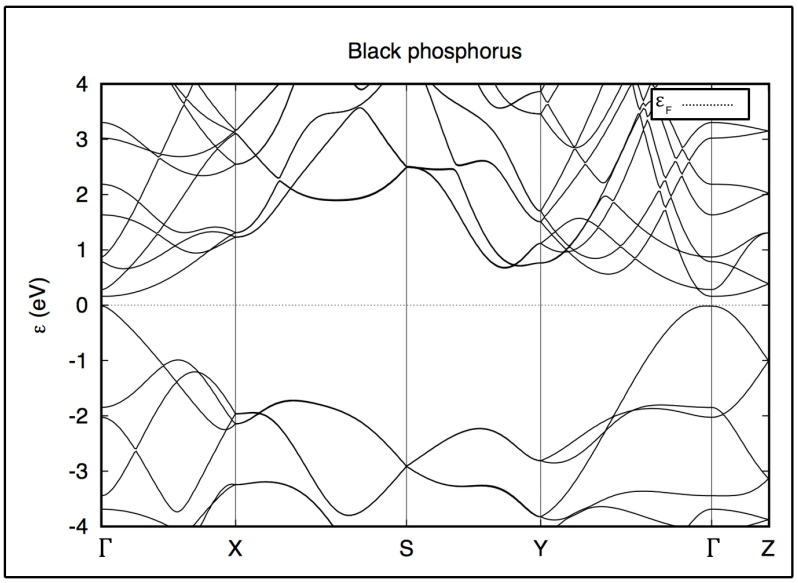

Figure 9.4: a) Bandstructure of bulk black phosphorus calculated in Castep using the sX functional. The anisotropic behaviour at the valance band maximum and conduction band minimum can be observed at the Γ point.

9.3.2 Band Offset

In order to estimate the charge state of defects, the ionisation potential (IP) was calculated in reference to common metals. For slab calculations, the IP is given by:

$$\epsilon_{HOMO} - \phi_{vacuum} \;=\; -IP \quad , \tag{9.1}$$

where ϵ_{HOMO} is the eigenvalue of the highest occupied Kohn-Sham orbital (HOMO) and ϕ_{vacuum} is the average electrostatic potential of the vacuum. Fig. 8.5 illustrates the IP for a monolayer, bilayer and a four layer slab. For a monolayer the VBM is at -5.5 eV, but increases to -5.2 eV for a bilayer and -5.1 eV for a 4 layer slab. A similar but inverted pattern is observed for the conduction band, lowering the CBM with increasing number of layers. The top of the valence band in BP shows mostly p_z character, where z is the direction of the surface normal. As 2D sheets of BP are stacked, the interactions between the layers directly perturb the p_z orbitals, leading to a narrowing of the bandgap. The work-function of several common metals is also indicated. Thus, when BP is put in electrical contact with a metal substrate, electrode or STM tip a common Fermi level will be established, possibly altering

Defect	$\mu_{P(ML)}$	$\mu_{P(gas)}$	Literature
59 MV	1.81	5.07	1.63,[241] 1.65,[218] 1.71[233]
5656 MV	2.38	5.3	2.05,[218] 2.0[233]
P_i	1.91	-1.35	1.79[241]
P_{ads}	1.56	-1.69	1.6[242]
5757 DV	1.51	8.02	1.35[218]
585-A DV	1.70	8.21	1.36,[241] 1.41,[218] 1.77[233]
555777 DV	2.85	9.36	2.28,[218] 2.76[233]
5555-6-7777 DV	1.93	8.44	1.54[218]
5959 DV	3.45	9.96	
585-B DV	3.93	10.44	3.29,[218] 3.2[233]
949 DV	3.65	10.16	
4-10-4 DV	2.02	8.53	2.27[233]
SW 1	1.8†	1.8†	1.4,[241] 1.62,[233] 1.32[219]
SW 2	0.9†	0.9†	1.22,[233] 1.01[219]
Frenkel (MV+P_i)	3.38†	3.38†	
Frenkel (MV+P_{ads})	3.08†	3.08†	

Table 9.1: Defect formation energies in eV of intrinsic defects in monolayer BP calculated using two P chemical potentials: $\mu_{P(ML)}$ refers to a P atom in a monolayer of BP, $\mu_{P(gas)}$ refers to an isolated P atom in vacuum. Reported values in literature use $\mu_{P(ML)}$, therefore DFEs with the same chemical potential were calculated in column 2. †independent of phosphorus chemical potential.

the charge state of a particular defect in the process.

9.3.3 Intrinsic Point Defects in Black Phosphorus

The main type of intrinsic defects in BP are point defects, namely mono-vacancies (MV), di-vacancies (DV), Stone-Wales defects (SW) and self-interstitials (P_i) as well as line defects such as step edges, grain boundaries and dislocations (line defects will not be discussed here). An overview of calculated DFEs is shown in Table 9.1

9.3.3.1 Phosphorus Vacancies

BP consists of only phosphorus atoms and in its bulk and monolayer form all lattice sites are equivalent due to symmetry. However, as a covalently bonded material, it shows various different vacancy structures for MVs and DVs. Fig. 9.5a illustrates the mono-vacancy structure with a DFE of 5.07 eV for the neutral charge state. The notation from graphene was adapted to BP, where the given numbers indicate how

many atoms constitute a ring structure. While pristine BP consists of 6 member rings, the MV adopts a 59 ring configuration. Upon creation of the MV three dangling bonds are formed and the atoms around the defect will relax to compensate two of these bonds. This leaves one dangling bond on a two coordinated P atom, creating an empty state in the middle of the band-gap of monolayer BP about 0.5 eV above the valance band maximum (VBM). IPR analysis reveals that this state is indeed localised on the two coordinated phosphorus atom and thus a peak is observed in the IPR spectrum in Fig. 9.6b.

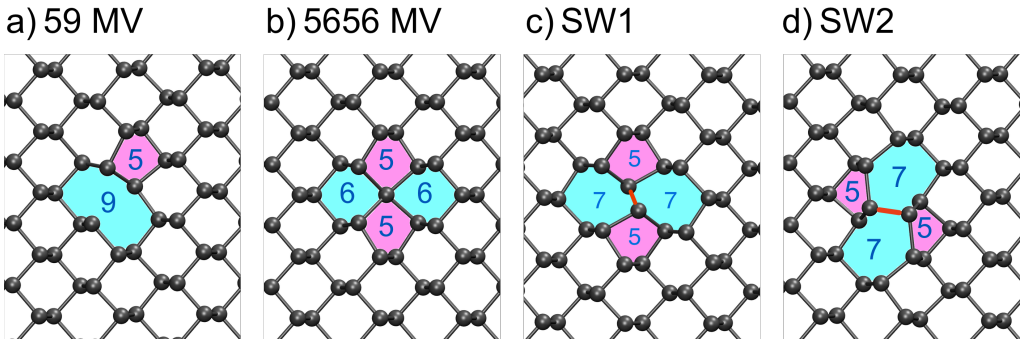

Figure 9.5: Defect structures in monolayer BP with their respective formation energies given above: a) Neutral (5|9) phosphorus mono-vacancy in monolayer BP. b) Negatively charged (55|66) mono-vacancy in monolayer BP. The central P atom is fourfold coordinated in a sp^3d^2 hybridisation state. c) + d) Stone-Wales type defects in monolayer BP.

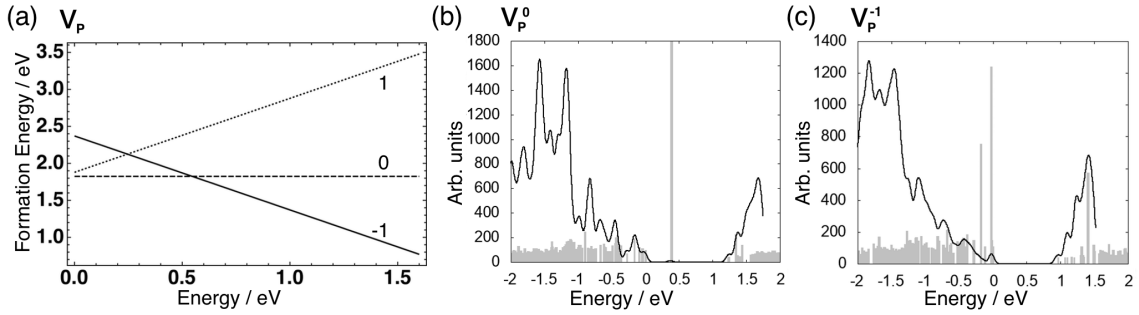

Figure 9.6: a) Defect formation energy diagram for a phosphorus vacancy in monolayer BP showing three charge states (-1e,0e,1e) showing the neutral and negative charge state as most stable depending on E_f. The transition point from neutral to negative charge state is at about 0.5 eV above the VBM. b) Density of states and overlaid IPR spectrum for a neutral P vacancy illustrating the localised dangling bond state in the bandgap of BP. c) Density of states and overlaid IPR spectrum for the negatively charged P vacancy showing localisation at the band edges but no states in the band gap.

Since the unpaired electron of the dangling bond can either be paired up or removed, a positively charged and negatively charged vacancy were also considered and their formation energy diagram is given in Fig. 9.6a. The lowest energy vacancy was found to be in the neutral charge state and the $\epsilon(0/-1)$ transition level was found at 0.5 eV above the VBM, where the negative charge state becomes energetically more favourable. However, the negatively charged defect adopts a different geometry as shown in Fig. 9.5b, where a P atom becomes sp^3d^2 hybridised. This allows it to bind to four neighbouring P atoms in a planar configuration, similar to the molecular structure of PF_6^- for example. The IPR spectrum and density of states of this defect are shown in Fig. 9.6c. The empty state in the minor spin channel of a neutral MV gets populated. This now doubly filled state sits at the VBM and both band edges show a more localised character in IPR analysis. The localised state in the conduction band can be attributed to an anti-bonding state between the four-coordinated P atom and its four nearest neighbours. The localised state near the VBM is a non-bonding state and the localised state deeper into the valence band is a bonding state between the four-coordinated atom and its four nearest neighbours. The additional potential of the negative charge leads to more localisation of deeper band states as well, which is due to constraints of the simulation cell. We note that the IPR analysis allowed us to easily identify defect-induced localised states, which would otherwise be a tedious manual checking process through all states.

The charge state of the vacancy is determined by the position of the Fermi level. As shown in Fig. 8.5 the VBM is at -5.5 eV (monolayer), but is raised to -5.1 eV for a four layer slab. Interestingly, the vacancy induced band gap level does not shift with increasing layer number and sits at the top of the valence band for a 4 layer slab system. Thus, less energy is required to excite an electron into the defect state and create a hole at the VBM, effectively p-doping the system. For a four layer slab the acceptor state is only 0.05 eV above the VBM, which is shallow enough for an electron to be excited into thermally.

The trapped electron at the MV will induce an additional electrostatic potential, which in turn induces additional states in the bandgap of BP. This can be described

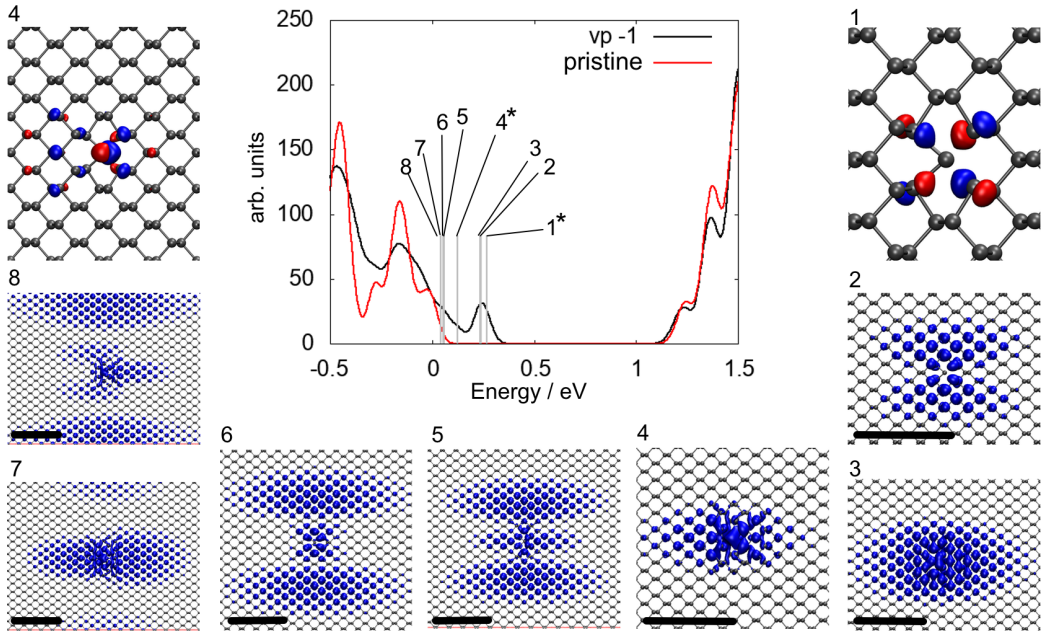

Figure 9.7: DOS of non-defective BP monolayer (red) and of a monolayer containing a negatively charged MV (black). States deeper in the valence band were used to align the two DOS plots and the x-axis is set to zero at the VBM. Additional states in the negatively charged MV plot are indicated by grey bars and their squared wave-functions are illustrated. The black scale bar equals 2 nm. State 2 represents a bonding state between the Sn atom and its nearest neighbours, where red and blue indicate the different phases of the wavefunction to illustrate the nature of the bonding orbital.

by a 2D hydrogen model of a bound electron-hole pair.[243,244] Defect states due to localised bound carriers have previously been reported in MoS_2[245] and graphene.[246] Fig. 9.7 illustrates the defect induced states for a negatively charged MV. State 1 and 4 are not induced by the electrostatic potential of the bound charge, but are due to the orbital bonding of the relaxed P atom to its neighbours. State 1 is a non-bonding state, which is located at 0.28 eV above the VBM and state 4 is a bonding state 0.14 eV above the VBM. States 2, 3, 5, 6, 7 and 8 are hydrogenic states, which show characteristic delocalised wave-functions. Interestingly, the order of states is changed, such that the sequence is $2p_y$, 1s, 2s, $3p_y$, $2p_x$. State 8 shows spacial anisotropic character, which makes it difficult to match a 2D hydrogenic state. Similarly, the s-states show discontinuous electron density along the

ac-direction in the outer lobes and are elongated along the ac-direction. This is possibly due to the anisotropic dielectric constant and electron/ hole masses along the ac- and zz-direction.

While the hydrogenic model is a convenient analogous system, it has its shortcomings. The order of states, the missing degeneracy of (2n+1), where n is the principal quantum number, as well as the absolute energy hierarchy of BP does not match the 2D hydrogenic model. Furthermore, the states are very extensive, which means interactions between the periodic images can shift the kinetic energy of states. However, hybrid functionals in DFT become excessively expensive to compute for large systems. It has previously been demonstrated that well parameterised tight binding calculations can be employed to study systems of >5000 atoms.[245] Furthermore, from Equation 8.4 it can be seen that the energy of the states depend on the dielectric ϵ of the material, as well as on the reduced mass of the electron hole pair. As shown in Fig. 9.4 the hole masses are anisotropic, which leads to anisotropic defect states. This difference in screening and effective masses is not well reproduced in the 2D hydrogen model.

Tersoff-Hamann (TH) simulations were employed to convert these wavefunctions into virtual STM images, as shown in Fig. 9.8. At +0.2±0.05 V bias no contrast is obtained from the pristine BP surface and the defect appears oval with a very bright centre. At lower bias (0 ±0.05 V) current is obtained from states at the VBM as well as the defect states. Thus, the image shows overall brighter contrast. The defect appears as three elongated bright features with a bright centre. These simulated TH images do not compare well with STM data (see section 9.2.1). The initial asignment of MVs to observed defect states in STM was done on the basis of wavefunctions of unrelaxed MVs. This is a poor description of the structure of the MV. Furthermore, while we do find states which resemble observed features in STM, other defect states lie very close in energy. Thus, in STM as well as in the TH model current is measured from several states in a narrow energy range simultaneously, giving rise to a convolved current contrast. Therefore, the p_x state is overpowered by contrast from the other states, that are almost degenerate with

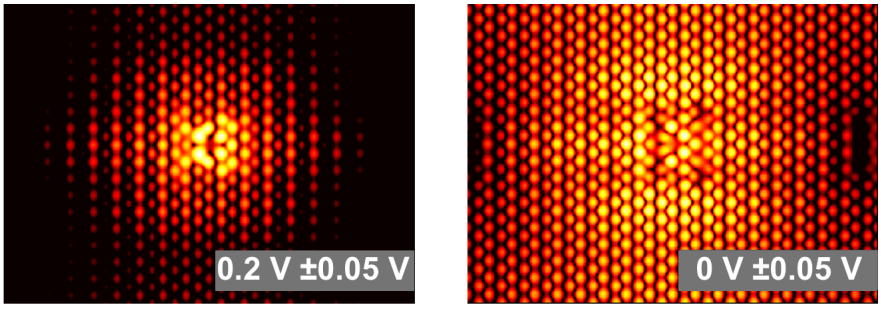

Figure 9.8: Simulated TH-STM images of a negatively charged MV in monolayer BP at selected biases. (dark=low current, white=high current)

it.

9.3.3.2 Divacancies

Due to the covalent bonding in BP, many DV structures exist, where two phosphorus atoms are missing in close proximity creating a bigger defect complex. The most energetically stable DV structure is shown in Fig. 9.9a. As in the MV case, the atoms next to the empty lattice sites relax in order to compensate dangling bonds and form a 5757 defect structure such that all atoms become three coordinated. Interestingly, a 5757 DV has a much lower DFE at 8.02 eV than a sum of two MVs and thus two mobile MVs are expected to coalesce to form the DV.

Apart from the 5757 vacancy, several other metastable structures were found and are shown in Fig. 9.9b-h. The 585-A DV has a DFE close to the 5757 one at 8.21 eV and is also more stable than two isolated MVs. Previously, this vacancy was reported to be the most stable DV structure,[219,241] but recent reports[218,219] as well as this work support the observation that the 5757 structure is lower in energy. The 555777 DV shown in Fig. 9.9c represents a more complex DV structure and with a formation energy of 9.36 eV is still more favourable than two separate vacancies. Similar to structures a and b, the atoms relax to compensate any dangling bonds created during vacancy formation such that all atoms are three coordinated. The 5555-6-7777 DV is very similar to the 555777 one and differs in just a rotation of a P-P bond, similar to a Stone-Wales defect. This DV configuration was found to have a formation energy of 8.44 eV.

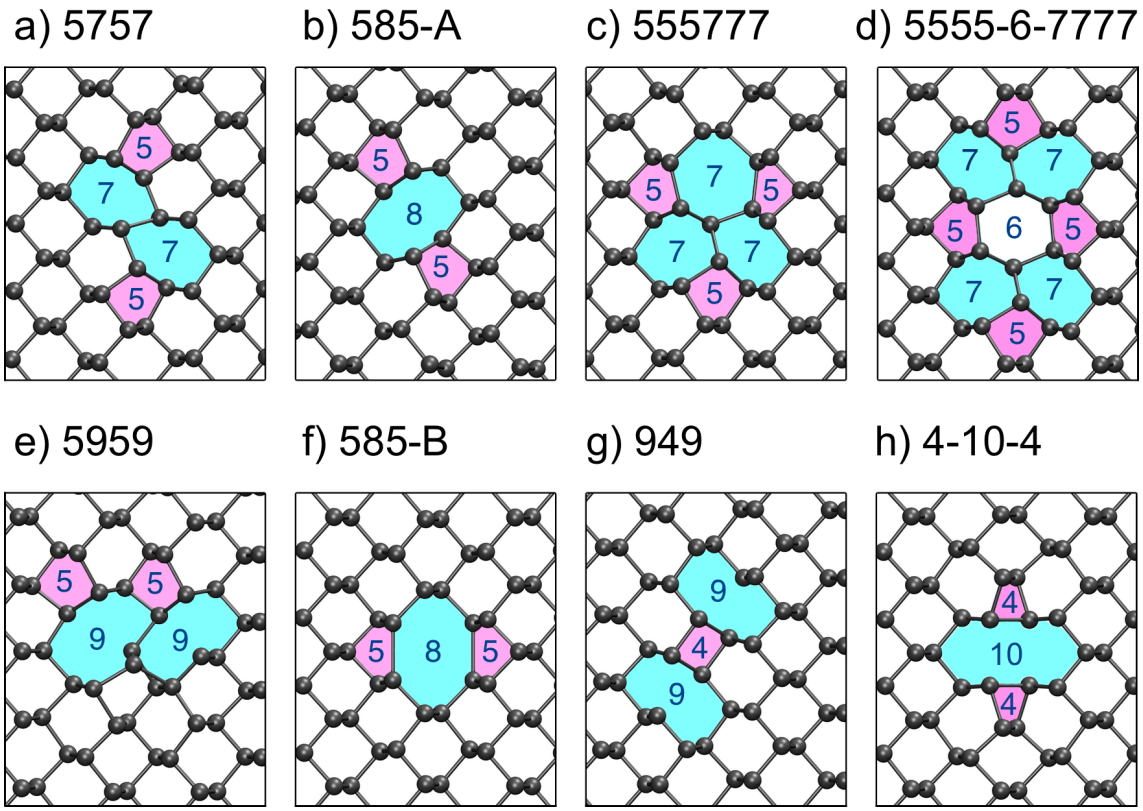

Figure 9.9: a-h) Geometric structure of eight DVs in monolayer BP. The DVs are coloured in as a visual aide and numbered according to how many atoms constitute a ring structure.

We note that the ordering of the defect structures compares well with previous results;[218,219] however, values of DFE in the second and forth column of Table 9.1 show small differences. These may result from different DFT functionals used, calculation set-up, basis set and code. Furthermore, BP is considered to be "soft" due to its low Young's modulus (166GPa and 44GPa along zz and ac, respectively) and thus strain due to defects in relatively small simulation cells and electrostatic interactions between periodically translated defects can lead to observed shifts in calculated formation energies. Unlike a MV, the lowest energy DVs do not create any KS states in the band gap.

9.3.3.3 Other Intrinsic Defects

Besides MVs and DVs, BP can also exhibit other structural defects, such as Stone-Wales-like defects or self-interstitials shown in Fig. 9.5c+d. An extra P atom adopts

an interstitial position between a P atom on an upper zigzag and a P atom on a lower zigzag by breaking the up-down P-P bond and is thus two fold coordinated. The formation energy of a P_i is -1.35 eV in a monolayer. Since one bond is broken and two new ones are formed, the energy can be compared to a P-P bond energy of 2.17 eV in pristine BP. The difference of 0.48 eV is attributed to surface deformation around the interstitial. Interestingly, the adsorption energy of a P adatom on a BP monolayer is lower than that of the self-interstitial by about 0.3 eV and thus, given the activation energy can be overcome, P interstitials will be converted into P adatoms. The barrier for P adatom diffusion along the zz direction is only $\sim$0.15 eV leading to fast diffusion across the surface at room temperature. Thus, surface adatoms can potentially passivate surface MVs or DVs. The aggregation of several P adatoms into bigger clusters was not investigated here.

Stone-Wales defects have previously been reported for graphene[247,248] and theoretical calculations predict their existence in BP as well.[233,241] SW defects require a change in connectivity of two atoms via a rotation of a P-P bond, which is highlighted in red in Fig. 9.5c+d. The formation energy of SW1 defect is 1.81 eV and of SW2 defect is 0.9 eV, which, unlike the MV case, does not rely on the choice of chemical potential for phosphorus, since no atoms are added or removed and thus can be used to compare different theoretical calculations. Reported values for the SW1 defect range from 0.84 eV to 1.62 eV,[219,233,241,249] highlighting a large spread in calculated DFEs, which arises from different DFT functionals, codes and calculation parameters (e.g. supercell size). The SW2 defect has the lowest DFE of the intrinsic defects considered and is thus expected to be the dominant defect formed.

In order to investigate the formation mechanism of SW defects, nudged elastic bands calculations (NEB) were performed. The forward barrier to form a SW1 defect is 3.08 eV and 2.17 eV for SW2 defect and the reverse barriers are 1.27 eV and 1.25 eV for both SW defects, respectively.

Combining the DFE for a MV and a P self-interstitial results in a Frenkel pair formation energy of 3.38 eV. A MV and a P adatom also form a Frenkel pair with a DFE of 3.08 eV. These energies are independent of the choice of chemical poten-

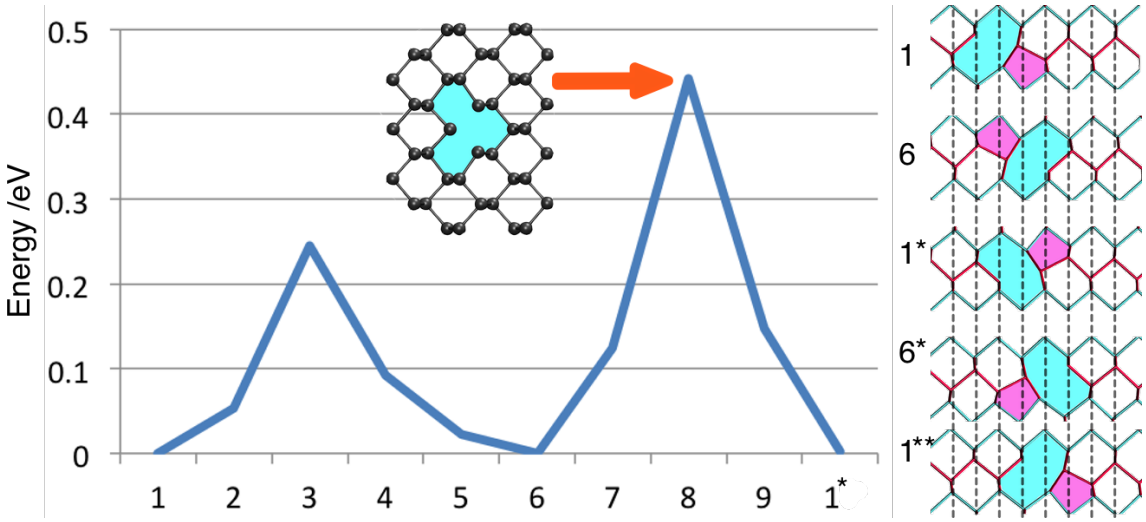

Figure 9.10: Diffusion barrier for a neutral mono-vacancy in single layer BP. The inset shows the transition structure. On the right the geometry of the vacancy at each minima in the diffusion path is illustrated. Note the asterisk signifies a commensurate structure translated by half a unit vector and two asterisks denote a commensurate structure after translation by a whole unit vector. Red lines represent the upper and blue lines the lower zigzag. The 5 and 9 member rings are coloured in pink and cyan as a visual aid.

tials used and can be directly compared to the formation energy of a Stone-Wales defect. At equilibrium conditions Frenkel defects are less favourable than SW defects. Formation barriers for both defects are too high for them to be formed in high concentrations at room temperature. Instead, they can be created under high-temperature non-equilibrium growth conditions.

9.3.4 Diffusion of Mono-vacancies in BP

Since DVs are more stable than MVs in monolayer BP, they can form upon collision of two diffusing MVs. In order to study the diffusion barrier and consequently the rate of diffusion of MVs in monolayer BP, NEB calculations were performed. In Fig. 9.10 the diffusion barrier is plotted for a neutral vacancy diffusing along the zz-direction. As previously reported in ref.,[218] diffusion of MVs was confirmed to be a two step process, however, the absolute barrier height for the same diffusion path was found to be about 0.1 eV larger. The first diffusion step involves a change in connectivity in the upper zigzag by moving a P atom 0.9 Å along the zz-direction and has an associated barrier of 0.25 eV (going from configuration 1 to 6 in Fig. 9.10).

The rate determining process involves a change of connectivity in the lower zigzag and has a higher barrier of 0.44 eV associated with it. Going from configuration 1 to 1^* corresponds to a translation of the vacancy by half a surface unit vector along zz and from 1 to 1^{**} corresponds to a translation of the vacancy by one whole unit vector.

As shown in the inset, the transition point structure is different to the symmetric structure found for the negatively charged vacancy (Fig. 9.5b). In the latter case, the central P atom becomes four-fold coordinated and sits in between the upper and the lower zigzag. The transition structure, however, does not show this relaxation of the central P atom and instead resembles an unrelaxed MV. In fact the four-fold coordinated geometry in its neutral charge state would be 0.1 eV higher in energy than the transition structure, which is in good agreement with ref.[218] Interestingly, the barrier is unchanged for a positively charged vacancy but is significantly reduced for a negatively charged vacancy. Due to the different bonding behaviour of the negative vacancy, the barrier for diffusion is lowered to ∼0.07 eV along the zz-direction. Hence a negatively charged vacancy is expected to be significantly more mobile than a neutral or positively charged vacancy. The calculated diffusion barriers E_B can be translated into hopping rates ν using an Arrhenius equation:

$$\nu = \nu_0(T) \exp^{\frac{-E_B}{k_B T}} \quad , \tag{9.2}$$

where ν_0 denotes a prefactor related to the hopping distance and attempt frequency as a function of temperature T and k_B is the Boltzmann constant. The prefactors were calculated by Cai et al.[218] employing the Vineyard method, which uses vibrational analysis to estimate attempt frequencies. Using Eq. 9.2 the hopping rates of a MV calculated at temperatures of 10 K, 70 K and 300 K are shown in Table 9.2. These three temperatures correspond to typical experimental conditions (liquid helium cooled, liquid nitrogen cooled and room temperature). At 10 K a MV in a monolayer of BP will be practically immobile as hopping rates for all three charge states are very low. Thus, these vacancies would be stable enough to be imaged

Temperature K	prefactor s^{-1}	neutral MV hopping rate s^{-1}	negative MV hopping rate s^{-1}
300	1.63E+11	4.49E+03	1.09E+10
70	3.81E+10	1.34E-19	9.98E+05
10	5.44E+09	1.30E-324	2.18E-41

Table 9.2: Hopping rates of neutral and negatively charged MVs along with their respective prefactors, which were adopted from Cai et al.[218]

using scanning probe techniques such as Atomic Force Microscopy (AFM) or STM. At 70 K the hopping rate for a positively charged or neutral vacancy is of the order 10^{-19} s^{-1} and the vacancies will still be immobile in experimentally relevant time scales, however, the hopping rate of a negatively charged vacancy is about one million hops per second and thus this vacancy is too mobile to be observed in scanning probe measurements. At room temperature, both vacancy states show very fast hopping rates, thus MVs will be diffusing at high rates on the surface of BP and coalesce into DVs upon collision. The defect concentration observed in STM is around 60 ppm,[250] which is roughly one defect every 80 lattice sites. At hopping rates of the order 10^3 s^{-1}, the probability of two MVs colliding rapidly converges to one, as the diffusion process can be treated as a Markov chain. Assuming diffusion is a random walk with RMS displacement of $\sqrt{N}$ (N = number of hops) one can easily deduce that at room temperature on average it takes two seconds for two neutral MVs to collide.

9.4 Discussion

In order for BP to make the transition from research laboratories to everyday devices, its physical properties need to be better understood. In particular point defects play a crucial role in device stability as well as carrier mobility and are still subject to extensive research.

Typically, concentrations of at least 10^{18} cm^{-3} are needed to observe doping in semiconductors and p/n-doped BP has been reported with doping concentrations of around 10^{15} cm^{-3}.[251] Experimentally observed p-doping as well as observed defects

in STM have previously been attributed to MVs.[217] However, the origin of MVs is unclear. Their DFE is too high to be created thermally at large concentrations. MVs have low diffusion barriers and therefore can migrate and be captured by other point or line defects. Thus any MVs created during the crystal growth process have ample time to find a lower energy structure. We have shown that a MV can coalesce with another MV to form a considerably more stable DV, which does not have an acceptor state associated with it. To date there are no experimental reports of DVs on the surface of cleaved BP from scanning probe measurements, impugning the interpretation that MVs are the dominant defect.

At room temperature concentrations of thermally created defects such as Frenkel pairs and SW defects are expected to be low due to their high DFEs. Thus, observed defects in experimental studies are likely defects, which are grown in during the crystal growth process. Since this is a non-equilibrium process, determination of accurate chemical potentials and reaction pathways is difficult. Therefore, the calculated DFE give insight into which defects are likely, but cannot be used to derive accurate defect concentrations. For example the barrier for a SW2 defect to reform into pristine BP is 1.25 eV, which means at room temperature the rate of SW annihilation is low. Thus if a SW defect is created during the crystal growth process, it will be stable at room temperature. A detailed experimental study of defects pre and post sample anneal could be informative to investigate recombination or defect annihilation and mobility processes.

Furthermore, STM experiments reveal extensive defect states at the surface of a cleaved BP crystal. The defect appearance can be categorised in two kinds, a p-orbital like state and an s-orbital like state (see 9.2.1). When scanning at a bias that resonates with states in the valence band, the defect appears p-like, whereas at a bias in resonance with the valence band edge the defect switches to an s-like appearance.

A negatively charged MV induces such states in the bandgap of BP. At lower bias (more negative) electrons can tunnel into the STM tip-states from the $2p_x$ state, as well as other states that are very close in energy ($<$0.05eV), which are located

at the VBM. This will give rise to a convolved current signature, as can be seen in Fig. 9.8.

As the bias is increased the tip states resonate with the 1s and $2p_y$ states, which are separated by only 0.003 eV. Therefore, a convoluted current contrast is observed again, due to a superposition of these two states (see Fig. 9.8). As the bias is increased even further such that the Fermi level of the tip is above the CBM of BP, empty states are imaged. The density in the conduction band around the defect appears to be locally depleted as indicated by a dark halo around the defect (see Fig. 9.1). The same feature can be observed in calculations of a negatively charged MV, where the CBM displays lower density in the vicinity of the defect. However, it is unclear where the observed bright contrast in the middle of the dark halo originates from, since calculations of MVs do not indicate any additional states at the CBM.

9.5 Conclusions

In summary, the electronic and geometric structure of a range of intrinsic defects were calculated and compared with experimental observations. Amongst the compensated defect structures, SW defects have lower DFE than Frenkel pairs and are thus predicted to be the dominant intrinsic defect. However, formation barriers are high, preventing high concentrations of SW defects to form at room temperature.

Consequently, experimentally observed defects are likely to originate from the crystal growth process. Since this is a non-equilibrium process, high energy defects can be formed and frozen into the crystal, if defect annihilation barriers are high. Thus, MVs could be formed during high temperature growth conditions. However, MVs were found to be metastable in BP, since DVs have lower DFEs. Various low energy DV structures were found. These DVs do not have any dangling bond and thus are electronically inactive, i.e. do not favour to accept or donate an electron. DV do not reproduce the observed defect state in the bandgap of BP, nor the hydrogenic states observed in STM. Low diffusion barriers make vacancy coalescence viable above liquid nitrogen temperatures, where hopping rates are high.

A negatively charged MV induces hydrogenic states near the VBM, which match experimentally observed states in STM measurements. However, the states are bunched closely together, such that simulated STM images reveal current from several states simultaneously. Therefore, the isolated p_x- and the s-state cannot be resolved and the simulated STM images do not match experimental ones. Furthermore, these hydrogenic states are expected to form for any localised bound charge, and thus are not exclusive to MVs. Therefore, in the next chapter experimentally observed extrinsic impurities are investigated.

Chapter 10

Characterisation of Extrinsic Defects in Black Phosphorus

10.1 Introduction

Similar to Si, BP can be n-type and p-type doped, which is particular interesting for future transistor applications.[207] Doping refers to the process of introducing impurity species into a semiconductor in a controllable manner in order to alter its electrical properties. Through dopants the carrier concentrations, i.e. electrons or holes, can be controlled, but other properties such as thermal conductivity, magnetisation and optical properties can also be affected. Varying the concentration of dopants spatially can be used to create pn-junctions or to introduce intrinsic electric fields. Furthermore, within the past decade the identification of effects due to a single dopant atom has been achieved, which opened the new field of solotronics.[252, 253]

Studies of the Seebeck effect and measurements of the electrical conductivity and the Hall effect in bulk BP indicate inherent p-type doping,[254, 255] yet its source is unknown. Intrinsic defects such as mono-vacancies have been proposed[217] as well as extrinsic impurities such as Sn.[225, 256]

Intentional doping of BP has been shown to lead to p- and n-type BP. For example tellurium and silver act as shallow donors in BP, leading to n-type conductivity.[255–257] Similarly, alkali metals act as shallow donors, transferring their s-electron to the conduction band of BP.[257–259] Interestingly, intercalating Na leads to a change in staking order of the BP layers, indicating that doping can also be used to alter the structure of BP crystals.[260] Experimentally it was shown that Cu

adatoms lead to n-doping as they act as shallow donors.[261] P-type doping was also reported in an experimental study for functionalising BP with MoO_3[262] as well as in theoretical work for nitrogen substitution.[263]

Furthermore, transition metals (TMs) have been reported in significant concentrations in BP samples[230] and are prime candidates for magnetic functionalisation of BP. The unpaired electrons of Fe impurities for example lead to an overall magnetic response of Fe doped BP samples: a recent experimental report found Fe doped BP crystals ($Fe_{5\%}P_{95\%}$) exhibit paramagnetism at room temperature.[264] Theoretical calculations predict that the spin state of a Mn adatom can be switched by applying strain, resulting in a strain-tuning spin switch.[265,266] TM adatoms have also been reported to enhance carrier mobilities and improve the stability of BP under ambient conditions, two crucial properties to enable the integration of BP in future technologies.[267]

In this study a wide range of extrinsic defects in BP are investigated, particularly with respect to their effect on the electronic structure of BP. Dopants considered include oxygen, I and Sn as well as the transition metals (TMs) Fe, Ni, Cu and Zn. The choice of impurity considered was driven by experimental reports of these elements. Oxygen is highly reactive with BP and clean BP samples oxidise quickly in an oxygen rich atmosphere.[213] Sn and I are present in the synthesis of BP crystals[232] and are reported together with TMs (Fe, Ni, Cu, Zn) in plasma mass spectrometry experiments.[230] Transition metal impurities are particularly interesting for magnetic functionalisation of BP, which will also be briefly discussed.

10.1.1 Principle of Doping

For an intrinsic semiconductor, the concentration of charge carriers is dependent on the density of states at the VBM and the probability to excite an electron across the bandgap, which can be modelled by a Fermi-Dirac distribution. The number of conduction band electrons is equal to the number of holes in the valence band. In order to increase the carrier concentration in the valence or conduction band, extrinsic doping can be employed. The introduction of suitable dopants can lead to additional states in the bandgap of the semiconductor. If a state is empty and lies

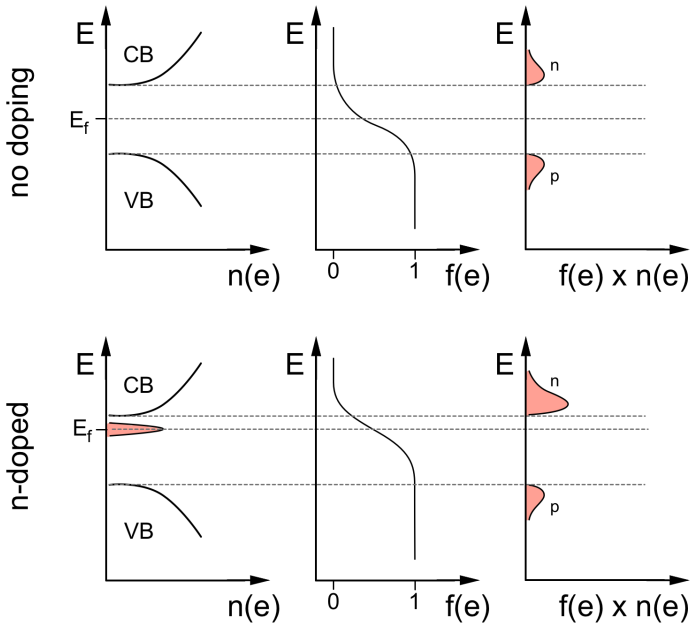

Figure 10.1: Illustration of the basic principle of doping: n(e) denotes the density of states; E_f is the Fermi level; CB and VB denote the conduction and valance bands, respectively; f(e) represents a probability distribution at temperature T and n and p the concentration of electron carriers and hole carriers, respectively.

close to the valence band, an electron can be excited into the state creating a hole carrier in the valence band. Similarly, an occupied state near the conduction band edge can get ionised, creating an additional conduction band electron. Fig. 10.1 illustrates this basic principle for a shallow donor state. Ideally the binding energy of defect induced states in the bandgap are a few tens of meV, such that they can be thermally ionised. States that lie deep in the bandgap are unfavourable as they require photon-assisted excitations and can contribute to carrier recombination via the two step Shockley−Read−Hall process for example. In the following section various defects will be investigated with respect to their influence on electronic and magnetic properties of BP.

10.2 Results

XPS and inductively coupled plasma mass spectrometry (ICP-MS) measurements indicate significant impurity concentrations of Sn and I, as well as Ni, Zn, Fe and Cu

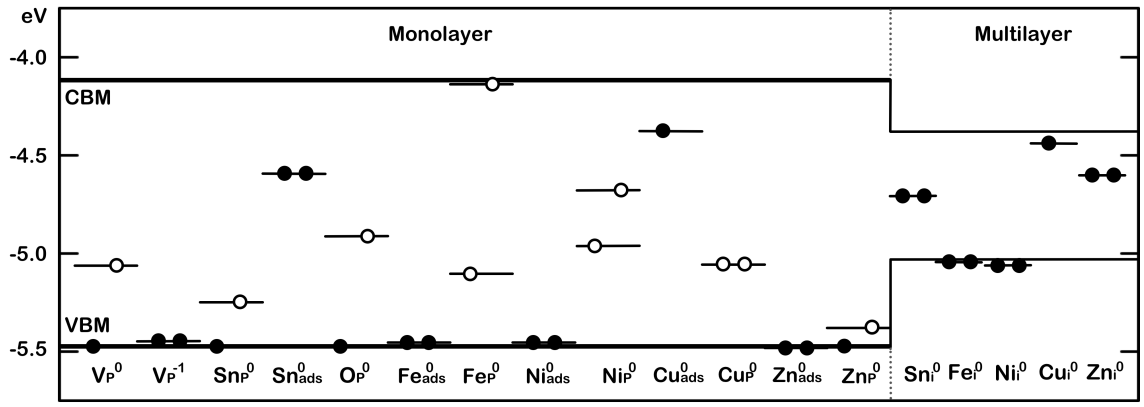

Figure 10.2: Schematic illustrating the defect induced Kohn-Sham states in the bandgap of BP. Filled circles indicate a filled state and empty circles an empty state, while a circle on the right/ left indicate the spin up/down channel. All energies are referenced to the vacuum level (0 eV). The energies for mono-vacancies (MV) are taken from Chapter 9

in lower concentrations.[230] Since it is not well understood how they get incorporated in BP, these impurities were investigated in substitutional, intercalated and surface adsorbed geometries. An overview of calculated defect formation energies is given in Table 10.1 and Fig. 10.2 illustrates defect induced states in the bandgap of BP.

10.2.1 Iodine Defects

I adsorbs on the surface 2.74 Å above a P atom lattice site with an adsorption energy of 0.30 eV. Since the I chemical potential was chosen to be the energy of half an I_2 molecule, the adsorption energy indicates it is unfavourable to break the I-I bond and adsorb on BP.

I was also investigated as a substitutional defect. Interestingly, a I_P^0 defect relaxes into a 59 MV with I binding to the 2 coordinated P atom and sticking out of the surface plane (see Fig. 10.5). The neutral charge state was found to be lowest in energy for all Fermi level positions throughout the bandgap and no bandgap states were created upon forming this defect. The DFE for I_P^0 was calculated to be 1.39 eV. Bader analysis shows almost no charge transfer between I and the BP lattice, indicative of a covalent bond between P and I.

Furthermore, the intercalation energy for a single I atom was calculated at 2.47 eV. The relatively large I atom is not favourable to intercalate between the BP

layers due to electronic overlap resulting in large lattice deformations (see Fig. 10.5). Whether a larger concentration can lead to a change in interlayer spacing or a change in stacking order, as has been reported for Na intercalation,[258] was not investigated.

Summary of Defect Formation Energies / eV			
element	adsorbed Energy /eV	substitutional Energy /eV	intercalated Energy /eV
O	-2.00	-0.38	-1.91
I	0.30	1.39	2.47
Sn	-2.76	-3.28	-1.82
Fe	-2.25	-2.52	-2.57
Ni	-3.07	-2.62	-3.93
Cu	-1.96	-2.20	-2.85
Zn	-0.20	-0.49	-0.17

Table 10.1: Formation energies for experimentally observed impurity elements in adsorbed (ML), substitutional (ML) and intercalated geometries (centre of 4L slab).

10.2.2 Tin Defects

Fig. 10.5 illustrates a Sn_P defect geometry. Unlike an I defect, the lattice around the substitutional Sn atom is very little perturbed, as Sn occupies a P lattice site with a slight relaxation of about 0.3 Å out of the surface plane. Since Sn is sp^3 hybridised and therefore four-valent and P is five-valent, a hole is induced at 0.26 eV above the VBM (see Fig. 10.2). IPR analysis reveals the hole is localised on the Sn atom, which is bonded to two upper layer P atoms and one P atom in the lower layer in a distorted tetrahedral configuration. The defect formation energy was calculated to be -3.28 eV for a neutral Sn_P and a CTL from neutral to the -1e charge state was found at 0.33 eV above the VBM. Since the P chemical potential is P in monolayer BP, the DFE can be compared to the cohesion energy of a P atom in BP, which is -3.25 eV. Since these two energies are very close, we predict Sn_P defects to form readily, given Sn atoms are present in the gas phase.

Substitutional Sn impurities were also investigated at various depths in a four layer slab, in order to gain insight into the defect behaviour as it is moved into the

slab approaching the bulk limit. A four layer slab consisting of 1296 atoms was doped with a single Sn atom in the upper row of the top layer, in the bottom row of the topmost layer and similarly in the second layer. The defect formation energy displayed a slight trend to lower energies as the Sn impurity was moved into the slab. An impurity in the top row of the top layer has a DFE of -3.50 eV, while the DFE for the second layer was reduced to -3.56 eV, indicating that substitution is marginally favoured in the bulk material compared to the surface. A substitutional Sn in the top row of the top layer of a four layer slab creates an acceptor state 0.15 eV above the VBM, which moves to 0.12 eV for the bottom of the top layer and ultimately to 0.05 eV for substitutional Sn in the top row of the second subsurface layer. This illustrates that the acceptor state in the bulk is more shallow than the acceptor state for the same defect on the BP surface.

The hole state can become filled by an applied external electric field and thus shifting the Fermi level or by exciting an electron into it from the VBM. Similar to the negatively charged MV, such a system can be approximated by the 2D hydrogen atom model. Fig. 10.3 illustrates the defect induced states at the top of the valence band. State 2 is a bonding state between a hybridised sp-orbital on Sn with p-orbitals of two neighbouring P atoms. As can be seen by the illustrated squared wavefunction, this state is much more localised than the other defect induced states. The additional states (1,3-7) are due to the electrostatic potential of the trapped charge. Interestingly, while the order of these states is different compared to the negatively charged MV, the overall shape of the states is comparable. This is not surprising, since in both cases the states are induced by the tapped electron and the long range nature of these states means that they experience the same long range screening.

The energetically highest state is a 1s-type state, which sits 0.5 eV above the VBM. The series continues with the bonding state, a $2p_y$, 2s and $3p_y$ state. The $2p_x$ state is located just below the VBM of pristine BP and shows some density at the edge of the simulation cell, which is attributed to constraints due to the supercell used.

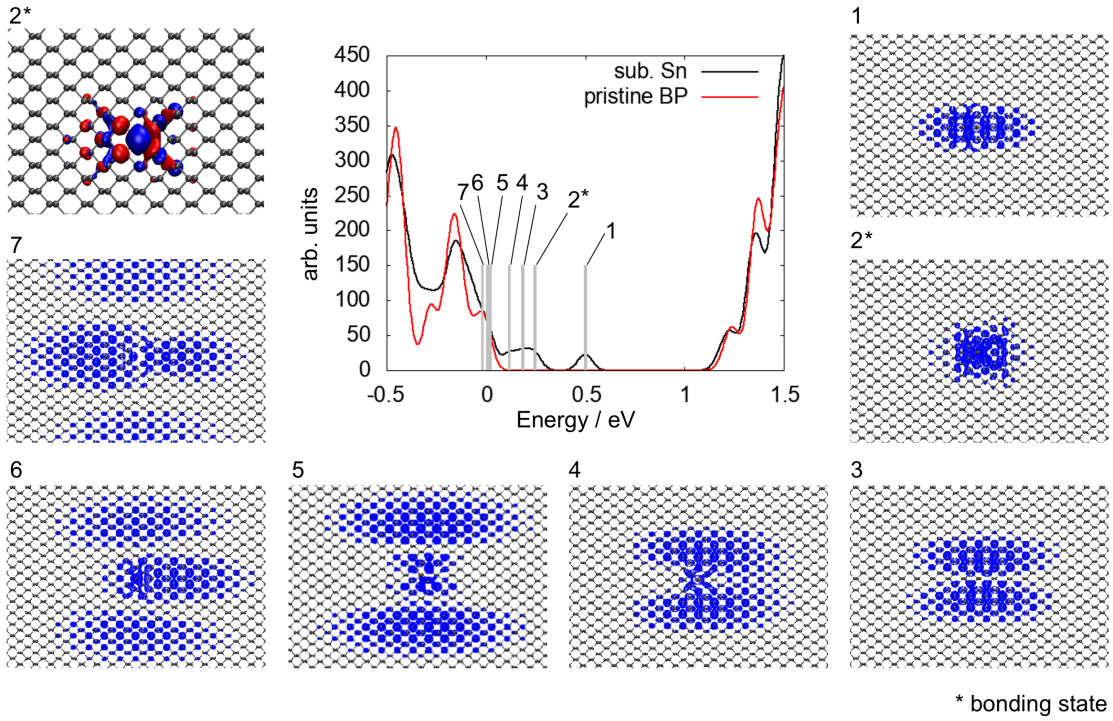

Figure 10.3: DOS of non-defective BP monolayer (red) and of a monolayer containing a negatively charged Sn_P defect (black). States deeper in the valence band were used to align the two DOS plots and the x-axis is set to zero at the VBM of pristine BP. Additional states in the negatively charged defect plot are indicated by grey bars and their squared wave-functions are illustrated. States 1 and 4 represent a bonding and a non-bonding state between the relaxed P atom and its nearest neighbours, where red and blue indicate the different phases of the wavefunction, in order to illustrate the nature of the bonding orbital.

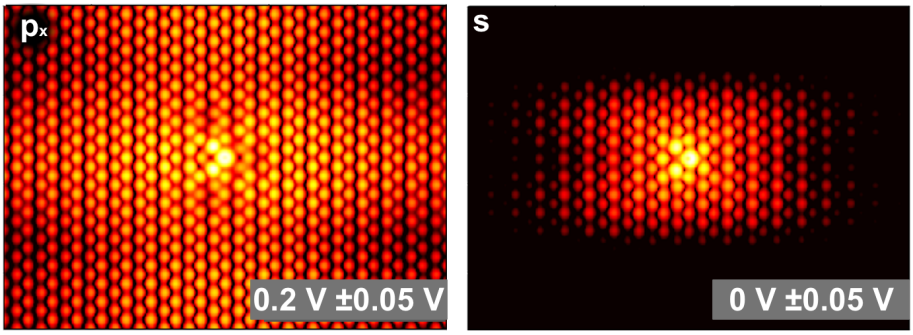

Figure 10.4: Simulated TH-STM images of Sn_P defect in monolayer BP. (dark = low current, white = high current)

Again a Tersoff-Harman (TH) model can be used to transpose wavefunctions into simulated STM images, which can then be compared to experimentally obtained images. Fig. 10.4 illustrates images obtained at bias 0V ± 0.05V and 0.2V ± 0.05V, respectively. The p-type and s-type states can clearly be identified. Since the p_x-state sits just at the VBM, a higher current is observed around the defect compared to the s-state, which sits in the bandgap and thus the surrounding BP layer does not conduct at that bias. It is worth noting that the current contrast is very sensitive to the bias setpoint, since the defect induced states are very close in energy and small changes in setpoint can change which states are being imaged. Particularly near the VBM the states are very close in energy and thus a convolution of states will contribute to the total current.

Adsorption of Sn was found to be less favourable than substitution, with an adsorption energy of -2.76 eV. Sn adsorbs 1.95 Å above the surface on top of a valley site, binding to two surface P atoms (see Fig. 10.5). A donor state is created in the bandgap of BP 0.43 eV below the CBM, as indicated in Fig. 10.2.

Lastly, intercalated Sn was investigated, with the atom placed at various positions between the second and third layer of a four layer BP slab. Sn adopts a four valent geometry, bonding to two P atoms of the upper and lower layer, respectively (see Fig. 10.5). However, the BP lattice displays large displacements around the intercalated Sn, resulting in a DFE of -1.82 eV. A donor state is induced in the bandgap of BP, 0.26 eV below the CBM, which is localised on Sn. Thus, substitutional Sn acts as an acceptor, while adsorbed and intercalated Sn act as electron donors.

10.2.3 Transition Metal Defects

Four transition metals (TM) were also considered, namely Fe, Ni, Cu and Zn. These impurities were investigated in three configurations: Adsorbed on a monolayer surface, as a substitutional defect in a monolayer and intercalated between the second and third layer of a four layer slab. A summary of DFEs is given in Table 10.1 along with the atomic structure in Fig. 10.5. Comparison of absolute DFEs of different impurity species is difficult, since they depend on the chemical potential used in the

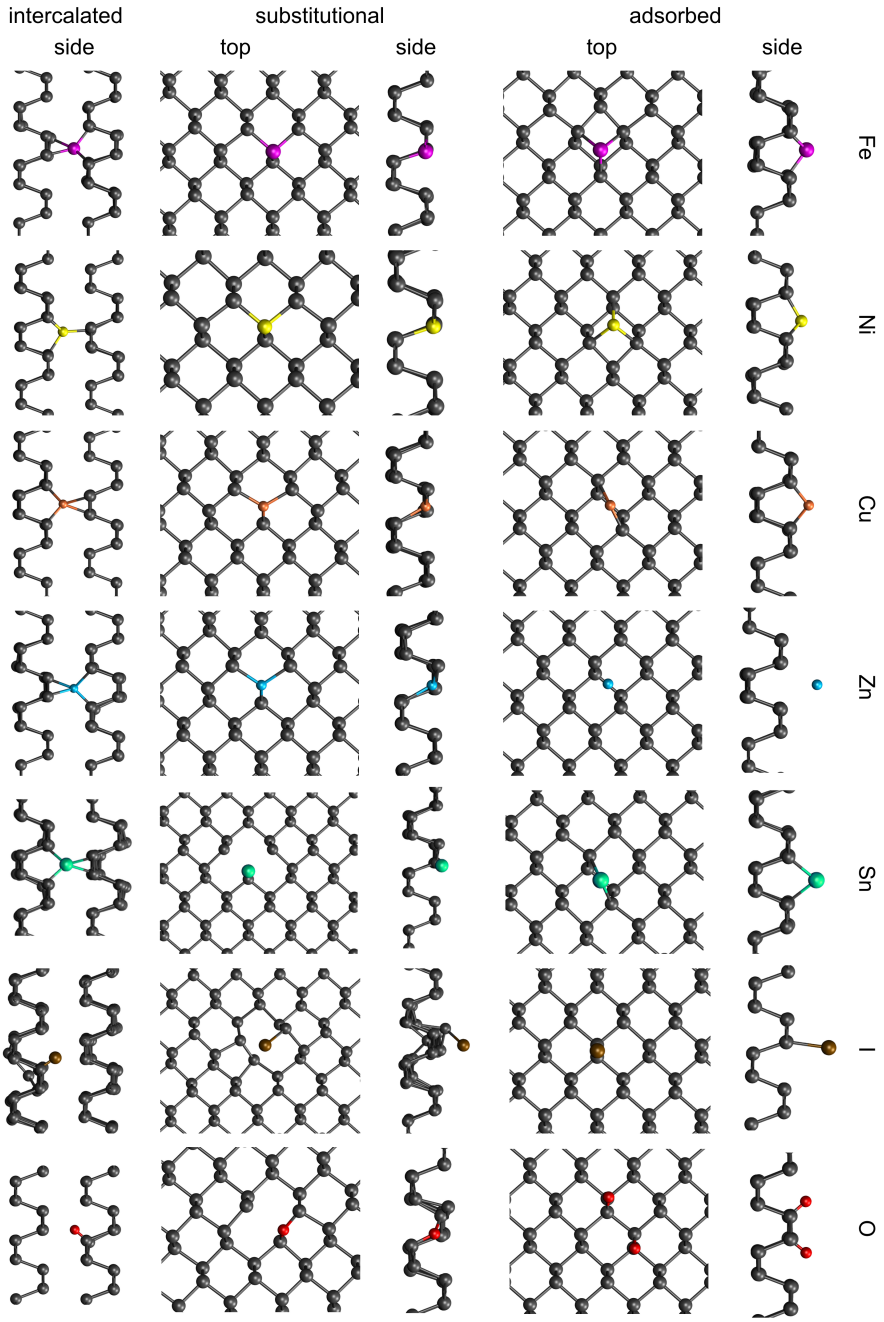

Figure 10.5: Summary of impurity defects in BP. Geometries are shown for Fe (magenta), Ni (yellow), Cu (orange), Zn (cyan), Sn (green), I (brown) and O (red) in adsorbed (top), substitutional (middle) and intercalated (bottom) configurations in side and top projection. (Grey = P)

calculations, whose exact determination is difficult. Intercalated TMs constitute the lowest energy configuration for the open shell elements Fe, Ni and Cu, while Zn preferentially sits in a substitutional configuration.

10.2.3.1 Intercalated TMs

Upon intercalation, the TM's 4s electrons get promoted to the 3d orbitals. For Cu and Zn the 3d shell is completely filled and thus electrons populate the radially more extensive 4s orbital. This rearrangement of electrons further leads to changes in the magnetic moment of Ni and Fe. Since the 4s electrons completely fill the 3d orbitals in Ni defects, Ni adopts a low spin singlet state. Similarly Fe changes from four unpaired electrons for the isolated atom to a triplet state in BP, where the high spin quintet state is 0.24 eV and the singlet state is 0.6 eV higher in energy than the triplet state and thus Fe_i is predicted to possess a magnetic moment of 2 μ_B, which is in line with observed paramagnetism for Fe doped BP.[264] Whether the spin arrangement for higher TM concentrations leads to different magnetisation such as a ferromagnetic state was not investigated in this work. Therefore, the results presented herein refer to low doping/impurity concentrations. Intercalated Fe does not induce and states in the bandgap of BP, but instead creates a filled state at the VBM, as illustrated in Fig. 10.2. Similarly, intercalated Ni creates a filled defect level just below the VBM, preserving the semiconducting nature of BP. Adding one more valence electron, Cu induces a filled state 0.09 eV below the CBM, acting as a donor in BP. A deeper donor level is created in the Zn system, where a filled defect level is induced 0.33 eV below the CBM.

10.2.3.2 Adsorbed TMs

Adsorbed TMs display similar trends as intercalated ones, where Cu and Zn interact more weakly with BP compared to Fe and Ni. Cu adsorbs on a valley site between two P rows and binds to one P atom of each row with a bond length of 2.21 Å. In doing so a donor state is induced at the bottom of the conduction band, leading to n-doping of BP, which is in agreement with previously reported experiments.[261] Zn also adsorbs in a valley site and binds to two surface P atoms with a bond

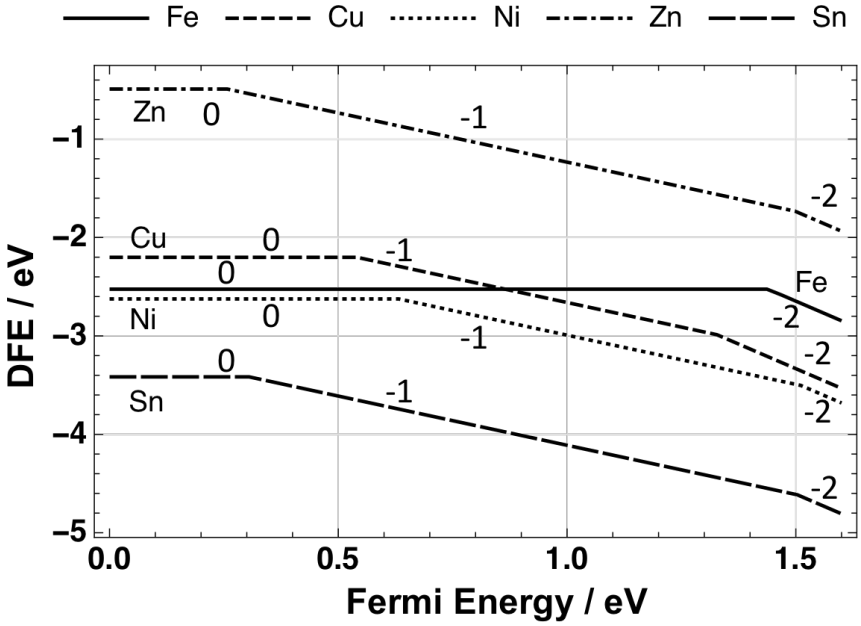

Figure 10.6: Plot of defect formations energies as a function of Fermi level position for a range of substitutional TMs in monolayer BP. Only the lowest energy charge state is ploted for each Fermi level position.

length of 2.95 Å. No bandgap states are induced by the adsorbate, leaving the BP lattice unperturbed. Indeed the small DFE of -0.20 eV and small charge transfer of +0.13 e indicates a weakly interacting Zn adatom. Fe does not exhibit the same bonding behaviour and instead binds to two P atoms of one row (2.27 Å) and one P atom of a neighbouring row (2.18 Å), sitting in a three coordinated valley site. Furthermore, as was observed for intercalated Fe, the S=1 spin state is lower in energy than the singlet state, as the 4s electrons populate the 3d orbitals. Amongst the adsorbed TMs Fe displays the largest charge transfer from the adatom to the BP lattice (+0.32 e). Filled defect states are observed at the VBM related to the Fe adatom. The same can be observed for Ni, which also adsorbs in a three coordinated valley site with two 2.20 Å bonds to one P row and a 2.11 Å bond to the other, adopting the low spin singlet state. The DFE for this configuration is -3.07 eV with very little (0.05 e) charge transfer between the adatom and the lattice.

10.2.3.3 Substitutional TMs

Substitutional TM impurities adopt a P lattice site with a maximum relaxation of 0.26 Å along the armchair direction and 0.05 Å along the out of plane direction.

Their respective defect geometries are shown in Fig. 10.5 and a DFE diagram is illustrated in Fig. 10.6. Cu induces a deep acceptor state 0.42 eV above the VBM. This state is localised on the TM atom and its three nearest neighbour P atoms. The DFE for a Cu_P defect is -2.20 eV. Zn in contrast has a higher DFE of -0.49 eV and a small spin splitting of about 0.1 eV can be observed. This leads to an empty state in the beta (minor) spin channel at the top of the valence band, creating a shallow acceptor state. A larger spin splitting of 0.25 eV was found for the Ni_P defect. For both spin channels an acceptor state was created in the bandgap, which is 0.52 eV above the VBM in the spin up (major) channel and 0.77 eV above the VBM in the spin down (minor) channel. The DFE for Ni_P was calculated to be -2.62 eV, the lowest of the TMs considered.

Lastly, a Fe_P defect was considered. An isolated Fe atom has a magnetic moment of μ_B =4, but upon incorporation into BP, the 4s electrons populate the 3d shell and the μ_B =2 becomes lower in energy. This defect was found to have a DFE of -2.52 eV. Interestingly, an empty state is created in the spin up channel at 0.42 eV above the VBM, however, the corresponding spin down state is located at about 0.05 eV below the CBM.

It is important to note that spin splitting is very sensitive to how exchange interactions are calculated. For the calculations presented here, the proportion of exact Hartree-Fock exchange used in the density functional was fitted for a pristine BP monolayer and bulk properties and not to reproduce TM spin splitting.

Fig. 10.6 illustrates a DFE diagram for substitutional TM defects. Interestingly, the positive charge state is energetically unfavourable for all four TMs considered. Instead at low Fermi energy, all TMs favour the neutral TM_P defect. A charge transition level (CTL) from neutral to -1, ϵ(0/-), is found at 0.6 eV for Ni, 0.55 eV for Cu and 0.28 eV for Zn. Thus, with increasing core charge the ϵ(0/-) CTL shifts to lower Fermi level positions. Zn, Cu, and Ni further display a ϵ(-/-2) CTL in the conduction band at 1.33 eV for Cu and 1.5 eV for Ni and Zn. Interestingly, at 1.43 eV the ϵ(0/-2) CTL is lower in energy than the ϵ(0/-) CTL of Fe.

10.3 Discussion

Experimental evidence for impurity species in BP is considerable. The presented results show that I does not react strongly with BP as P-I bonds are weak. That phosphorus reacts weakly with I can also be seen in the low standard enthalpy of formation of -46 kJ/mol (0.47 eV per molecule) for PI_3, a possible intermediate reactant during crystal growth. Thus we do not expect a large concentration of I related defects in BP. Furthermore, Sn is typically added in excess to bind any I in $Sn(IV)I_4$ and thus prevent reaction with BP.

Sn can be observed in XPS and ICP-MS and SIMS measurements reveal evenly dispersed Sn impurities in BP. I have shown that substitutional Sn is the favoured configuration for Sn defects. In a monolayer, a shallow acceptor state 0.26 eV above the VBM is created, which moves closer to the band edge in a four layer slab. While most literature reported calculations are performed on a monolayer, most experimental data are obtained from bulk crystals or multilayer BP. Thus, our results highlight the need to consider not only monolayer systems, but also BP slabs to be able to compare with experiments directly.

As the defect level becomes more shallow in multi-layer BP, electrons can get excited into it thermally and thus creating hole carriers in BP, which may be the source of observed p-doping, a process not possible for the deep acceptor state in monolayer BP. Such a trapped electron would also induce additional states due to the electrostatic potential of the bound charge. Our data shows, that these states are very extensive and anisotropic in nature. Simulated STM images at selected biases compare well with observed defects in STM measurements, and thus Sn_P defects are proposed to be the source of such defects.

Other dopants, which lead to p-doping are also presented: substitutional oxygen, substitutional and intercalated TMs and P self-interstitials. While most of these defects lead to p-doping, chemical analysis of BP crystals reveals an order of magnitude lower concentrations of TM elements compared to Sn[230] Furthermore, SIMS measurements performed by M. Wentink only detect Sn in significant concentrations, with traces of I and O observed as well, but no TMs could be detected.

Thus, TMs are not considered to be the main contributors to p-doping in BP.

Nevertheless, results on Fe doping indicate that magnetic BP can be achieved. A Fe surface adatom as well as substitutional and intercalated Fe will adopt a spin triplet state. Our calculations represent a disperse low density limit and the long range alignment of spin for higher defect densities was not investigated. However, it has been shown experimentally that Fe doped BP crystals exhibit para-magnetism at room temperature, indicating that no long range alignment into a ferromagnetic state takes place.[264]

Lastly, oxygen interacts strongly with the lone pairs of phosphorus, creating O adatoms and intercalated oxygen, while substitution is less favourable. Oxygen adatoms and interstitials do not contribute to p-doping of BP, since no hole states are created, but substitutional oxygen does. While oxygen has been observed in XPS and SIMS, it is unclear how a large concentration of O_P defects could be created, since they represent a meta-stable state almost 2 eV higher in energy than O_{ads} and O_{int}. Thus, we predict oxygen to adopt O_{ads} and O_{int} configurations instead.

10.4 Conclusion

BP has attracted a lot of attention due to its semi-conducting nature with high hole mobilities, anisotropic behaviour and a tunable bandgap. It has successfully been tested in a p-type field effect transistor, yet the generated current was low.[207]

In this chapter a range of extrinsic dopants were investigated with respect to their effect on the electronic structure of BP. Sn and I are particularly interesting, since these two species are present in large concentrations in BP samples due to their role in the crystal growth process. I does not interact strongly with BP, favouring to passivate dangling bonds as a mono-valent impurity. Although high concentrations of I were detected in IC-PMS measurements, the presented results show that I does not favour to be a dispersed impurity and is predicted to accumulate in defective regions such as e.g. grain boundaries.

Sn however is found to interact more strongly, leading to p-doping when incorporated as a substitutional defect. In a monolayer the induced acceptor state is deep,

whereas in a multi-layer slab an electron can get ionised into the acceptor state thermally, due to its small binding energy. The additional states induced by such a trapped electron are extensive and are approximated by a 2D hydrogen model. Simulated STM images at selected biases match experimental data well. Thus, Sn_P defects are the proposed underlying defect giving rise to observed features in STM as well as observed p-doping. The most promising n-type dopant is Cu as a surface adatom or intercalated in between the BP layers.

Furthermore, magnetic functionalisation can be achieved by intentionally doping BP with Fe. Fe will adopt a triplet state as an adsorbed, substitutional or intercalated defect species, requiring 0.6 eV to flip to a low spin configuration for intercalated Fe. Thus, such isolated defects have possible uses in solotronics applications, quantum computing, memory devices or optoelectronics.

In order to elucidate on the feasibility of BP doping more experimental data is required. While the presented theoretical data suggests doping BP is possible, it is unclear from our results, how such impurities can be implanted into BP. Intentional doping of BP would supplement my theoretical findings. Specifically, experimental studies before and after intentional sputtering with Sn may be usuful to validate these theoretical findings.

Furthermore, effects on carrier mobilities and scattering as well as BP degradation needs to be better understood. Thus, this report will motivate further studies outlining promising candidates for BP functionalisation. A particular problem related to novel BP based technologies is device stability due to BP degradation under ambient conditions. The stability and possible degradation reactions of BP are investigated in the following chapter (Chapter 11).

Chapter 11

Stability of Black Phosphorus Under Ambient Conditions: Interactions with O_2, H_2O and H_2

11.1 Introduction

Among the phosphorus allotropes black phosphorus (BP) is the most stable. BP exhibits a range of interesting properties (see Chapter 8.1), which make BP a viable candidate for many future applications such as gas sensors,[268,269] hydrogen storage,[270] photo-catalysts[271–273] and field-effect transistors.[207,215,274] Yet early experiments were hampered by poor stability of BP in ambient conditions: for example fast oxidation,[275,276] decimation of carrier mobilities[277] and laser induced degradation[278] was reported. Clean surfaces can however be obtained by handling BP crystals in dry nitrogen or cleaving under ultra-high vacuum conditions.[217,272,279] Since such conditions do not reflect those for commercial applications, passivation techniques are being explored to protect BP from ambient air. Encapsulation of BP in AlO_x was shown to prevent rapid decline in charge carrier mobilities and ON/OFF ratio.[277] Thus, in order to facilitate the integration of BP in commercial technologies, the degradation process needs to be better understood.

In this work the adsorption of oxygen, water and hydrogen on pristine and defective BP was investigated using density functional theory (DFT) in conjunction with a hybrid functional. Oxygen was investigated in adsorbed, interstitial and substitutional configurations in order to determine the energetically most favourable state.

Further, the interaction of water and hydrogen with pristine, defective and oxidised BP was investigated. Lastly, reaction enthalpies are calculated from first principles for proposed degradation reactions taking place at the surface of BP under oxygen, water and hydrogen exposure.

11.2 Methods

Density functional theory was used to calculate the electronic structure of a number of defects and adsorbates. The calculations were performed using the CP2K code,[164] which employs a mixed Gaussian and plane wave basis-set (GPW). The DZ_MOLOPT_GTH basis set was used together with Goedecker-Teter-Hutter (GTH) pseudopotentials.[165] The plane wave cutoff was converged at 400 Ry, SCF convergence was set to 10^{-6} a.u. and residual forces on atoms were smaller than 0.01 eV/Å. Since GGA functionals predict a metallic behaviour for BP,[216] the PBE0-TC-LRC hybrid functional[280] was used with a cutoff radius of 2 Å and 10% HF exchange. In order to reduce the computational cost of the hybrid functional calculations, the auxiliary density matrix method (ADMM)[24] was used, which uses a reduced basis set for the HF exchange calculation and thus allows cells up to 1500 atoms large. Since DFT does not reproduce correct dispersion forces, DFT-D3 was employed, which uses Grimme D3 corrections to include attractive vdW interactions. Including vdW interactions is imperative to get the correct interlayer spacing of 3.35 Å as well as adsorption energies for molecules on the surface. A more detailed description and evaluation of the set up can be found in Section 9.3.1.

11.3 Results

11.3.1 Oxygen Impurities

The reactivity of BP with oxygen is a key factor hindering the integration of BP in novel applications. After brief exposure to oxygen, the surface of BP roughens and electrical transport properties degrade rapidly, for example the conductivity decreases by almost two orders of magnitude for oxidised BP and the OFF state current appears broadened.[281] However, it is not clearly understood if the change

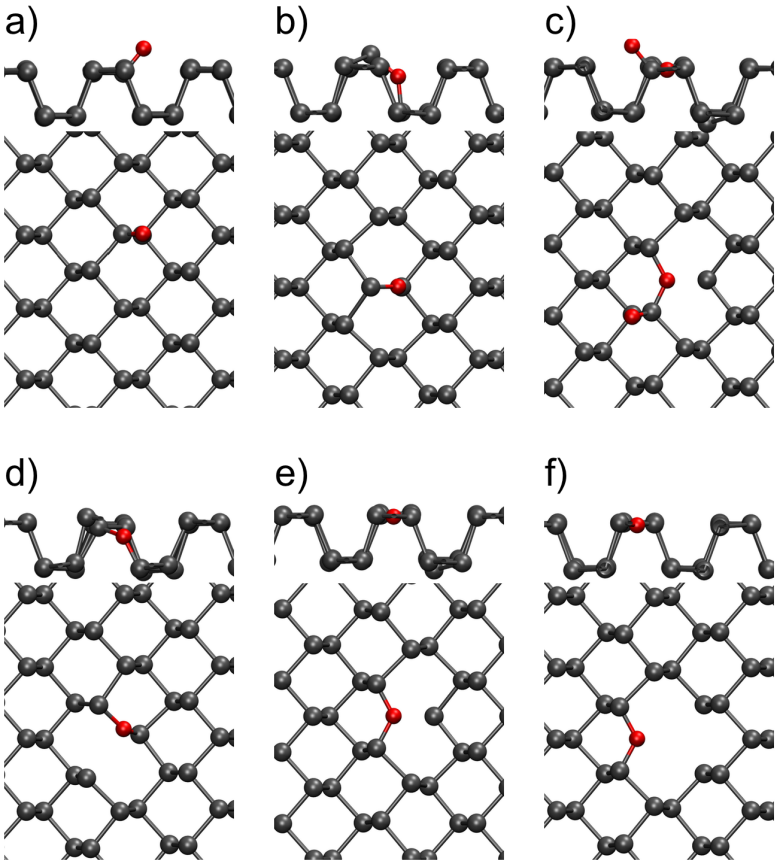

Figure 11.1: Side and top view of oxygen defects in monolayer BP: (a) adsorbed on pristine surface, (b) interstitial, (c) O_2 on v_P, (d+e) substitutional, (f) O_P+v_P. (Grey = P, red = O)

in properties is due to reduced surface contact or inherent to BP. In this section several oxygen defects are calculated in order to gain insight into the oxidation process. For that purpose the DFEs of adsorbed and interstitial O were calculated with respect to an O_2 molecule in its triplet ground state configuration. Hence, DFEs can be directly compared between each other.

Fig. 11.1 illustrates various different oxygen defects in BP. The most stable configuration is surface adsorbed oxygen. The lone pair on phosphorus protruding from the surface is susceptible to oxygen attachment, forming strong P-O double bonds (1.49 Å) as shown in (a). In order to react to phosphorus, the O-O bond of an O_2 molecule, at a bond energy of 5.61 eV, needs to be broken. Previous reports found a barrier of 0.99 eV to dissociate adsorbed O_2 molecule in its triplet state.[282] However, as the oxygen molecule approaches the surface the degeneracy of its π^*_{2p}

orbitals is lifted and the singlet state becomes energetically favourable. Oxygen in its singlet state has a much smaller barrier to dissociate of 0.15 eV. Therefore, a non-radiative transition such as intersystem crossing from triplet to singlet can occur for an adsorbed O_2 molecule and subsequently it can dissociate.[282] An adsorbed oxygen atom has a DFE of -2.0 eV (thus an O_2 molecule has a DFE of -4.0 eV in agreement with -3.92 eV reported in the literature[282]), indicative of strong bonding between BP and oxygen and the density of states shows no bandgap states have been created. Interestingly, intercalated oxygen atom will adopt the same geometry as adsorbed O, forming P=O bonds (1.49 Å) with the lone pair of surface P atoms and a DFE of -1.91 eV per O atom (thus -3.82 eV per O_2 molecule). The difference in DFE is due to the steric hinderance of the O atom in between the BP layers, leading to a small distortion of the BP lattice around the intercalated atom. Since the DFE for surface adsorbed and intercalated oxygen is negative, oxygen favours to react with BP, given the dissociation barrier can be overcome.

In Fig. 11.1b the second most stable configuration is illustrated: an oxygen interstitial. An oxygen atom can get incorporated in the BP lattice in between the upper and lower row of P atoms in a valley position of the monolayer with a DFE of -1.4 eV. The oxygen atom is inserted between an upper and a lower row P atom breaking their bond and leading to a large displacement of the upper P atom in the out of plane direction. The P-O-P angle is 134°, much wider than the optimal tetrahedron bond angle of 109.5° and the phosphorus-pentoxide angles of 102° and 123°, indicating a strained bond angle. No bandgap states are induced by this defect. Since this configuration is 0.6 eV less stable than a surface adsorbed oxygen atom, it will be converted given the activation energy to move the O atom out of the slab can be overcome.

Apart from pristine BP surfaces, the interaction of oxygen with a defective surface containing one MV was investigated also. As reported in Section 9.3.4 MVs have low diffusion barriers. Therefore, they can collide with surface adsorbed oxygen and form defect complexes, which are illustrated in Fig. 11.1c-f.

Fig. 11.1c illustrates the lowest energy configuration of two surface adsorbed

O atoms interacting with a surface MV. One O atom fills the vacancy, creating an O_P defect, while the second remains in an O adatom geometry, bonding to a neighbouring P atom. This compound defect has a DFE of -0.82 eV compared to the isolated MV and surface adsorbed O atoms. A dangling bond is created in the lower P row, inducing a bandgap state in the minor spin channel 0.71 eV above the VBM. The bandgap state is observed at the same energy for substitutional oxygen (configuration (e)), indicating the dangling bond is not affected by the additional adsorbed O atom.

A second stable compound defect was found, in which the O atom fills the vacancy, creating a O_P defect as shown in Fig. 11.1d. A bandgap state 0.5 eV above the VBM is created, which again is related to a dangling bond on an under-coordinated P atom, this time in the upper row of BP. The DFE for "up-down" O_P (d) is -0.46 eV, while it is -0.14 eV for "up-up" O_P (e) both in reference to an isolated MV and surface adsorbed oxygen atom. Therefore, these two defects can coalesce to form an "up-down" O_P defect, given the activation energy can be overcome.

The last oxygen defect considered consists of an adsorbed O atom plus a DV. Although the barrier for O adatom diffusion is unknown, the interaction with a immobile DV was investigated. The compound structure these two defects form is shown in Fig. 11.1f. With a DFE of 1.15 eV in reference to the isolated defects, this structure is thermodynamically unstable.

Surface adsorption was found to be a favoured interaction between BP and oxygen in the low density limit, where adsorbed oxygen atoms are sparsely covering the surface and can favourably interact with surface MVs. Fig. 11.2 illustrates a higher concentration of oxygen on a monolayer surface. One dissociated O_2 molecule per surface unit cell was adsorbed on one side of a monolayer, resulting in a chemical composition of P_4O_2. Unlike the low coverage case, the surface displays large relaxations, adopting a buckled structure in both the upper and lower rows and the formation energy is reduced to -0.7 eV. Thus the degeneracy between the left and right side of a zigzag row is broken, lowering the surface symmetry. Two oxygen environments can be identified: one oxygen environment describes the formation of

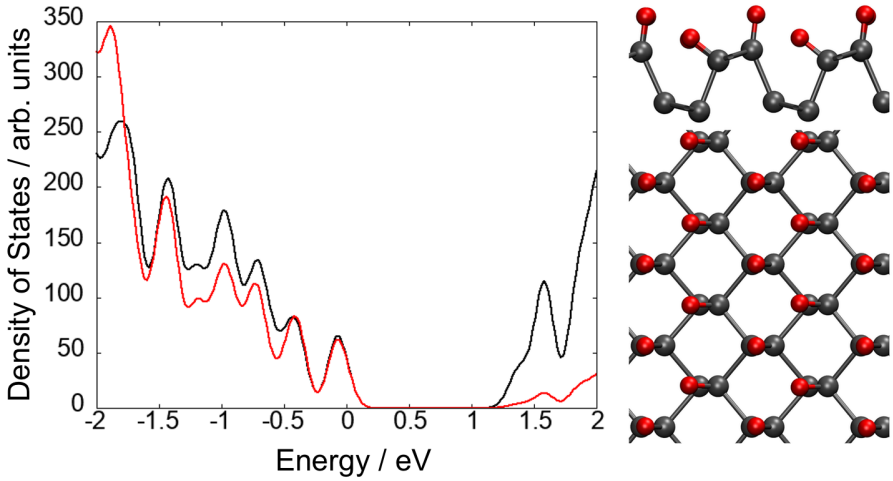

Figure 11.2: Density of states as well as optimised geometry for high density of oxygen chemisorbed on BP. The resulting structure has the composition P_4O_2. (dark-grey = P, red = O)

1.47 Å bonds with one side of the zigzag, pointing along the surface normal and the other environment describes O forming 1.49 Å bonds with P atoms of the other side of the zigzag, pointing at a ≈45° angle to the surface normal towards a P atom of a neighbouring row. The bandgap for this system opens up to 1.33 eV, where the valence band shows mixed P and O character and the conduction band mostly phosphorus character. Continued oxidation of the surface will further increase the bandgap, for example the reported value for P_4O_{10} is 8.5 eV,[283] suggesting that controlled oxidation could be used to engineer the bandgap of BP beyond the monolayer value.

11.3.2 Water Adsorption

The stability of BP under ambient conditions is of particular interest for future applications. While in Section 11.3.1 the interactions with molecular and atomic oxygen is discussed, in this section the interaction of BP with water will be investigated. Fig. 11.3a shows the minimum energy adsorption geometry of a water molecule on a pristine BP monolayer surface. H_2O adsorbs 2.98 Å above the surface with one hydrogen pointing along the zz direction and one pointing towards the surface. The adsorption energy for a single molecule is -0.17 eV and the potential energy landscape shows many local minima close in energy, indicating a flat energy

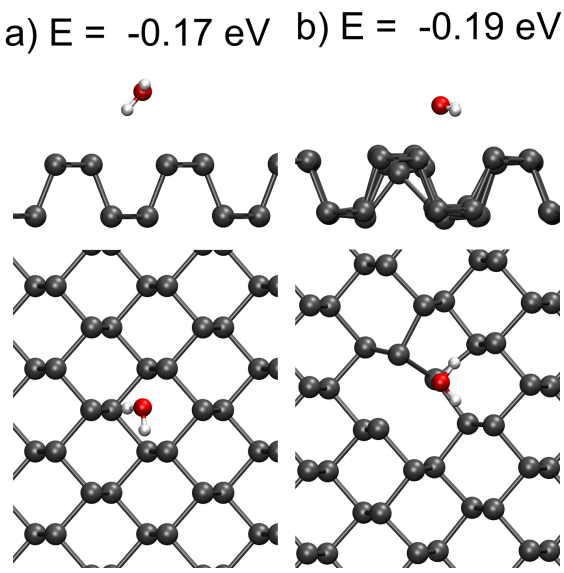

Figure 11.3: Adsorption of H_2O on monolayer BP (a) without a surface defect and (b) with a surface vacancy. Adsorption energies are given above the respective configuration. (dark grey = P, light grey = H, red = O)

landscape. The intermolecular dissociation energy of a water dimer at 0.218 eV[284] is larger than the adsorption energy, indicating that the BP surface is hydrophobic. Indeed, water contact angle measurements confirm a freshly cleaved BP surface exhibits hydrophobicity with a contact angle of ∼90°.[285]

Fig. 11.3b illustrates the adsorption of a water molecule on a surface MV. The water molecule adsorbs above the vacant P lattice site at a distance of 2.76 Å with an adsorption energy of -0.19 eV. This indicates that water adsorbing on a MV is marginally preferential compared to adsorption on a pristine surface. However, at room temperature the energy difference becomes negligible.

Adsorption of water on an adsorbed dissociated oxygen molecule was also studied, in order to investigate the stability of BP under ambient conditions. A water molecule adsorbing on surface adsorbed oxygen has an increased adsorption energy of -0.21 eV, where a hydrogen bond is formed between the water and a surface oxygen atom. The increased adsorption energy with respect to the strength of hydrogen bonds in water (∼0.22 eV) indicates that the surface becomes less hydrophobic upon oxidation. However, dissociation of water on an oxidised surface is not energetically favourable. Splitting water on surface adsorbed oxygen into two adsorbed hydroxyl

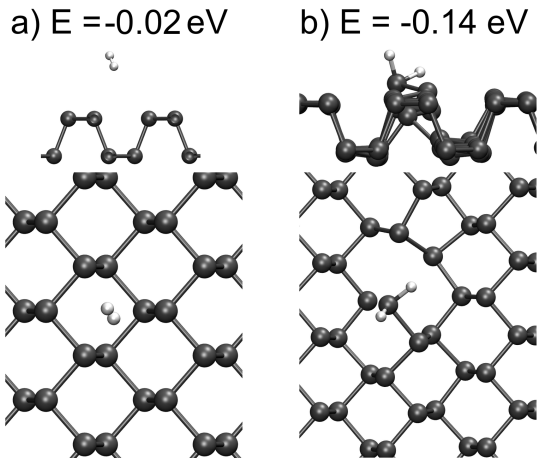

Figure 11.4: Adsorption of H_2 on monolayer BP (a) without a surface defect and (b) with a surface vacancy. Adsorption energies are given above the respective configuration. (dark grey = P, light grey = H)

groups is 1.46 eV higher in energy than the adsorbed molecular species. This indicates that water will adsorb more strongly on surface oxidised BP, but will not readily dissociate to form hydroxyl groups.

11.3.3 Hydrogen Adsorption

Typically, hydrogen is one of the main contaminants in semiconductor fabrication, since many growth techniques, such as vapour phase transport, chemical vapour deposition or molecular beam epitaxy, include hydrogen in the growth environment. It can strongly affect the physical properties of semiconductors and in an interstitial monoatomic form it is electronically active.[286] Monovalent hydrogen can passivate grain boundaries or vacancies in a material, which is of importance to technological applications such as solar cells and further, passivation of dangling bonds on surfaces can have a large impact on surface reconstruction.[287–292] The interactions of hydrogen molecules as well as atomic hydrogen with semiconductors have been the focus of many studies.[293–296] For a wide number of semiconductors, hydrogen acts as an amphoteric impurity, meaning it can either act as a donor or an acceptor. Additionally, the $\epsilon(+/0)$ transition level often lies higher in energy than the $\epsilon(+/-)$ transition level, highlighting the importance to also consider hydrogen ions in first principle calculations. In these cases hydrogen will always counteract the prevailing

conductivity: in a p-doped sample H^+ is favoured, whereas in n-doped samples H^- is favoured.[286, 293, 294]

11.3.3.1 Molecular Adsorption of H_2

In this subsection the interaction of a hydrogen molecule with pristine BP as well as with a MV is investigated. Fig. 11.4a illustrates the adsorption of a H_2 molecule on the surface of a pristine BP monolayer. H_2 adsorbs as a molecular species with an unchanged H-H bond length of 0.75 Å at a distance of 2.98 Å above the BP surface. It interacts very weakly with BP with a small adsorption energy of just 0.02 eV per molecule, which is close to the adsorption energy of 0.07 eV reported in literature.[270] No charge transfer occurs between the molecule and BP, indicating the attractive interaction is due to van der Waals forces.

H_2 adsorption on a surface MV was also investigated. Fig. 11.4b illustrates the interaction of H_2 with a MV. The lowest energy 59-MV in BP has a dangling bond on a two coordinated P atom, which acts as an attachment site for hydrogen. H_2 chemisorbs with a binding energy of -0.14 eV in a dissociated geometry, forming two P-H bonds. Consequently, the P-P bond between the P atom on the lower row and the P atom, on which H_2 chemisorbs, gets broken, creating a dangling bond on the bottom P atom, while the top one is now three coordinated (two P-H bonds and one P-P bond). The BP lattice undergoes large deformation upon this adsorption process, as can be seen in the side view graphic in Fig. 11.4b. Whether a H_2 molecule dissociates will depend on the respective activation barrier, which was not calculated.

11.3.3.2 Atomic H Adsorption

Atomic hydrogen was also investigated in BP, in particular with respect to its role in dangling bond passivation. Atomic hydrogen can adsorb on the pristine monolayer with a DFE of -0.67 eV (0.95 eV with respect to the chemical potential of H_2). A defect formation energy diagram is shown in Fig. 11.5 for atomic H adsorption on pristine BP and on a 59-MV. At low Fermi level the positive charge state is lowest in energy. The $\epsilon(+/0)$ transition level was found to be at 0.6 eV above the VBM

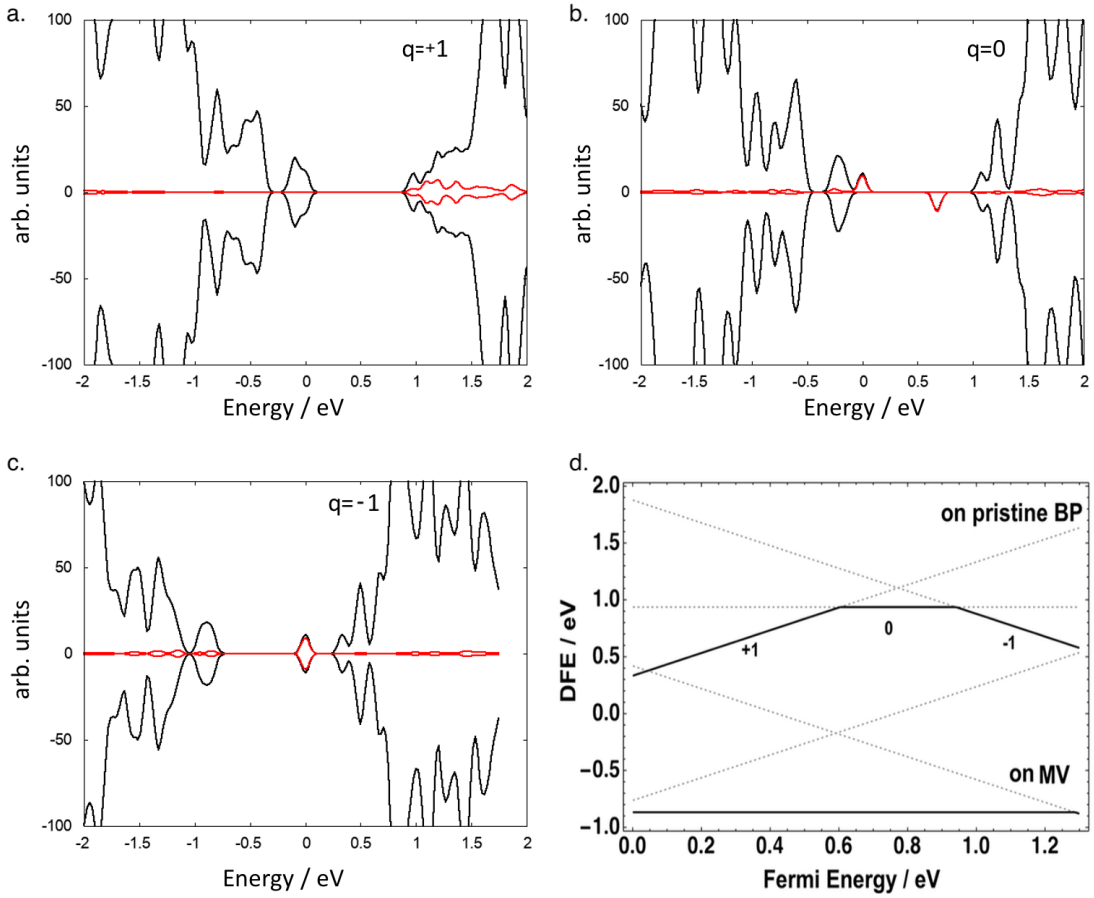

Figure 11.5: DOS plots for atomic hydrogen on pristine monolayer BP in (a) positive charge state, (b) neutral and (c) negative charge state. (black = P, red = H); (d)Defect formation energy diagram for atomic hydrogen on pristine monolayer BP and on a MV.

and the $\epsilon(0/-)$ transition level at 0.94 eV above the VBM, both within the bandgap of monolayer BP. H adsorbed on BP induces a filled state in the major spin channel on top of the VBM and an acceptor state 0.83 eV above the VBM in the minor spin channel. No bandgap state is observed for the positively charged defect and a doubly occupied state 0.83 eV above the VBM can be seen for the negatively charged H defect.

H adsorption on a MV was also investigated and the corresponding defect formation energies are plotted in Fig. 11.5. Only neutral H binding to the undercoordinated P atom was found to be stable for all Fermi level positions. In passivating the dangling bond on the P atom of the MV the bandgap state gets quenched,

recovering a clean bandgap of 1.22 eV. The DFE calculated with respect to half a H_2 molecule is -0.86 eV, which increases to -3.15 eV with respect to an isolated H atom. Thus, chemisorption of a single H atom is favoured compared to chemisorption of H_2 and can be used to passivate MV in BP, as long as the H-H bond can be broken upon forming the P-H bonds, which may have a large activation energy associated with it. While dosing atomic hydrogen could passivate dangling bonds, atomic hydrogen also binds strongly to pristine BP. However, further study is needed to investigate the stability of BP under H_2 dosing or H-plasma exposure. In the following section possible degradation reactions are proposed and reaction enthalpies calculated from DFT total energies.

11.3.4 BP Degradation

BP interacts very strongly with molecular oxygen, which increases the adsorption energy of water molecules. Furthermore, pristine BP interacts weakly with molecular hydrogen, while a MV can be passivated by reacting with a H atom. Interestingly, $HPO(OH)_2$ and $OP(OH)_3$ have been observed in NMR measurements, when BP is dipped in oxygen rich water.[213] Thus, the presence of oxygen and water on the surface is proposed to lead to surface degradation of BP. Assuming pristine BP, H_2O and O_2 are the only reactants, following reactions are possible:

$$2\mathrm{P} + \frac{3}{2}\mathrm{O_2} + 3\mathrm{H_2O} \xrightarrow{-4.65\ \mathrm{eV}} 2\,\mathrm{P(OH)_3} + DV \tag{11.1}$$

$$2\mathrm{P} + \frac{5}{2}\mathrm{O_2} + 3\mathrm{H_2O} \xrightarrow{-10.73\ \mathrm{eV}} 2\,\mathrm{OP(OH)_3} + DV\,. \tag{11.2}$$

Equation 11.1 describes the oxidation of BP to form phosphonic acid. The reaction is exothermic, releasing 2.33 eV per $P(OH)_3$ molecule produced. Similarly, Equation 11.2 describes the oxidation of BP to form phosphoric acid. The reaction is even more exothermic, releasing 5.37 eV per phosphoric acid molecule produced. (Note: the reaction enthalpies were derived from zero point energy calculations and do not take into account temperature dependent effects).

Fig. 11.6 illustrates the oxidation and subsequent hydrolysis of BP for the re-

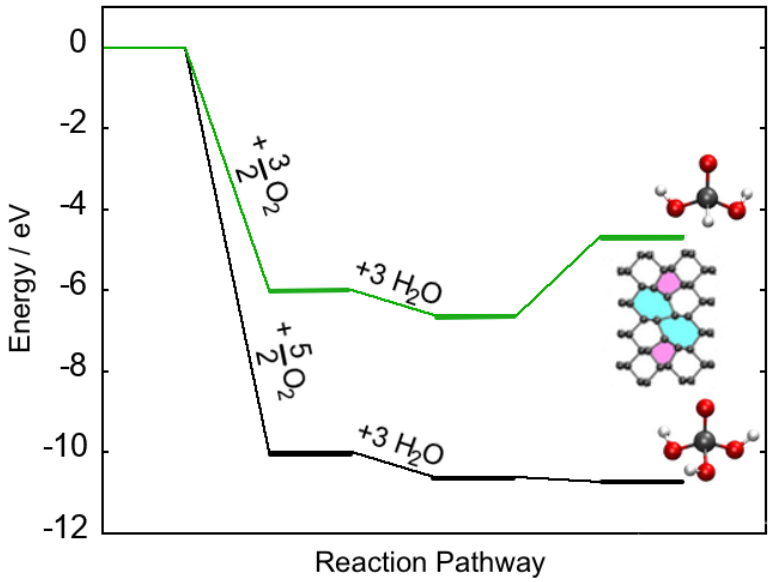

Figure 11.6: Plot of relative reaction energies for oxidation of BP and subsequent hydrolysis. The green line refers to reaction 11.1 and the black line corresponds to reaction 11.2. The insets illustrate the final acid structures and the newly created divacancy on the BP surface.

actions given above. Assuming that oxidation of the BP surface takes place, reaction 11.1 becomes less favourable. Surface oxidation and wetting of the surface is -6.6 eV lower than the starting configuration of pristine BP and water/oxygen in the gas phase, while subsequent hydrolysis of BP to form phosphonic acid is endothermic. This indicates that at low oxygen concentrations, the surface may get oxidised, but hydrolysis is hindered by a large energy penalty to form the final reaction product.

In excess of oxygen, the balance shifts, as indicated by the black line. Surface oxidation yields -10.0 eV and subsequent wetting a further -0.6 eV. Forming phosphoric acid and a di-vacancy however is still lower by 0.13 eV, indicating that this process is exothermic at each stage of the reaction path. Since total energies were calculated and no reaction barriers, these reactions can still be hindered by large activation energies. The calculation of reaction barriers requires knowledge of the reaction path, which is unknown. However, experimental observation of phosphoric acid formation upon oxygen and water exposure indicates barriers are small enough to be overcome at room temperature.[212, 213]

Additionally, it was shown that BP interacts weakly with molecular hydrogen, while atomic hydrogen can be used to passivate dangling bonds related to MVs. A competing reaction, which could take place when reacting BP with H_2 is hydrogenation.

$$2P + 3H_2 \xrightarrow{+3.14\ \text{eV}} 2\ PH_3 + 2\ v_P \tag{11.3}$$

$$PH_3 + 2\,O_2 \xrightarrow{-10.75\ \text{eV}} OP(OH)_3 \tag{11.4}$$

Equation 11.3 describes the hydrogenation reaction of BP, through which phosphine gas is produced. Assuming it is a surface mediated reaction in which P vacancies are formed, this reaction was found to be endothermic, since 3.14 eV per 2 PH_3 molecules produced are required to sustain the reaction. Under-coordinated sites such as grain boundaries, step edges or dislocations would however be less stable against hydrogenation, since atoms are typically less strongly bound at line defects. The produced phosphine gas is highly reactive with oxygen, readily reacting to form phosphoric acid, as shown by Equation 11.4 leading to it being listed as a toxic gas by the centre for disease control.[297] Thus, reaction with molecular hydrogen and molecular oxygen is an alternative degradation reaction to the one given by Equation 11.2.

11.4 Discussion

Adsorption of molecular and atomic species can be used to alter the electronic properties of BP. Oxygen displayed the strongest interactions with BP, in particular adsorption of oxygen molecules, which can dissociate and strongly bind to the lone pairs of surface P atoms. At low coverage the BP lattice is minimally deformed, whereas at higher coverages the surface displays large relaxations and surface buckling. Buckling has been observed in scanning probe experiments, however its origin is still disputed.[217,224,279] But since samples are cleaved in ultra-high vacuum to expose fresh surfaces prior to measurements, it is unlikely that oxygen is the main source of buckling. Oxidation further impacts the electronic structure of BP, widen-

ing the bandgap for highly oxidised BP. Interestingly, the bandgap only opens by about 0.1 eV between BP and P_4O_2, whereas further oxidation to P_4O_{10} drastically widens the gap to over 8 eV, creating an insulating phosphorus oxide. No P-P bonds were broken to produce the P_4O_2 oxide structure, while P_4O_{10} consists of PO_4 tetrahedra, resulting in P-O-P bonds between P atoms. This difference in bonding results in the opening of the bandgap.

Alternative oxygen configurations represent metastable states, such as interstitial oxygen, which is 0.6 eV less stable than adsorbed oxygen. Metastable states can serve as intermediate states, e.g. surface adsorbed molecular oxygen in its singlet state is an intermediate between oxygen in the gas phase and dissociated adsorbed oxygen, lowering the barrier for O_2 dissociation. Interstitial oxygen sits in between the top row and the bottom row of P atoms and can serve as an intermediate state for oxygen diffusion from the surface into the crystal. However, a considerable amount of energy (>0.6 eV) needs to be supplied in order to facilitate the migration of O into the surface. Consequently, the concentration of O interstitials is expected to be low and most oxygen atoms will adapt a surface adatom position. The interaction of a diffusion MV and surface adsorbed oxygen was found to produce defect complexes, which are thermodynamically stable, such as O_P defects.

Substitutional oxygen will result in p-doping, since an acceptor state is created in the bandgap. For monolayer BP the acceptor state lies in the middle of the bandgap, but becomes a shallow state for a four layer slab. Thus, in monolayer BP O dopants are not electronically active, since the state associated with the defect lie in the middle of the bandgap, but are shallow in multilayer BP, where they can get thermally ionised creating free carriers.

H_2O adsorbs weakly on BP, indicating a hydrophobic surface. The potential energy landscape is very shallow and many minima exist close in energy, which are readily accessible via rotation and translation of the molecule. Water preferentially physisorbs on the surface with a slight preference for adsorption over MVs. Dissociation was found to be unfavourable, indicating that BP is stable under pure H_2O exposure.

Adsorption of water is stronger on surface adsorbed oxygen, making the surface less hydrophobic. Dissociation of water on O_{ads} was found to be unfavourable with an associated energy cost of 0.45 eV. Nevertheless, reacting BP with oxygen and water to produce phosphoric acid is exothermic, while the reaction of adsorbed oxygen with water to give phosphonic acid is endothermic. Therefore, the degradation of BP is sensitive to the oxygen concentration in the presence of water. Indeed, it has been observed that the production of phosphoric acid levels off, as the oxygen concentration in water is depleted and small quantities of phosphonic acid are produced.[212, 213]

Lastly, H_2 adsorption was found to be very weak on pristine BP and slightly more favourable on a MV. A H_2 molecule can dissociate on a MV given enough energy is supplied to break the H-H bond. However, a MV reacts strongly with atomic hydrogen with an adsorption energy of -3.15 eV, passivating the dangling bond and thus eliminating the acceptor state in the bandgap. The reaction of BP with H_2 to form phosphine is endothermic (see Equation 11.3), which illustrates the potential to employ H-dosing to passivate dangling bonds in BP. However, how hydrogen diffuses through the crystal and the reaction mechanism for vacancy passivation are unclear, motivating further studies. Particularly, the energy required to dissociate H_2 would be required to estimate reaction rates.

11.5 Conclusions

Understanding of the interactions between BP and ambient atmosphere is vital in order to guarantee its stability in future applications. In this work we investigated possible interactions between oxygen and BP, showing that surface adsorption is the most favourable process. High concentrations of oxygen on BP surfaces opens the bandgap of BP, similar as oxidation of graphene induces a small bandgap.[298] Thus oxidation can be used to engineer the bandgap of BP beyond the monolayer value of 1.5 eV. Metastable states such as O interstitials could facilitate oxygen diffusion from the surface into the bulk, yet the exact mechanism needs to be better understood. Further, it was shown that water interacts weakly with BP, proving

BP is stable in pure H_2O. However, it was found that surface degradation can take place in the presence of both water and oxygen, producing phosphoric acid.

These findings contribute towards a better understanding of the degradation process under ambient conditions. Since the reactions considered use pristine BP monolayers as reference, reaction enthalpies may be underestimated. Under-coordinated sites such as grain boundaries or other line defects may be more reactive, since atoms at such boundaries are less strongly bound. Furthermore, while the reaction enthalpies calculated in this work indicate whether a reaction is energetically favourable, reaction barriers dictate the reaction rate. Therefore, the data presented serves as motivation for further study of the degradation mechanism.

Chapter 12

General Conclusions

The work presented in this thesis spans a range of different areas within materials modelling from the self-assembly of organic films to novel 2D materials characterisation. For that purpose the thesis is divided into three parts.

In Part I the self-assembly of large organic molecules is studied. The process relies on a precise balance between molecule-surface and intermolecular interactions. Therefore, these interactions were investigated piecewise. Chapter 4 is investigating the molecule-surface interactions. Particularly, the importance of considering temperature effects such as entropy is highlighted. As a molecule is adsorbing on the surface, its degrees of freedom, specifically its translational, rotational and conformational ones, become constrained, leading to a reduction in entropy of the system, which in turn reduces the adsorption free energy. For large flexible organics this change in entropy can diminish the adsorption free energy and consequently lead to desorption.

The same approach was applied to lateral interactions, intermolecular as well as between molecules and monatomic step edges in Chapter 5. As molecules diffuse across the surface, they can get attached to step edges, where their translational and rotational motion becomes even more constrained. It was shown that for flexible molecules the contribution from conformational entropy can be significant, leading to a large reduction in entropy. However, the flexibility of the molecule at the same time allows it to alter its geometry in order to maximise the interaction with the step edge, which a rigid molecule can not do. Therefore, despite a large reduction in entropy upon step adhesion for the flexible organic, the free energy is still negative and adhesion is favoured, which is counter-intuitive. These resuls proved

to be able to explain experimental observations, which contradicted the commonly accepted mechanism for nucleation and highlighted the need to move from a static to a dynamic interpretation of self-assembly.

Part II is investigating the role of Ti_i in the reduction process of rutile TiO_2. Experimental observations support the presumption that reduction of TiO_2 emanates from surface oxygen removal at the surface and subsequent Ti diffusion into the bulk in the form of Ti_i. Therefore, Chapter 6 is studying Ti_i in the bulk crystal and Chapter 7 explores Ti_i at the (110) surface and the indiffusion process as a function of surface reduction.

Diffusion of Ti_i has a low barrier along the [001] and [110] direction in the bulk crystal, leading to fast diffusion at elevated temperatures. Additionally, the DFE of Ti_i as well as v_O is reduced at higher temperatures and lower gas pressure. Therefore, during a sample annealing process in vacuum oxygen can leave the crystal, creating surface vacancies, which in turn diminishes the barrier for Ti_i creation at the surface. To separate the interstitial from the defect complex has a large associated barrier, but due to efficient screening the bulk diffusion barrier is recovered thereafter. Thus, surface indiffusion of Ti_i is facilitated by surface oxygen removal.

A novel 2D material, black phosphorus, is researched in Part III. Chapter 9 is looking at intrinsic defects, which were previously proposed to be the source of experimentally observed defects. However, the detailed study shows that intrinsic defects, specifically monovacancies, are not able to fully explain all experimental observations. Thus, in Chapter 10 extrinsic defects are considered, with the emphasis on Sn related defects. Calculations of Sn_P defects reproduce experimental data well and are proposed to be the main defect in black phosphorus, giving rise to p-doped character, shallow acceptor states and hydrogenic defect states in STM. Since these impurities are incorporated during crystal growth, new growth procedures can be developed to target reduced contamination. Lastly, black phosphorus was found to degrade under ambient conditions and Chapter 11 is investigating degradation reactions involving oxygen, water and hydrogen. The formation of a surface phosphorus oxide layer and reaction to phosphoric acid in the presence of water is exothermic,

explaining the fast degradation of black phosphorus under ambient conditions.

12.1 Outlook and Future Work

The study of surfaces of functional materials is still challenging due to the complexity of the system. The self-assembly process can not be modelled directly, since the timescales for growth are very long. Where typically temperature enhanced dynamics is used to increase the probability of overcoming activation energies, it was shown that self-assembled films can become unstable at moderate temperatures. Artificial intelligence can help to bridge the gap, being able to model vast configurations of film structures and find stable polymorphs. The stability of such films at elevated temperatures however, is still hard to model, since phase transitions and kinetics of amorphisation are very slow. Metadynamics could be employed to explore the potential energy landscape at non-zero temperatures, which was previously successfully used for the study of organic crystals.

The chemical activity of reduced TiO_2 is also still not fully understood. While the reported work will aid understanding of the Ti_i defects, v_O and their behaviour at crystal surfaces is still unknown. Furthermore, the study of surface defects has been focussed mainly on the (110) surface, yet other crystallographic surfaces can have significant impact on the reduction of TiO_2. The work presented is indicating that Ti interstitials and O vacancies are interconnected and the reduction of the bulk crystal may well rely on the interplay between these two defects.

Functional 2D materials post graphene are seeing an increase in research activity in recent years. While most work focusses on the study of fundamental properties of the pristine materials, the defect chemistry, surfaces and interfaces with substrates, solvents, electrolytes and adsorbates is vital to enable the transition from lab work benches to real world applications. The presented work outlines the scope for functionalisation of black phosphorus and highlights some challenges relating to sample purity and stability under ambient operating conditions. More work is required to understand the degradation reaction mechanism, surface rippling, elimination of impurity defects and influence of substrates on the performance of black phos-

phorus in order for black phosphorus to reach its full potential as a new ulta-thin semiconductor.

Appendix A

Convergence of Calculations of Entropy

Methods to compute entropies and free energies from molecular dynamics (MD) simulations have been developed for many years and the most popular ones are summarised in ref.[117] Instead of calculating free energies directly, they can be expressed as averages over ensembles of atomic configurations. Such ensembles can be obtained from Monte Carlo (MC) or MD simulations. Despite this seemingly simple process, calculating free energies and their entropic contributions is far from trivial. In order to obtain converged results ergodicity needs to be satisfied. The ergodic principle states that an infinite trajectory (in time) should sample all possible states of a system. In practice, the ergodic assumption allows the extraction of the phase space average from a time series average of trajectories generated via MD simulations. However, in practice these trajectories are finite and it is difficult to predict how long the trajectories need to be a priori.

The challenge of converging entropy calculations is described in this section. TCB forms stable dimers in MD simulations at 300 K, indicating small barriers for dimer formation (see Fig. 5.8). Upon forming a dimer entropy is lost as the two TCB molecules become more constrained. Plotting the change in entropy ($T\Delta S$) as a function of MD run time for this process gives an indicator of whether convergence was reached, as illustrated in Figure A.1. It is important to note that the exponential decay curve was fitted for guidance only and may not be a mathematically accurate representation of the decay rate. At less than 10 ns the change in entropy can be overestimated by an order of magnitude. Only for very long run times (<50 ns) is

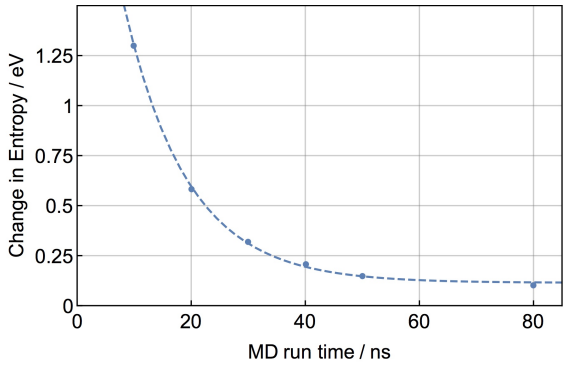

Figure A.1: Convergence of entropy change (TΔS) upon dimer formation with respect to MD simulation time at 300 K. The dashed line is an exponential fit to the data and illustrated for guidance only.

convergence slowly reached to acceptable accuracy ($\sim$0.02 eV) for this process.

Bibliography

[1] Hyuk Kang, Kang Taek Lee, Boyong Jung, Yeon Jae Ko, and Seong Keun Kim. Intrinsic lifetimes of the excited state of dna and rna bases. *Journal of the American Chemical Society*, 124(44):12958–12959, 2002.

[2] Ahren W. Jasper, Chaoyuan Zhu, Shikha Nangia, and Donald G. Truhlar. Introductory lecture: Nonadiabatic effects in chemical dynamics. *Faraday Discuss.*, 127:1–22, 2004.

[3] Kirk A. Peterson, Rick A. Kendall, and Thom H. Dunning. Benchmark Calculations with Correlated Molecular Wave Functions. II. Configuration Interaction Calculations on First Row Diatomic Hydrides. *Journal of Chemical Physics*, 99(3):1930–1944, 1993.

[4] Andreas Grneis, Martijn Marsman, and Georg Kresse. Second-order mllerplesset perturbation theory applied to extended systems. ii. structural and energetic properties. *The Journal of Chemical Physics*, 133(7):074107, 2010.

[5] Frederick R. Manby, Hans-Joachim Werner, Thomas B. Adler, and Andrew J. May. Explicitly correlated local second-order perturbation theory with a frozen geminal correlation factor. *The Journal of Chemical Physics*, 124(9):094103, 2006.

[6] Kieron Burke. Perspective on density functional theory. *The Journal of Chemical Physics*, 136(15):150901, 2012.

[7] D Alf and M J Gillan. The energetics of oxide surfaces by quantum montecarlo. *Journal of Physics: Condensed Matter*, 18(35):L435, 2006.

[8] John P. Perdew, Kieron Burke, and Matthias Ernzerhof. Generalized gradient approximation made simple. *Phys. Rev. Lett.*, 77:3865–3868, 1996.

[9] Pierre-Franois Loos and Peter M. W. Gill. The uniform electron gas. *Wiley Interdisciplinary Reviews: Computational Molecular Science*, 6(4):410–429, 2016.

[10] John P. Perdew, Kieron Burke, and Matthias Ernzerhof. Generalized Gradient Approximation Made Simple. *Phys. Rev. Lett.*, 77(18):3865–3868, 1996.

[11] A. D. Becke. Density-functional exchange-energy approximation with correct asymptotic behavior. *Phys. Rev. A*, 38:3098–3100, 1988.

[12] Chengteh Lee, Weitao Yang, and Robert G. Parr. Development of the colle-salvetti correlation-energy formula into a functional of the electron density. *Phys. Rev. B*, 37:785–789, 1988.

[13] Lianhua He, Fang Liu, Geoffroy Hautier, Micael J. T. Oliveira, Miguel A. L. Marques, Fernando D. Vila, J. J. Rehr, G.-M. Rignanese, and Aihui Zhou. Accuracy of generalized gradient approximation functionals for density-functional perturbation theory calculations. *Phys. Rev. B*, 89:064305, 2014.

[14] S.J. Binnie, E. Sola, D. Alf, and M.J. Gillan. Benchmarking dft surface energies with quantum monte carlo. *Molecular Simulation*, 35(7):609–612, 2009.

[15] Björn Wehinger, Alexeï Bosak, and Paweł T. Jochym. Soft Phonon Modes in Rutile TiO2. *Physical Review B - Condensed Matter and Materials Physics*, 93(1):1–7, 2016.

[16] S. Grimme. Semiempirical GGA-type Density Functional Constructed With a Long-range Dispersion Correction. *J. Comput. Chem.*, 27:1787–1799, 2006.

[17] David Bohm and David Pines. A collective description of electron interactions. i. magnetic interactions. *Phys. Rev.*, 82:625–634, 1951.

[18] O. Anatole von Lilienfeld, Ivano Tavernelli, Ursula Rothlisberger, and Daniel Sebastiani. Optimization of effective atom centered potentials for london dispersion forces in density functional theory. *Phys. Rev. Lett.*, 93:153004, 2004.

[19] Stefan Grimme, Robert Huenerbein, and Stephan Ehrlich. On the importance of the dispersion energy for the thermodynamic stability of molecules. *ChemPhysChem*, 12(7):1258–1261, 2011.

[20] Thomas Weymuth, Jonny Proppe, and Markus Reiher. Statistical analysis of semiclassical dispersion corrections. *J. Comput. Theory Comput.*, 14:2480–2494, 2018.

[21] Aliaksandr V. Krukau, Oleg A. Vydrov, Artur F. Izmaylov, and Gustavo E. Scuseria. Influence of the exchange screening parameter on the performance of screened hybrid functionals. *The Journal of Chemical Physics*, 125(22):224106, 2006.

[22] John P. Perdew, Matthias Ernzerhof, and Kieron Burke. Rationale for mixing exact exchange with density functional approximations. *The Journal of Chemical Physics*, 105(22):9982–9985, 1996.

[23] Marco Hser and Reinhart Ahlrichs. Improvements on the direct scf method. *Journal of Computational Chemistry*, 10(1):104–111.

[24] Manuel Guidon, Jrg Hutter, and Joost VandeVondele. Auxiliary density matrix methods for hartreefock exchange calculations. *Journal of Chemical Theory and Computation*, 6(8):2348–2364, 2010.

[25] Sereina Riniker. Fixed-charge atomistic force fields for molecular dynamics simulations in the condensed phase: An overview. *Journal of Chemical Information and Modeling*, 58(3):565–578, 2018.

[26] Tao Liang, Andrew C. Antony, Sneha A. Akhade, Michael J. Janik, and Susan B. Sinnott. Applied potentials in variable-charge reactive force fields for electrochemical systems. *The Journal of Physical Chemistry A*, 122(2):631–638, 2018.

[27] S. B. Zhang and John E. Northrup. Chemical potential dependence of defect formation energies in GaAs: Application to Ga self-diffusion. *Physical Review Letters*, 67(17):2339–2342, 1991.

[28] T. R. Durrant, S. T. Murphy, M. B. Watkins, and A. L. Shluger. Relation Between Image Charge and Potential Alignment Corrections For Charged Defects in Periodic Boundary Conditions. *The Journal of Chemical Physics*, 149(2):024103, 2018.

[29] Stephan Lany and Alex Zunger. Assessment of correction methods for the band-gap problem and for finite-size effects in supercell defect calculations: Case studies for zno and gaas. *Phys. Rev. B*, 78:235104, 2008.

[30] G. Makov and M. C. Payne. Periodic boundary conditions in ab initio calculations. *Phys. Rev. B*, 51:4014–4022, 1995.

[31] Stephan Lany and Alex Zunger. Accurate prediction of defect properties in density functional supercell calculations. *Modelling and Simulation in Materials Science and Engineering*, 17(8):084002, 2009.

[32] Oliver A Dicks and Alexander L Shluger. Theoretical Modeling of Charge Trapping in Crystalline and Amorphous Al 2 O 3. *Journal of Physics: Condensed Matter*, 29(31):314005, 2017.

[33] M. Calixto and E. Romera. Inverse Participation Ratio and Localization in Topological Insulator Phase Transitions. *Journal of Statistical Mechanics: Theory and Experiment*, 2015(6), 2015.

[34] J. Tersoff and D. R. Hamann. Theory of the scanning tunneling microscope. *Phys. Rev. B*, 31:805–813, 1985.

[35] J Tersoff and Dr Hamann. Theory of the Scanning Tunneling Microscope. *Phys. Rev. B*, 31(2):805–813, 1985.

[36] M. V. Bollinger, J. V. Lauritsen, K. W. Jacobsen, J. K. Nørskov, S. Helveg, and F. Besenbacher. One-dimensional metallic edge states in mos_2. *Phys. Rev. Lett.*, 87:196803, 2001.

[37] D. Wortmann, S. Heinze, Ph. Kurz, G. Bihlmayer, and S. Blügel. Resolving complex atomic-scale spin structures by spin-polarized scanning tunneling microscopy. *Phys. Rev. Lett.*, 86:4132–4135, 2001.

[38] J. Bardeen. Tunnelling from a many-particle point of view. *Phys. Rev. Lett.*, 6:57–59, 1961.

[39] Gábor Mándi and Krisztián Palotás. Chen's derivative rule revisited: Role of tip-orbital interference in stm. *Phys. Rev. B*, 91:165406, 2015.

[40] S. Heinze, M. Bode, A. Kubetzka, O. Pietzsch, X. Nie, S. Blügel, and R. Wiesendanger. Real-space imaging of two-dimensional antiferromagnetism on the atomic scale. *Science*, 288(5472):1805–1808, 2000.

[41] Graeme Henkelman, Blas P. Uberuaga, and Hannes Jnsson. A climbing image nudged elastic band method for finding saddle points and minimum energy paths. *The Journal of Chemical Physics*, 113(22):9901–9904, 2000.

[42] Hannes Jonnson, Greg Mills, and Karsten W. Jacobson. *Nudged elastic band method for finding minimum energy paths of transitions.* World Scientific.

[43] Christine Peter, Chris Oostenbrink, Arthur Van Dorp, and Wilfred F Van Gunsteren. Estimating Entropies From Molecular Dynamics Simulations. *J. Chem. Phys.*, 120(6):2652–2661, 2004.

[44] Harald A. Posch, William G. Hoover, and Franz J. Vesely. Canonical dynamics of the nosé oscillator: Stability, order, and chaos. *Phys. Rev. A*, 33:4253–4265, 1986.

[45] A. Mason, S. C. Mukhopadhyay, and K. P. Jayasundera. *Sensing Technology: Current Status and Future Trends III.* Springer, New York City, USA, 2015.

[46] Nirmalya K. Chaki and K. Vijayamohanan. Self-assembled Monolayers as a Tunable Platform for Biosensor Applications. *Biosens. Bioelectron.*, 17(1-2):1–12, 2002.

[47] Roya Maboudian, W.Robert Ashurst, and Carlo Carraro. Self-assembled monolayers as anti-stiction coatings for mems: Characteristics and recent developments. *Sensor Actuat. A-Phys.*, 82:219 – 223, 2000.

[48] Flemming Besenbacher, Jeppe V. Lauritsen, and Stefan Wendt. Stm studies of model catalysts. *Nano Today*, 2(4):30 – 39, 2007.

[49] X. Zhang and J. Shen. Self-assembled ultrathin films: From layered nanoarchitectures to functional assemblies. *Adv. Mater.*, 11:1139–1143, 1999.

[50] C. Joachim, J.K. Gimezewski, and A. Aviram. Electronics using hybrid-molecular and mono-molecular devices. *Nature*, 408:541–548, 2000.

[51] James R. Heath. Molecular electronics. *Annu. Rev. Mater. Sci.*, 39(1):1–23, 2009.

[52] H. Song, M. A. Reed, and T. Lee. Single molecule electronic devices. *Adv. Mater.*, 23:1583–1608, 2011.

[53] Julia L. Neff, Markus Kittelmann, Ralf Bechstein, and Angelika Kühnle. Decisive Influence of Substitution Positions in Molecular Self-Assembly. *PCCP*, 16(29):15437, 2014.

[54] J. Zhou, S. Dag, S. D. Senanayake, B. C. Hathorn, S. V. Kalinin, V. Meunier, D. R. Mullins, S. H. Overbury, and A. P. Baddorf. Adsorption, desorption, and dissociation of benzene on tio_2(110) and $Pdtio_2$(110): Experimental characterization and first-principles calculations. *Phys. Rev. B*, 74:125318, 2006.

[55] Angelika Khnle. Self-assembly of organic molecules at metal surfaces. *Current Opinion in Colloid Interface Science*, 14(2):157 – 168, 2009.

[56] Bartosz Such, Thomas Trevethan, Thilo Glatzel, Shigeki Kawai, Lars Zimmerli, Ernst Meyer, Alexander L. Shluger, Catelijne H. M. Amijs, Paula de Mendoza, and Antonio M. Echavarren. Functionalized truxenes: Adsorption and diffusion of single molecules on the kbr(001) surface. *ACS Nano*, 4(6):3429–3439, 2010.

[57] Wolfgang Heckel, Tim Wrger, Stefan Mller, and Gregor Feldbauer. Van der waals interaction really matters: Energetics of benzoic acid on tio_2 rutile surfaces. *J. Phys. Chem. C*, 121(32):17207–17214, 2017.

[58] Ania Amrous, Franck Bocquet, Laurent Nony, Christian Loppacher, Frank Palmino, Fréderic Cherioux, David Z. Gao, Filippo Federici Canova, Matthew B. Watkins, Alexander L. Shluger, and et al. Molecular Design and Control Over the Morphology of Self-Assembled Films on Ionic Substrates. *Adv. Mater. Interf.*, 1(9):1400414, dec 2014.

[59] Philipp Rahe, Markus Kittelmann, Julia L Neff, Markus Nimmrich, Michael Reichling, Philipp Maass, and Angelika Kühnle. Tuning molecular self-assembly on bulk insulator surfaces by anchoring of the organic building blocks. *Adv. Mater.*, 25(29):3948–3956, aug 2013.

[60] Mario Einax, Wolfgang Dieterich, and Philipp Maass. Colloquium: Cluster growth on surfaces: Densities, size distributions, and morphologies. *Rev. Mod. Phys.*, 85:921–939, 2013.

[61] Julian Gaberle, David Z. Gao, Alexander L. Shluger, Ania Amrous, Franck Bocquet, Laurent Nony, Franck Para, Christian Loppacher, Simon Lamare, and Fréderic Cherioux. Morphology and Growth Mechanisms of Self-Assembled Films on Insulating Substrates: Role of Molecular Flexibility and Entropy. *Journal of Physical Chemistry C*, 121(8):4393–4403, 2017.

[62] Alexander Schwarz, David Z. Gao, Knud Lämmle, Josef Grenz, Matthew B. Watkins, Alexander L. Shluger, and Roland Wiesendanger. Determining adsorption geometry, bonding, and translational pathways of a metal-organic complex

on an oxide surface: Co-salen on nio(001). *J. Phys. Chem. C*, 117(2):1105–1112, 2013.

[63] T. Waldmann, J. Klein, H. E. Hoster, and R. Jurgen Behm. Stabilization of large adsorbates by rotational entropy: A time-resolved variable-temperature stm study. *ChemPhysChem*, 14:162–169, 2013.

[64] J. Gaberle, D. Z. Gao, F. Federici Canova, M. B. Watkins, and A. L. Shluger. Calculating the entropy loss on adsorption of organic molecules at insulating surfaces. *J. Phys. Chem. C*, 120:3913–3921, 2016.

[65] David Z. Gao, Filippo Federici Canova, Matthew B. Watkins, and Alexander L. Shluger. Efficient Parametrization of Complex Molecule-Surface Force Fields. *J. Comput. Chem.*, 36:1187–1195, 2015.

[66] B.R. Brooks, R.E. Bruccoleri, D.J. Olafson, D.J. States, S. Swaminathan, and M. Karplus. Charmm: A program for macromolecular energy, minimization and dynamics calculations. *J Comput. Chem.*, 4:187–217, 1983.

[67] C R A Catlow, K M Diller, and M J Norgett. Interionic potentials for alkali halides. *Journal of Physics C: Solid State Physics*, 10(9):1395–1412, 1977.

[68] Steve Plimpton. Fast parallel algorithms for short-range molecular dynamics. *J. Comput. Phys.*, 117:1–19, 1995.

[69] T. Kustmann, A. Schlarb, M. Fendrich, T Wagner, R Möller, and R Hoffmann. Dynamic force microscopy study of 3,4,9,10-perylenetetracarboxylic dianhydride on kbr(001). *Phys. Rev.*, 71:121403(R), 2005.

[70] A. Sasahara, Hiroshi Uetsuka, T. Ishibashi, and H. Onishi. A needle-like organic molecule imaged by noncontact atomic force microscopy. *Appl. Surf. Sci.*, 188:265–271, 2002.

[71] Y. Namai, K. Fukui, and Y. Iwasawa. The dynamic behaviour of ch3oh and no2 adsorbed on ceo2(111) studied by noncontact atomic force microscopy. *Nanotechnology*, 15:S49–S54, 2004.

[72] L. Nony, R. Bennewitz, O Pfeiffer, E Gnecco, A Baratoff, E. Meyer, T Eguchi, A Gourdon, and C Joachim. Cu-tbpp and ptcda molecules on insulating surfaces studied by ultra-high-vacuum non-contact afm. *Nanotechnology*, 15:S91–S96, 2004.

[73] S. A. Burke, J. M. Mativetsky, R Hoffmann, and P. Grütter. Nucleation and submonolayer growth of c60 on kbr. *Phys. Rev. Lett.*, 94:096102(1–4), 2005.

[74] T. Dienel, C. Loppacher, S C B Mannsfeld, R Forker, and T. Fritz. Growth-mode-induced narrowing of optical spectra of an organic adlayer. *Adv. Mater.*, 20:959–963, 2008.

[75] S. A. Burke, W. Ji, J. M. Mativetsky, J. M. Topple, S. Fostner, H.-J. Gao, H. Guo, and P. Grütter. Strain induced dewetting of a molecular system: Bimodal growth of ptcda on nacl. *Phys. Rev. Lett.*, 100:186104, May 2008.

[76] J. Schütte, R. Bechstein, P. Rahe, M. Rohlfing, A. Kühnle, and H. Langhals. Imaging perylene derivatives on rutile $tio_2(110)$ by noncontact atomic force microscopy. *Phys. Rev. B*, 79:045428, Jan 2009.

[77] Felix Loske, Ralf Bechstein, Jens Schütte, Frank Ostendorf, Michael Reichling, and Angelika Kühnle. Growth of ordered c60 islands on tio2(110). *Nanotechnology*, 20(6):065606, 2009.

[78] M. Kittelmann, P. Rahe, and A. Kühnle. Molecular self-assembly on an insulating surface: Interplay between substrate templating and intermolecular interactions. *J. Phys.: Condens. Matter*, 24:354007, 2012.

[79] Knud Lämmle, Thomas Trevethan, Alexander Schwarz, Matthew Watkins, Alexander Shluger, and Roland Wiesendanger. Unambiguous determination of the adsorption geometry of a metal-organic complex on a bulk insulator. *Nano Lett.*, 10(8):2965–2971, 2010.

[80] K. Iwata, S. Yamazaki, P. Mutombo, P. Hapala, M. Ondracek, P. Jelinek, and Y. Sugimoto. Chemical structure imaging of a single molecule by atomic force microscopy at room temperature. *Nat. Commun.*, 6:1–7, 2015.

[81] David Zhe Gao, Josef Grenz, Matthew Benjamin Watkins, Filippo Federici Canova, Alexander Schwarz, Roland Wiesendanger, and Alexander L Shluger. Using Metallic Noncontact Atomic Force Microscope Tips for Imaging Insulators and Polar Molecules: Tip Characterization and Imaging Mechanisms. *ACS nano*, 8(5):5339–51, may 2014.

[82] Jun Zhang, Pengcheng Chen, Bingkai Yuan, Wei Ji, Zhihai Cheng, and Xiaohui Qiu. Real-space identification of intermolecular bonding with atomic force microscopy. *Science*, 342(6158):611–614, 2013.

[83] Sampsa K. Hämäläinen, Nadine van der Heijden, Joost van der Lit, Stephan den Hartog, Peter Liljeroth, and Ingmar Swart. Intermolecular contrast in atomic force microscopy images without intermolecular bonds. *Phys. Rev. Lett.*, 113:186102, 2014.

[84] R. Pawlak, L. Nony, Franck Bocquet, Vincent Oison, Michel Sassi, Jean Marc Debierre, Christian Loppacher, and Louis Porte. Supramolecular assemblies of 1,4-benzene diboronic acid on kcl(001). *J. Phys. Chem. C*, 114:9290–9295, 2010.

[85] Clemens Barth, Marc Gingras, Adam S Foster, Andris Gulans, Guy Félix, Teemu Hynninen, Romain Peresutti, and Claude R Henry. Two-dimensional Nanostructured Growth of Nanoclusters and Molecules on Insulating Surfaces. *Adv. Mater.*, 24(24):3228–32, 2012.

[86] C. Kemball. *Entropy of Adsorption, in Advances in Catalysis and Related Subjects, vol. II.* Academic Press, New York City, USA, 1950.

[87] N Ben Tal, B Honig, C K Bagdassarian, and A Ben Shaul. Association Entropy in Adsorption Processes. *Biophys. J.*, 79(3):1180–7, sep 2000.

[88] C. L. Freeman and J. H. Harding. Entropy of molecular binding at solvated mineral surfaces. *J. Phys. Chem. C*, 118:1506–1514, 2013.

[89] R. Hentschke, B. L. Schtirmann, and J. P. Rabe. Molecular dynamics simulations of ordered alkane chains physisorbed on graphite. *J. Chem. Phys.*, 96:6213–6221, 1992.

[90] D. Alfe and M. J. Gillan. Ab initio statistical mechanics of surface adsorption and desorption. *J. Chem. Phys.*, 127:114709, 2007.

[91] Charles T. Campbell and Jason R. V. Sellers. Enthalpies and entropies of adsorption on well-defined oxide surfaces: Experimental measurements. *Chemical Reviews*, 113(6):4106–4135, 2013.

[92] Frédéric Rossel, Marina Pivetta, François Patthey, Elizabeta Ćavar, Ari P. Seitsonen, and Wolf-Dieter Schneider. Growth and Characterization of Fullerene Nanocrystals on NaCl/Au(111). *Physical Review B*, 84(7):075426, 2011.

[93] Samuel Genheden and Ulf Ryde. Will Molecular Dynamics Simulations of Proteins Ever Reach Equilibrium? *Phys. Chem. Chem. Phys.*, 14:8662, 2012.

[94] Aaron R. Dinner, Andrej Šalib, Lorna J. Smitha, Christopher M. Dobsona, and Martin Karplus. Understanding Protein Folding via Free-Energy Surfaces from Theory and Experiment. *TIBS*, 25:331, 2000.

[95] EM Boczko and CL Brooks. First-principles calculation of the folding free energy of a three-helix bundle protein. *Science*, 269:393, 1995.

[96] E. Guàrdia, R. Rey, and J.a. Padró. Potential of Mean Force by Constrained Molecular Dynamics: A Sodium Chloride Ion-Pair in Water. *Chem. Phys.*, 155:187, 1991.

[97] J. Aqvist. Ion-Water Interaction Potentials Derived From Free Energy Perturbation Simulations. *J. Phys. Chem.*, 94:8021, 1990.

[98] Hoi Yu Tang and Ian J. Ford. Free Energies of Molecular Clusters Determined by Guided Mechanical Disassembly. *Phys. Rev. E Stat. Nonlin. Soft Matter Phys.*, 91:1, 2015.

[99] David E. Smith, Ling Zhang, and A. D. J. Haymet. Entropy of association of methane in water: A new molecular dynamics computer simulation. *J. Am. Chem. Soc.*, 114:5875–5876, 1992.

[100] D Alfè and M J Gillan. Absolute Rate of Thermal Desorption From First-principles Simulation. *J. Phys. Condens. Matter*, 18(37):L451–7, sep 2006.

[101] Hannes Jonsson and Greg Mills. Quantum and Thermal Effect in H2 Dissociative Adsorbtion: Evaluation of Free Energy Barriers in Multidimensional Quantum System. *Phys. Rev. Lett.*, 72:1124, 1994.

[102] H. Fox, M.J. Gillan, and a.P. Horsfield. Methods for Calculating the Desorption Rate of Molecules From a Surface at Non-Zero Coverage: Water on MgO(001). *Surf. Sci.*, 603:2171, 2009.

[103] Hagai Meirovitch, Srinath Cheluvaraja, and Ronald P. White. Methods for Calculating the Entropy and Free Energy and Their Application to Problems Involving Protein Flexibility and Ligand Binding. *Curr. Protein Pept. Sci.*, 10:229, 2009.

[104] Kendra King Frederick, Michael S Marlow, Kathleen G Valentine, and a Joshua Wand. Conformational Entropy in Molecular Recognition by Proteins. *Nature*, 448(7151):325–329, 2007.

[105] Stephen D. Pickett and Michael J.E. Sternberg. Empirical scale of side-chain conformational entropy in protein folding. *Journal of Molecular Biology*, 231(3):825 – 839, 1993.

[106] Ming Ma, Gabriele Tocci, Angelos Michaelides, and Gabriel Aeppli. Fast diffusion of water nanodroplets on graphene. *Nat Mater*, 15(1):66–71, jan 2016.

[107] Robert Gomer. Diffusion of adsorbates on metal surfaces. *Rep. Prog. Phys.*, 53:917–1002, 1990.

[108] J Weckesser, J V Barth, and K Kern. Direct observation of surface diffusion of large organic molecules at metal surfaces: Pvba on pd(110). *J. Chem. Phys.*, 110(11):5351–5354, 1999.

[109] Guillaume Copie, Fabrizio Cleri, Younes Makoudi, Christophe Krzeminski, Maxime Berthe, Frédéric Cherioux, Frank Palmino, and Bruno Grandidier. Surface-induced optimal packing of two-dimensional molecular networks. *Phys. Rev. Lett.*, 114(6):066101, 2015.

[110] K Tahara, S Furukawa, H Uji-I, T Uchino, T Ichikawa, J Zhang, W Mamdouh, M Sonoda, F C De Schryver, S De Feyter, and Y Tobe. Two-dimensional porous molecular networks of dehydrobenzo 12 annulene derivatives via alkyl chain interdigitation. *J. Am. Chem. Soc.*, 128(51):16613–16625, 2006.

[111] S Fremy, A Schwarz, K Lmmle, M Prosenc, and R Wiesendanger. The monomer-to-dimer transition and bimodal growth of cosalen on nacl(001): A high resolution atomic force microscopy study. *Nanotechnology*, 20(40):405608, 2009.

[112] Pawel Szabelski, Wojciech Rzysko, and Damian Nieckarz. Directing the self-assembly of tripod molecules on solid surfaces: A monte carlo simulation approach. *J. Phys. Chem. C*, 120(24):13139–13147, 2016.

[113] Fabien Silly, Ulrich K. Weber, Adam Q. Shaw, Victor M. Burlakov, Martin R. Castell, G. A D Briggs, and David G. Pettifor. Deriving molecular bonding from a macromolecular self-assembly using kinetic monte carlo simulations. *Phys. rev. B*, 77(20):201408, 2008.

[114] Simone Conti and Marco Cecchini. Predicting Molecular Self-Assembly at Surfaces: A Statistical Thermodynamics & Modeling Approach. *Phys. Chem. Chem. Phys*, 18:31480–31493, 2016.

[115] Thomas Trevethan, Bartosz Such, Thilo Glatzel, Shigeki Kawai, Alexander L Shluger, Ernst Meyer, Paula de Mendoza, and Antonio M Echavarren. Organic Molecules Reconstruct Nanostructures on Ionic Surfaces. *Small*, 7(9):1264–70, 2011.

[116] Michael Roos, Achim Breitruck, Harry E Hoster, and R Jürgen Behm. Entropic stabilization of large adsorbates on weakly binding substrates-a thermal desorption and scanning tunneling microscopy study. *Physical chemistry chemical physics : PCCP*, 12(4):818–22, 2010.

[117] Daniel Trzesniak, Anna-Pitschna E. Kunz, and Wilfred F. van Gunsteren. A comparison of methods to compute the potential of mean force. *ChemPhysChem*, 8(1):162–169, 2007.

[118] Artur Ciesielski, Pawel J. Szabelski, Wojciech Rzysko, Andrea Cadeddu, Timothy R. Cook, Peter J. Stang, and Paolo Samorí. Concentration-dependent supramolecular engineering of hydrogen-bonded nanostructures at surfaces: Predicting self-assembly in 2d. *J. Am. Chem. Soc.*, 135(18):6942–6950, 2013.

[119] Amandine Bellec, Claire Arrigoni, Guillaume Schull, Ludovic Douillard, Cöline Fiorini-Debuisschert, Fabrice Mathevet, David Kreher, Andrö Jean Attias, and Fabrice Charra. Solution-growth kinetics and thermodynamics of nanoporous self-assembled molecular monolayers. *J. Chem. Phys.*, 134(12):124702, 2011.

[120] Rico Gutzler, Thomas Sirtl, Juìrgen F. Dienstmaier, Kingsuk Mahata, Wolfgang M. Heckl, Michael Schmittel, and Markus Lackinger. Reversible phase transitions in self-assembled monolayers at the liquid-solid interface: Temperature-controlled opening and closing of nanopores. *J. Am. Chem. Soc.*, 132(14):5084–5090, 2010.

[121] Steven De Feyter and Kunal S Mali. Principles of molecular assemblies leading to molecular nanostructures. *Philos. Trans. R. Soc. London A*, 371(2000):20120304, 2013.

[122] Daniel E. Hooks, Torsten Fritz, and Michael D. Ward. Epitaxy and molecular organization on solid substrates. *Adv. Mater.*, 13(4):227–241, 2001.

[123] Michael D. Ward. Soft crystals in flatland: Unraveling epitaxial growth. *ACS Nano*, 10(7):6424–6428, 2016.

[124] Shui-Yang Lien, Dong-Sing Wuu, Wen-Chang Yeh, and Jun-Chin Liu. Tri-layer antireflection coatings (sio2/sio2tio2/tio2) for silicon solar cells using a solgel technique. *Solar Energy Materials and Solar Cells*, 90(16):2710 – 2719, 2006.

[125] Th. Maggos, J.G. Bartzis, M. Liakou, and C. Gobin. Photocatalytic degradation of nox gases using tio2-containing paint: A real scale study. *Journal of Hazardous Materials*, 146(3):668 – 673, 2007.

[126] Masanori Ando, Tetsuhiko Kobayashi, and Masatake Haruta. Combined effects of small gold particles on the optical gas sensing by transition metal oxide films. *Catalysis Today*, 36(1):135 – 141, 1997.

[127] Vaidyanathan Subramanian, Eduardo E. Wolf, and Prashant V. Kamat. Catalysis with tio2/gold nanocomposites. effect of metal particle size on the fermi level equilibration. *Journal of the American Chemical Society*, 126(15):4943–4950, 2004.

[128] M. Kawachi, M. Yasu, and T. Edahiro. Fabrication of sio2-tio2 glass planar optical waveguides by flame hydrolysis deposition. *Electronics Letters*, 19(15):583–584, July 1983.

[129] K Kalyanasundaram. Applications of Functionalized Transition Metal Complexes in Photonic and Optoelectronic Devices. *Coordination Chemistry Reviews*, 177(1):347–414, 1998.

[130] Emilio Palomares, John N. Clifford, Saif A. Haque, Thierry Lutz, and James R. Durrant. Control of Charge Recombination Dynamics in Dye Sensitized Solar Cells by the Use of Conformally Deposited Metal Oxide Blocking Layers. *Journal of the American Chemical Society*, 125(2):475–482, 2003.

[131] B. Karunagaran, Periyayya Uthirakumar, S.J. Chung, S. Velumani, and E.-K. Suh. Tio2 thin film gas sensor for monitoring ammonia. *Materials Characterization*, 58(8):680 – 684, 2007.

[132] H. Tang, K. Prasad, R. Sanjins, and F. Lvy. Tio2 anatase thin films as gas sensors. *Sensors and Actuators B: Chemical*, 26(1):71 – 75, 1995.

[133] Akira Fujishima and Kenichi Honda. Electrochemical Photolysis of Water at a Semiconductor Electrode. *Nature*, 238(5358):37–38, 1972.

[134] Walter Langel. Car Parrinello Simulation of H 2 O Dissociation on Rutile. *Surface Science*, 496(111):141–150, 2002.

[135] Meng Ni, Michael K.H. Leung, Dennis Y.C. Leung, and K. Sumathy. A review and recent developments in photocatalytic water-splitting using tio2 for hydrogen production. *Renewable and Sustainable Energy Reviews*, 11(3):401 – 425, 2007.

[136] Shahed U. M. Khan, Mofareh Al-Shahry, and William B. Ingler. Efficient photochemical water splitting by a chemically modified n-tio2. *Science*, 297(5590):2243–2245, 2002.

[137] Ulrike Diebold. The Surface Science of Titanium Dioxide. *Surface Science Reports*, 48(5-8):53–229, 2003.

[138] Eiichi Yagi, Ryukiti R. Hasiguti, and Masakazu Aono. Electronic conduction above 4 k of slightly reduced oxygen-deficient rutile tio_{2-x}. *Phys. Rev. B*, 54:7945–7956, 1996.

[139] Chi Ming Yim, Chi Lun Pang, and Geoff Thornton. Probing the Local Electronic Structure of the Cross-Linked (1x2) Reconstruction of Rutile TiO2 (110). *Surface Science*, 650:71–75, 2016.

[140] C. M. Yim, M. B. Watkins, M. J. Wolf, C. L. Pang, K. Hermansson, and G. Thornton. Engineering Polarons at a Metal Oxide Surface. *Physical Review Letters*, 117(11):1–5, 2016.

[141] G. Charlton, P. B. Howes, C. L. Nicklin, P. Steadman, J. S. G. Taylor, C. A. Muryn, S. P. Harte, J. Mercer, R. McGrath, D. Norman, T. S. Turner, and G. Thornton. Relaxation of TiO 2 (110) -(1 1) Using Surface X-Ray Diffraction. *Physical Review Letters*, 78(3):495–498, 1997.

[142] Chi Lun Pang, Robert Lindsay, and Geoff Thornton. Structure of Clean and Adsorbate-Covered Single-Crystal Rutile TiO2 Surfaces. *Chemical Reviews*, 113(6):3887–3948, 2013.

[143] Michael Henderson. A Surface Perspective on Self-Diffusion in Rutile TiO2. *Surface Science*, 419(2-3):174–187, 1999.

[144] Min Li, Wilhelm Hebenstreit, Ulrike Diebold, Michael A. Henderson, and Dwight R. Jennison. Oxygen-induced restructuring of rutile tio2(110): Formation mechanism, atomic models, and influence on surface chemistry. *Faraday Discuss.*, 114:245–258, 1999.

[145] V. M. Khomenko, K. Langer, H. Rager, and A. Fett. Electronic absorption by ti3+ ions and electron delocalization in synthetic blue rutile. *Physics and Chemistry of Minerals*, 25(5):338–346, 1998.

[146] Michael A. Henderson, William S. Epling, Charles H. F. Peden, and Craig L. Perkins. Insights into photoexcited electron scavenging processes on tio2 obtained from studies of the reaction of o2 with oh groups adsorbed at electronic defects on tio2(110). *The Journal of Physical Chemistry B*, 107(2):534–545, 2003.

[147] Michael Nolan, Simon D. Elliott, James S. Mulley, Roger A. Bennett, Mark Basham, and Paul Mulheran. Electronic structure of point defects in controlled self-doping of the tio_2 (110) surface: Combined photoemission spectroscopy and density functional theory study. *Phys. Rev. B*, 77:235424, 2008.

[148] Victor E. Henrich, G. Dresselhaus, and H. J. Zeiger. Observation of two-dimensional phases associated with defect states on the surface of tio$_2$. *Phys. Rev. Lett.*, 36:1335–1339, 1976.

[149] P. F. Chester. Electron spin resonance in semiconducting rutile. *Journal of Applied Physics*, 32(10):2233–2236, 1961.

[150] E. Serwicka, M. W. Schlierkamp, and R. N. Schindler. Localisation of Conduction Band Electrons in Polycrystalline TiO$_2$ Studied by ESR. *Zeitschrift für Naturforschung A*, 36(3):226–232, 1981.

[151] P. Le Fèvre, J. Danger, H. Magnan, D. Chandesris, J. Jupille, S. Bourgeois, M.-A. Arrio, R. Gotter, A. Verdini, and A. Morgante. Stoichiometry-related auger lineshapes in titanium oxides: Influence of valence-band profile and of coster-kronig processes. *Phys. Rev. B*, 69:155421, 2004.

[152] R. A. Bennett, P. Stone, N. J. Price, and M. Bowker. Two (1×2) reconstructions of TiO_2(110): Surface rearrangement and reactivity studied using elevated temperature scanning tunneling microscopy. *Phys. Rev. Lett.*, 82:3831–3834, 1999.

[153] Huilei Zhao, Fuping Pan, and Ying Li. Journal of materiomics. 3(1):17–32, 2017.

[154] Olga Dulub, Wilhelm Hebenstreit, and Ulrike Diebold. Imaging cluster surfaces with atomic resolution: The strong metal-support interaction state of pt supported on tio$_2$(110). *Phys. Rev. Lett.*, 84:3646–3649, 2000.

[155] Michael Henderson. A Surface Science Perspective on TiO2 Photocatalysis. *Surface Science Reports*, 66(6-7):185–297, 2011.

[156] Piotr M. Kowalski, Bernd Meyer, and Dominik Marx. Composition, Structure, and Stability of the Rutile TiO_2(110) Surface: Oxygen Depletion, Hydroxylation, Hydrogen Migration and Water Adsorption. *Physical Review B*, 79(11):115410, 2009.

[157] Cristiana Di Valentin, Gianfranco Pacchioni, and Annabella Selloni. Reduced and n-Type doped TiO2: Nature of Ti3+ Species. *Journal of Physical Chemistry C*, 113(48):20543–20552, 2009.

[158] Emanuele Finazzi, Cristiana Di Valentin, and Gianfranco Pacchioni. Nature of ti Interstitials in Reduced Bulk Anatase and Rutile TiO 2. *Journal of Physical Chemistry C*, 113(9):3382–3385, 2009.

[159] B. Montanari and N. M. Harrison. Lattice Dynamics of TiO2 Rutile: Influence of Gradient Corrections in Density Functional Calculations. *Chemical Physics Letters*, 364(5-6):528–534, 2002.

[160] Peter Deák, Bálint Aradi, and Thomas Frauenheim. Polaronic Effects in TiO_2 Calculated by the HSE06 Hybrid Functional: Dopant Passivation by Carrier Self-trapping. *Physical Review B - Condensed Matter and Materials Physics*, 83(15):1–7, 2011.

[161] Duncan John Mowbray and Annapaola Migani. Optical Absorption Spectra and Excitons of Dye-substrate Interfaces: Catechol on TiO2(110). *Journal of Chemical Theory and Computation*, 12(6):2843–2852, 2016.

[162] Peter Deák, Bálint Aradi, and Thomas Frauenheim. Oxygen Deficiency in TiO2: Similarities and Differences Between the Ti Self-interstitial and the O Vacancy in Bulk Rutile and Anatase. *Physical Review B - Condensed Matter and Materials Physics*, 92(4):1–7, 2015.

[163] A. Janotti, J. B. Varley, P. Rinke, N. Umezawa, G. Kresse, and C. G. Van de Walle. Hybrid Functional Studies of the Oxygen Vacancy in TiO2. *Physical Review B*, 81(8):085212, 2010.

[164] Joost VandeVondele, Matthias Krack, Fawzi Mohamed, Michele Parrinello, Thomas Chassaing, and Jürg Hutter. Quickstep: Fast and Accurate Density Functional Calculations Using a Mixed Gaussian and Plane Waves Approach. *Comp. Phys. Commun.*, 167(2):103–128, 2005.

[165] J. VandeVondele and J. Hutter. Gaussian basis sets for accurate calculations on molecular systems in gas and condensed phases. *J. Chem. Phys.*, 127:114105–1–9, 2007.

[166] Karen Johnston, Martin R. Castell, Anthony T. Paxton, and Michael W. Finnis. SrTiO3(001)(2x1) Reconstructions: First-Principles Calculations of Surface Energy and Atomic Structure Compared With Scanning Tunneling Microscopy Images. *Phys. Rev. B*, 70(8):1–12, 2004.

[167] J.D. Cox, D.D. Wagman, and V.A. Mendvedev. Codata key values for thermodynamics. *Hemisphere Publishing Corp., New York*, 1989.

[168] Simon Klüpfel, Peter Klüpfel, and Hannes Jónsson. The Effect of the Perdew-Zunger Self-Interaction Correction to Density Functionals on the Energetics of Small Molecules. *J. Chem. Phys.*, 137(12):1–11, 2012.

[169] C. J. Howard, T. M. Sabine, and F. Dickson. Structural and Thermal Parameters for Rutile and Anatase. *Acta Crystallographica Section B Structural Science*, 47(4):462–468, 1991.

[170] Yasuhisa Tezuka, Shik Shin, Takehiko Ishii, Takeo Ejima, Shoji Suzuki, and Shigeru Sato. Photoemission and Bremsstrahlung Isochromat Spectroscopy Studies of Ti02 (Rutile) and SrTi03. *Journal of the Physical Society of Japan*, 63(1):347–357, 1994.

[171] J. Pascual, J. Camassel, and H. Mathieu. Fine Structure in the Intrinsic Absorption Edge of TiO2. *Physical Review B*, 18(10):5606–5614, 1978.

[172] Wei Kang and Mark S. Hybertsen. Quasiparticle and optical properties of rutile and anatase tio_2. *Phys. Rev. B*, 82:085203, 2010.

[173] S. Wendt, R. Schaub, J. Matthiesen, E.K. Vestergaard, E. Wahlström, M.D. Rasmussen, P. Thostrup, L.M. Molina, E. Lægsgaard, I. Stensgaard, B. Hammer, and F. Besenbacher. Oxygen Vacancies on TiO2(110) and Their Interaction

With H2O and O2: A Combined High-resolution STM and DFT Study. *Surface Science*, 598(1-3):226–245, 2005.

[174] Ulrike Diebold, Jeremiah Lehman, Talib Mahmoud, Markus Kuhn, Georg Leonardelli, Wilhelm Hebenstreit, Michael Schmid, and Peter Varga. Intrinsic Defects on a TiO2(110)(11) Surface and Their Reaction With Oxygen: A Scanning Tunneling Microscopy Study. *Surface Science*, 411(1):137–153, 1998.

[175] Scott J. Thompson and Steven P. Lewis. Revisiting the (110) Surface Structure of TiO2: A Theoretical Analysis. *Physical Review B - Condensed Matter and Materials Physics*, 73(7):2–5, 2006.

[176] Zeineb Helali, Alexis Markovits, Christian Minot, Adnene Dhouib, and Manef Abderrabba. Improved Convergence of Rutile-TiO 2(1 1 0) slab properties with thickness by one-side saturation. *Chemical Physics Letters*, 531:90–93, 2012.

[177] Thomas Bredow, Livia Giordano, Fabrizio Cinquini, and Gianfranco Pacchioni. Electronic Properties of Rutile TiO2 Ultrathin Films: Odd-even Oscillations With the Number of Layers. *Physical Review B - Condensed Matter and Materials Physics*, 70(3):1–6, 2004.

[178] Jun He. *First Principles Calculations of Intrinsic Defects and Extrinsic Impurities in Rutile TiO2*. PhD thesis, 2006.

[179] Haowei Peng. First-Principles Study of Native Defects in Rutile TiO2. *Physics Letters, Section A: General, Atomic and Solid State Physics*, 372(9):1527–1530, 2008.

[180] Jun He and Susan B. Sinnott. Ab initio Calculations of Intrinsic Defects in Rutile TiO2. *Journal of the American Ceramic Society*, 88(3):737–741, 2005.

[181] Samir Abdelouahed and Keith P. McKenna. Relevance of Non-Equilibrium Defect Generation Processes to Resistive Switching in TiO2. *J. Appl. Phys.*, 118(13), 2015.

[182] A. T. Brant, E. M. Golden, N. C. Giles, Shan Yang, M. A. R. Sarker, S. Watauchi, M. Nagao, I. Tanaka, D. A. Tryk, A. Manivannan, and L. E. Halliburton. Triplet ground state of the neutral oxygen-vacancy donor in rutile tio_2. *Phys. Rev. B*, 89:115206, 2014.

[183] D. C. Cronemeyer. Infrared absorption of reduced rutile tio_2 single crystals. *Phys. Rev.*, 113:1222–1226, 1959.

[184] Peter Deák, Bálint Aradi, and Thomas Frauenheim. Quantitative Theory of the Oxygen Vacancy and Carrier Self-Trapping in Bulk TiO 2. *Physical Review B - Condensed Matter and Materials Physics*, 86(19):1–8, 2012.

[185] J R Akse and H B Whitehurst. Diffusion of Titanium in Slightly Reduced Rutile. *J. Phys. Chem. Solids*, 39:457–465, 1978.

[186] Likai Yan, Justin E Elenewski, Wei Jiang, and Hanning Chen. Computational Modeling of Self-Trapped Electrons in Rutile TiO2. *Physical Chemistry Chemical Physics*, 17:29949–29957, 2015.

[187] Fan Zuo, Le Wang, Tao Wu, Zhenyu Zhang, Dan Borchardt, and Pingyun Feng. Self-doped ti3+ enhanced photocatalyst for hydrogen production under visible light. *Journal of the American Chemical Society*, 132(34):11856–11857, 2010.

[188] Hakim Iddir, Serdar Öüt, Peter Zapol, and Nigel D Browning. Diffusion Mechanisms of Native Point Defects in Rutile Ti O2: Ab Initio Total-Energy Calculations. *Physical Review B - Condensed Matter and Materials Physics*, 75(7):2–5, 2007.

[189] Abu Md Asaduzzaman and Peter Krüger. A First Principles Study on Charge Dependent Diffusion of Point Defects in Rutile TiO2. *Journal of Physical Chemistry C*, 114(46):19649–19652, 2010.

[190] C Catlow and R James. Disorder in tio_{2-x}. *Proceedings of the Royal Society of London A: Mathematical, Physical and Engineering Sciences*, 384(1786):157–173, 1982.

[191] M. Aono and R. R. Hasiguti. Interaction and Ordering of Lattice Defects in Oxygen-Deficient Rutile TiO2-x. *Physical Review B*, 48(17):12406–12414, 1993.

[192] Tor S. Bjørheim, Akihide Kuwabara, and Truls Norby. Defect Chemistry of Rutile TiO2from First Principles Calculations. *Journal of Physical Chemistry C*, 117(11):5919–5930, 2013.

[193] Li Bin Shi and Yong Ping Wang. A Study on Native Defects and Magnetic Properties in Undoped Rutile TiO2 using LDA and LDA+UO p+UTi Methods. *Journal of Magnetism and Magnetic Materials*, 405:1–8, 2016.

[194] Alberto Naldoni, Mattia Allieta, Saveria Santangelo, Marcello Marelli, Filippo Fabbri, Serena Cappelli, Claudia L. Bianchi, Rinaldo Psaro, and Vladimiro Dal Santo. Effect of nature and location of defects on bandgap narrowing in black tio2 nanoparticles. *Journal of the American Chemical Society*, 134(18):7600–7603, 2012.

[195] Zhou Wang, Chongyin Yang, Tianquan Lin, Hao Yin, Ping Chen, Dongyun Wan, Fangfang Xu, Fuqiang Huang, Jianhua Lin, Xiaoming Xie, and Mianheng Jiang. H-doped black titania with very high solar absorption and excellent photocatalysis enhanced by localized surface plasmon resonance. *Advanced Functional Materials*, 23(43):5444–5450, 2013.

[196] Michael Bowker and Roger a Bennett. The Role of Ti 3+ Interstitials in TiO 2 (110) Reduction and Oxidation. *Journal of Physics: Condensed Matter*, 21(47):474224, 2009.

[197] Hiroshi Onishi and Yasuhiro Iwasawa. Reconstruction of tio2(110) surface: Stm study with atomic-scale resolution. *Surf. Sci.*, 313(1):L783 – L789, 1994.

[198] Min Li, Wilhelm Hebenstreit, Leo Gross, Ulrike Diebold, M. a. Henderson, D. R. Jennison, P. a. Schultz, and M. P. Sears. Oxygen-Induced Restructuring of the TiO2(110) Surface: A Comprehensive Study. *Surf. Sci.*, 437(1):173–190, 1999.

[199] Charles A. Jenkins and Damien M. Murphy. Thermal and photoreactivity of tio2 at the gassolid interface with aliphatic and aromatic aldehydes. *The Journal of Physical Chemistry B*, 103(6):1019–1026, 1999.

[200] P a Mulheran, M Nolan, C S Browne, M Basham, E Sanville, and R a Bennett. Surface and Interstitial Ti Diffusion at the Rutile TiO(2)(110) Surface. *Physical chemistry chemical physics : PCCP*, 12(33):9763–9771, 2010.

[201] Kandis Leslie Gilliard-Abdulaziz and Edmund G. Seebauer. Microkinetic Model for Reaction and Diffusion of Titanium Interstitial Atoms Near a TiO2(110) Surface. *Physical Chemistry Chemical Physics*, 20(6):4587–4596, 2018.

[202] Y. Aiura, Y. Nishihara, Y. Haruyama, T. Komeda, S. Kodaira, Y. Sakisaka, T. Maruyama, and H. Kato. Effects of Surface Oxygen Vacancies on Electronic States of TiO2(110), TiO2(001) and SrTiO3(001) Surfaces. *Physica B*, 194:1215—-1216, 1994.

[203] Michael A. Henderson, William S. Epling, Charles H.F. Peden, and Craig L. Perkins. Insights into Photoexcited Electron Scavenging Processes on TiO2 Obtained From Studies of the Reaction of O2 With OH Groups Adsorbed at Electronic Defects on TiO2(110). *Journal of Physical Chemistry B*, 107(2):534–545, 2003.

[204] W Gopel, J.A. Anderson, D. Frankel, M. Jaehnig, K. Phillips, J.A. Schäfer, and G. Rocker. Surface Defects of TiO2(110): A Combined XPS, XAES and ELS Study. *Surface Science*, 139:333–346, 1984.

[205] Michael A. Henderson. Evidence for Bicarbonate Formation on Vacuum Annealed TiO2(11O) Resulting From a Precursor-Mediated Interaction Between CO2and H2O. *Surface Science*, 400(1-3):203–219, 1998.

[206] Robert W. Keyes. The electrical properties of black phosphorus. *Phys. Rev.*, 92:580–584, 1953.

[207] Likai Li, Yijun Yu, Guo Jun Ye, Qingqin Ge, Xuedong Ou, Hua Wu, Donglai Feng, Xian Hui Chen, and Yuanbo Zhang. Black Phosphorus Field-effect Transistors. *Nature Nanotechnology*, 9(5):372–377, 2014.

[208] A. S. Rodin, A. Carvalho, and A. H. Castro Neto. Strain-induced gap modification in black phosphorus. *Phys. Rev. Lett.*, 112:176801, 2014.

[209] Liangbo Liang, Jun Wang, Wenzhi Lin, Bobby G. Sumpter, Vincent Meunier, and Minghu Pan. Electronic Bandgap and Edge Reconstruction in Phosphorene Materials. *Nano Lett.*, 14(11):6400–6406, 2014.

[210] Ø Prytz and E Flage-Larsen. The Influence of Exact Exchange Corrections in van der Waals Layered Narrow Bandgap Black Phosphorus. *J. Phys: Condens. Matter*, 22:015502, 2010.

[211] Jingsi Qiao, Xianghua Kong, Zhi-xin Hu, Feng Yang, and Wei Ji. High-mobility Transport Anisotropy and Linear Dichroism in Few-layer Black Phosphorus. *Nat. Comm.*, 5:1–7, 2014.

[212] Gaoxue Wang, William J. Slough, Ravindra Pandey, and Shashi P. Karna. Degradation of Phosphorene in Air: Understanding at Atomic Level. *2D Mater.*, 3:025011, 2016.

[213] Yue Wang, Bingchao Yang, Bensong Wan, Xuekui Xi, Zhongming Zeng, Enke Liu, Guangheng Wu, Zhongyuan Liu, and Wenhong Wang. Degradation of Black Phosphorus: A Real-time ³¹ P NMR study. *2D Materials*, 3(3):035025, 2016.

[214] Xiaolong Liu, Joshua D. Wood, Kan Sheng Chen, Eunkyung Cho, and Mark C. Hersam. In Situ Thermal Decomposition of Exfoliated Two-dimensional Black Phosphorus. *Journal of Physical Chemistry Letters*, 6(5):773–778, 2015.

[215] Joon Seok Kim, Yingnan Liu, Weinan Zhu, Seohee Kim, Di Wu, Li Tao, Ananth Dodabalapur, Keji Lai, and Deji Akinwande. Toward Air-Stable Multilayer Phosphorene Thin-Films and Transistors. *Sci. Rep.*, 5:1–7, 2015.

[216] A. N. Rudenko, Shengjun Yuan, and M. I. Katsnelson. Toward a Realistic Description of Multilayer Black Phosphorus: From GW Approximation to Large-scale Tight-binding Simulations. *Phys. Rev. B*, 92(8):1–10, 2015.

[217] Brian Kiraly, Nadine Hauptmann, Alexander N Rudenko, Mikhail I Katsnelson, and Alexander A Khajetoorians. Probing Single Vacancies in Black Phosphorus at the Atomic Level. *Nano Lett.*, 17:3607–3612, 2017.

[218] Yongqing Cai, Qingqing Ke, Gang Zhang, Boris I. Yakobson, and Yong Wei Zhang. Highly Itinerant Atomic Vacancies in Phosphorene. *JACS*, 138:10199–10206, 2016.

[219] Wei Hu and Jinlong Yang. Defects in Phosphorene. *J. of Phys. Chem. C*, 119:20474–20480, 2015.

[220] Ting Hu and Jinming Dong. Geometric and Electronic Structures of Mono- and Di-Vacancies in Phosphorene. *Nanotechnology*, 26:065705, 2015.

[221] Thomas Olsen, Simone Latini, Filip Rasmussen, and Kristian S. Thygesen. Simple Screened Hydrogen Model of Excitons in Two-Dimensional Materials. *Physical Review Letters*, 116(5):1–5, 2016.

[222] Alexey Chernikov, Timothy C. Berkelbach, Heather M. Hill, Albert Rigosi, Yilei Li, Ozgur Burak Aslan, David R. Reichman, Mark S. Hybertsen, and Tony F. Heinz. Exciton Binding Energy and Nonhydrogenic Rydberg Series in Monolayer WS2. *Physical Review Letters*, 113(7):1–13, 2014.

[223] P. Umari, O. Petrenko, S. Taioli, and M. M. De Souza. Communication: Electronic band gaps of semiconducting zig-zag carbon nanotubes from many-body perturbation theory calculations. *J. Chem. Phys.*, 136(18):181101, 2012.

[224] C. D. Zhang, J. C. Lian, W. Yi, Y. H. Jiang, L. W. Liu, H. Hu, W. D. Xiao, S. X. Du, L. L. Sun, and H. J. Gao. Surface Structures of Black Phosphorus Investigated with Scanning Tunneling Microscopy. *J. Phys. Chem. C*, 113(43):18823–18826, 2009.

[225] Zhizhan Qiu, Hanyan Fang, Alexandra Carvalho, A. S. Rodin, Yanpeng Liu, Sherman J. R. Tan, Mykola Telychko, Pin Lv, Jie Su, Yewu Wang, A. H. Castro Neto, and Jiong Lu. Resolving the Spatial Structures of Bound Hole States in Black Phosphorus. *Nano Lett.*, 17(11):6935–6940, 2017.

[226] Yuzheng Guo and John Robertson. Vacancy and Doping States in Monolayer and Bulk Black Phosphorus. *Sci. Rep.*, 5:14165, 2015.

[227] Run Long, Weihai Fang, and Alexey V Akimov. Nonradiative Electron Hole Recombination Rate Is Greatly Reduced by Defects in Monolayer Black Phosphorus: Ab Initio Time Domain Study. *J. Phys. Chem. Lett.*, 7:653–659, 2016.

[228]

[229] Stefan Lange, Peer Schmidt, and Tom Nilges. Au3SnP7 Black Phosphorus: An Easy Access to Black Phosphorus. *Inorganic Chemistry*, 46(10):4028–4035, 2007.

[230] Carmen C. Mayorga-Martinez, Zdeněk Sofer, David Sedmidubský, Jan Luxa, Bahareh Kherzi, and Martin Pumera. Metallic Impurities in Black Phosphorus Nanoflakes Prepared by Different Synthetic Routes. *Nanoscale*, pages 1540–1546, 2018.

[231] Tom Nilges, Marcel Kersting, and Thorben Pfeifer. A Fast Low-pressure Transport Route to Large Black Phosphorus Single Crystals. *Journal of Solid State Chemistry*, 181(8):1707–1711, 2008.

[232] Marianne Köpf, Nadine Eckstein, Daniela Pfister, Carolin Grotz, Ilona Krüger, Magnus Greiwe, Thomas Hansen, Holger Kohlmann, and Tom Nilges. Access and in Situ Growth of Phosphorene-precursor Black Phosphorus. *Journal of Crystal Growth*, 405:6–10, 2014.

[233] Xiaoli Sun and Zhiguo Wang. Sodium Adsorption and Diffusion on Monolayer Black Phosphorus With Intrinsic Defects. *Appl. Surf. Sci.*, 427:189–197, 2018.

[234] Jin-wu Jiang and Harold S Park. Negative Poisson's Ratio in Single-Layer Black Phosphorus. *Nat. Comm.*, 5:1–7, 2014.

[235] Likai Li, Jonghwan Kim, Chenhao Jin, Guo Jun Ye, Diana Y Qiu, Felipe H Jornada, Zhiwen Shi, Long Chen, Zuocheng Zhang, Fangyuan Yang, Kenji Watanabe, Takashi Taniguchi, Wencai Ren, Steven G Louie, Xian Hui Chen, Yuanbo Zhang, and Feng Wang. Direct Observation of the Layer-dependent Electronic Structure in Phosphorene. *Nat. Nanotechnol.*, 12(1):21–25, 2016.

[236] V. Sorkin, Y. Cai, Z. Ong, G. Zhang, and Y. W. Zhang. Recent advances in the study of phosphorene and its nanostructures. *Crit. Rev. Solid State*, 42(1):1–82, 2017.

[237] Yongqing Cai, Gang Zhang, and Yong Wei Zhang. Layer-Dependent Band Alignment and Work Function of Few-Layer Phosphorene. *Scientific Reports*, 4:1–6, 2014.

[238] H. Rydberg, M. Dion, N. Jacobson, E. Schröder, P. Hyldgaard, S. I. Simak, D. C. Langreth, and B. I. Lundqvist. Van der waals density functional for layered structures. *Phys. Rev. Lett.*, 91:126402, 2003.

[239] Xiaobin Chen, Fuyang Tian, Clas Persson, Wenhui Duan, and Nan Xian Chen. Interlayer Interactions in Graphites. *Scientific Reports*, 3:1–5, 2013.

[240] Stewart J. Clark and John Robertson. Screened exchange density functional applied to solids. *Phys. Rev. B*, 82:085208, 2010.

[241] Yuanyue Liu, Fangbo Xu, Ziang Zhang, Evgeni S. Penev, and Boris I. Yakobson. Two-dimensional Mono-elemental Semiconductor With Electronically Inactive Defects: The Case of Phosphorus. *Nano Lett.*, 14(12):6782–6786, 2014.

[242] Dan Wang, Dong Han, Xian-Bin Li, Nian-Ke Chen, Damien West, Vincent Meunier, Shengbai Zhang, and Hong-Bo Sun. Charged Defects in Two-Dimensional Semiconductors of Arbitrary Thickness and Geometry: Formulation and Application to Few-Layer Black Phosphorus. *Physical Review B*, 96(15):155424, 2017.

[243] X. L. Yang, S. H. Guo, F. T. Chan, K. W. Wong, and W. Y. Ching. Analytic solution of a two-dimensional hydrogen atom. i. nonrelativistic theory. *Phys. Rev. A*, 43:1186–1196, 1991.

[244] D. G. W. Parfitt and M. E. Portnoi. The two-dimensional hydrogen atom revisited. *Journal of Mathematical Physics*, 43(10):4681–4691, 2002.

[245] M. Aghajanian, A. A. Mostofi, and J. Lischner. Bound States of Charged Adatoms on MoS2: Screening and Multivalley Effects. *ArXiv e-prints*, 2018.

[246] Dillon Wong, Fabiano Corsetti, Yang Wang, Victor W. Brar, Hsin-Zon Tsai, Qiong Wu, Roland K. Kawakami, Alex Zettl, Arash A. Mostofi, Johannes Lischner, and Michael F. Crommie. Spatially resolving density-dependent screening around a single charged atom in graphene. *Phys. Rev. B*, 95:205419, 2017.

[247] Konstantin N. Kudin, Bulent Ozbas, Hannes C. Schniepp, Robert K. Prud'homme, Ilhan A. Aksay, and Roberto Car. Raman spectra of graphite oxide and functionalized graphene sheets. *Nano Lett.*, 8:36–41, 2008.

[248] Jie Ma, Dario Alfè, Angelos Michaelides, and Enge Wang. Stone-wales defects in graphene and other planar sp^2-bonded materials. *Phys. Rev. B*, 80:033407, 2009.

[249] M. Umar Farooq, Arqum Hashmi, and Jisang Hong. Anisotropic Bias Dependent Transport Property of Defective Phosphorene Layer. *Sci. Rep.*, 5:1–11, 2015.

[250] J. V. Riffle, C. Flynn, B. St. Laurent, C. A. Ayotte, C. A. Caputo, and S. M. Hollen. Impact of Vacancies on Electronic Properties of Black Phosphorus Probed by STM. *J. Appl. Phys.*, 123(4):044301, 2018.

[251] Han Liu, Yuchen Du, Yexin Deng, and Peide D. Ye. Semiconducting Black Phosphorus: Synthesis, Transport Properties and Electronic Applications. *Chem. Soc. Rev.*, 44(9):2732–2743, 2015.

[252] Paul M. Koenraad and Michael E. Flatté. Single Dopants in Semiconductors. *Nature Materials*, 10(2):91–100, 2011.

[253] J. Kobak, T. Smoleński, M. Goryca, M. Papaj, K. Gietka, A. Bogucki, M. Koperski, J. G. Rousset, J. Suffczyński, E. Janik, M. Nawrocki, A. Golnik, P. Kossacki, and W. Pacuski. Designing Quantum Dots for Solotronics. *Nature Communications*, 5, 2014.

[254] E. Flores, J. R. Ares, A. Castellanos-Gomez, M. Barawi, I. J. Ferrer, and C. Sánchez. Thermoelectric Power of Bulk Black Phosphorus. *Applied Physics Letters*, 106(2), 2015.

[255] A. Morita. Semiconducting Black Phosphorus. *Applied Physics A Solids and Surfaces*, 39(4):227–242, 1986.

[256] Alexandra Carvalho, Min Wang, Xi Zhu, Aleksandr S. Rodin, Haibin Su, and Antonio H. Castro Neto. Phosphorene: From Theory to Applications. *Nature Reviews Materials*, 1(11), 2016.

[257] Tao Hu and Jisang Hong. First-Principles Study of Metal Adatom Adsorption on Black Phosphorene. *Journal of Physical Chemistry C*, 119(15):8199–8207, 2015.

[258] Xue-fang Yu, Hiroshi Ushiyama, and Koichi Yamashita. Comparative Study of Sodium and Lithium Intercalation and Diffusion Mechanism in Black Phosphorus From First-principles Simulation. *Chem. Lett.*, 43(12):1940–1942, 2014.

[259] Jimin Kim, Seung Su Baik, Sae Hee Ryu, Yeongsup Sohn, Soohyung Park, Byeong-Gyu Park, Jonathan Denlinger, Yeonjin Yi, Hyoung Joon Choi, and Keun Su Kim. Observation of tunable band gap and anisotropic dirac semimetal state in black phosphorus. *Science*, 349(6249):723–726, 2015.

[260] K. P S S Hembram, Hyun Jung, Byung Chul Yeo, Sung Jin Pai, Seungchul Kim, Kwang Ryeol Lee, and Sang Soo Han. Unraveling the Atomistic Sodiation Mechanism of Black Phosphorus for Sodium Ion Batteries by First-Principles Calculations. *Journal of Physical Chemistry C*, 119(27):15041–15046, 2015.

[261] Steven P. Koenig, Rostislav A. Doganov, Leandro Seixas, Alexandra Carvalho, Jun You Tan, Kenji Watanabe, Takashi Taniguchi, Nikolai Yakovlev, Antonio H. Castro Neto, and Barbaros Özyilmaz. Electron Doping of Ultrathin Black Phosphorus with Cu Adatoms. *Nano Letters*, 16(4):2145–2151, 2016.

[262] Du Xiang, Cheng Han, Jing Wu, Shu Zhong, Yiyang Liu, Jiadan Lin, Xue Ao Zhang, Wen Ping Hu, Barbaros Özyilmaz, A. H.Castro Neto, Andrew Thye Shen Wee, and Wei Chen. Surface Transfer Doping Induced Effective Modulation on Ambipolar Characteristics of Few-Layer Black Phosphorus. *Nature Communications*, 6, 2015.

[263] Xiaoyu Xuan, Zhuhua Zhang, and Wanlin Guo. Doping-Stabilized Two-Dimensional Black Phosphorus. *Nanoscale*, 10(17):7898–7904, 2018.

[264] Xiaohong Jiang, Xinwei Zhang, Fang Xiong, Zhenghe Hua, Zhihe Wang, Shaoguang Yang, Xiaohong Jiang, Xinwei Zhang, Fang Xiong, Zhenghe Hua, and Zhihe Wang. Room Temperature Ferro-Magnetism in Transition Metal-Doped Black Phosphorous. *Appl. Phys. Lett.*, 112:192105, 2018.

[265] Hongbo Wang, Shasha Zhu, Fengren Fan, Zhengwei Li, and Hua Wu. Structure and Magnetism of Mn, Fe, or Co Adatoms on Monolayer and Bilayer Black Phosphorus. *Journal of Magnetism and Magnetic Materials*, 401:706–710, 2016.

[266] Zongyu Huang, Yanbing Wu, Xiang Qi, Chaoyu He, Xiaohui Ren, and Jianxin Zhong. Electronic and Magnetic Properties of Monolayer and Bilayer Phosphorene Doped with Transition-Metal Atoms. *Physica Status Solidi (B) Basic Research*, 1700370:1–7, 2017.

[267] Zhinan Guo, Si Chen, Zhongzheng Wang, Zhenyu Yang, Fei Liu, Yanhua Xu, Jiahong Wang, Ya Yi, Han Zhang, Lei Liao, Paul K. Chu, and Xue Feng Yu. Metal-Ion-Modified Black Phosphorus with Enhanced Stability and Transistor Performance. *Advanced Materials*, 29(42):1–8, 2017.

[268] Geonyeop Lee, Suhyun Kim, Sunwoo Jung, Soohwan Jang, and Jihyun Kim. Suspended Black Phosphorus Nanosheet Gas Sensors. *Sensor Actuat. B Chem.*, 250:569–573, 2017.

[269] Ahmad N. Abbas, Bilu Liu, Liang Chen, Yuqiang Ma, Sen Cong, Noppadol Aroonyadet, Marianne Köpf, Tom Nilges, and Chongwu Zhou. Black Phosphorus Gas Sensors. *ACS Nano*, 9(5):5618–5624, 2015.

[270] Qing Fang Li, X. G. Wan, Chun Gang Duan, and Jer Lai Kuo. Theoretical Prediction of Hydrogen Storage on Li-decorated Monolayer Black Phosphorus. *Journal of Physics D: Applied Physics*, 47(46):465302, 2014.

[271] Mingshan Zhu, Yasuko Osakada, Sooyeon Kim, Mamoru Fujitsuka, and Tetsuro Majima. Black Phosphorus: A Promising two Dimensional Visible and Near-Infrared-Activated Photocatalyst for Hydrogen Evolution. *Applied Catalysis B: Environmental*, 217:285–292, 2017.

[272] Alexandre Favron, Etienne Gaufrès, Frédéric Fossard, Anne Laurence Phaneuf-Laheureux, Nathalie Y.W. Tang, Pierre L. Lévesque, Annick Loiseau, Richard Leonelli, Sébastien Francoeur, and Richard Martel. Photooxidation and Quantum Confinement Effects in Exfoliated Black Phosphorus. *Nature Materials*, 14(8):826–832, 2015.

[273] Ye Zhou, Maoxian Zhang, Zhinan Guo, Lili Miao, Su-Ting Han, Ziya Wang, Xiuwen Zhang, Han Zhang, and Zhengchun Peng. Recent Advancement in Black Phosphorus-Based Photonics, Electronics, Sensors and Energy Devices. *Mater. Horiz.*, 4:997–1019, 2017.

[274] Andres Castellanos-Gomez. Black Phosphorus: Narrow Gap, Wide Applications. *Journal of Physical Chemistry Letters*, 6(21):4280–4291, 2015.

[275] Shueh Lin Yau, Thomas P. Moffat, Allen J. Bard, Zhengwei Zhang, and Michael M. Lerner. STM of the (010) Surface of Orthorhombic Phosphorus. *Chemical Physics Letters*, 198(3-4):383–388, 1992.

[276] M. T. Edmonds, A. Tadich, A. Carvalho, A. Ziletti, K. M. ODonnell, S. P. Koenig, D. F. Coker, B. zyilmaz, A. H. Castro Neto, and M. S. Fuhrer. Creating a stable oxide at the surface of black phosphorus. *ACS Applied Materials & Interfaces*, 7(27):14557–14562, 2015.

[277] Joshua D. Wood, Spencer A. Wells, Deep Jariwala, Kan Sheng Chen, Eunkyung Cho, Vinod K. Sangwan, Xiaolong Liu, Lincoln J. Lauhon, Tobin J. Marks, and Mark C. Hersam. Effective Passivation of Exfoliated Black Phosphorus Transistors Against Ambient Degradation. *Nano Letters*, 14(12):6964–6970, 2014.

[278] A. Yoshihara, T. Fujimura, Y. Oka, H. Fujisaki, and I. Shirotani. Surface Brillouin Scattering in Black Phosphorus. *Physical Review B*, 34(10):7467–7470, 1986.

[279] Zhongwei Dai, Wencan Jin, Jie-Xiang Yu, Maxwell Grady, Jerzy T. Sadowski, Young Duck Kim, James Hone, Jiadong Zang, Richard M. Osgood, and Karsten Pohl. Surface Buckling of Phosphorene Materials: Determination, Origin and Influence on Electronic Structure. *Physical Review Materials*, 1:074003, 2017.

[280] Manuel Guidon, Jrg Hutter, and Joost VandeVondele. Robust periodic hartreefock exchange for large-scale simulations using gaussian basis sets. *J. Chem. Theory Comput.*, 5(11):3010–3021, 2009.

[281] Joshua O. Island, Gary A. Steele, Herre S. J. van der Zant, and Andres Castellanos-Gomez. Environmental Instability of Few-layer Black Phosphorus. *2D Materials*, 2, 2015.

[282] A. Ziletti, A. Carvalho, D. K. Campbell, D. F. Coker, and A. H. Castro Neto. Oxygen Defects in Phosphorene. *Physical Review Letters*, 114(4):26–29, 2015.

[283] A. Ziletti, A. Carvalho, P. E. Trevisanutto, D. K. Campbell, D. F. Coker, and A. H. Castro Neto. Phosphorene Oxides: Bandgap Engineering of Phosphorene by Oxidation. *Physical Review B - Condensed Matter and Materials Physics*, 91(8):1–12, 2015.

[284] Biswajit Santra, Angelos Michaelides, Martin Fuchs, Alexandre Tkatchenko, Claudia Filippi, and Matthias Scheffler. On the Accuracy of Density-Functional Theory Exchange-Correlation Functionals for H Bonds in Small Water Clusters. II. the Water Hexamer and van der Waals Interactions. *Journal of Chemical Physics*, 129(19), 2008.

[285] Yuan Huang, Jingsi Qiao, Kai He, Stoyan Bliznakov, Eli Sutter, Xianjue Chen, Da Luo, Fanke Meng, Dong Su, Jeremy Decker, Wei Ji, Rodney S. Ruoff, and Peter Sutter. Interaction of Black Phosphorus with Oxygen and Water. *Chemistry of Materials*, 28(22):8330–8339, 2016.

[286] Chris G. Van de Walle and Jörg Neugebauer. Hydrogen in Semiconductors. *Annual Review of Materials Research*, 36(1):179–198, 2006.

[287] N.M. Johnson, C. Doland, F. Ponce, J. Walker, and G. Anderson. Hydrogen in crystalline semiconductors: A review of experimental results. *Physica B: Condensed Matter*, 170(1):3 – 20, 1991.

[288] Chris G. Van de Walle. Theoretical aspects of hydrogen in crystalline semiconductors. *Physica B: Condensed Matter*, 170(1):21 – 32, 1991.

[289] J.A. Schaefer. Electronic and structural properties of hydrogen on semiconductor surfaces. *Physica B: Condensed Matter*, 170(1):45 – 68, 1991.

[290] C.M. Bertoni, F. Finocchi, F. Bernardini, and M.Buongiorno Nardelli. Hydrogen on semiconductor surfaces: Theory of the electronic structure. *Physica B: Condensed Matter*, 170(1):429 – 435, 1991.

[291] Yannick Wimmer, Al-Moatasem El-Sayed, Wolfgang Gös, Tibor Grasser, and Alexander L. Shluger. Role of hydrogen in volatile behaviour of defects in sio2-based electronic devices. *Proceedings of the Royal Society of London A: Mathematical, Physical and Engineering Sciences*, 472(2190), 2016.

[292] Al-Moatasem El-Sayed, Yannick Wimmer, Wolfgang Goes, Tibor Grasser, Valery V. Afanas'ev, and Alexander L. Shluger. Theoretical models of hydrogen-induced defects in amorphous silicon dioxide. *Phys. Rev. B*, 92:014107, 2015.

[293] Chris G Van de Walle and J Neugebauer. Universal Alignment of Hydrogen Levels in Semiconductors, Insulators and Solutions. *Nature*, 423:626, 2003.

[294] T. Su, P. C. Taylor, G. Ganguly, and D. E. Carlson. Direct role of hydrogen in the staebler-wronski effect in hydrogenated amorphous silicon. *Phys. Rev. Lett.*, 89:015502, 2002.

[295] Chris G. Van de Walle, P. J. H. Denteneer, Y. Bar-Yam, and S. T. Pantelides. Theory of hydrogen diffusion and reactions in crystalline silicon. *Phys. Rev. B*, 39:10791–10808, 1989.

[296] ChihTang Sah, Jack YuanChen Sun, and Joseph JengTao Tzou. Deactivation of the boron acceptor in silicon by hydrogen. *Applied Physics Letters*, 43(2):204–206, 1983.

[297] National Institute for Occupational Safety and Health (NIOSH), PHOSPHINE: Lung Damaging Agent, 2017-11-09 retreived from website on 18/07/2018: `https://www.cdc.gov/niosh/ershdb/emergencyresponsecard_29750035.html`.

[298] M. Wu, C. Cao, and J. Z. Jiang. Light Non-metallic Atom (B, N, O and F)-doped Graphene: A First-principles Study. *Nanotechnology*, 21(50), 2010.